OPTIMIZATION AND DESIGN OF COILS FOR ELECTROMAGNETIC INDUCTION SYSTEMS

A Dissertation
Presented to
The Academic Faculty

by

Mark Alan Reed

In Partial Fulfillment
of the Requirements for the Degree
Doctor of Philosophy in the
School of Electrical and Computer Engineering

Georgia Institute of Technology

August 2021

OPTIMIZATION AND DESIGN OF COILS FOR ELECTROMAGNETIC INDUCTION SYSTEMS

Approved by:

Dr. Waymond R. Scott, Jr., Advisor
School of Electrical and Computer Engineering
Georgia Institute of Technology

Dr. Morris B. Cohen
School of Electrical and Computer Engineering
Georgia Institute of Technology

Dr. Andrew F. Peterson
School of Electrical and Computer Engineering
Georgia Institute of Technology

Dr. Samer Naif
School of Earth and Atmospheric Sciences
Georgia Institute of Technology

Dr. Gregory D. Durgin
School of Electrical and Computer Engineering
Georgia Institute of Technology

Date Approved: May 18, 2021

To my parents, Ed and Patty, for their love and support over the years.

ACKNOWLEDGEMENTS

I would like to thank my advisor, Dr. Waymond Scott, for his guidance, mentorship, and endless patience, without which this work would not have been possible. I very much appreciate the time and effort devoted to reviewing my dissertation by my committee members, Dr. Andrew Peterson, Dr. Gregory Durgin, Dr. Morris Cohen, and Dr. Samer Naif.

I would also like to thank the other researchers in the Electromagnetics Lab whom I have had the privilege to know and work with over the years. The wisdom, company, and insights of the likes of Yoni Gabbay, Michael McFadden, Mu-Hsin Wei, and James Sustman have been indispensable both in completing this research and staying sane along the way. Both Yoni and Mike have been particularly helpful in lending their expertise in various areas with which I was less familiar.

I appreciate the support of my friends over the years as I worked through the various problems that inevitably arise with novel research. Corey and Sadie Mayo have been helpful both with diversions from research when I needed them and with aid in other areas, and Kathleen Tokuda has been a wonderful cycling companion who has always had a nugget of wisdom when I needed one.

Finally, none of this would have been possible without the support of my parents, Ed and Patty Reed, who have always been encouraging and supportive of my pursuits.

TABLE OF CONTENTS

LIST OF TABLES

LIST OF FIGURES

SUMMARY

This dissertation presents a new method of optimizing coils for electromagnetic induction (EMI) systems used in subsurface sensing. The new optimization method uses stream functions to represent wire coils rather than attempting to optimize wire coils directly. Stream functions allow a more general optimization than is possible with conventional wire coils.

To support the new optimization procedure, a set of normalized metrics was also developed. These metrics take into account important coil characteristics, such as target sensitivity, soil sensitivity, power dissipation, coil coupling, thermal noise, etc.

The metrics are applicable to both conventionally-defined wire coils and to the stream function representation, and the metrics allow comparison between wire coils and stream function coils. The metrics are independent of system electronics and also coil parameters such as conductor type and size and overall coil dimensions.

The new optimization method was used to optimize coils represented as stream functions. The new method makes use of several techniques including the exploitation of problem symmetry to reduce the number of unknowns. Even with various methods to reduce the number of unknowns, the problem would be intractable without exploiting the partial convexity of the problem statement. By using a convex optimization technique, coils can be optimized in hours instead of the unfathomable number of years a brute-force technique would require.

The coils that were optimized using the stream-function representation have new, interesting wire paths. These coils were shown to perform significantly better than those optimized using a conventional representation, especially when the performance in magnetic soils was considered. The resulting coils are superior to the canonical wire coils from Chapter 6, and their combined metric, $\widehat{S}_{\mathrm{ggm}} + \widehat{S}_{\mathrm{ggms}}$, is from 2.3 to 10.2 dB better depending on which groups of coils are being compared.

CHAPTER I

INTRODUCTION

Systems using electromagnetic induction (EMI) have many varied applications, including the detection of obscured conductive objects, medical imaging, nondestructive testing, and wireless, short-range power transfer. The details of these methods may differ slightly, but the coils used to transmit and receive fields are very important in each application. Improvements in the performance of these systems can be made by optimizing the coil winding patterns. An optimization procedure for induction coils was developed in the context of coils used for the detection of objects buried in the ground. Normalized metrics for the comparison of these coils were also developed to aid in their optimization. This work focuses on coils for use in continuous-wave (CW) EMI systems in particular, but minor modifications could be made to optimize coils for other uses.

Systems that use electromagnetic induction have been in use for over a century to detect obscured metallic objects. Alexander Graham Bell constructed a crude induction balance sensing system in an attempt to locate the bullet lodged in President Garfield's back, and induction-based sensors were put to use in the detection of mines and unexploded ordnance as far back as World War I [4,69]. EMI systems, such as those designed by Gerhard Fisher, were later put to use by treasure hunters to search for buried objects such as lost coins or rings [69]. Currently, there are many systems of varying complexity being used for the detection of many different types of buried conductive objects.

EMI systems have proven to be effective tools for detecting buried metallic objects, but they suffer from several limitations and trade-offs. While EMI systems are very good at detecting conductive objects, their range is limited to one or two coil diameters because of the quasi-static nature of the fields. Their range decreases dramatically when the targets are small, weakly conductive, or buried in mineralized soil. If the system is a continuous-wave system, which transmits and receives concurrently, it is highly desirable for the transmit and

receive coils not to couple to one another because the target signals are often very weak. Coil configurations that have negligible coupling have been known for many years, but these configurations typically have the detriment of limiting either the range of detection or the coils' rejection of the soil response.

The current work aims to create coil designs that have minimum mutual coupling while minimizing the signal induced in the receive coil by the soil and maximizing their sensitivity to targets. Normalized metrics to allow comparison with other coils were developed to aid these goals.

Many traditional methods for designing coils are very restrictive in the winding patterns that the coils can take. A more generalized representation for the coils was created using stream functions. This representation has the benefit of allowing a partially convex optimization procedure to be used, which allows optimizations to be done in a reasonable amount of time over many dimensions. The optimization also allows the field directions produced by the system to be optimized to improve target imaging, and it can be extended to allow the creation of arrays of multiple coils.

Coils were optimized using the stream function method, and the new coils are anywhere from 2.3 to 10.2 dB better than existing wire coils that are examined in Chapter 6 when the soil sensitivity is considered in addition to the target sensitivity. These traits enhance the ability of systems to detect buried objects, particularly in mineralized soil.

The stream functions were then converted to a simple wire-wound representation. By calculating the normalized metrics for the stream functions and for the wires by using two different methods, the validity of using stream functions as a method of representing and optimizing coils was demonstrated. Not only do stream functions provide a more general method of representing coils, but the new coil families generated using the optimization could also be refined as wire coils, further improving their performance.

1.1 EMI Sensing Principles

Continuous-wave EMI systems use a transmit coil driven with a time-varying current to produce a magnetic field, which induces eddy currents in conductive targets. The eddy

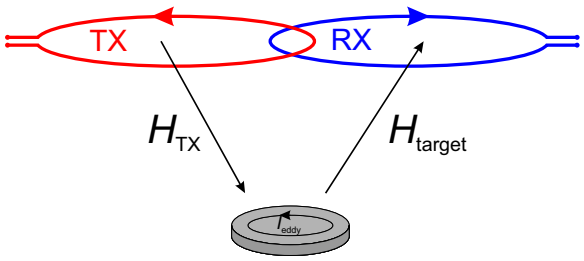

Figure 1: Illustration of a simple EMI system and target.

currents then produce a secondary field that induces an electromotive force (EMF) in the receive coil, as illustrated in Figure 1 [1]. The EMF induced in the receive coil indicates the presence of conductive objects.

EMI systems typically operate at frequencies of up to a few hundred kilohertz, and the fields produced by EMI systems are magneto-quasistatic. Therefore, the displacement current can be neglected and a quasistatic analysis can be used [22].

1.1.1 Coil Sensitivity and Target Detection

The transmit coil creates a magnetic field at the target that induces a magnetic dipole moment on the target as a result of the target's magnetic polarizability. The dipole moment of the target then induces a voltage at the receive coil. The full expression for the open-circuit voltage induced in the receive coil by a target that has been excited by a signal from the transmit coil is

$$V_{\mathrm{RX}} = \frac{j\omega\mu_0}{I_{\mathrm{RX}}} \vec{H}_{\mathrm{RX}} \cdot \bar{\bar{m}} \cdot \vec{H}_{\mathrm{TX}} \,, \tag{1}$$

where ω is angular frequency, μ_0 is magnetic permeability, $\vec{H}_{\mathrm{TX}}$ is the transmit field, $\bar{\bar{m}}_{\mathrm{p}}$ is a dyad representing the magnetic polarizability of the target, and $\vec{H}_{\mathrm{RX}}$ is the field produced by the receive coil if it is driven by the current I_{RX} [53,62]. The dyad $\bar{\bar{m}}_{\mathrm{p}}$ is dependent upon the target's shape and orientation relative to the coil head [1,64]. If the target is positioned in a manner such that the coils couple into the eddy current modes of the target, a voltage will be induced in the receive coil, and detection will be straightforward. However, if the target is positioned such that the transmit coil does not couple into the eddy current modes of the target, very little voltage will be induced in the receive coil, and detection will be difficult. Therefore, if the transmit and receive coils each produce fields that are oriented in

a single direction, the system may be blind to a target in certain orientations relative to the coil head. Movement of the coil head about the target can partially mitigate this issue by altering the direction of the fields at the target. On the other hand, systems with more than two coils may have coils transmitting and/or receiving in many or all possible orientations rather than relying on the operator to move the coil head relative to the target [51].

Though EMI systems are good at detecting conductive objects near the surface of the earth, their range is limited. In a way this is desirable because many items of interest are often buried close to the surface, and the sensor naturally excludes clutter (detected objects or anomalies that are not targets) that is buried deeper than the sensor's maximum detection depth. However, the range of EMI systems is typically on the order of one coil diameter, and when the coils are only 25 cm in diameter, the range becomes limiting [1].

Detection is particularly difficult when there is an excessive amount of interference in the search area or the targets are very small, weakly conductive, or are buried in magnetically permeable soil. Even if the targets are large, the signals received from them will be small compared to the signal of the transmit coil [1]. Therefore, system design typically requires that the transmit and receive coils have minimum mutual coupling, lest the receive coil senses only the transmit coil and not the target.

1.1.2 Coil Coupling

The transmit and receive coils can couple to one another both inductively and capacitively. The inductive coupling can be minimized through winding techniques or by properly positioning the coils with respect to one another. As long as the coils are separated sufficiently, capacitive coupling between the coils is not problematic, but the coils may be shielded individually if necessary. A significant portion of the remaining signal in the receive coil resulting from coupling can be removed through signal processing techniques [52].

1.1.3 Soil Response

In addition to sensing electrically conductive materials, EMI systems also sense magnetically permeable materials by aligning the dipole moments within the material. The alignment increases the magnetic field, which is then sensed by the system in the same manner as

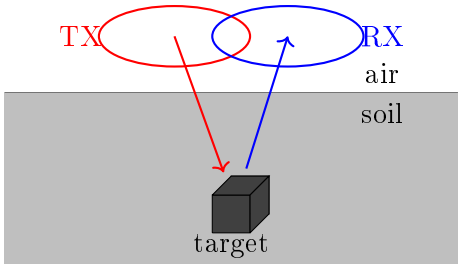

Figure 2: Two-coil head illuminating target buried in soil.

conductive materials [1]. Unfortunately, magnetically permeable soil can present issues for EMI systems by inducing a non-negligible voltage in the receive coil [11]. The induced voltage can be significant, making detection of the much smaller target response difficult or impossible.

The soil response (the voltage induced in the receive coil by the soil) can be viewed as indirect coupling between the transmit and receive coils. The soil response of a pair of coils can be determined by integrating the product of the sensitivity and the soil susceptibility, χ, over the soil half space (such as the system in Figure 2) as

$$V_{\text{soil}} = j\omega\mu_0 \int_{\text{soil}} \chi \frac{\vec{H}_{\text{TX}} \cdot \vec{H}_{\text{RX}}}{I_{\text{RX}}} dV \,. \tag{2}$$

In an attempt to mitigate the effects of the soil, systems often include a ground-balance feature that attempts to remove the signal generated by the soil from the signal that includes the target and the soil [54].

Because the portion of the head's sensitivity map that penetrates the soil changes as the head's height above the ground varies, it is clear that the voltage induced by a mineralized soil will change as the head height is varied. This change in the soil response can make detection difficult, even if the coils have been ground-balanced.

Coils can also couple capacitively with the ground or the target, problems which can be mitigated through proper shielding of the coil head [39, 50].

1.2 Ground Penetrating Radar

Ground penetrating radar (GPR) is also used for subsurface sensing, but GPR-based systems typically encounter different problems than those of EMI systems. For example, EMI systems

do not produce a propagating wave, so there is no round trip time [20]. Therefore, depth data is more difficult to obtain with an EMI system than with a GPR.

EMI systems are better at locating conductive objects and typically have much better discrimination of conducting objects than GPRs, but EMI systems typically cannot detect non-conductive targets. EMI systems are sometimes combined with GPR systems to either reduce false alarm rates or to allow detection of both conductive and non-conductive objects [9,34]. However, the coils of the EMI system and the antennas of the GPR must be designed with their co-location in mind.

1.3 Excitation Types

Two primary excitation types—pulsed-induction and continuous-wave—are in use for EMI systems. The focus for this work is continuous-wave systems, but some of the coil principles for CW systems can be applied to pulsed systems that require separate transmit and receive coils.

1.3.1 Continuous-wave

The simplest continuous-wave systems transmit a single frequency and provide the most rudimentary object detection, but most CW designs use at least a single transmit coil and a separate single receive coil in their coil head. Co-location of the transmit and receive coils in a single coil head is a common feature of many designs because it makes the detector compact and also improves target pinpointing.

The need for separate transmit and receive coils is dictated by the nature of continuous transmission. It is problematic to simultaneously transmit a signal using one coil and receive a signal of the same frequency on the same coil. The receive electronics typically do not have the dynamic range and stability that would be necessary to detect a very small target signal that is combined with the large excitation created by the transmit coil, necessitating separate transmit and receive coils with very low coupling between the transmit coil and the receive coil.

The most advanced CW systems, such as the Georgia Tech EMI system, transmit and receive on multiple frequencies simultaneously, which allows gathering amplitude and phase

data over a broad range of frequencies [6,50,64]. In the Georgia Tech EMI system, multiple measurements made over a broad frequency range allow advanced signal processing to be used to classify objects and to estimate the location of the objects [64].

1.3.2 Pulsed-Induction

Pulsed-induction sensors transmit a time-domain pulse that excites targets using the same mechanisms as a CW system [7]. Pulsed induction systems have the advantage of not requiring the transmit and receive coils to be nulled to one another (or needing only one coil for both transmit and receive). In the case of a pulsed system that does not have separate transmit and receive coils or has coils that are inductively coupled, the system must wait to sample the fields until the voltage induced in the receive coil by the transmit coil has died down. If sampling the signal is not delayed, the receive electronics will be saturated by the large transmit pulse [7].

Pulsed induction sensors make use of the change in the decay rate of the pulse to infer information about the target. Small targets or targets of low conductivity create very small signals that decay quickly. If the signals decay too quickly, a pulsed system will time-gate out the received signal and detect nothing.

1.4 Coil Configurations

Many coil configurations, ranging from single-coil designs to multi-coil arrays, have been used over the years in CW EMI systems. The simplest handheld CW systems use a single coil, but two-coil designs are both more prevalent and more sophisticated. A few small systems also use multiple transmit or multiple receive coils, but most arrays are not hand-held [51]. The following section will discuss some of the most common two-coil heads.

1.4.1 Two-coil Heads

Two-coil CW systems must have coils with minimum mutual coupling. Perhaps the most obvious way to create a coil pair with minimum coupling is to make the two coils orthogonal so that no flux from the transmit coil passes through the receive coil, as illustrated in Figure 3(a). Some early designs did just that, but these coils have poor spatial resolution and are

often very bulky [14,67]. It is rare to see a modern orthogonal-coil system used for anything other than geophysical sensing, such as mapping groundwater or finding large anomalies, because it performs poorly when attempting to pinpoint small objects.

Rather than restricting the flux created by the transmit coil from passing through the receive coil, most other designs work on an induction balance principle, where the coils are wound so that equal and opposite amounts of flux from the transmit coil pass through the receive coil, making the voltage induced in the receive coil sum to zero. One such coil pair is the dipole/quadrupole (Figure 3(b)), which typically uses a dipole as the transmit coil and a quadrupole (a figure-8) coil as the receive. These coils provide excellent rejection of magnetic soils and rejection of interference from other electromagnetic sources, but they have poor depth performance, both because the field of the quadrupole decays much more quickly with distance than the field created by a dipole and because the fields of the transmit and receive coils are orthogonal on the coil head's axis. The quadrupole has the added benefit of being immune to the change in soil response that most heads see when their height above a mineralized soil half-space is varied [10].

The double-D (Figure 3(c)) consists of two partially overlapping, dipole-like coils that may be of varying shapes. The partial overlap of the coils provides the balance that minimizes the mutual coupling between the coils and also creates narrow peaks in the center of their sensitivity map, allowing good target pinpointing [35]. The double-D does not perform as well in magnetic soils as the dipole/quadrupole, but the double-D has better detection depth in weakly magnetic soils where it sufficiently rejects the soil response when held at the proper height [11, 35]. It first appeared in the 1930s, but has since been produced in various forms by many companies [24, 44].

Bucked-primary concentric coil heads (Figure 3(d)), where the primary coil has two sets of loops wound in opposite directions such that the net flux through the receive coil is zero, have been used as well [26,58, 70]. These coils appear to have good depth performance and spatial resolution but perform poorly in mineralized soils. A bucked-secondary concentric, in which the transmit and receive coils of the bucked-primary coil are swapped, is also possible [66].

Stacked coaxial coils, like those shown in Figure 3(e), have been used as detector heads on commercial detectors produced by a few companies, such as Geophex [15,29]. They may cancel the signal induced by the soil to some degree, but it is unclear how well they perform in this regard.

The omega coil (Figure 3(f)), where a largely circular transmit coil has a portion folded inward over a smaller, circular receive coil, has also been used by manufacturers [25,39]. Its chief advantages appear to be its simple construction and the ease with which the coils can be nulled by adjusting the small portion of the transmit coil that is folded back.

Many other small coil heads have been designed. These heads include small arrays, coils with orthogonal cancellation windings or external bucking transformers, and other unusual configurations [50,63,68]. However, these coils all must trade off the features of good soil rejection, good depth performance, compact size, good spatial resolution, and minimum coupling.

1.5 Optimization

It appears that many coil heads were designed by trial and error with minimum coupling as the primary goal. There has been very little published on coil design, and essentially nothing has been published concerning the optimization of coils specifically for EMI systems. There is a method for calculating the sizes and locations of the coils in a nulled-primary system, but no optimization is performed [70]. Companies do some optimization of their designs for EMI systems, but the methods are trade secrets.

There has, however, been material published on the design and optimization of coils for use in magnetic resonance imaging (MRI). These methods are designed for optimizing shim or gradient coils and attempt to create coils with specified fields in a certain area. They may attempt to create coils with minimum inductance, minimum resistance, or both. Self-shielded coils are also a possibility. However, none of these methods deal with creating two coils with minimum mutual coupling.

Simple, brute force methods, where a few parameters are varied and all possible answers are evaluated, have been used for very simple problems, but such an approach is hardly

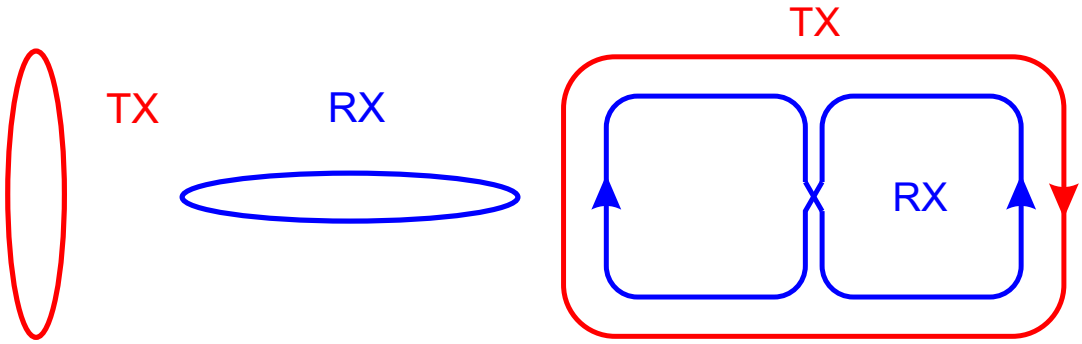

(a) Orthogonal coils.

(b) Dipole/quadrupole coil head.

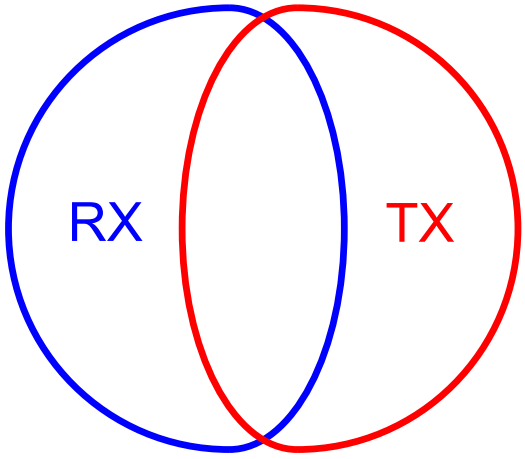

(c) Double-D coil head.

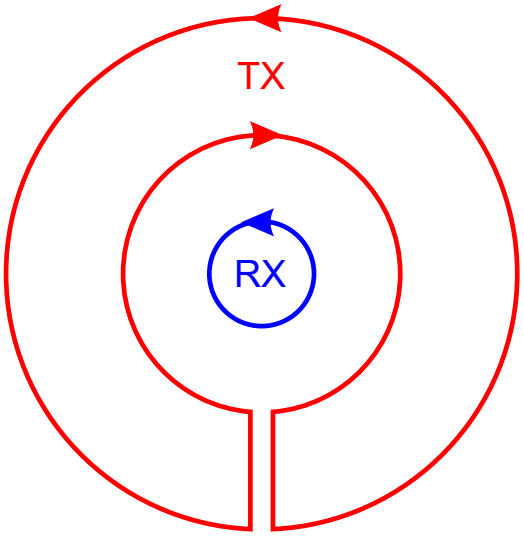

(d) Bucked-primary concentric coil head.

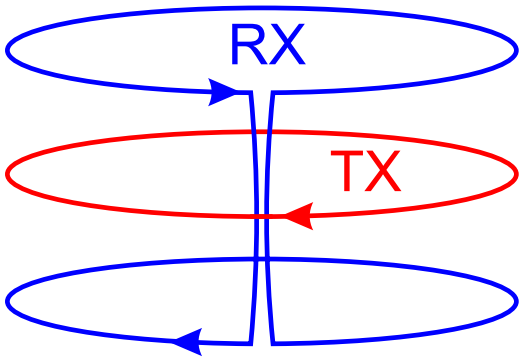

(e) Stacked coaxial coil head.

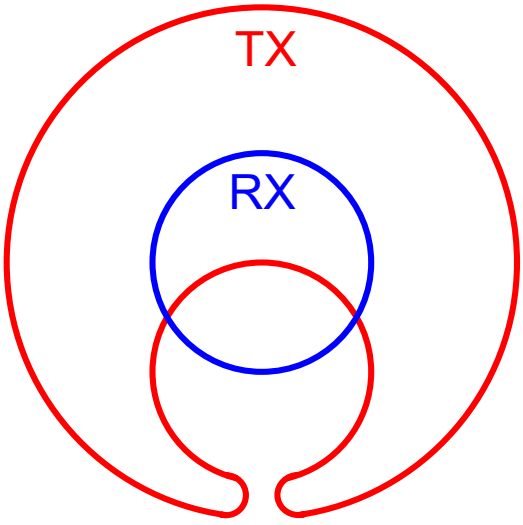

(f) Omega coil head.

Figure 3: Common extant coil heads.

appropriate for more difficult problems [31]. The target field approach specifies magnetic fields using Bessel functions. Then an inversion is performed to determine the necessary current distributions to create the specified fields [60].

Variational methods may be employed along with the target field approach to minimize the inductance of the coil [61]. Another method solves for the current needed to create a specified field by representing the coil with a wire grid and then formulating the problem as a matrix equation that may be solved either directly or numerically [32]. Such a method is geometrically restrictive, and appears difficult to modify for additional constraints.

The simulated annealing method has been used to create optimal MRI coils as well [41,59]. The mutual inductance between two coils could be incorporated into the simulated annealing method. However, this method can be computationally intensive, and though it is better than some other methods at finding an optimal solution, a global maximum is not guaranteed. It is also geometrically restrictive.

Coils have also been represented by stream functions as a way to lower the constraints on current paths. In one case, the energy of the coils was minimized using a least-squares procedure [43]. A later paper used a stream function representation to design coils with a specific field, maximum current density, and minimum stored energy [45]. In the second paper, the convexity of the problem was exploited, but only a single coil was considered.

1.6 Dissertation Organization

This dissertation is divided into three main parts plus appendices. Part 1 details the modeling and optimization of spiral wire coils using simple basis functions. Only maximizing the coil sensitivity and minimizing the coil coupling is considered. Proof of concept coils were produced, and some interesting measurements, including coil resonance issues, are presented. These coils demonstrate some of the practical difficulties with coil design.

Part 2 introduces normalized metrics that can be used to characterize and optimize wire coils. These metrics allow fair comparison between coils of differing types. Part 2 also includes the optimization of various types of wire coils using these new metrics. The optimization considers power dissipation and soil sensitivity in addition to the target sensitivity

and mutual coupling of earlier coils.

Part 3 generalizes the normalized metrics from the wire coils of Part 2 to coils defined using stream functions. These metrics are then used to optimize coils using a stream function representation. The stream functions allow more general coils that are not limited to the paths of the wire coils from Part 2. The shape of the coil is created as part of the optimization. The stream functions require a large number of unknowns, so a bi-convex optimization procedure was developed to efficiently optimize these coils. The best coils created using the new optimization were then converted to wire coils, and the metrics of the wire coils were compared to the metrics of the corresponding stream functions, demonstrating good agreement. These new coils are shown to peform better with respect to target and soil sensitivity metrics than the canonical coils of Chapter 6.

PART 1

Simple Optimization of Spiral, Wire-Wound Coil Geometries

CHAPTER II

MODELING WIRE-WOUND COILS WITH CONVENTIONALLY CONSTRAINED PATHS

To begin the investigation of the feasibility of optimization of wire coils for EMI systems, a simple polynomial representation of wire spirals was developed along with a two-stage optimization procedure that allows coils to be designed for minimum mutual coupling and maximum sensitivity. Several different iterations of spiral wire coils were designed and produced using these methods. Testing of these coils revealed multiple implementation difficulties that will be valuable in the production stream-function coils. Additionally, attempts to compare the new spiral coils to existing designs revealed that normalized metrics were needed to be confident in the accuracy of comparisons to other coils. The development of these metrics is detailed in Chapter 5.

2.1 Modeling Wire Coils

Consider coils configured in a system such as that shown on the right of Figure 4, where the transmit coil lies in the plane $z = -\delta$ and with $\delta > 0$, and the receive coil lies in the plane $z = 0$. The axis for each coil is coincident with the z-axis. Since EMI systems typically operate at frequencies below 1 MHz, a magnetoquasistatic analysis, which is used here, will suffice [22].

2.1.1 Representation of coils

To achieve dipole-like behavior and minimal mutual coupling, the current distribution ($\hat{\phi}$-directed in a polar coordinate system) on both coils must vary with the radius, ρ. Additionally, these coils must be easy to implement for use in a sensing system. Spiral coils can be wound so that the current distribution varies and even reverses. They are also easy to use for both the transmission or reception of signals since they require only a single feed.

However, optimizing a spiral coil is very difficult due to the large number of degrees of

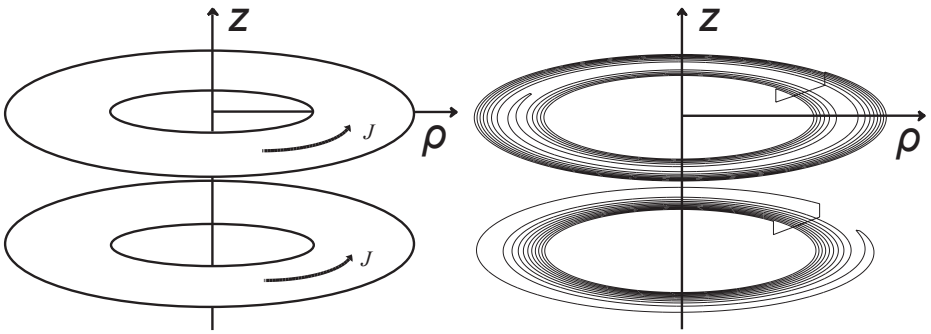

Figure 4: An illustration of a system composed of two annuli of current, where the axis of symmetry of each annulus is the z-axis (left), and a representation of the same system as two nonuniformly-wound spiral coils, with the transmit coil on top (right).

freedom and the fact that the problem is not convex. Instead the current density of a spiral coil can be approximated by using an infinitely thin annulus with a surface current density that varies with ρ and remains constant in ϕ, similar to the coils in the system on the left in Figure 4. To simplify the coil model, the surface current density, $J_\rho(\rho)$, is represented by a set of basis functions, $F_n(\rho)$,

$$J_\rho(\rho) = \sum_{n=0}^{N} a_n F_n(\rho)\,. \tag{3}$$

The current on the annulus will be optimized, and then the spiral will be implemented by creating physical wire coils carrying a current, I. These coils are defined by the path $\phi = w(\rho)$, where ϕ is the angular coordinate and ρ the radial coordinate in a polar coordinate system. The $\hat{\phi}$-directed surface current density is represented on the annulus in terms of the spiral function,

$$J_\rho(\rho)\hat{\phi} = \frac{I}{2\pi}\frac{dw(\rho)}{d\rho}\hat{\phi}\,. \tag{4}$$

This operation averages the current over the ϕ-coordinate and makes the approximation that the current on the spiral is entirely in the $\hat{\phi}$-direction, ignoring the presence of the $\hat{\rho}$-directed current that will be present in a spiral. Using (3) and (4), ϕ is found as a function of ρ,

$$\phi = w(\rho) = \sum_{n=0}^{N} \frac{2\pi a_n}{I} \int F_n(\rho) d\rho\,. \tag{5}$$

Expressing ϕ in this manner allows a spiral to be easily defined and optimized by adjusting the basis function coefficients, a_n.

2.1.2 Coil Magnetic Field

Using the Biot-Savart law and (3), the magnetic field, $\vec{H}$, of an annulus of current can be written as

$$\vec{H}(\vec{r}) = \sum_{n=0}^{N} a_n \int_{\rho_{min}}^{\rho_{max}} \int_0^{2\pi} \frac{F_n(\rho')\rho' \hat{\phi} \times (\vec{r} - \vec{r}')}{4\pi |\vec{r} - \vec{r}'|^3} d\phi' d\rho' = \underbrace{\begin{bmatrix} a_0 & a_1 & \dots & a_N \end{bmatrix}}_{\mathbf{a}^\top} \underbrace{\begin{bmatrix} \vec{\xi_0}(\vec{r}) \\ \vec{\xi_1}(\vec{r}) \\ \vdots \\ \vec{\xi_N}(\vec{r}) \end{bmatrix}}_{\xi(\vec{r})}, \quad (6)$$

where the observer is at a position, $\vec{r}$, and where $\vec{r}' = \rho'\hat{\rho} + z'\hat{z}$. Coordinate variables relating to sources are denoted by primed variables. In this particular case, $z' = -\delta$ for the transmit coil, and $z' = 0$ for the receive coil. This expression can be written as a product of $\mathbf{a}$ and ξ, where the vector $\mathbf{a}$ contains basis function coefficients, and ξ contains the pre-computed integral. Pre-computing the integral in (6) significantly reduces the complexity of the problem. The coefficients, $\mathbf{a}$, can be adjusted using an optimization algorithm to produce the maximum possible field.

2.1.3 Calculation of coil energy

When a system of two coils is optimized, both the energy stored in the magnetic field of a single coil and the mutual energy of two coils must be constrained. The energy of a single coil with magnetic field, H, can be expressed as [56]

$$W_s = \frac{\mu_0}{2} \int_V H^2 dV \,, \quad (7)$$

where μ_0 is the permeability of free space. Similarly, the mutual energy of a pair of spiral coils with fields of $\vec{H}_{\mathrm{TX}}$ and $\vec{H}_{\mathrm{RX}}$ can be expressed as [56]

$$W_m = \mu_0 \int_V \vec{H}_{\mathrm{TX}} \cdot \vec{H}_{\mathrm{RX}} dV \,. \quad (8)$$

In order to use W_s and W_m in an optimization routine, these energies must be written in terms of the coefficients of basis functions, as shown in Appendix A. Let $\mathbf{a}$ represent the coefficients of basis functions for the transmit coil current density and $\mathbf{b}$ the receive coil coefficients. Then the mutual energy of the transmit and receive coils can be shown to be

$$W_m = \mathbf{b}^\top \mathbf{M} \mathbf{a}\,, \tag{9}$$

where $\mathbf{M}$ is the mutual inductance matrix between the currents represented by the transmit and receive coil basis functions. The energies stored in both loops are computed analogously to W_m as

$$W_{\mathrm{TX}} = \frac{1}{2}\mathbf{a}^\top \mathbf{L}_{\mathrm{TX}} \mathbf{a}\,, \tag{10}$$

$$W_{\mathrm{RX}} = \frac{1}{2}\mathbf{b}^\top \mathbf{L}_{\mathrm{RX}} \mathbf{b}\,, \tag{11}$$

where $\mathbf{L}_{\mathrm{TX}}$ and $\mathbf{L}_{\mathrm{RX}}$ are the inductance matrices between the currents expressed by the basis functions for the transmit and receive coils, respectively.

2.1.4 Coil energy and coupling factor

As a metric for evaluating the mutual coupling, the coupling factor, c, is used. The coupling factor is normally defined in terms of the mutual inductance, M, between the coils and the self inductances, L_{TX} and L_{RX} of the coils. However, the coupling factor may be written in terms of the energies stored in the fields of the transmit and receive coils as

$$c = \frac{M}{\sqrt{L_{\mathrm{TX}} L_{\mathrm{RX}}}} = \frac{W_m}{2\sqrt{W_{\mathrm{TX}} W_{\mathrm{RX}}}}\,. \tag{12}$$

As can be seen, minimizing the mutual energy, W_m, minimizes the coupling factor.

2.1.5 Received Voltage

The transmit coil creates a time-varying magnetic field, $\vec{H}_{\mathrm{TX}}$, that induces a dipole moment, $\vec{M}$, on a target near the coil. The dipole moment is related to $\vec{H}_{\mathrm{TX}}$ by its magnetic polarizability dyadic, $\bar{\bar{m}}$, with units of m^3: $\vec{M} = \bar{\bar{m}} \cdot \vec{H}_{\mathrm{TX}}$. The dipole moment induces an open-circuited voltage, V_{RX}, at the terminals of the receive coil that can be computed using reciprocity as in equation (6) of [62],

$$V_{\mathrm{RX}} = \frac{-j\omega\mu_0}{I_{\mathrm{RX}}} \vec{M} \cdot \vec{H}_{\mathrm{RX}}\,. \tag{13}$$

$\vec{H}_{\mathrm{RX}}$ is the field that would be produced if the receive coil were driven by a current of I_{RX}.

Substituting the expression for $\vec{m}$ into (13) gives an equation for the open-circuit voltage of the receive coil in terms of the transmit and receive coil fields, the receive coil current, and the magnetic polarizability dyadic of the target,

$$V_{\mathrm{RX}} = \frac{j\omega\mu_0}{I_{\mathrm{RX}}} \vec{H}_{\mathrm{RX}} \cdot \bar{\bar{m}} \cdot \vec{H}_{\mathrm{TX}} \,. \tag{14}$$

Since the current is simply related to the inductance and the stored energy by $I_{\mathrm{RX}} = \sqrt{\frac{2W_{\mathrm{RX}}}{L_{\mathrm{RX}}}}$, (14) becomes

$$V_{\mathrm{RX}} = \frac{j\omega\mu_0\sqrt{L_{\mathrm{RX}}}}{\sqrt{2W_{\mathrm{RX}}}} \vec{H}_{\mathrm{RX}} \cdot \bar{\bar{m}} \cdot \vec{H}_{\mathrm{TX}} \,. \tag{15}$$

In this optimization, both L_{RX} and W_{RX} are constrained to be constants. Also, the field is optimized on the z-axis where the magnetic fields of both coils are entirely z-directed. Thus, a reasonable measure of the possible value of V_{RX} can be found by making $\bar{\bar{m}}$ proportional to the identity dyad. With these simplifications, V_{RX} is simply proportional to the dot product of the transmit and receive coil magnetic fields,

$$V_{\mathrm{RX}} \propto \vec{H}_{\mathrm{RX}} \cdot \vec{H}_{\mathrm{TX}} \,. \tag{16}$$

2.2 Optimization

The operation of maximizing the voltage in the receive coil has been shown to be proportional to maximizing the dot product of the transmit and receive coil magnetic fields, which is defined as the objective function,

$$O = \vec{H}_{\mathrm{RX}} \cdot \vec{H}_{\mathrm{TX}} \,. \tag{17}$$

O may be computed efficiently using (6) and can be viewed as a measure of the sensitivity of the coils. Similar measures of the sensitivity are defined in [11, 55]. The problem has been written in such a manner that it may be primarily solved by a two-stage, iterative optimization procedure. The "outer" optimization is a standard nonlinear minimization algorithm that performs an operation analogous to

$$\mathbf{a} = \underset{\mathbf{a}\in\mathbf{R}^N}{\arg\max}\{\vec{H}_{\mathrm{TX}}(\mathbf{a}) \cdot \vec{H}_{\mathrm{RX}}(\mathbf{b})\}, \text{ subject to: } W_{\mathrm{TX}} = 1 \,, \tag{18}$$

which attempts to find an $\mathbf{a}$ such that the objective function, O, is maximized. This operation also constrains the energy stored in the transmit coil to be one so that the currents will

be bounded. This constraint is imposed by normalizing the initial transmit current density function coefficients, $\mathbf{a_g}$, so that the transmit coil energy must always be one,

$$\mathbf{a} = \frac{\mathbf{a_g}}{\sqrt{\frac{1}{2}\mathbf{a_g}^\top \mathbf{T}\mathbf{a_g}}}\,. \tag{19}$$

In addition to simplifying the implementation of the optimization algorithm, this normalization also reduces the degrees of freedom by one.

During each iteration of (18), the following "inner" optimization is performed,

$$\mathbf{b} = \underset{\mathbf{b}\in\mathbf{R}^N}{\arg\max}\{|\vec{H}_{\mathrm{RX}}(\mathbf{b})|\},\ \text{subject to: } W_{\mathrm{RX}} = 1, W_m = 0\,. \tag{20}$$

In this "inner" optimization, the maximum field of the receive coil at the chosen point is found, with the constraints that the energy stored in the receive coil be one to bound the currents and the mutual energy of the transmit and receive coils be zero. Other constraints, such as constraining the moment of the receive coil, could also be added. The operation in (20) must be performed on each iteration of (18) because the mutual energy is calculated using $\mathbf{a}$. Most importantly, (20) is convex, so it guarantees that the solution is a global maximum. It also may be performed very quickly when formulated as a convex optimization problem, which was specified using the Matlab package CVX [18, 19].

2.3 Spiral Conversion

This optimization procedure is designed to optimize the current density on two annuli of current, such as those on the left side of Figure 4, and thus it does not work perfectly for the desired spiral coils (right of Figure 4). Therefore, if the annuli are optimized for a specific separation, $\delta = \delta_a$, and subsequently made into coils using (5), the coupling factor of the annuli will null at $\delta = \delta_a$. However, the coils will exhibit a non-negligible coupling factor when their separation is δ_a. It was found empirically that slightly adjusting the spacing of these same spiral coils to a different separation, $\delta = \delta_s$, allows the coupling factor to be nulled. If a downhill simplex method—where each iteration requires performing the preceding optimization upon annuli and then converting them to spirals—is used, annuli can be found with a separation of δ_a that yield spirals with a nulled coupling factor at a desired coil separation, δ_s. The algorithm converges within a few iterations because the

initial error in the position of the null is not great, and a set of coils with the correct spacing is obtained.

CHAPTER III

OPTIMIZATION OF WIRE-WOUND SPIRAL COILS

With the basic metrics and optimization procedure previously defined in Chapter 2, coils can be optimized and built. The first pair of coils detailed in this work was built before the optimization procedure was amended to account for the approximation made when transforming the annuli of current to spiral coils. As a result, the coils do not null at the proper spacing. They are singled-sided coils that served as a proof-of-concept to verify that the design and optimization procedures worked as intended and could be transferred to a physical design. The second set was designed as double-sided coils manufactured on printed circuit boards (PCBs) after this procedure was introduced.

3.1 Basis functions and spiral winding theory

Both coil pairs were optimized using a polynomial basis of order one, $F(\rho) = a_0 + a_1\rho$, to describe the current density $J_\rho(\rho)$. Using (5) and the polynomial basis, ϕ can be found as a function of ρ for our test cases,

$$\phi(\rho) = \frac{2\pi}{I}\left(a_0\rho + \frac{a_1\rho^2}{2}\right), \tag{21}$$

as is explained in detail in Appendix D. As noted previously, other basis functions could be chosen. Choosing an order of one instead of higher orders constrains the solution space, which simplifies the outer optimization in (18). Because the outer optimization is not convex, there is the danger of finding a local rather than global maximum. Thus, reducing the size of the vector $\mathbf{a}$ decreases the possibility of a non-optimal solution and increases the speed of the algorithm. Choosing a simple set of basis functions also limits the complexity of the current distribution on the annulus, thereby limiting the complexity of the spiral, which makes winding the spiral simpler.

In addition to limiting the complexity of the coil with the choice of basis functions, the value of I can be used to adjust the winding density. A larger I will decrease the density,

and vice versa. Winding density is a concern, particularly for the transmit coil, which may carry a relatively high amount of power. A desire to increase the number of turns to raise the coil inductance must be balanced with a need for low resistance, which, in the case of a PCB requires wider traces and thus a lower winding density.

3.1.1 Experimental Setup

The experimental setup for measuring both the magnetic field produced on axis by each coil and the coupling factor between the two coils at low frequencies is relatively simple. To measure the field, H_{coil}, produced by one of the coils, the coil was driven by the RF output of a network analyzer. A $1\,\Omega$ resistor was connected in series with the coil and connected to the reference channel on the network analyzer to serve as a measure of the current, I_{coil}, flowing in the coil. A second, much smaller coil was connected to channel A of the network analyzer and used as a field probe. By manually calibrating the field probe with a gauss meter and then measuring V_a/V_r, the voltages measured by the network analyzer on channels A and R, respectively, the quantity H_{coil}/I_{coil} could be calculated. The coupling factor was measured in a similar manner by replacing the small field probe with the receive coil. The mutual inductance of the coils could then be related in a simple manner to the quantity V_a/V_r.

A custom front-end for the network analyzer was used to measure the coupling over a range of frequencies. The custom interface is impedance-matched to the analyzer and has a low noise figure as well as a high input impedance to lessen the impact of instrument loading.

3.1.1.1 Comparison Coils

The optimized spiral coils are compared with two commonly used transmit/receive coil pairs - a double-D coil pair (Figure 5(a)) and a dipole/quadrupole coil pair (Figure 5(b)). Both comparison coil pairs have outer radii equal to the radii of the spiral test coils. The cross sectional areas of the wires used in the single turn comparison coils are equal to the combined cross sectional areas of the multiple turns of wire used in the spiral test coils. These comparisons are by no means perfect, but they serve to show that the optimization

(a) Double-D. (b) Dipole/quadrupole.

Figure 5: Comparison coil system geometries.

has promise to create coils better than those designs currently in widespread usage. A much more involved treatment of fairly comparing coil designs whose physical parameters have not been finalized is provided in Chapter 5.

3.1.2 Single-Sided Coils

The first prototype system presented is a single-sided coil design, meaning that each coil consists of a spiral with turns existing in only one plane. This system was designed using the optimization procedure described in (18) and (20) and did not use the additional algorithm introduced to adjust for the coupling factor null position error caused by approximating an annulus of current as a spiral. Consequently, a design null location of 1 cm differed from both the theoretical location after conversion to a spiral, which is calculated with Neumann's formula, and the experimentally measured null location. Measurements for this system were taken at 3 kHz.

3.1.2.1 System Geometry

The single-sided coil parameters are $\rho_{min} = 8.1\,\text{cm}$, the minimum radius, $\rho_{max} = 12.6\,\text{cm}$, the maximum radius, $\delta = 1\,\text{cm}$, the separation between the two coils, and $z_{opt} = 50.0\,\text{cm}$, the point on the z-axis at which the objective function, O, was maximized.

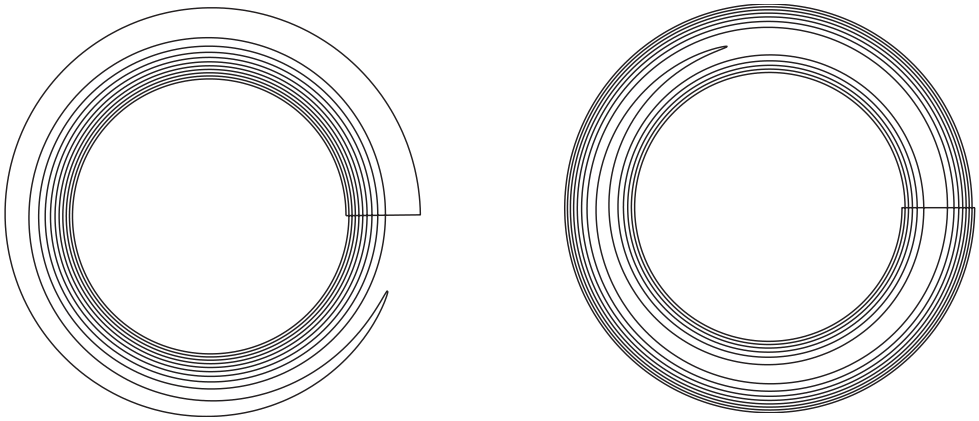

(a) Transmit coil. (b) Receive coil.

Figure 6: Optimized coils for use in a single-sided coil system with inter-coil spacing of 1.0 cm.

3.1.2.2 Theoretical Results

After optimization, the coil designs in Figure 6(a) and Figure 6(b) are the result. Note the reversal of the winding direction in each coil; this reversal is necessitated by the desire for both minimal mutual coupling between the two coils and positive dipole moments.

Figure 7 shows the overall theoretical responses of the optimized spiral system, a comparably-sized dipole-quadrupole system, and comparably-sized double-D coil system, each with a stored energy of one in both coils. The optimized spiral system shows an improvement of 14.5 dB in the product of the magnetic field strength of the transmit and receive coils over the dipole-quadrupole system at the optimization point of 0.5 m on the z-axis and an improvement of 1.5 dB over the double-D system. It should be noted that the product of the magnitudes of the transmit and receive coil magnetic fields have been used rather than the dot product. This gives a reasonable metric for comparison with the quadrupole/dipole system, which has perpendicular transmit and receive magnetic fields on axis resulting from the quadrupole coil. The objective function will be improved upon in the characterization of coils in later chapters.

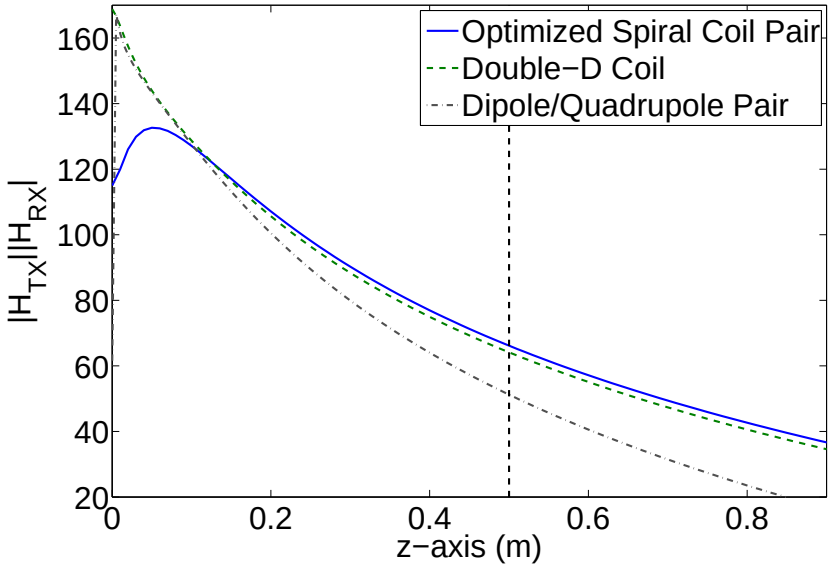

Figure 7: A theoretical comparison of the product of the magnitude of the magnetic fields from the single-sided coil pair along the z-axis with a more traditional dipole/quadrupole pair and a double-D coil pair. All structures have equal outer radii.

Table 1: Coil Inductance

Inductance	Calculated	Measured
L_{TX}	28.97 μH	29.33 μH
L_{RX}	25.29 μH	26.06 μH

3.1.2.3 Experimental Results

The optimized coil profiles were manufactured as grooves in a 3D printed composite form, and 20 by 40 mil transformer wire was then wound into the grooves by hand to create the coils. Portions of the transmit and receive coils created in this manner are shown in Figure 8. As a method of verifying the accuracy of the coils, their self inductances were measured and compared with theory. The measured inductances deviate by no more than 3% from their theoretical values (Table 1). The on-axis, normalized field strength of the optimized coils was measured at 3 kHz in the laboratory and then compared with theory (Figure 9). The measured fields on axis agree with theory to within 6%.

As a final verification of the agreement of the theory and final coils, the coupling factor, c, between the optimized transmit and receive coils at various separations was both calculated and measured (Figure 10). As previously mentioned, the desired location of the coupling

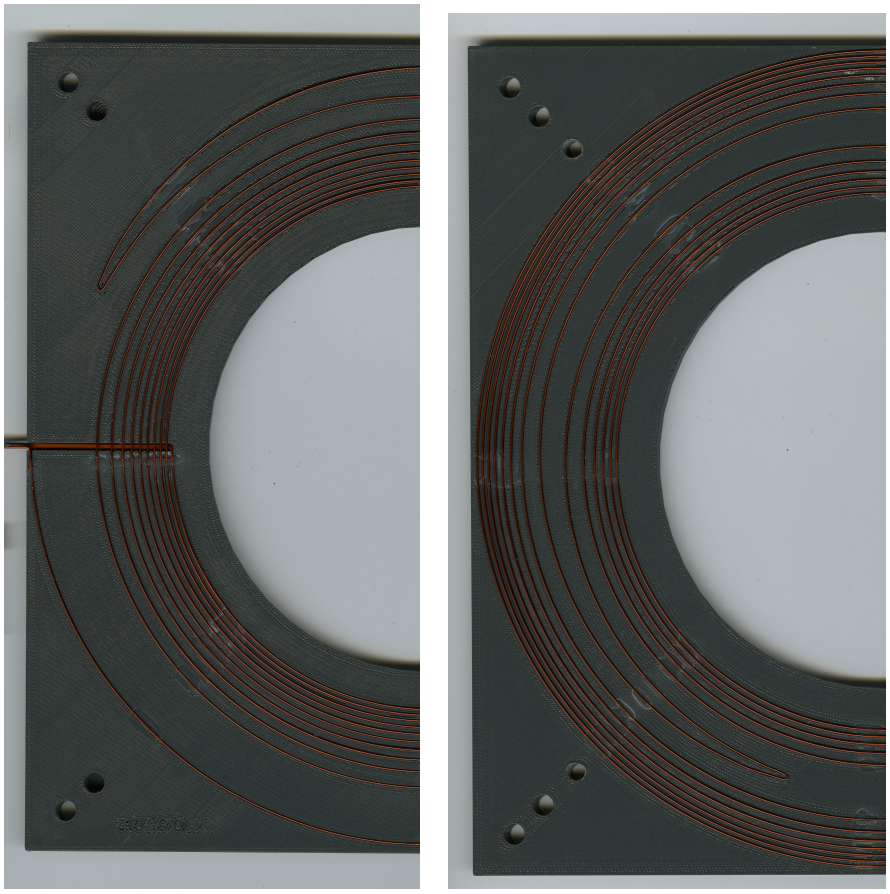

(a) Transmit coil. (b) Receive coil.

Figure 8: Portions of the single-sided transmit coil (a) and the single-sided receive coil (b) constructed using a composite form and 20 x 40 mil transformer wire.

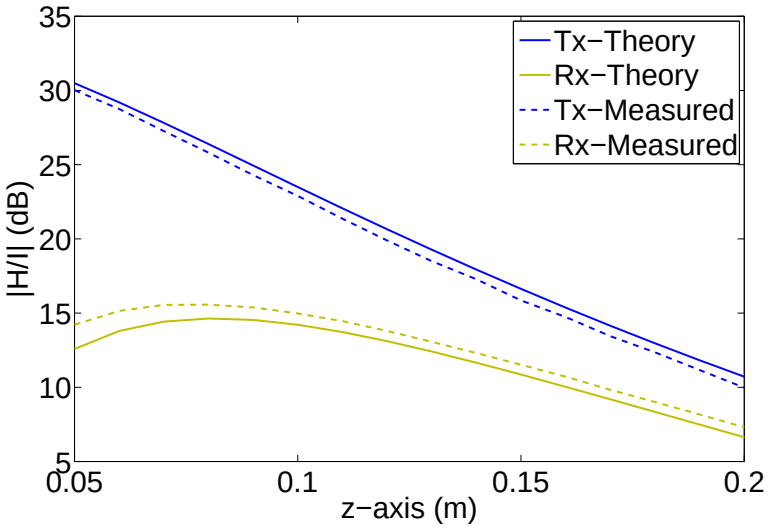

Figure 9: Experimentally measured fields of single-sided transmit and receive coils compared with theory.

factor null does not coincide with the theoretical null calculated using Neumann's formula. The desired null is at a separation of 1 cm, while the null calculated from the spirals in Figures 6(a) and 6(b) is actually at 8.1 mm. The theoretical and experimental coupling factor measurements differ by a maximum value of 6.6×10^{-3} and the experimental null is at approximately 8.2 mm of separation, which is 0.1 mm from null at 8.1 mm calculated from theory, and 1.8 mm from the desired null at 1 cm.

3.1.3 Double-Sided PCB Coils

3.1.3.1 System Geometry

This pair of coils was initially designed as a pair of single sided coils, which were then later transformed into double-sided coils. The single-sided coil parameters are the minimum radius, $\rho_{min} = 8.1\,\text{cm}$, the maximum radius, $\rho_{max} = 12.6\,\text{cm}$, the separation between the two coils, $\delta = 7.5\,\text{mm}$, and $z_{opt} = 50.0\,\text{cm}$, the point on the z-axis at which the objective function, O, will be maximized.

3.1.3.2 Theoretical Results

The coil designs in Figure 11 are the result of the optimization. Like the first pair of coils, the windings reverse direction to achieve both minimal mutual coupling between the two

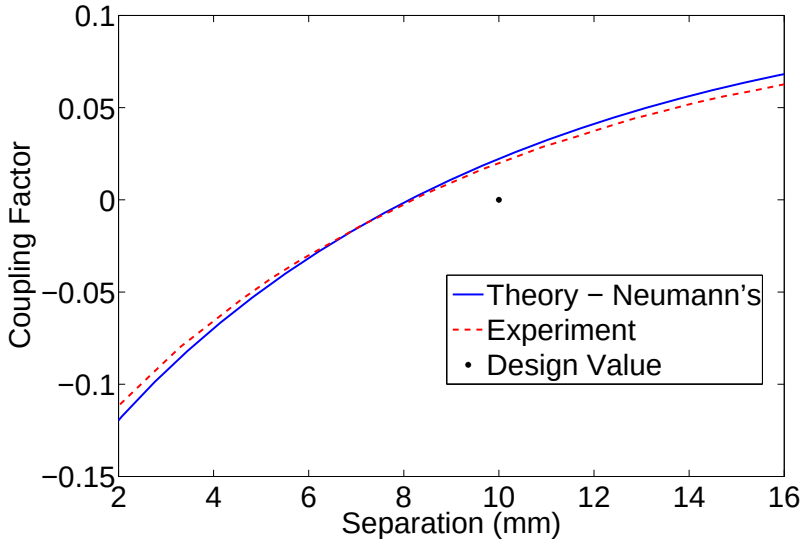

Figure 10: Experimentally measured coupling factor of single-sided coil pair compared with the coupling factor computed with Neumann's formula and the design value.

coils and positive dipole moments.

As can be seen in Figure 6, the first set of coils designed has feeds that are not entirely on the exterior of the coil. Their inductances are also lower than desirable for use in some sensor systems. Both problems can be solved by making both the transmit and receive coils double-sided. Thus, for example, the single-sided transmit coil produced by the optimization in (18) was mirrored, creating two identical, but y-coordinate inverted coils. These were then spaced apart by 63 mils and connected in series, creating a system with two double-sided coils. Any error in the coupling factor null due to the double-sided coils was removed by the operation that adjusts for the similar coupling factor error encountered with single-sided coils.

Figure 12 shows the overall theoretical responses of the optimized spiral system, a comparably-sized dipole-quadrupole system, and comparably-sized double-D coil system, each with a stored energy of one in both coils. The optimized spiral system shows an improvement of 16.0 dB in the product of the magnetic field strength of the transmit and receive coils over the dipole-quadrupole system at the optimization point of 0.5 m on the z-axis and an improvement of 2.4 dB over the double-D system. As with the single-sided coils, the product of the magnitudes of the transmit and receive coil magnetic fields has

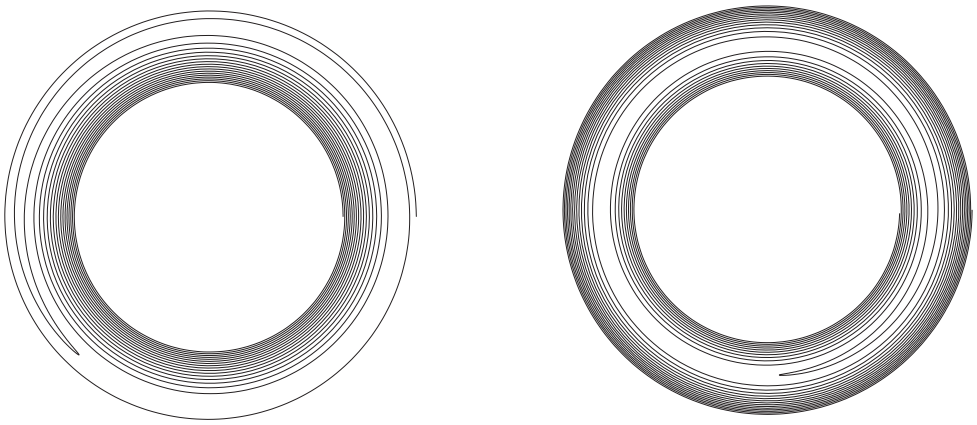

(a) Transmit coil. (b) Receive coil.

Figure 11: Optimized spiral-wound coils for use in a double-sided coil system with inter-coil spacing of 7.5 mm.

been used rather than the dot product.

3.1.3.3 Experimental Results

The optimized coils were subsequently manufactured on two-sided printed circuit boards of FR-4 with 3 oz copper. Portions of these two coils are show in Figure 13. The trade-off between the winding density and the width of the traces is apparent on the transmit coil in Figure 13(a). To decrease the resistance of the transmit coil and allow it to carry more current, the trace widths are variable, widening from 30 to 80 mils as the traces become further apart. This technique was not used on the receive coil due to lower current requirements. As a method of verifying the accuracy of the coils, their self inductances were measured and compared with theory. The measured inductances deviate by no more than 3% from their theoretical values (Tables 2 to 5). The on-axis, normalized field strength of the optimized coils was also measured at 100 Hz in the laboratory and then compared with theory (Figure 14). The measured fields on axis agree with theory to within 3%.

As a final verification of the correctness of both theory and coil designs, the coupling factor, c, between the optimized transmit and receive coils at various separations was both calculated and measured (Figure 15). The theoretical and experimental coupling factor measurements differ by a maximum value of 7.4×10^{-3} and null at approximately 7.4 mm

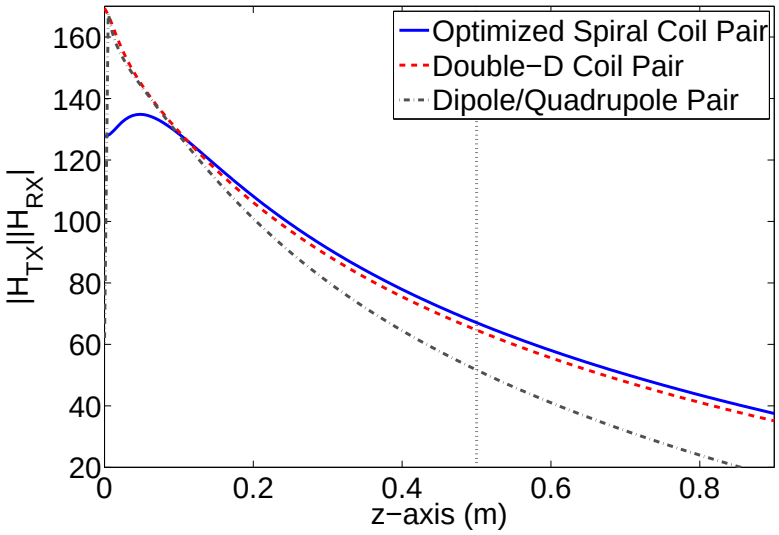

Figure 12: Theoretical comparison of the product of magnitude of the magnetic fields from the double-sided spiral coil pair along the z-axis with a more traditional dipole/quadrupole pair and a double-D coil pair. All structures have equal outer radii.

(a) Transmit coil.

(b) Receive coil.

Figure 13: Portions of the the double-sided coils printed on PCBs using 3 oz copper.

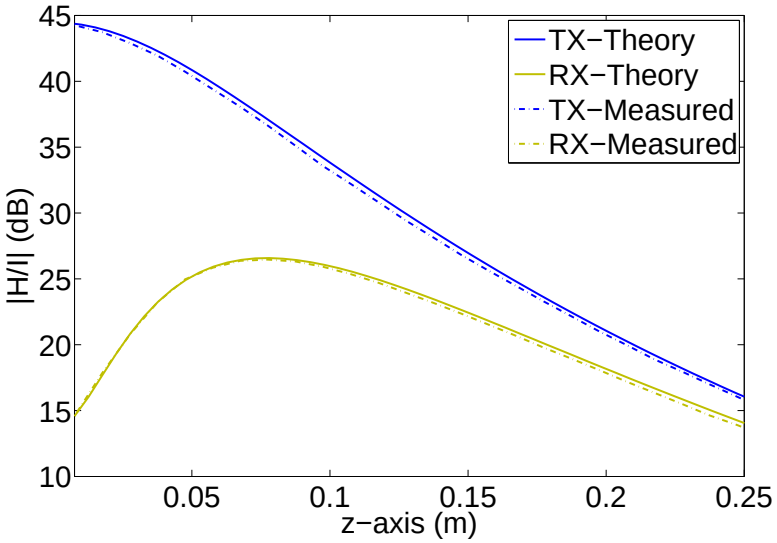

Figure 14: Comparison of the simulated magnetic field of the double-sided coil pair with the measured field of the physical system.

Table 2: TX PCB Theory

PCB	L (μH)	R (Ω)
Theory	317.07	3.18

of separation, which is 0.1 mm from the desired separation of 7.5 mm.

Table 3: RX PCB Theory

PCB	L (μH)	R (Ω)
Theory	333.75	20.98

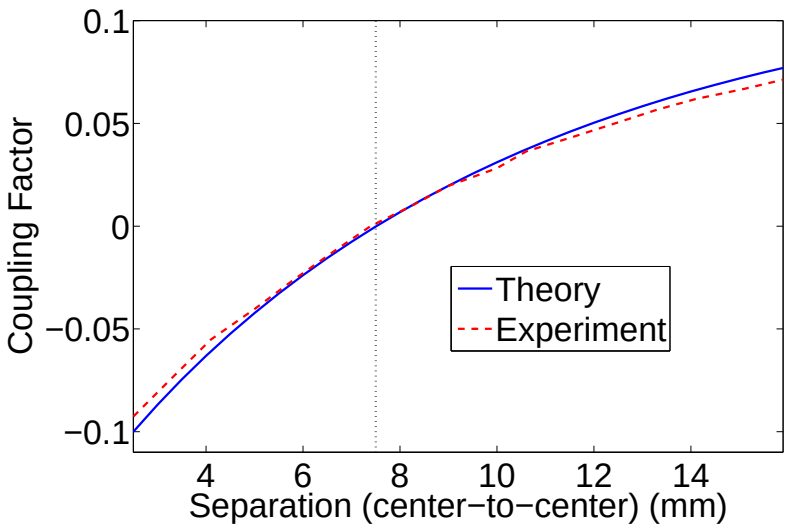

Figure 15: Coupling factor measured for varying separations of the double-sided coil pair compared with the coupling factor computed using Neumann's formula.

Table 4: TX PCB

PCB	L (μH)	R (Ω)
A	317.7	3.62
B	317.8	3.72
C	317.7	3.68
D	317.8	3.59

Table 5: RX PCB

PCB	L (μH)	R (Ω)
A	341.7	24.08
B	341.4	23.08
C	341.4	22.06
D	341.9	25.07

CHAPTER IV

SPIRAL COILS AND RESONANCE

The coils designed and built in the preceding chapter showed that the optimization could produce viable coils, but there were several issues. The coils exhibited non-negligible drift when connected to the Georgia Tech EMI system as a result of uneven heating of the transmit coil caused by the variable trace widths. This led to the creation of a new pair of coils optimized in the same manner as before. However, the transmit coil is designed to use magnet wire with a rectangular cross section that was hand-wound in a polycarbonate form. The receive coil was designed on a PCB as before.

After the new coils were manufactured, an investigation of resonances within the coils was undertaken.

4.0.1 Coil Geometry

The transmit coil was wound with 0.48 by 1.93 mm rectangular magnet wire on both sides to reduce its resistance. The wire on either side is spaced apart by 0.5 mm, creating a total coil thickness of approximately 4.4 mm. The wires are held in place by grooves machined into a polycarbonate form. The receive coil was produced on a 1.6 mm thick double-sided FR-4 PCB with 3 ounce copper traces that are 0.254 mm wide.

Both coils have an inner diameter of 17.78 cm and an outer diameter of 26.67 cm. The coils were designed to have a nulled coupling factor at a center-to-center separation, δ, (because the coils are of non-negligible thickness, the center of a coil was defined as midway between the two sides for simplicity) of 9.5 mm. The coils were optimized for maximum on-axis sensitivity at $z = 53.3$ cm. The coils are arranged as in Figure 4, with the transmit coil lying in the $z = 0$ plane.

After optimization using the method described in Section 3, coils with the wire paths shown in Figure 16 on either side were the result. Figure 17(a) and Figure 17(b) are pictures of the coils after production.

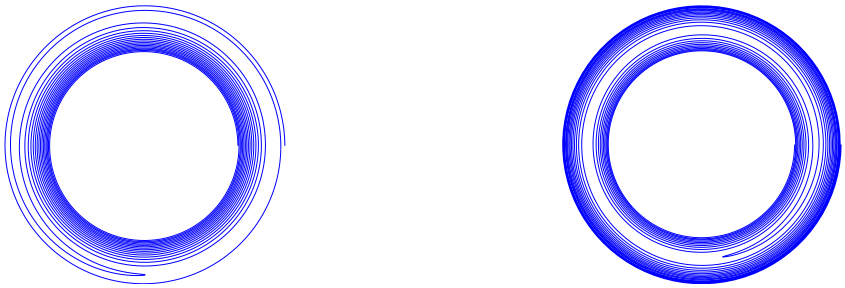

(a) Transmit coil. (b) Receive coil.

Figure 16: Coil geometries.

4.1 Results

4.1.1 Coil comparisons

The optimized coils are first compared with two common coil types—double-D (Figure 18(a)) and dipole/quadrupole (Figure 18(b)) coils—used in EMI systems. Both pairs of coils have outer radii equivalent to the radii of the optimized coils, and the energy stored in all coils is normalized to a value of 1 J for purposes of comparison.

The sensitivity of the optimized coil pair is then compared to the sensitivities of the double-D and quadrupole/dipole coils using the above models and the Biot-Savart law. In Figure 19, the spiral coils show an improvement in sensitivity of 2.5 dB over the double-D coil pair and 15.4 dB over the dipole/quadrupole coil pair at the optimization point of 53.3 cm.

4.1.2 Experimental measurements

To verify that the physical coils match the design, the self inductances and the resistances of the coils were also measured and compared with theory. The measured inductances (L_{TX} = 309 μH and L_{RX} = 365 μH) deviate from theory by less than 5%, and the measured resistances (R_{TX} = 0.55 Ω and R_{RX} = 22.8 Ω) deviate by less than 8% from theory.

The individual on-axis magnetic fields of the transmit and receive coils were measured at 1 kHz and then normalized to the current flowing in the coils. These fields, shown in Figure 20, exhibit good agreement with the fields calculated using the Biot-Savart law.

(a) Transmit coil. (b) Receive coil.

Figure 17: Photos of half of the transmit and receive coils produced using wire wound in polycarbonate and on a PCB, respectively.

(a) Double-D coil. (b) Dipole/quadrupole coil.

Figure 18: Comparison coil geometries.

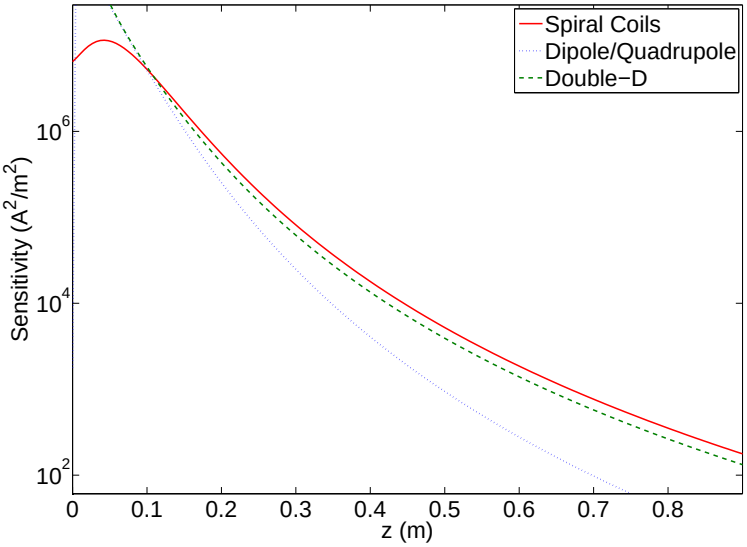

Figure 19: Comparison of the sensitivities of the optimized coil pair, a double-D coil pair, and a quadrupole/dipole coil pair, all with equal stored energy and outer radii.

Next, the coupling factor of the coils was measured over a range of spacings at 1 kHz and compared in Figure 21 with the coupling factor computed using Neumann's formula. The coils were designed to null at 9.5 mm center-to-center spacing, as marked by the dashed black lines in Figure 21. The measured null is at approximately 9.4 mm. The resolution of the measurement system is approximately 1.0 mm, so, as with the field comparison, this agreement is very good. It can be concluded that these coils match the coils that were designed.

4.2 Capacitive Loading

These coils were designed to be used with a system that operates at frequencies up to approximately 100 kHz, so the mutual coupling over a wide band is of interest. Ideally, the mutual coupling would be flat across all frequencies, but due to various coupling mechanisms, it is not. For simplicity, the effective mutual inductance, M_{eff}, which, by (12), is proportional to the coupling factor will be used. M_{eff} is defined in terms of the voltage at the output of the receive coil, V_{RX}, and the current flowing into the transmit coil, I_{TX}, as

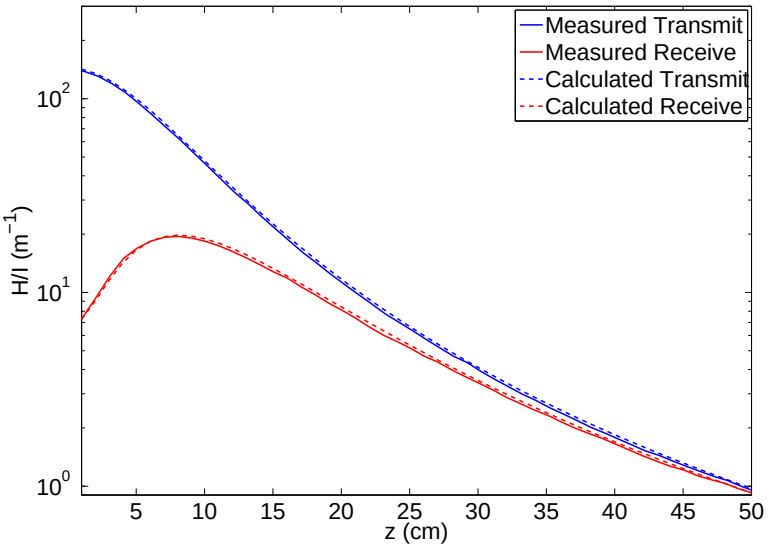

Figure 20: A comparison of the measured and calculated transmit and receive coil fields, normalized by the current.

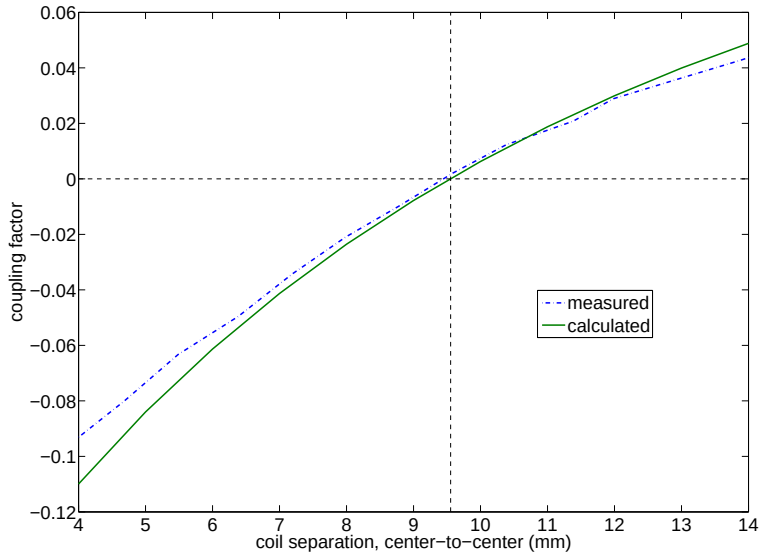

Figure 21: Coupling factor of coils, both measured and computed. The intersection of the dashed lines indicates the design value.

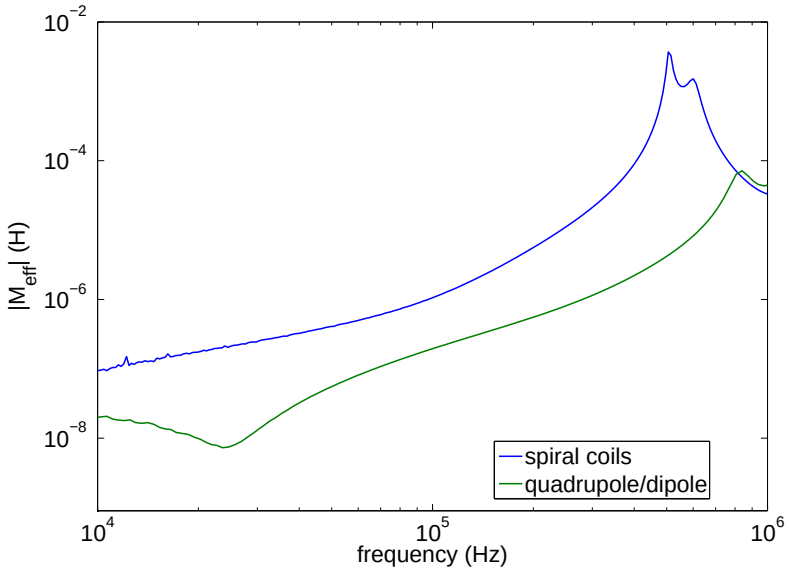

Figure 22: A comparison of the effective mutual inductance of the spiral coils with a quadrupole/dipole pair.

$$M_{eff} = \frac{V_{RX}}{j\omega I_{TX}} \,. \tag{22}$$

The coupling of the coils was first nulled at 10 kHz, and then the effective mutual inductance was measured from 10 kHz to 1 MHz. Although the band of interest only reaches to 100 kHz, there are resonances at higher frequencies that increase the in-band coupling. This measurement is shown in Figure 22, where it is compared with the measured effective mutual inductance of a quadrupole/dipole coil of equal outer diameter. Ideally, the effective mutual inductance would be a flat line, but, due to the resonances at 500 kHz and 600 kHz, it is not. Therefore, the resonances are problematic. The effective mutual inductance of the spiral coils is approximately 20 dB higher than the quadrupole/dipole coils. This is partially due to inaccuracies in the coil spacing and partially due to the resonances.

The transmit and receive coils are both self resonant, with the 500 kHz resonance resulting from the transmit coil and the 600 kHz resonance from the receive coil. There is also a much higher resonance at 1.5 MHz from the receive coil that is not shown. These resonances result from capacitive loading of the coils. For example, because the sides of the receive coil are close together (less than 1.6 mm), there is a significant amount of capacitance between

the traces on either side of the coil. The transmit coil has a similar problem, though it only has one resonance.

4.2.1 Circuit model

The receive coil can be viewed as three inductors, where the windings between the winding reversal and the outer edge of the coil on one side is one inductor of value L_2, the same windings on the other side form another inductor of equal value L_2, and the windings between the reversal and the inner edge of the coil on both sides are lumped into a single, third inductor with value L_1. The manner in which the coil is broken up into lumped elements is shown in Figure 23(b). Because the transmit coil has so few turns between the reversal and the outer edge of the coil, it can be viewed as a single inductor with value L_T (Figure 23(a)).

These ideas can be transformed into a lumped-element circuit model, as seen in Figure 24, with a few capacitors representing the distributed capacitances within the coils. The transmit coil is shown on the left, and the receive on the right, with the output of the transmit coil being across the resistor, R. For clarity, this circuit is slightly simplified from the circuit used for calculations. The resistances of the coil windings and the effects of coupling between all inductors have been omitted from the figure, though they are included in the model. Note also the dot convention, which indicates that the inductor L_1 is wound in the opposite direction of L_2. It should be clear from this circuit model that the reversal of the receive coil causes its two resonances.

The lumped-element model can be used to approximate the frequency response of the coils. There are several important parameters to consider when analyzing the frequency response of the coils. The curve from 10 kHz to the first resonance is dependent upon both the capacitances, C_1 and C_T, as well as the coil spacing. The self and mutual inductances of all the inductors may be calculated using Neumann's formula, and the resistances can be calculated as well. However, there is not a simple method of calculating the values of the lumped capacitors that are used to model the distributed capacitance within the coils. Therefore, the nelder-mead simplex method was used to fit the model to the measured data

by adjusting the coil spacing and capacitance values. This curve fit, shown in Figure 25 yields a spacing of approximately 9.4 mm and capacitor values of $C_1 = 286$ pF, $C_2 = 209$ pF, and $C_T = 212$ pF.

The model can be verified to be an approximation of reality by checking that changing the value of C_1 by soldering a 300 pF capacitor in parallel with the inner windings changes the resonance equally in both the model and the measurements. As can be seen in Figure 26, this is the case. The lowest resonance moves from 500 kHz to 425 kHz in both the model and measured data. The same check is performed with a 120 pF capacitor, and the data graphed in Figure 27. This moves the lowest resonance to approximately 470 kHz for both the model and measurement. The curves do not match exactly between the model and measurements for either case, but this is not unexpected. The spacing of the coils partially controls this curve, and the spacing has changed minutely between measurements because the coils must be disassembled to add the capacitor. Figure 28 shows the change in the model over a range of three spacings to illustrate this effect. Varying the spacing by only 0.05 mm causes a great difference in the depth of the null at low frequencies.

With the caveats that small changes in spacing can greatly affect the low-frequency null and that the use of lumped-elements is imperfect, it is claimed that the model is adequate for predicting and understanding the behavior of these coils because the model correctly predicts the movement of the resonances resulting from the addition of capacitors.

4.2.2 Resonance cancellation

It has been shown that changing the value of C_1 affects the location of the lowest resonance. Now, consider the effect of C_1 within the simple circuit model. With C_1 in the model, the current through either inductor labeled L_2 will not be equal to the current through L_1. If C_1 is removed, this should remove a resonance and make the current through L_2 equal to the current through L_1. Figure 29 shows that after removing C_1, the effective mutual inductance stays flat past 100 kHz. Also, at 100 kHz, M_{eff} has been reduced by 24 dB over the model of our coils that includes C_1. Thus, not only has removing C_1 removed a resonance, but it has also greatly reduced the in-band effects of the mismatch in the currents through L_1 and

L_2 on the effective mutual inductance of the coils.

It is now postulated that the negative effects of C_1 can be mitigated by adding the capacitors C_3 to the coil, as shown in Figure 30. In theory, these capacitors could make the currents through L_1 and L_2 more equal. Because this model is very simple, exactness is not expected, but it should provide a rough idea as to the behavior of the coil with capacitors added. If the value of C_3 is swept in the model, Figure 31 results. Thus, the model predicts that the addition of capacitors in parallel with the outer receive coil windings could reduce the in-band effects of C_1 significantly. At 300 kHz, capacitors of 79 pF reduce the effective mutual inductance by 22 dB, and at 100 kHz, there is a 13.7 dB reduction.

As a quick test of this theory, the coils were reassembled and then the mutual coupling nulled with no added capacitors. Then, without disassembling the coils, several different capacitors (78 pF, 150 pF, and 220 pF) were soldered across the outer coil windings on both sides. Figure 32 shows the results. The design value of 79 pF does not reduce the mutual inductance as expected, but it does have an effect. Cursory experimentation with other capacitor values on hand illustrates that improvements can be made. At 100 kHz, 220 pF capacitors lower the effective mutual inductance of the coils by 11.8 dB, and at 60 kHz, the mutual inductance is reduced by 12.3 dB.

With some fine tuning, this may be an effective method for reducing the effect of resonances within the receive coil. However, if this does not prove to be as effective as hoped, other avenues will need to be explored to reduce capacitive coupling within the coils.

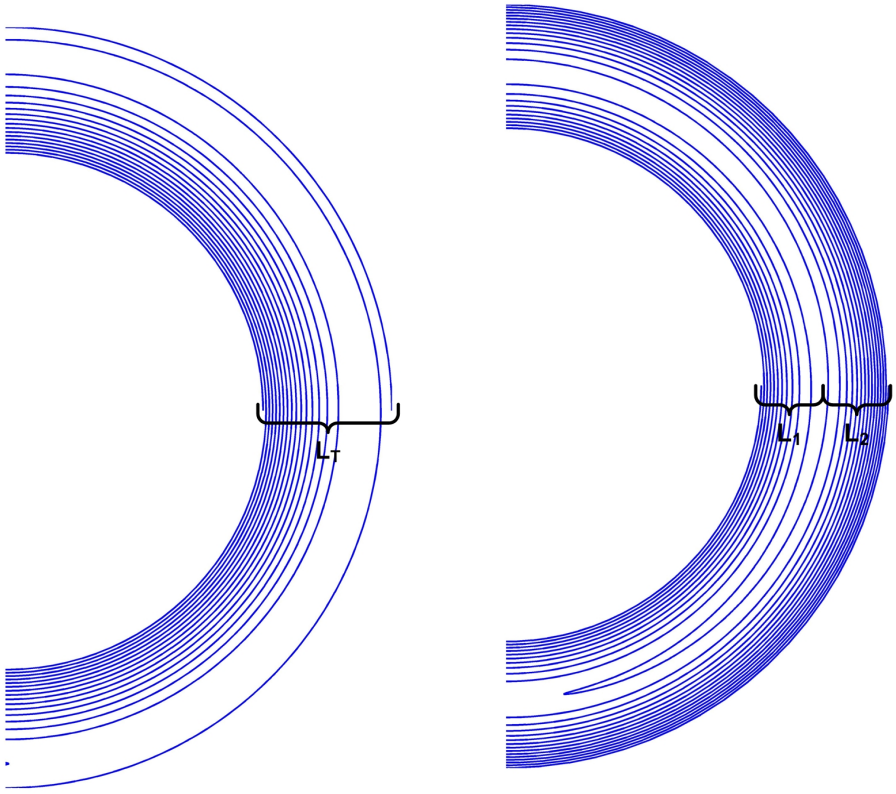

(a) The transmit coil, where L_T encompasses both sides of the coil.

(b) The receive coil, where L_1 encompasses the corresponding turns on both sides of the coil. There are two inductors with the value L_2, each representing turns on one side.

Figure 23: Illustration of the conversion of coils to lumped inductors.

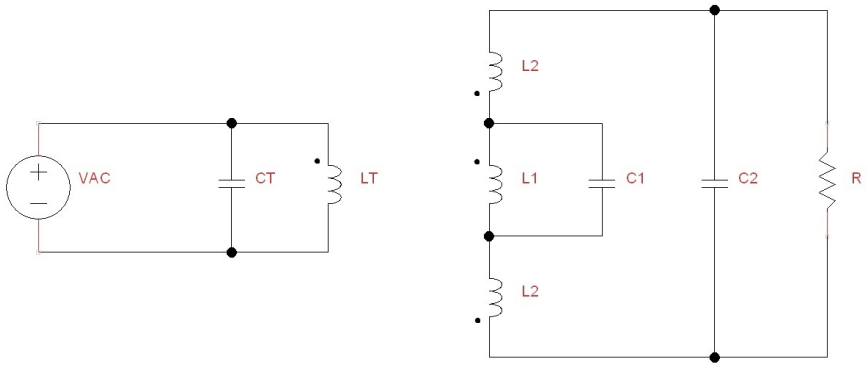

Figure 24: Lumped element model of the transmit coil (left) and receive coil (right). The output of the receive coil is across R, a 14 $k\Omega$ resistor in the measurement equipment. The resistances of the inductors and the dependent sources that result from mutual coupling between all inductors have been omitted from the diagram for simplicity.

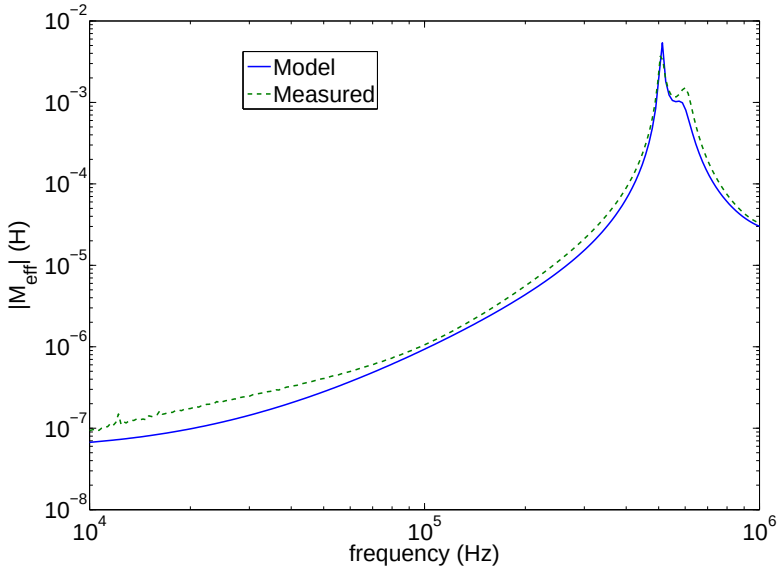

Figure 25: Comparison of the model for the effective mutual inductance of the coils to the measured data.

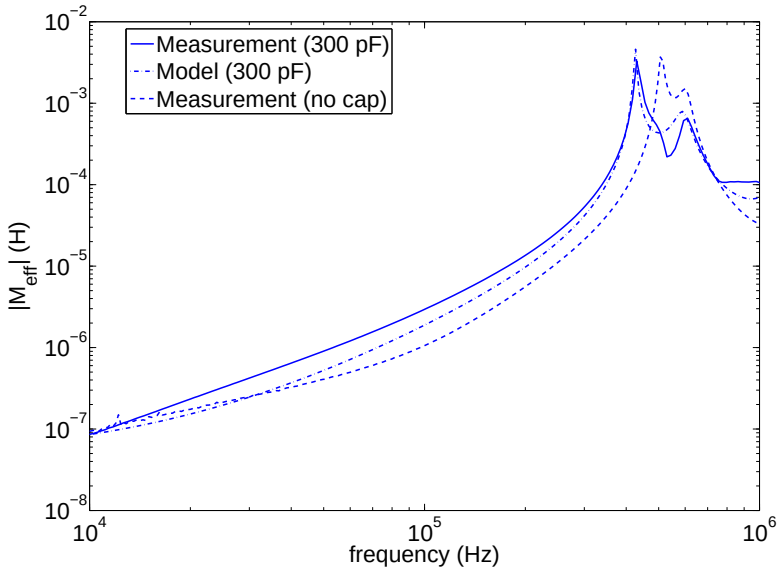

Figure 26: The model and physical coil with a 300 pF capacitor in parallel with C_1. The measurement without an additional capacitor is included for comparison.

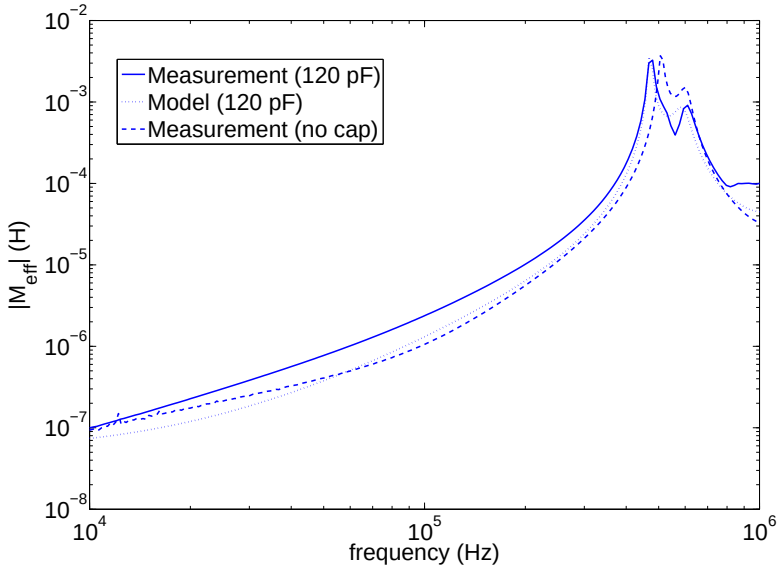

Figure 27: The model and physical coil with a 120 pF capacitor in parallel with C_1. The measurement without an additional capacitor is included for comparison.

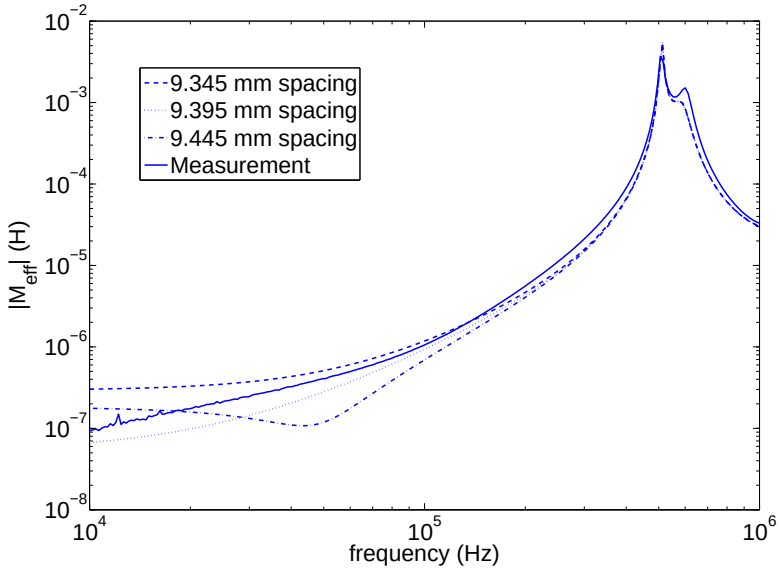

Figure 28: Model of the effective mutual inductance for three different coil spacings. The middle spacing is the result of the original model fit. The original measurement that the model was fitted to is also included for comparison.

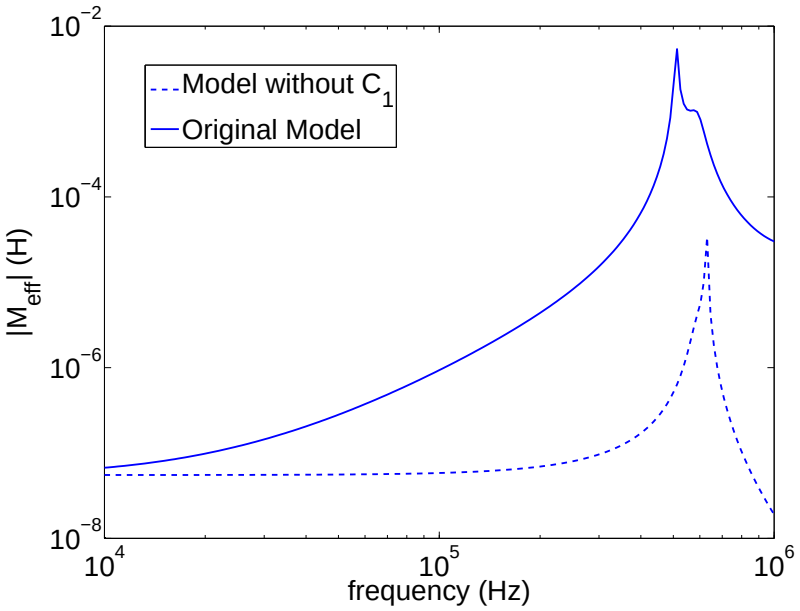

Figure 29: The effect of removing C_1 from the model.

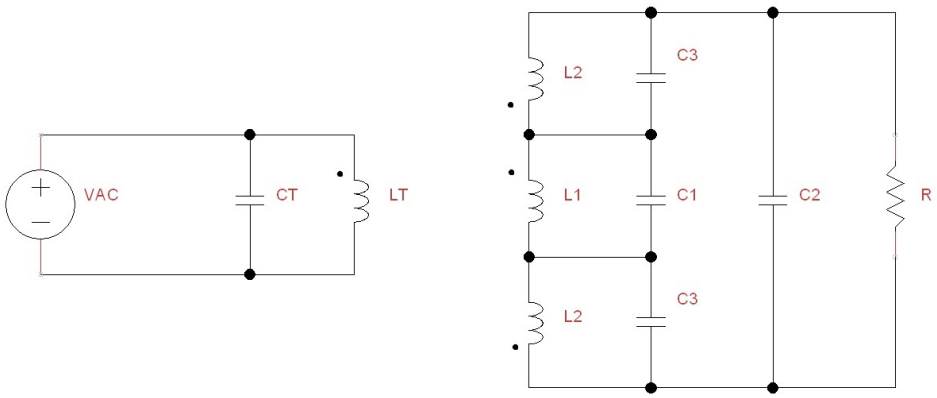

Figure 30: Circuit model of the transmit coil (left) and receive coil (right). The output of the receive coil is across R, a 14 $k\Omega$ resistor that is part of the measurement system.

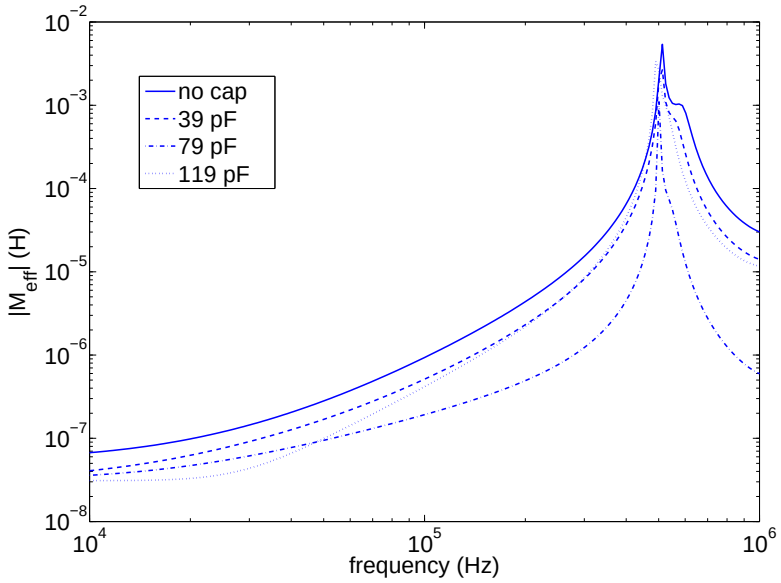

Figure 31: Illustration of the effect of different values of capacitor C_3 on the model.

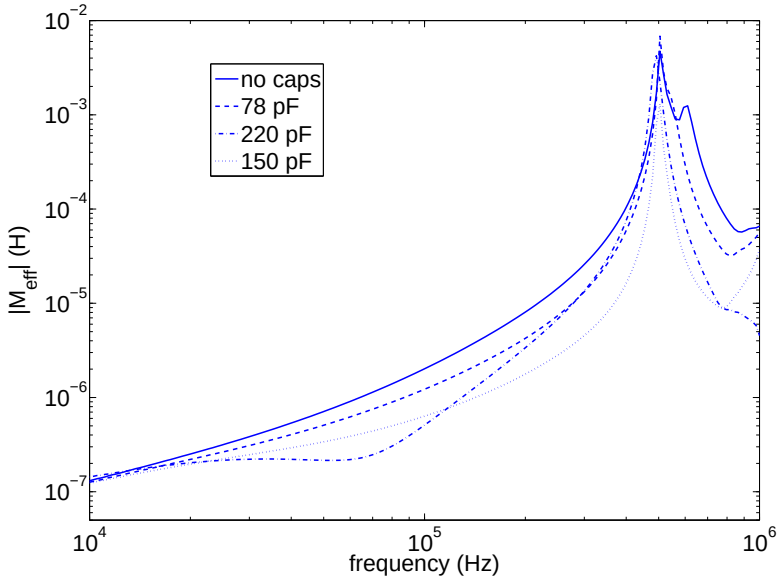

Figure 32: Effective mutual inductance of physical coils with various capacitors placed across the outer receive coil windings.

PART 2

Comparison and Optimization of Traditional, Wire-Wound Coil Geometries

CHAPTER V

NORMALIZED METRICS FOR WIRE COILS

The work in previous chapters has dealt with creating coil heads through various optimization procedures. During this work, it became apparent that adequately comparing different coil head designs to one another is cumbersome because many factors determine how well different coil heads perform when constructed and attached to a system. For example, coil dimensions, wire diameters, transmit power, amplifier noise, and winding geometry all influence both target sensitivity and soil sensitivity.

Metrics are needed to compare coil heads based only upon their winding geometry, so creating normalized target and soil sensitivity metrics that remove these extraneous factors is desirable. It is also important that the metrics be directly comparable and extensible to the stream function coil heads so that the metrics may be used in future work on optimized coil heads.

There are not any existing methods of comparing coil heads for EMI systems that have these properties, nor does there appear to be any literature that compares coil heads fairly while accounting for both target and soil sensitivity using normalized metrics. For example, there are papers that design and compare EMI coils based on their ability to produce uniform fields and based on the behavior of their fields at specific locations [2, 3]. There are also papers that optimize and compare coils for maximum power transfer or to create optimal air-core magnetometers [28, 38]. Finally, work exists that compares various MRI coils and also work that compares a few common EMI coil types with respect to their performance in soil but not including target sensitivity [12, 13, 71]. None of these provides the overarching normalized metrics we need for comparing our optimized coils or a complete optimization and analysis of the performance of some of the coil types most commonly used in EMI systems.

After the creation of normalized coil metrics, yet another problem arises—both the target

and soil sensitivity are multi-dimensional. Target sensitivity varies as the target is moved relative to the coil head, and soil sensitivity generally varies with the height of the coil head above the soil and the tilt of the head with respect to the soil. The multi-dimensionality must be reduced to ease coil head comparisons.

In the following sections, normalized metrics are developed. The metrics are then used to optimize and compare double-D, dipole/quadrupole, and concentric coil heads to one another in Chapter 6.

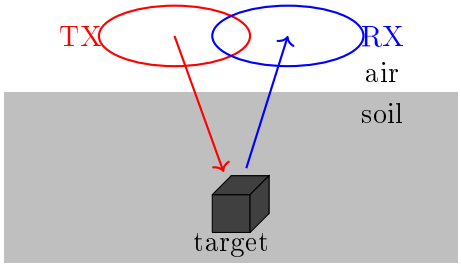

Figure 33: Two-coil head illuminating a target buried in soil.

5.1 Target Sensitivity

As stated before, when a conductive target is placed within the field produced by the transmit coil, energy is coupled between the transmit and receive coils through the target, resulting in an induced voltage at the terminals of the receive coil (Figure 33). This voltage can be—and often is—taken as a measure of target sensitivity, and is what was used when creating the spiral-wound wire coils.

Using reciprocity, the induced voltage can be written as

$$V_{\mathrm{r}} = j\omega\mu_0 I_{\mathrm{TX}} \frac{\vec{H}_{\mathrm{RX}} \cdot \bar{\bar{m}} \cdot \vec{H}_{\mathrm{TX}}}{I_{\mathrm{RX}} I_{\mathrm{TX}}}, \tag{23}$$

where $\bar{\bar{m}}$ is the magnetic polarizability dyad of the target[1], I_{TX} is the current flowing in the transmit coil, $\vec{H}_{\mathrm{TX}}$ is the transmit field at the target location, and $\vec{H}_{\mathrm{RX}}$ is the field that would be produced at the target location if the receive coil were driven by the current I_{RX} [62]. A comparison between coils using the expression in (23) is not as meaningful as it

[1]The target is assumed to be representable by the dipole model, and the fields across the target are assumed to be relatively uniform.

may appear. V_{r} cannot simply be normalized by $j\omega\mu_0 I_{\mathrm{TX}}$ to give a fair comparison between two different coil head designs.

5.1.1 Power Dissipation and Thermal Noise

The quantities $\vec{H}_{\mathrm{TX}}$ and $\vec{H}_{\mathrm{RX}}$ contain information about the geometries of the transmit and receive coils, respectively. However, the geometry can also include multiple turns of the same shape. For a given current, these turns effectively increase the field compared to a single turn, i.e. a dipole coil with multiple, identically shaped turns appears better than a dipole with a single turn if only V_{r} is considered. So, to fairly compare two coil heads, their sensitivities can be normalized by their lengths (effectively removing the advantage of extra turns).

The resistance of the coils is an important parameter that must be accounted for correctly because it directly impacts the power consumption of the transmit coil and the noise response of the receive coil. All else being equal, if one transmit coil dissipates less power than another, then the coil that heats less is superior. Similarly, receive coils that produce small amounts of thermal noise are desirable. Ideally, the dissipated power or thermal noise should be kept constant between coil heads that are being compared.

The resistance of a coil is easily computed if the current is assumed to be uniform in the wires:

$$R = \frac{l^2}{\sigma V}\,, \tag{24}$$

which in this form consists of the conductor length, l, the volume of the conductor, V, and the conductivity, σ. Increasing the conductivity or conductor volume and decreasing the length will decrease the dissipated power or thermal noise voltage of a coil, and vice versa.

These concepts can be introduced into the target sensitivity calculations. First, consider the power dissipated by the transmit coil,

$$P_{\mathrm{TX}} = \frac{l_{\mathrm{TX}}^2 I_{\mathrm{TX}}^2}{\sigma V_{\mathrm{TX}}}\,. \tag{25}$$

Rearranging (25) results in an expression for the current,

$$I_{\mathrm{TX}} = \frac{\sqrt{P_{\mathrm{TX}}\sigma V_{\mathrm{TX}}}}{l_{\mathrm{TX}}}\,, \tag{26}$$

which can be substituted into the I_{TX} term in the numerator of (23). I_{TX} can be assumed to be positive and real without loss of generality and is also assumed to be uniformly distributed in the wire.

Next, consider the expression for the the thermal noise voltage of the receive coil,

$$|V_{\mathrm{n}}| = \sqrt{4kTR_{\mathrm{RX}}\Delta f}\,, \tag{27}$$

where k is Boltzmann's constant, T is the temperature, R_{RX} is the resistance, and Δf is the bandwidth. Substituting the resistance of the receive coil, $R_{\mathrm{RX}} = l_{\mathrm{RX}}^2/\sigma V_{\mathrm{RX}}$ into the expression for the thermal noise voltage of the receive coil gives

$$|V_n| = \sqrt{\frac{4kT\Delta f l_{\mathrm{RX}}^2}{\sigma V_{\mathrm{RX}}}}\,. \tag{28}$$

It should be noted that only the thermal noise of the receive coil is considered in this paper. Other forms of noise such as environmental noise, amplifier noise, and motion induced noise are not considered.

5.1.2 Creating a Normalized Sensitivity

The transmit current expression from (26) can be substituted into the induced voltage equation, (23), but including the thermal noise voltage requires a ratio. This ratio is the SNR at the terminals at the receive coil, and it can be calculated by combining (23), (26), and (28) as

$$\frac{|V_{\mathrm{r}}|}{|V_{\mathrm{n}}|} = \frac{\omega\mu_0\sigma\sqrt{P_{\mathrm{TX}}V_{\mathrm{RX}}V_{\mathrm{TX}}}}{\sqrt{4kT\Delta f}}\frac{\vec{H}_{\mathrm{RX}}\cdot\bar{\bar{m}}\cdot\vec{H}_{\mathrm{TX}}}{I_{\mathrm{RX}}l_{\mathrm{RX}}I_{\mathrm{RX}}l_{\mathrm{RX}}}\,. \tag{29}$$

Note that the terms $\vec{H}_{\mathrm{TX}}/I_{\mathrm{TX}}$ and $\vec{H}_{\mathrm{RX}}/I_{\mathrm{RX}}$ are independent of the currents.

Quantities such as the transmit power, the volumes of the conductors, receiver bandwith, etc. influence the SNR, but they are not characteristics of winding patterns. It is therefore desirable to normalize the SNR by everything on the left half of (29). The remaining expression is multiplied by the fourth power of the radius,[2] r—though other characteristic

[2]Care must be taken in choosing the characteristic dimension as it has a strong effect on the normalized sensitivity. For example, if square and round coils are being compared, choosing the radius of the round coils is clear, but for the square coils, choosing the radius to the center of the side or the corner makes a sqrt(2) difference in the radius. The sqrt(2) difference in the characteristic dimension results in a factor of 4 difference in the normalized sensitivity. The correct choice of the radius in this example depends on the physical constraints desired for the coils. One choice is correct if the coils are constrained to fit into a square and the other is correct if the coils are constrained to fit into a circle.

dimensions could be chosen—to make the normalized sensitivity independent of coil and system size (but not target size). This gives an expression for normalized target sensitivity,

$$\widehat{S}_{\mathrm{T}} = r^4 \frac{\vec{H}_{\mathrm{RX}} \cdot \widehat{\bar{\bar{m}}} \cdot \vec{H}_{\mathrm{TX}}}{I_{\mathrm{RX}} l_{\mathrm{RX}} I_{\mathrm{TX}} l_{\mathrm{TX}}} \,, \tag{30}$$

where the magnetic polarizability of the target, $\bar{\bar{m}}$, has been normalized by its spectral norm: $\widehat{\bar{\bar{m}}} = \bar{\bar{m}}/||\bar{\bar{m}}||$. Note that the sensitivity is a function of the symmetry of the target. For this work, $\bar{\bar{m}}$ is chosen to be the identity dyad, which represents an infinitesimal, spherical (rotationally symmetric) target.

5.2 Soil Sensitivity

Mineralized soil (soil where the magnitude of the magnetic susceptibility, χ, is nonzero) will induce a voltage in the receive coil by changing the effective coupling between the transmit and receive coils. This voltage[3] can be a significant problem if the soil is heavily mineralized or the target is small or weakly conductive. Comparing the performance of coils in mineralized soil is therefore important, so a normalized soil sensitivity metric will now be developed.

The voltage induced in the receive coil as a result of energy coupled through the soil between the transmit and receive coils can be written as

$$V_{\mathrm{s}} = j\omega\mu_0 I_{\mathrm{TX}} \int_{\mathrm{soil}} \chi \frac{\vec{H}_{\mathrm{TX}} \cdot \vec{H}_{\mathrm{RX}}}{I_{\mathrm{TX}} I_{\mathrm{RX}}} dV \,, \tag{31}$$

where χ is the magnetic susceptibility of the soil, and under the Born approximation, $\vec{H}_{\mathrm{TX}}$ and $\vec{H}_{\mathrm{RX}}$ are calculated in free space. This expression can be considerably simplified by recognizing that the method of images can be used and the Born approximation eschewed [8]. The integral can be written in terms of the mutual inductance, $\widehat{M}_{\widehat{\mathrm{TX}},\mathrm{RX}}$, between a transmit coil that is mirrored about the air/soil interface and the receive coil [13]:

$$V_{\mathrm{s}} = j\omega I_{\mathrm{TX}} \frac{\chi}{2+\chi} \widehat{M}_{\widehat{\mathrm{TX}},\mathrm{RX}} \,, \tag{32}$$

where the soil is assumed to be homogeneous and isotropic.

[3] Highly conductive soils can also induce an unwanted voltage in the receive coil. However, a treatment of the effects of conductive soils is beyond the scope of this paper.

A cursory examination shows that (23) and (32) are similar. It is sensible to once again substitute (26) into (32) and divide by (28), which gives the following expression,

$$\frac{|V_{\mathrm{s}}|}{|V_{\mathrm{n}}|} = \frac{\omega\sigma\sqrt{P_{\mathrm{TX}}V_{\mathrm{RX}}V_{\mathrm{TX}}}}{\sqrt{4kT\Delta f}}\frac{\chi}{2+\chi}\frac{\widehat{M}_{\widehat{\mathrm{TX}},\mathrm{RX}}}{l_{\mathrm{TX}}l_{\mathrm{RX}}}\,. \tag{33}$$

Next, note that the mutual inductance can be written in terms of the coil fields as

$$\widehat{M}_{\widehat{\mathrm{TX}},\mathrm{RX}} = 2\mu_0\int_{\mathrm{soil}}\frac{\vec{H}_{\mathrm{TX}}\cdot\vec{H}_{\mathrm{RX}}}{I_{\mathrm{TX}}I_{\mathrm{RX}}}dV\,, \tag{34}$$

so (33) must be normalized by the factor

$$2\mu_0\frac{\omega\sigma\sqrt{P_{\mathrm{TX}}V_{\mathrm{RX}}V_{\mathrm{TX}}}}{\sqrt{4kT\Delta f}}\frac{\chi}{2+\chi} \tag{35}$$

to remove quantities that are not characteristics of the winding pattern and multiplied by the characteristic dimension, r, in order to make the normalized sensitivity independent of coil and system size. The result of these operations is the normalized soil sensitivity,

$$\widehat{S}_{\mathrm{s}} = r\frac{\widehat{M}_{\widehat{\mathrm{TX}},\mathrm{RX}}}{2\mu_0 l_{\mathrm{TX}}l_{\mathrm{RX}}}\,. \tag{36}$$

Note that the mutual inductance term can be calculated for arbitrary geometries easily using Neumann's formula [36, 56].

5.3 Optimization Parameters

The target sensitivity, $\widehat{S}_{\mathrm{T}}$, of each coil head varies spatially in three dimensions, and the soil sensitivity, $\widehat{S}_{\mathrm{s}}$, varies with both the height of the coil head above the soil and its tilt relative to the soil. The dimensionality of these parameters must be reduced to help with comparisons, with the caveat that the choices are somewhat arbitrary, though it is believed that they are apt for the coils being analyzed.

5.3.1 Mean Target Sensitivity

The coil heads that are being compared are all designed to be handheld, two-coil heads (with one transmit and one receive coil) that are intended primarily to be swept side-to-side by an operator. In general, it is desirable to have a sensitivity pattern[4] that is broad along

[4]Here we will consider the sensitivity "pattern" to be a quantity analogous to an antenna pattern that describes how well the coil head detects a target—in this case a sphere

the y-axis (down-track direction), while the pattern in the x-direction (cross-track) is less important (see Figure 34)—in fact, a narrow cross-track pattern helps to improve target localization. Finally, good depth performance is obviously of interest.

Therefore, there are three dimensions to consider: x (cross-track), y (down-track), and z (depth). It is logical to calculate the sensitivity over a cube of some finite portion of the coil head's search region and then attempt to reduce the sensitivity pattern within this cube to a manageable quantity.

Knowledge of the general pattern shapes is useful in determining metrics for these coils. In particular, the double-D pattern is generally broad down-track and narrow cross-track with the peak close to the origin. The pattern of a concentric coil head is rotationally symmetric about the origin, and the pattern of a dipole/quadrupole peaks in the center of the two quadrupole loops while nulling on the y-axis.

Therefore, for some coils, such as the double-D and the dipole/quadrupole, it is first necessary to take the maximum of the sensitivity in the x-dimension of the sensitivity cube because the pattern is not centered:

$$\widehat{S}_{\mathrm{m}}(y,z) = \max_{x}\left(\left|\widehat{S}_{\mathrm{T}}(x,y,z)\right|\right) . \tag{37}$$

This reduces the sensitivity cube to a 2-D sensitivity matrix that is a function of y and z.

Next, to encourage a broad downtrack pattern, the geometric mean over 80%[5] of the coil head's maximum dimension ($2r$) in the y-dimension is taken:

$$\widehat{S}_{\mathrm{gm}}(z) = \operatorname{geo\_mean}_{y}\left(\max_{x}\left(\left|\widehat{S}_{\mathrm{T}}(x,y,z)\right|\right)\right) . \tag{38}$$

This results in a sensitivity metric that is a function only of z, reducing the 2-D sensitivity matrix to a sensitivity vector. A geometric mean rather than a max or an arithmetic mean is used because a broad pattern in the y-direction is desirable, and regions of poor sensitivity within the sensitivity cube are given more importance by a geometric mean than an arithmetic mean. For example, a single location with zero sensitivity will make the geometric mean zero.

[5] An arbitrary choice, but one that we believe to be appropriate. A different dimension could be chosen depending upon the coil application.

$\widehat{S}_{\text{gm}}$ is a function of depth, so another geometric mean, $\widehat{S}_{\text{ggm}}$ is taken over $\widehat{S}_{\text{gm}}$—this time in the z-dimension, reducing the sensitivity matrix to a scalar value—to create a volume target sensitivity metric[6].

5.3.2 Soil Sensitivity

Like the target sensitivity, the soil sensitivity has multiple dimensions—it varies as the coil head is tilted relative to the soil (or as the surface of the ground becomes rough) and as the height of the head above the soil changes. However, the worst case within the normal range of soil heights and tilts over which the coils will be used is the most important. The soil response of all three coil head types generally increases as they are brought closer to the surface of the soil, but because coil heads are generally operated above a certain height and because the soil response will be calculated at each height with the coils tilted, we have arbitrarily chosen to calculate the soil response for the coil heads starting at $0.2r$ above the soil. In addition to the minimum height that has been chosen, it makes sense to calculate the soil sensitivity for various soil heights (h_{s}) and tilts (t_{c}) and then take the maximum over all heights ($0.2r < h_{\text{s}} < 1.0r$) and tilts ($0 < t_{\text{c}} < 10$ degrees) within a reasonable range. The rotational symmetry of the concentric head requires only one tilt angle while the double-D and dipole/quadrupole heads require two angles each.

Finally, low soil sensitivity is desirable but not at the expense of target sensitivity. To this end, it is desirable to balance good target sensitivity with low soil sensitivity, so it makes sense to take the ratio our various mean target sensitivity metrics and the maximum soil sensitivity:

$$\widehat{S}_{\text{gms}} = \frac{\widehat{S}_{\text{gm}}}{\max\left(\left|\widehat{S}_{\text{s}}\right|\right)}, \tag{39}$$

and

$$\widehat{S}_{\text{ggms}} = \frac{\widehat{S}_{\text{ggm}}}{\max\left(\left|\widehat{S}_{\text{s}}\right|\right)}. \tag{40}$$

[6]Taking a mean over depth seems like a poor metric since $\widehat{S}_{\text{gm}}$ decreases dramatically with depth. This would be true for an arithmetic mean because the strong responses would overwhelm the weak responses, but it is not true for the geometric mean because it equally weighs the strong and weak responses. The geometric mean can be thought of as an arithmetic mean of the log of the response.

5.3.3 Target Sensitivity versus Soil Sensitivity

Designing coil heads with high target sensitivity and low soil sensitivity is desirable. However, these two traits are not always positively correlated, so both traits must be considered independently in an optimization. In the quest to design a good "all-around" coil head, trading off some raw target sensitivity for a large reduction in soil sensitivity is possibly desirable, but, obviously, reducing the target sensitivity too much in the quest for low soil sensitivity will negatively impact performance in lightly mineralized soils. A metric that strikes a balance between the two traits is necessary.

The metric $\widehat{S}_{\text{ggm}}$ gives a simple measure of target sensitivity. The metric $\widehat{S}_{\text{ggms}}$ gives a simple measure of the target sensitivity relative to the soil sensitivity, but it does not consider the absolute value of the target sensitivity. A coil with very poor target sensitivity can still appear very good if the soil sensitivity is negligible.

For this work, this is handled by making a parametric graph, Figure 62, which plots $\widehat{S}_{\text{ggm}}$ against $\widehat{S}_{\text{ggms}}$ for a range of double-D coil parameters for all coil heads considered and is used to choose optimized double-D, concentric, and dipole/quadrupole coil heads. This considers both the target sensitivity of a coil head and the target sensitivity versus the soil sensitivity of a coil head. If lines of -1 slope (such as the dashed lines in Figure 62) were drawn through each coil, the best performing coil head would be the one with the greatest y-intercept.

CHAPTER VI

OPTIMIZING AND COMPARING WIRE-WOUND COILS

6.1 Coil Analysis

Now double-D, concentric, and dipole/quadrupole coil heads can be optimized. Each coil head type is characterized by one or two geometric parameters, which can be swept over reasonable ranges to vary the shape of the coil head. Metrics from the previous sections are calculated as the coil heads are permuted, and the best coils of each type can then be determined and compared to one another. All coils are constrained to fit into a square box with side lengths of $2r$ by $2r$.

These coil heads are typically constructed as tightly wound multi-turn coils. The windings are generally sufficiently close together so that they can be accurately modeled as a single large turn for the purpose of computing their magnetic fields. Then the normalized metrics, (30) and (36), will be essentially the same whether applied to the multi-turn coil or the single turn approximation because the length of the wire used in the metrics is proportional to the number of turns in the coil. For simplicity, the coils modeled here will use this single wire approximation. Note that the un-normalized metrics for the multi-turn and single turn approximation will also be essentially the same when the quantities such as the transmit power, the volumes of the conductors, receiver bandwith, etc. are the same.

6.1.1 Double-D coils

An example of the double-D coil head geometry chosen for analysis is shown in Figure 34. The coils are constrained to both fit in and fill a box that is $2r$ on each side. Each coil is made out of the halves of two ellipses with the same semi-major axis and different semi-minor axes, r_1 and r_2. During analysis, the ratio r_1/r_2 is swept over $10^{-1} < r_1/r_2 < 10^{1.5}$, while the overall width of each coil is determined by the overlap needed to null the coupling between the transmit and receive coils. A subset of the coils created for analysis is shown in Figure 35.

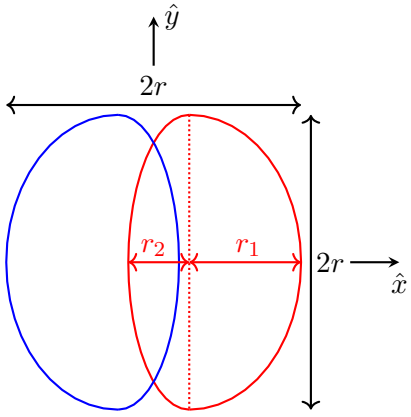

Figure 34: Optimal double-D coil geometry enclosed in a bounding box showing semi-minor axes r_1 and r_2, with the transmit coil in red and the receive in blue.

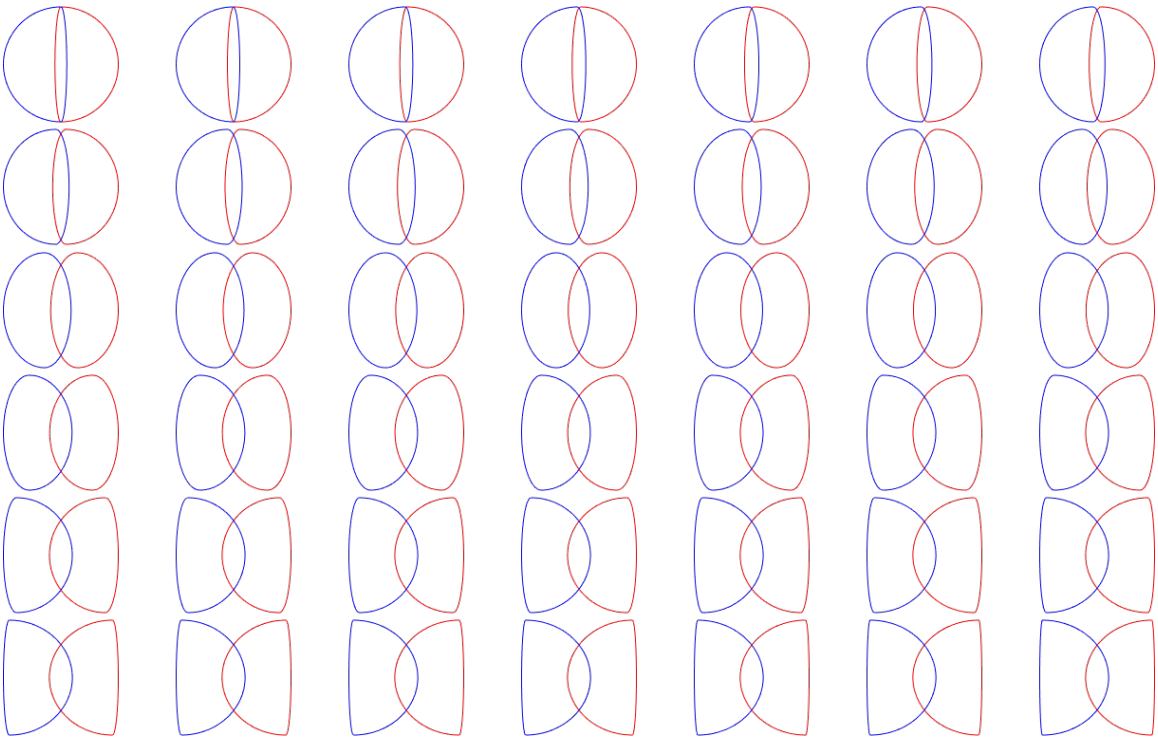

Figure 35: Subset of the double-D coils being analyzed.

The metrics $\widehat{S}_{\text{ggm}}$, $\widehat{S}_{\text{ggms}}$, and $\max\left(\widehat{S}_{\text{s}}\right)$ were calculated over the range of r_1/r_2 and plotted in Figure 36 against r_1/r_2, and $\widehat{S}_{\text{ggm}}$ and $\widehat{S}_{\text{ggms}}$ are also plotted against one another as a black line in Figure 62.

The optimal coil is much more apparent in Figure 62 than in Figure 36, illustrating the difficulty of choosing an optimal coil based on separate graphs of $\widehat{S}_{\text{ggm}}$, $\widehat{S}_{\text{ggms}}$, and $\widehat{S}_{\text{s}}$. Note

how $\widehat{S}_{\text{ggm}}$ and $\widehat{S}_{\text{s}}$ are roughly correlated, but $\widehat{S}_{\text{ggm}}$ and $\widehat{S}_{\text{ggms}}$ are poorly correlated. The best coil head is chosen and plotted as a circle on Figures 36 and 62. The geometry of the optimized coil head, for which $r_1/r_2 = 0.623$, is shown in Figure 34. It has $\widehat{S}_{\text{ggm}} = -66.68$ dB and $\widehat{S}_{\text{ggms}} = -13.72$ dB.

Figure 38 shows soil sensitivity cuts at various heights above the soil and tilts about the x-axis (θ) and the y-axis (ϕ) in degrees. The graphs appear off-center because the two coils of the double-D do not lie in exactly the same plane—there is an offset of $r/60$ in the z-direction to avoid nonphysical solutions resulting from overlapping coil turns. Interestingly, as the double-D is tilted, its soil sensitivity tends to improve. Figures 37, 39 and 40 illustrate the narrow cross-track and broad down-track sensitivity pattern of the double-D.

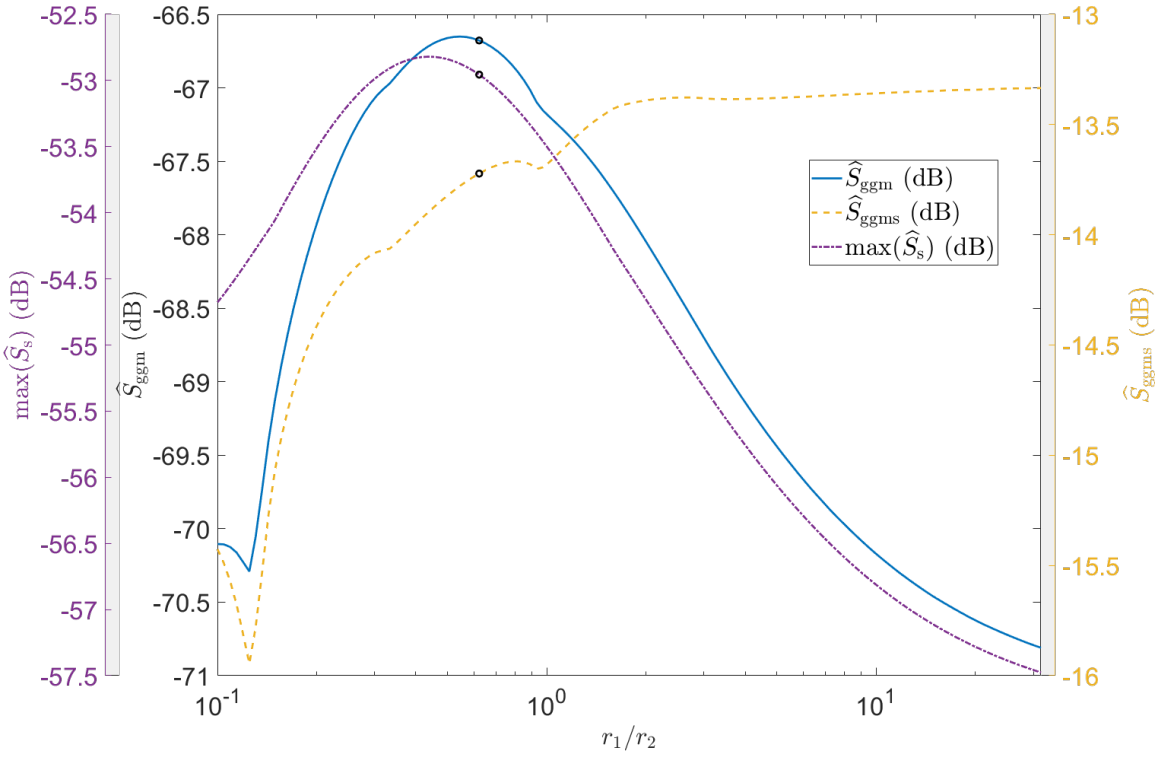

Figure 36: $\widehat{S}_{\text{ggm}}$, $\widehat{S}_{\text{ggms}}$, and $\max\left(\widehat{S}_{\text{s}}\right)$ for the range of double-D coils. The optimal coil is marked on each curve with a black circle.

The soil sensitivity was calculated at many heights above the ground, both for a level coil and for a coil that has been both tilted and rotated to account for all possible orientations. The maximum tilt used is the amount of tilt that would nearly touch the ground at the coil's

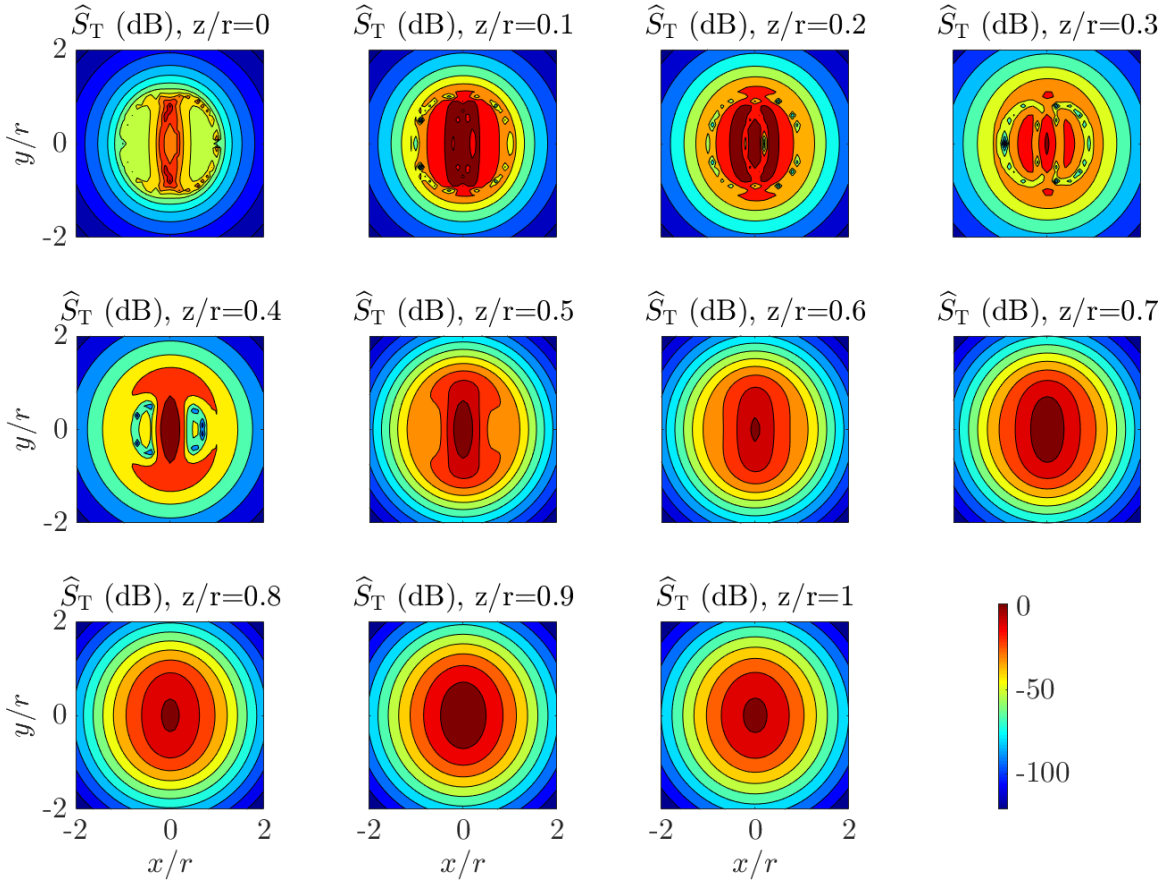

Figure 37: Double-D target sensitivity cuts in the $x-y$ plane for multiple depths of z/r.

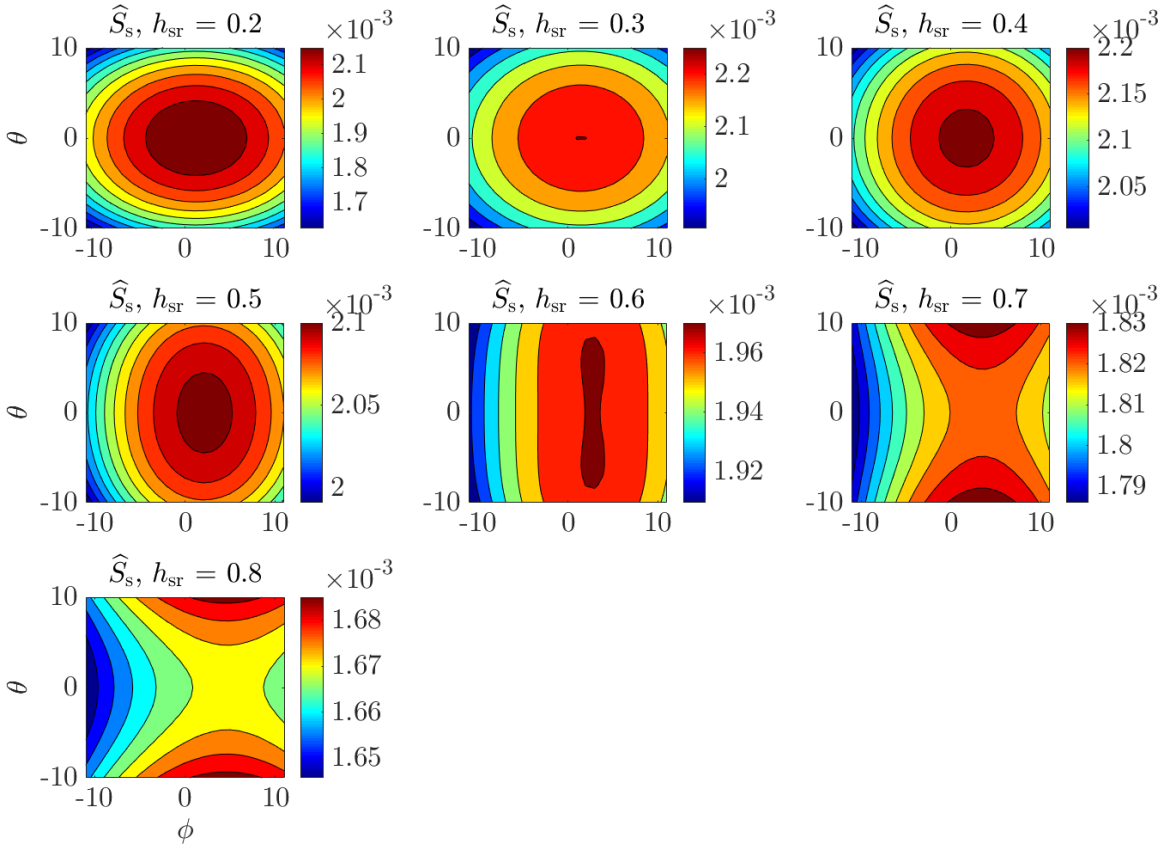

Figure 38: Optimal double-D soil sensitivity for various heights above the soil and tilts relative to the soil.

closest reasonable distance from the soil. The max tilt happens to be about ten degrees. The soil sensitivity for level coils plus minimum and maximum soil sensitivities is plotted in Figure 43.

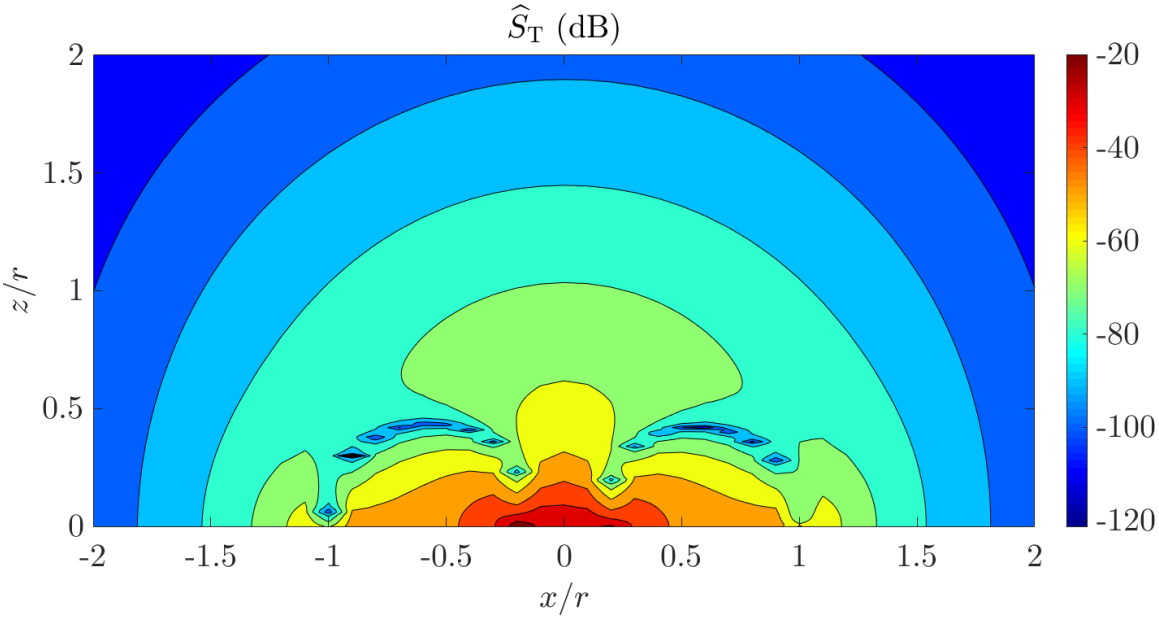

Figure 39: Optimal double-D x-z plane target sensitivity cut.

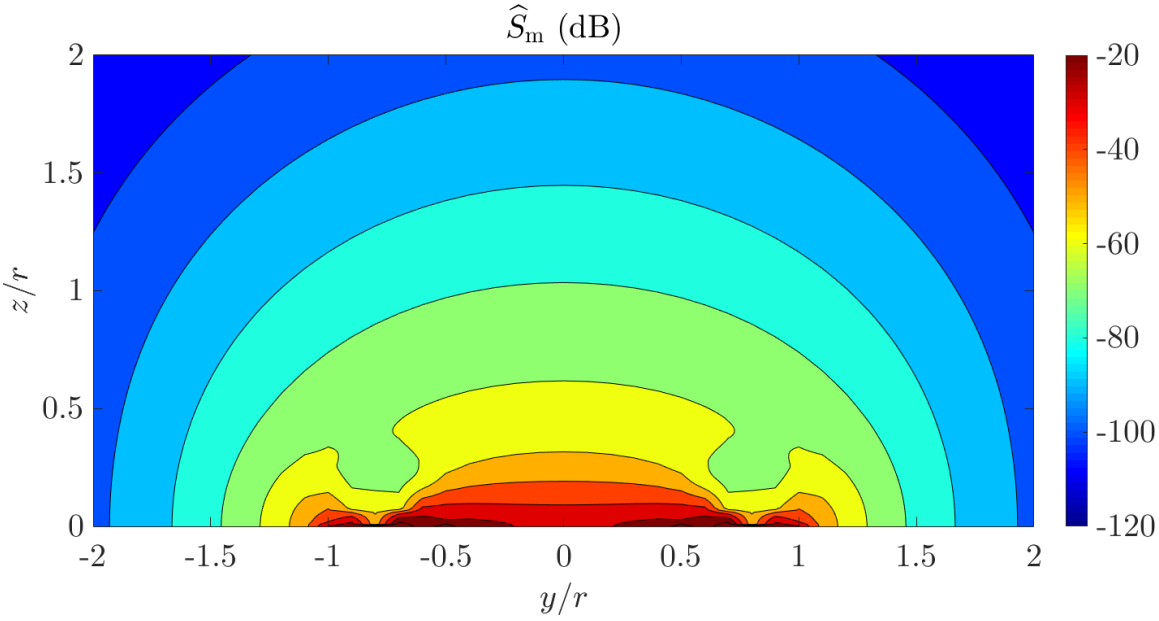

Figure 40: $\widehat{S}_{\mathrm{m}}$ of the optimal double-D coil head.

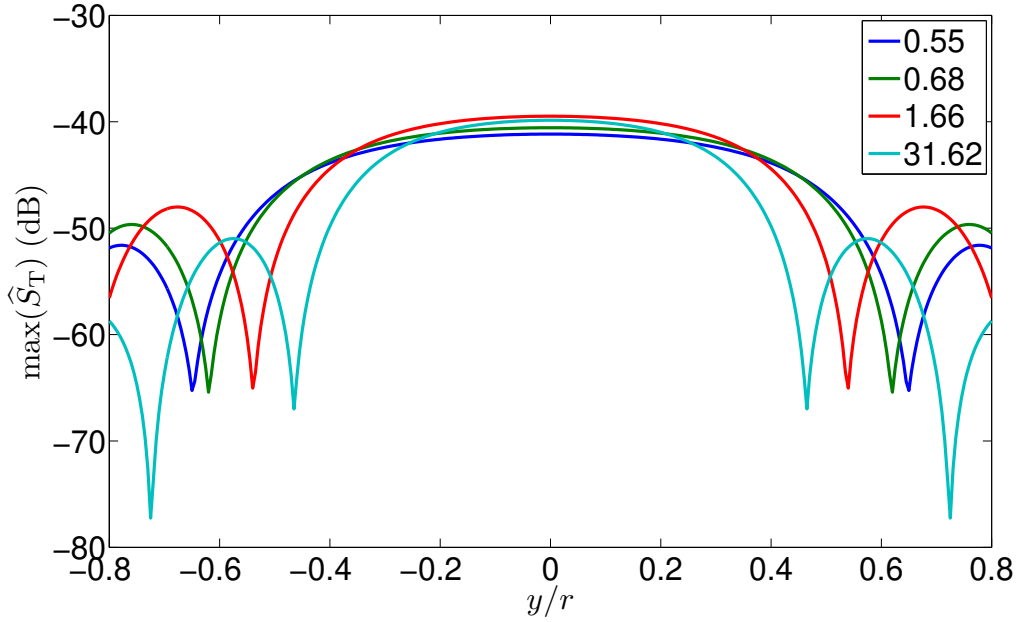

Figure 41: The maximum of the target sensitivity in x for several heads labeled by their r_1/r_2 at a target distance of $z = 0.2r$.

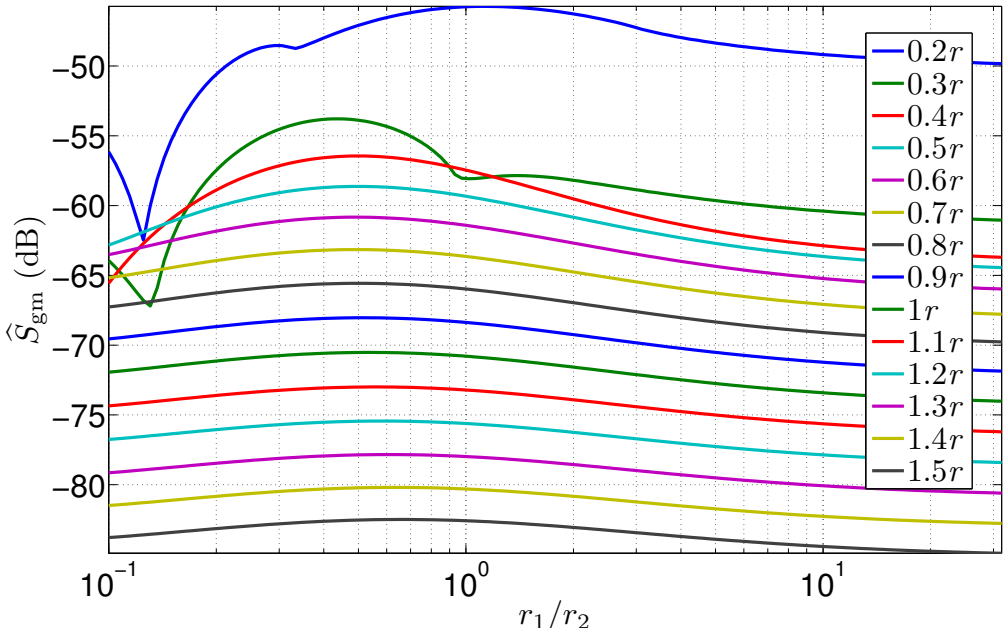

Figure 42: The results of (38) for different depths, given in terms of r.

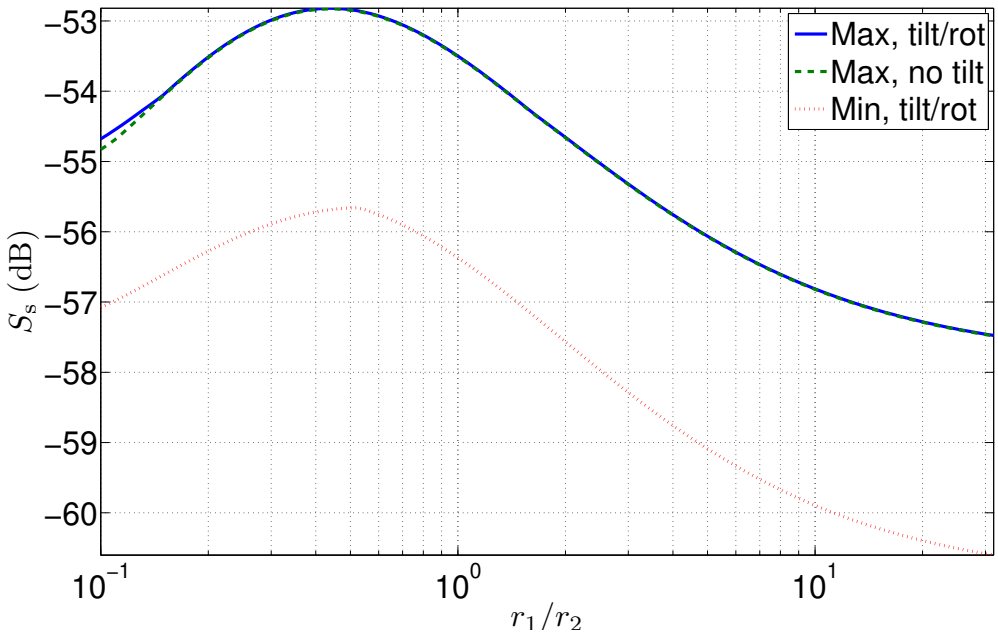

Figure 43: Soil sensitivity for the coils showing max sensitivity for level coils, max sensitivity for all tilts and rotations, and minimum for all tilts and rotations.

6.1.2 Concentric Coils

Concentric coil heads, such as the one pictured in Figure 44(a) with interconnected turns, will not be analyzed. This coil head consists of a single transmit coil and a receive coil with two counterwound sections, one inner and one outer. The mutual inductance between the transmit and receive coils is nulled by adjusting the turns ratio between the inner and outer sections of the receive coil. In the figure, the turns ratio, n, is two: $n = {}^{t_{\mathrm{RX,inner}}}/_{t_{\mathrm{RX,outer}}}$ (where t is the number of turns). It is assumed that the turns are tightly wound, so that the radius of each turn in a bundle is the same.

In order to simplify the representation, the coils were modeled differently from the coil head shown in Figure 44(a), ignoring the connection between the inner and outer portions of the receive coil. There are now effectively two receive coils, and the weighted sum of the voltage at the "terminals" of each receive coil will be the total received voltage (Figure 44(b)).

The single transmit coil has radius r_{T} and the two counterwound receive coils have radii r_1 and r_2, respectively. Each receive coil was modeled with a single turn, so the turns ratio is now analogous to a ratio of currents, $n = {}^{I_{\mathrm{RX1}}}/_{I_{\mathrm{RX2}}}$, where I_{RX1} and I_{RX2} are the currents flowing in the two receive coils. The transmit coil was spaced ${}^{r}/_{25}$ away from the receive coil in the z-direction to avoid nonphysical solutions where the two coils could become superimposed.

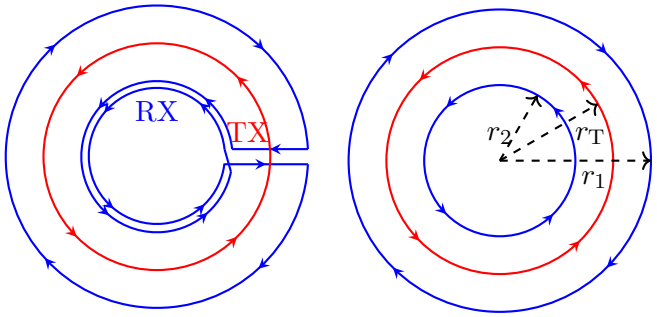

(a) Concentric coil head geometry.

(b) Modified concentric coil head geometry.

Figure 44: Illustration of a normal concentric coil and the concentric coil model used for coil optimization.

The coils are parameterized by two ratios, $\alpha_{\mathrm{T}} = {}^{r_{\mathrm{T}}}/_{r_1}$ and $\alpha_{\mathrm{R}} = {}^{r_2}/_{r_1}$, and the two parameters were swept over the ranges $10^{-0.7} < \alpha_{\mathrm{T}} < 10^{1}$ and $10^{-0.7} < \alpha_{\mathrm{R}} < 10^{-0.1}$. With the geometry set for each α_{T} and α_{R}, the turns ratio that gives null coupling between the transmit and receive coils was calculated.

6.1.3 Turns Ratio Calculation

The mutual coupling, c, between the transmit and receive coils must be zero for the coil head to operate properly. Achieving this with a single receive coil with two counterwound sections is relatively straightforward. With a current flowing through the receive coil, the ratio of turns between the two counterwound sections was adjusted until the flux through the transmit coil is zero. In the model, the turns ratio adjusts the ratio of currents.

The coupling factor for a single transmit and single receive coil is

$$c = \frac{M_{\mathrm{TR}}}{\sqrt{L_{\mathrm{T}} L_{\mathrm{R}}}} = \frac{W_{\mathrm{M}}}{\sqrt{2 W_{\mathrm{LT}} W_{\mathrm{LR}}}}\,, \tag{41}$$

where M_{TR} is the mutual inductance between the transmit and receive coils, L_{T} and L_{R} are the transmit and receive coil self inductances, respectively, W_{M} is the energy coupled between the transmit and receive coils, and W_{LT} and W_{LR} are the self energies of the transmit and receive coils, respectively.

It is apparent that nulling the coupling amounts to setting the energy coupled between the transmit and receive coils to zero. This energy is

$$E_{\mathrm{M}} = I_{\mathrm{TX}} \begin{bmatrix} M_{\mathrm{TX,RX1}} & M_{\mathrm{TX,RX2}} \end{bmatrix} \begin{bmatrix} I_{\mathrm{RX1}} \\ I_{\mathrm{RX2}} \end{bmatrix}. \tag{42}$$

By recognizing that the only important factor in the currents is the ratio between the two receive currents, the following substitutions can be made:

$$\begin{bmatrix} M_{\mathrm{TX,RX1}} & M_{\mathrm{TX,RX2}} \end{bmatrix} \begin{bmatrix} 1 \\ n \end{bmatrix} = 0\,. \tag{43}$$

The mutual inductances can be calculated quickly using a formula in [56]. The turns ratio is then

$$n = \frac{M_{\mathrm{TX,RX1}}}{M_{\mathrm{TX,RX2}}}\,. \tag{44}$$

6.1.4 Target Sensitivity

The expression in (30) can be used directly for the coils in Figure 44(a), but it requires modification for use with the three coil model. First, define the normalized magnetic field as

$$\widehat{H}_\alpha = \vec{H}_\alpha / I_\alpha \,, \tag{45}$$

where α denotes the coil with current I_α and field $\vec{H}_\alpha$.

Consider the numerator of (30), and recognize that the receive field is no longer simple and must be altered:

$$\vec{H}_{\mathrm{RX}} = I_{\mathrm{RX1}}\widehat{H}_{\mathrm{RX1}} + I_{\mathrm{RX2}}\widehat{H}_{\mathrm{RX2}} \,. \tag{46}$$

Redefine the two fields in terms of a single current using the turns ratio:

$$\vec{H}_{\mathrm{RX}} = I_{\mathrm{RX1}}\widehat{H}_{\mathrm{RX1}} + nI_{\mathrm{RX1}}\widehat{H}_{\mathrm{RX2}} = I_{\mathrm{RX1}}\left(\widehat{H}_{\mathrm{RX1}} + n\widehat{H}_{\mathrm{RX2}}\right) \,. \tag{47}$$

Now consider the denominator of (30), specifically the term $I_{\mathrm{RX}}l_{\mathrm{RX}}$:

$$I_{\mathrm{RX}}l_{\mathrm{RX}} = I_{\mathrm{RX1}}l_{\mathrm{RX1}} + I_{\mathrm{RX2}}l_{\mathrm{RX2}} \,, \tag{48}$$

where l_{RX1} and l_{RX2} are the lengths of the two receive coils. Redefining in terms of I_{RX1} and the turns ratio gives

$$I_{\mathrm{RX}}l_{\mathrm{RX}} = I_{\mathrm{RX1}}\left(l_{\mathrm{RX1}} + nl_{\mathrm{RX2}}\right) \,. \tag{49}$$

Combining terms gives a new normalized target sensitivity as

$$\widehat{S}_{\mathrm{T}} = r^4 \frac{\widehat{H}_{\mathrm{TX}} \cdot \widehat{\bar{\bar{m}}} \cdot \left(\widehat{H}_{\mathrm{RX1}} + n\widehat{H}_{\mathrm{RX2}}\right)}{l_{\mathrm{TX}}\left(l_{\mathrm{RX1}} + nl_{\mathrm{RX2}}\right)} \,. \tag{50}$$

6.1.5 Soil Sensitivity

However, (36) must be modified in a manner similar to (30) to account for the multiple receive coils:

$$\widehat{S}_{\mathrm{s}} = r \frac{\widehat{M}_{\widehat{\mathrm{TX}},\mathrm{RX1}} + n\widehat{M}_{\widehat{\mathrm{TX}},\mathrm{RX2}}}{2\mu_0 l_{\mathrm{TX}}\left(l_{\mathrm{RX1}} + nl_{\mathrm{RX2}}\right)} \,. \tag{51}$$

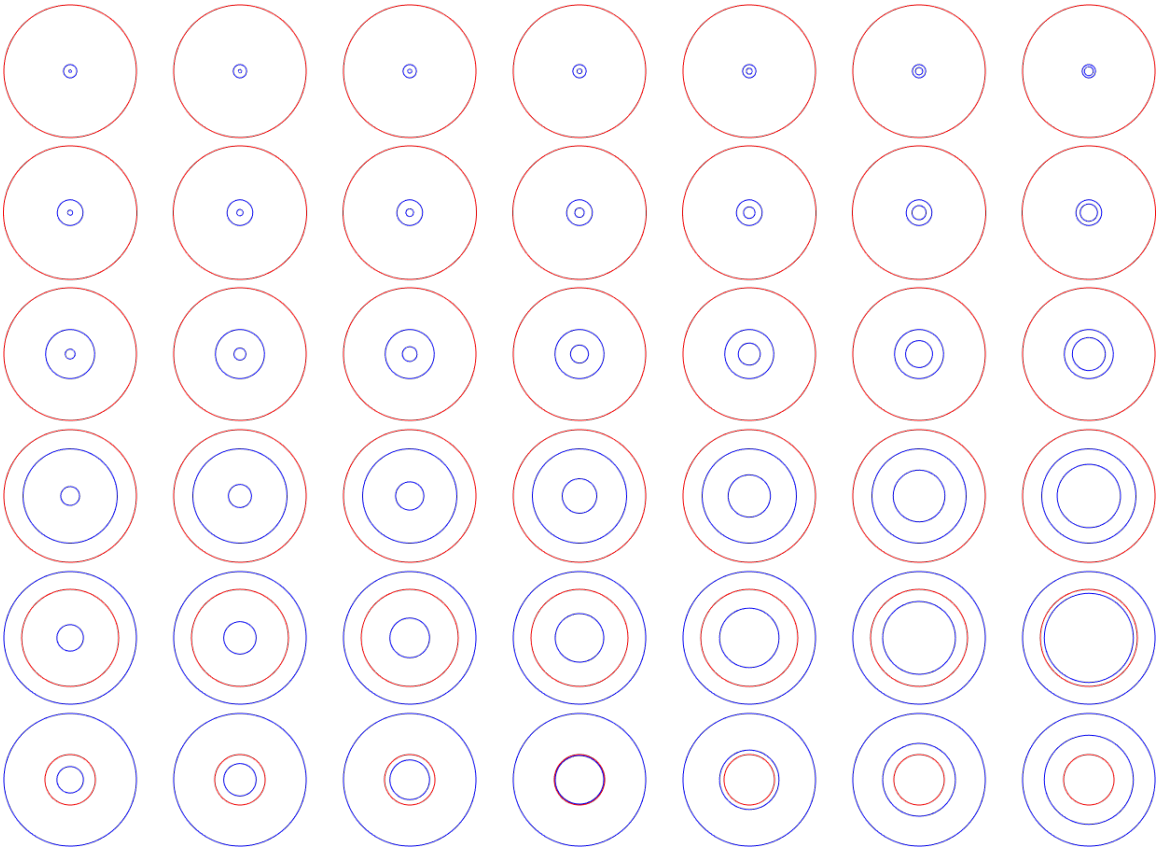

Figure 45: Subset of the concentric coils being analyzed.

6.1.6 Coil analysis

A subset of the range of concentric coils being analyzed is shown in Figure 45.

Once again, $\widehat{S}_{\text{ggm}}$ and $\widehat{S}_{\text{ggms}}$ were calculated for the range of coils and plotted in Figure 62 as a red area. The optimal coil was then chosen and plotted on the same graph as a black x.

The optimized coil has $\widehat{S}_{\text{ggm}} = -63.93$ dB and $\widehat{S}_{\text{ggms}} = -17.09$ dB, and the geometry is shown in Figure 46. The coil head has $\alpha_t = 0.42$ and $\alpha_r = 0.42$, and thus the transmit coil and inner receive coil have the same radius. The turns ratio of the receive coil is 0.292. The broad target sensitivity pattern of this concentric coil head is illustrated in Figure 47, and the soil sensitivity of this coil versus height above the soil and tilt relative to the soil is shown in Figure 49. The symmetry of concentric coils causes an interesting property—as the coil head is tilted, the soil sensitivity remains largely constant.

Figures 50 and 51 show the values of $\widehat{S}_{\text{ggm}}$ and $max\left(\left|\widehat{S}_{\text{s}}\right|\right)$ for each coil head that was considered. On these two graphs, $\widehat{S}_{\text{ggm}}$ is roughly correlated with soil sensitivity, $\widehat{S}_{\text{s}}$. The ratio of these two quantities is shown in Figure 52. The correlation between Figures 50 and 52 is less clear than that between $\widehat{S}_{\text{ggm}}$ and $\widehat{S}_{\text{s}}$—hence the need for a ratio. Comparing Figure 52 to Figure 50 shows how a coil that appears good when considering $\widehat{S}_{\text{ggms}}$—for example, any of the coils in the top portion with $\widehat{S}_{\text{ggms}} = -5$ dB—is ~ 70 dB down in raw target sensitivity compared to the best coils in Figure 50.

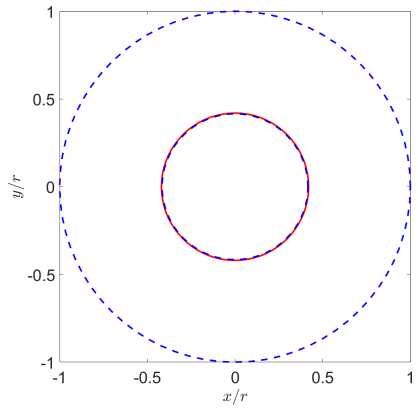

Figure 46: Optimal concentric coil geometry.

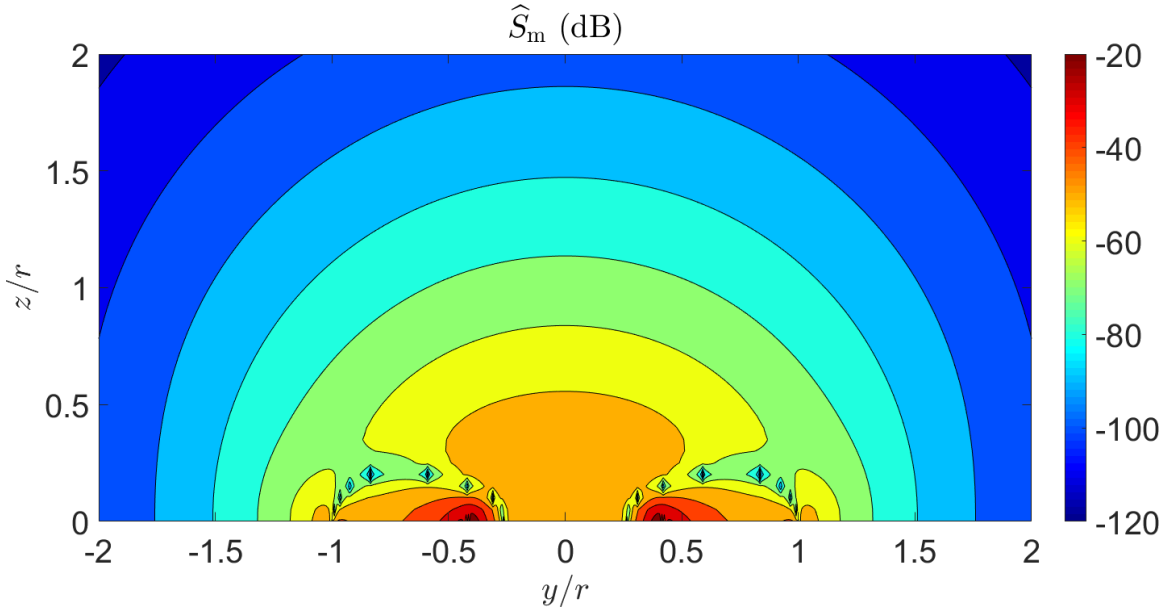

Figure 47: $\widehat{S}_{\text{m}}$ of the optimal concentric coil.

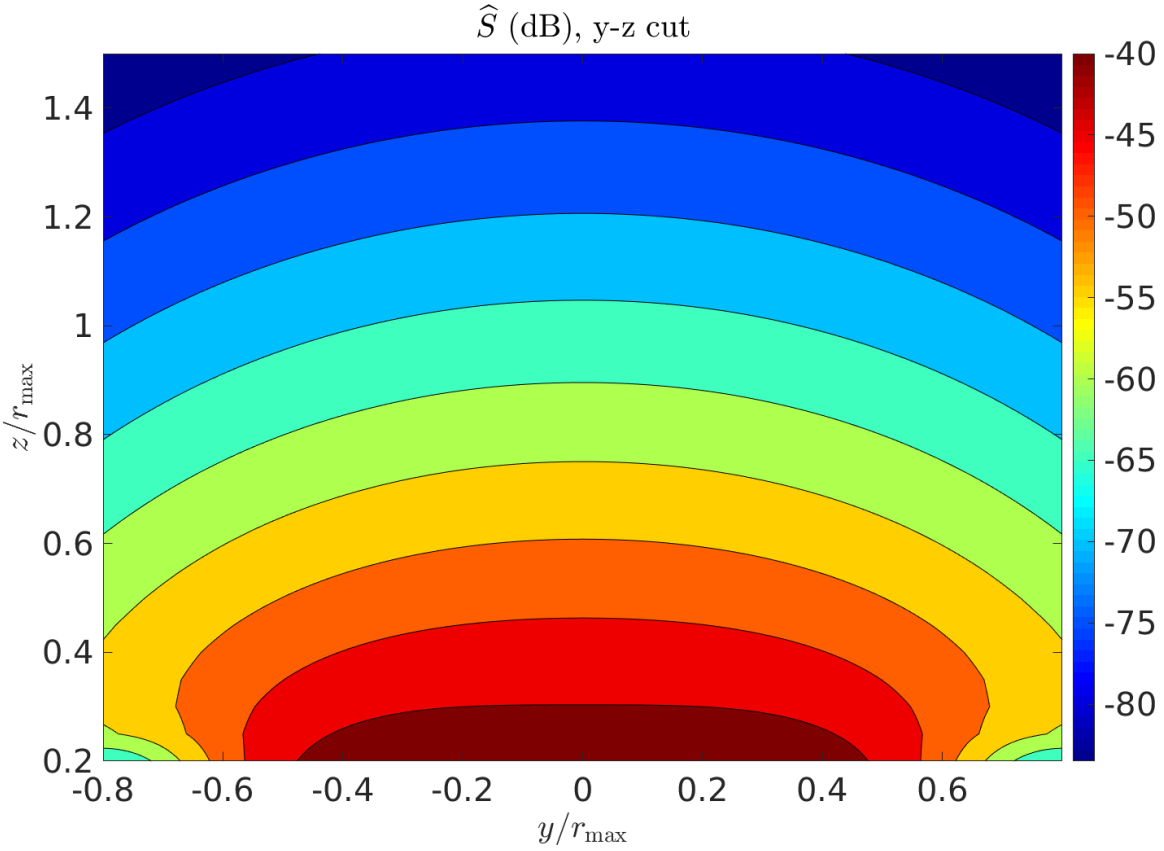

Figure 48: Sensitivity in the y-z plane of the optimal concentric coil.

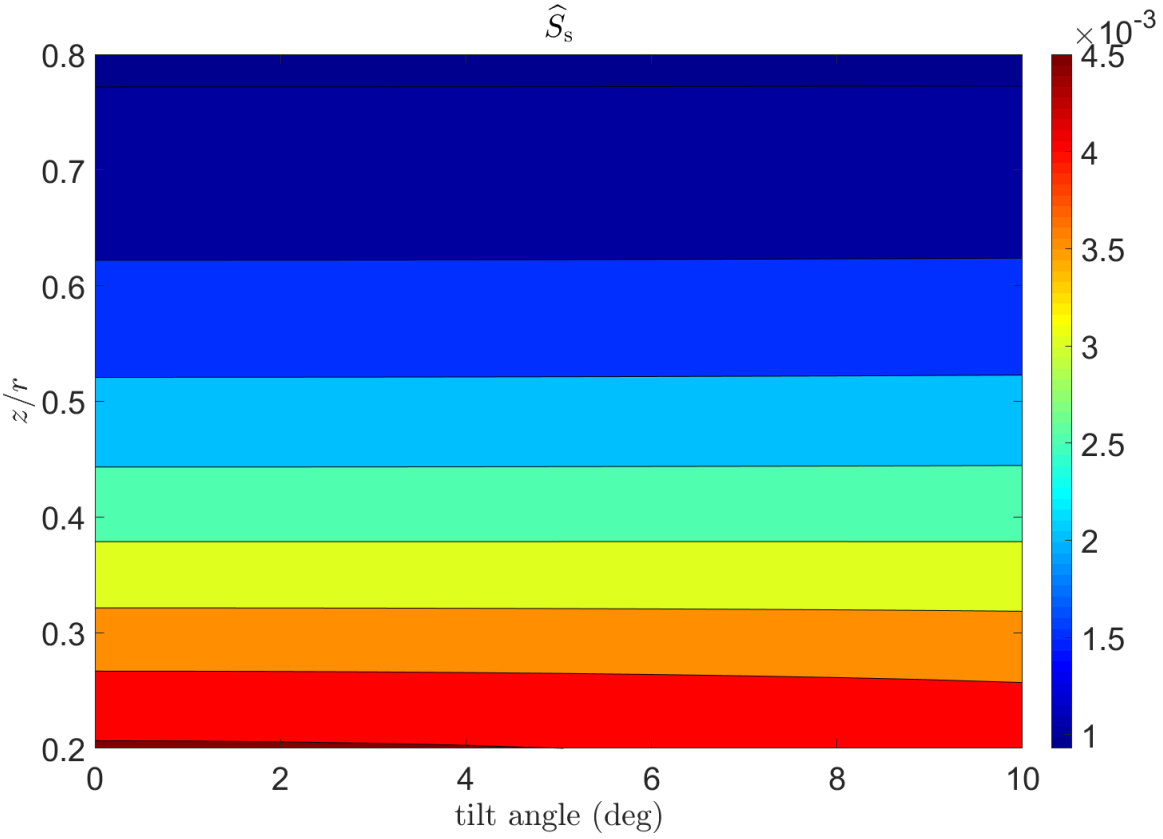

Figure 49: Soil sensitivity of the optimal concentric coil for many heights above the soil and tilts relative to the soil.

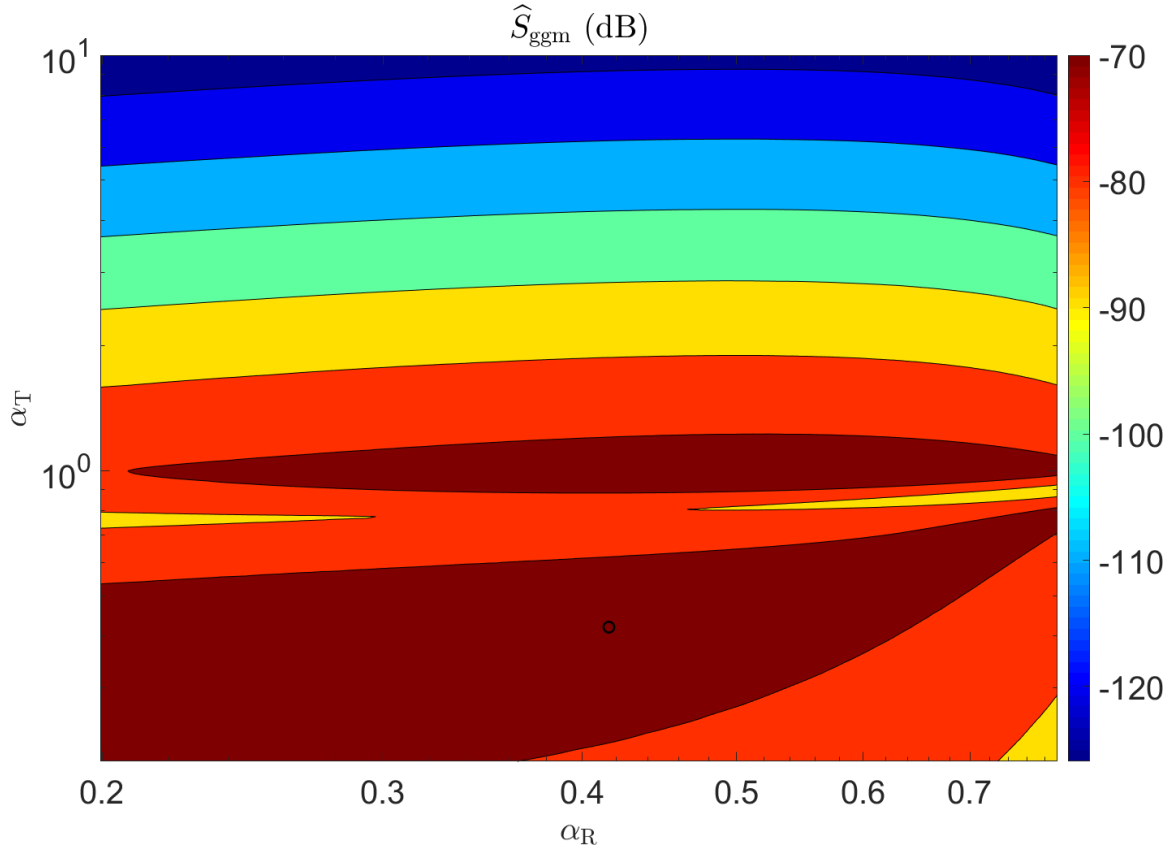

Figure 50: $\widehat{S}_{\mathrm{ggm}}$ for many concentric coils. The optimal coil is marked with a circle.

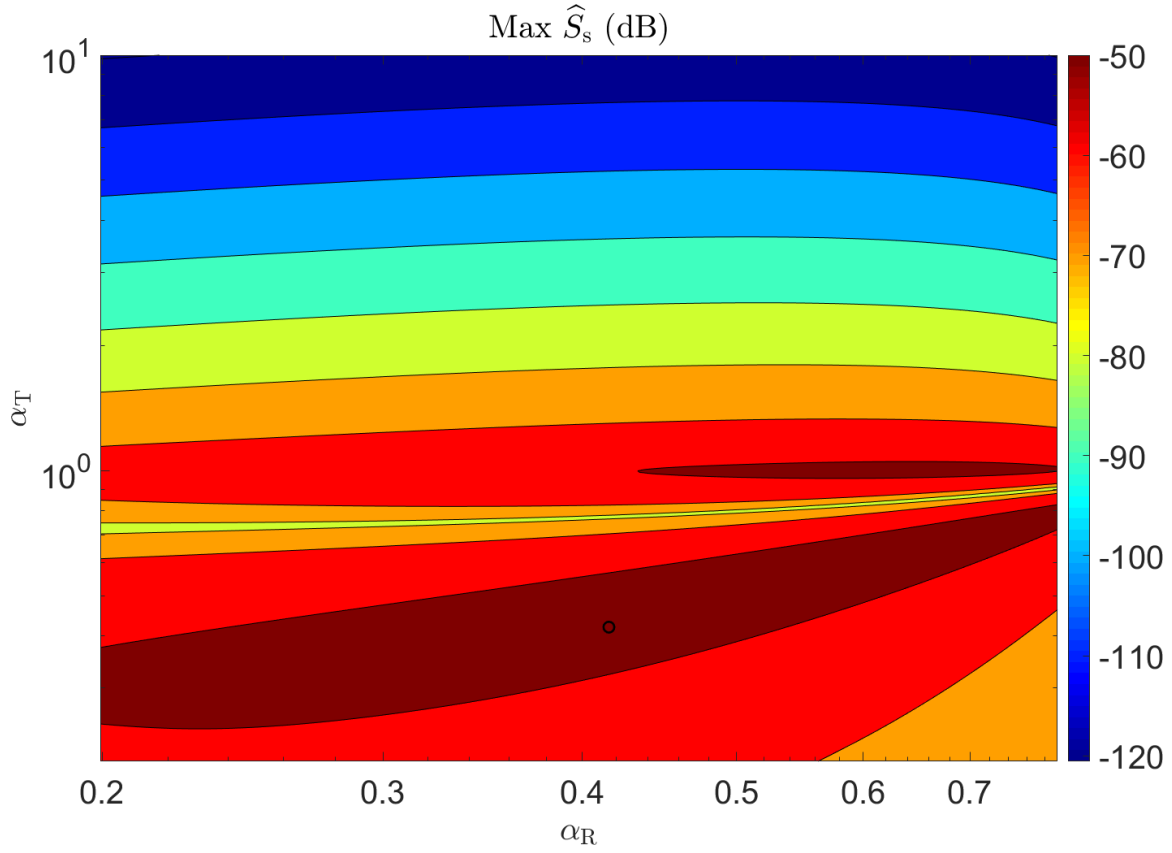

Figure 51: Maximum of the soil sensitivity for each concentric coil head.

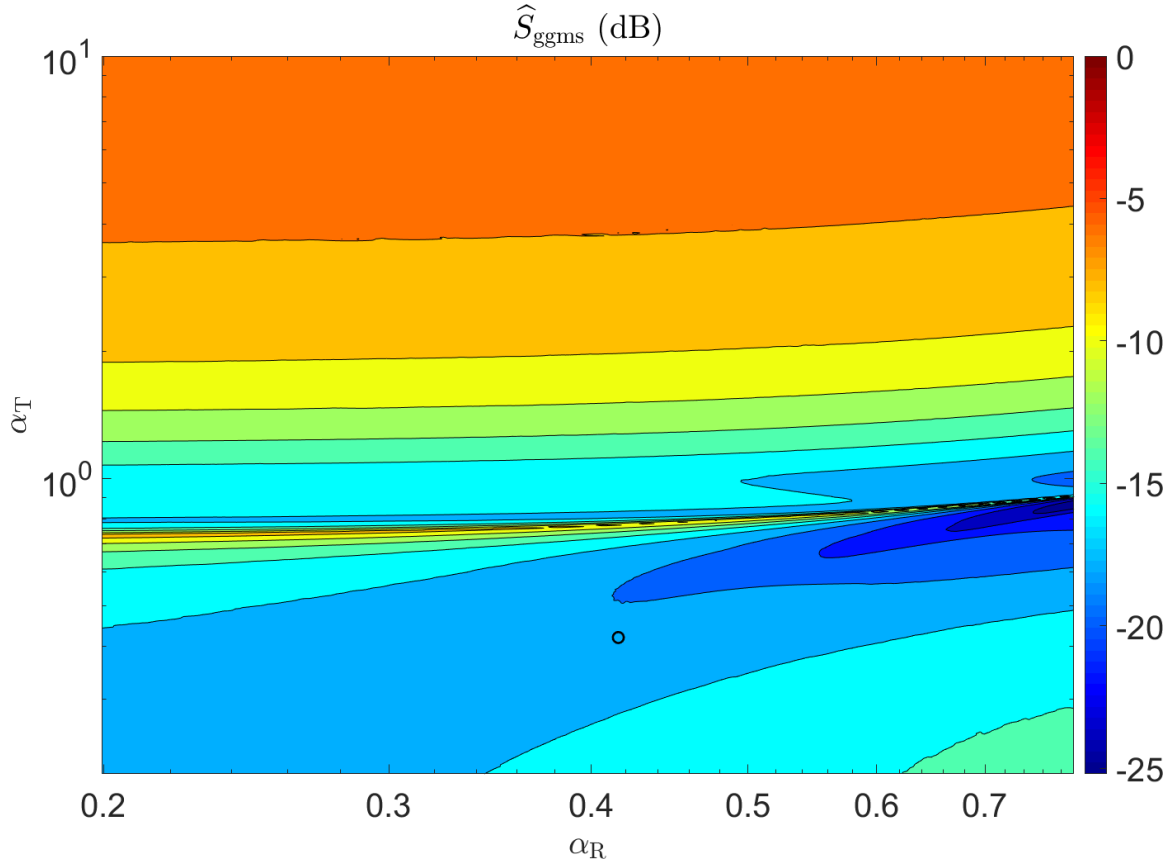

Figure 52: $\widehat{S}_{\mathrm{ggms}}$ for many concentric coils. The optimal coil is marked with a circle.

6.1.7 Dipole/quadrupole coils

Finally, a dipole/quadrupole coil head was optimized. The dipole coil is the transmit, and the quadrupole coil (a figure-8) is the receive coil that provides the nulled coupling between the two coils. The geometry of the coil is shown in Figure 53. Two parameters were varied during the optimization: c_r, the maximum radius of the dipole, and c_s, the spacing between the two coils. In calculating the shape of the dipole coil, the point at which c_r intersects the bounding box is where the coil is flattened against the box, and the corners are smoothly radiused. A similar strategy was used for the quadrupole with a bounding box with sides equal to $2r - 2c_\mathrm{s}$.

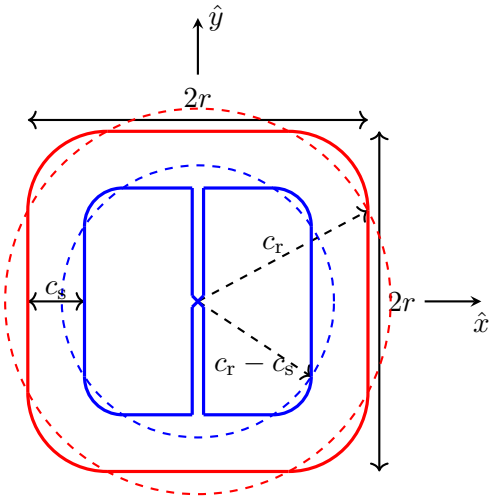

Figure 53: Dipole/quadrupole coil geometry with dipole in red and quadrupole in blue.

The variables c_r and c_s are taken to be in relation to the size of the bounding box as $c_\mathrm{rr} = c_\mathrm{r}/r$ and $c_\mathrm{sr} = c_\mathrm{s}/r$ and are swept over $1 <= c_\mathrm{rr} <= 1.3$ and $0.1 <= c_\mathrm{sr} <= 0.8$. A subset of the dipole/quadrupole coils being analyzed is shown in Figure 54.

Figure 56 shows $\widehat{S}_\mathrm{ggm}$ for all the coil heads and Figure 55 the maximum soil sensitivity with the optimal coil marked with a black circle. The target sensitivity is roughly correlated with the soil sensitivity, and roughly inversely correlated with $\widehat{S}_\mathrm{ggms}$ (Figure 57). However, the correlation is once again not good enough to choose an optimal coil solely from $\widehat{S}_\mathrm{ggm}$ or $\widehat{S}_\mathrm{s}$.

The optimal coil head geometry, which has $c_\mathrm{sr} = 0.44$ and $c_\mathrm{rr} = 1.1$, is shown in Figure 58.

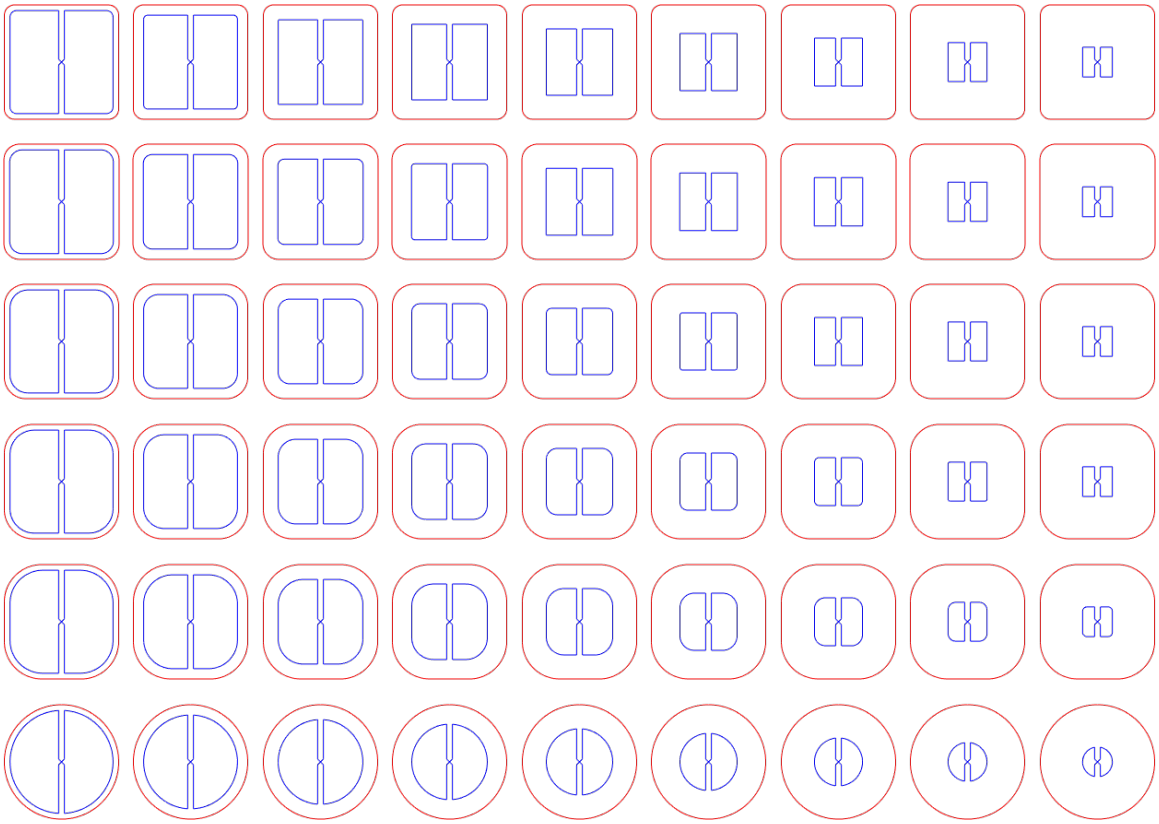

Figure 54: Subset of the dipole/quadrupole coils being analyzed.

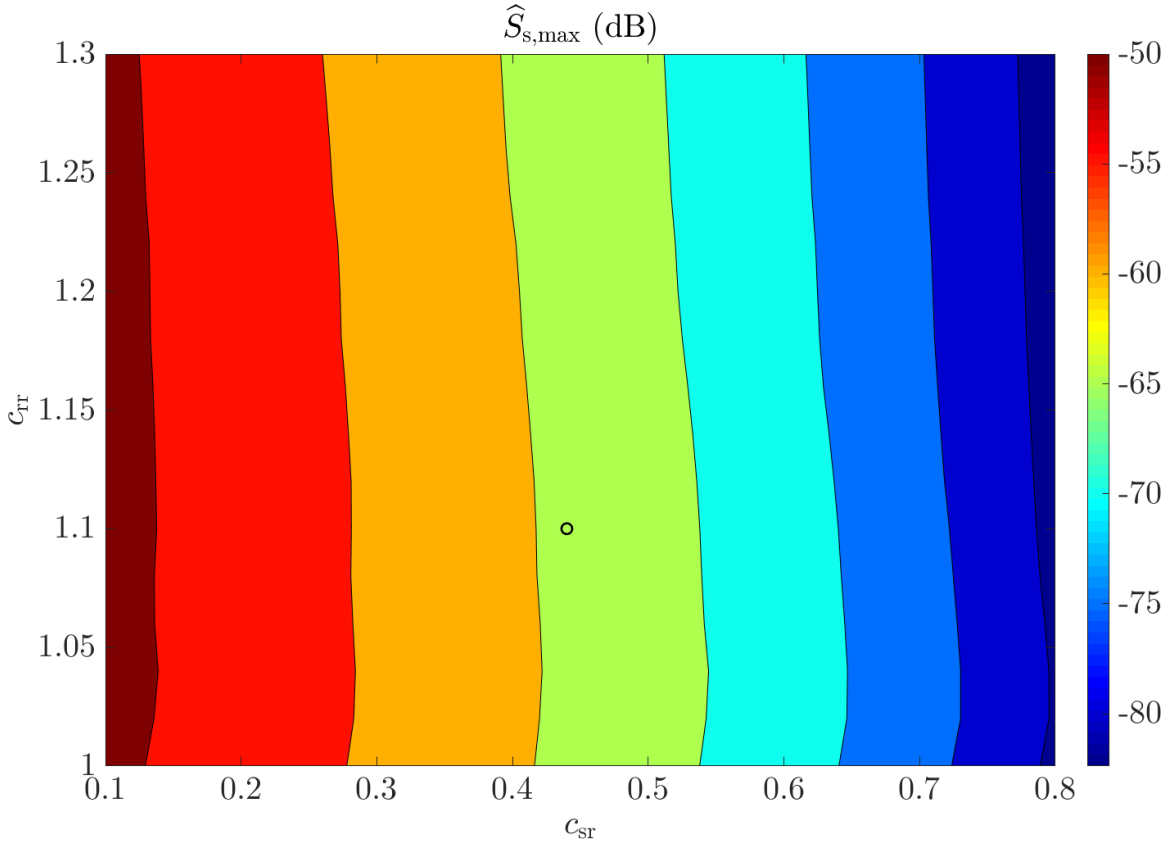

Figure 55: Maximum dipole/quadrupole soil sensitivity for all coil heads considered.

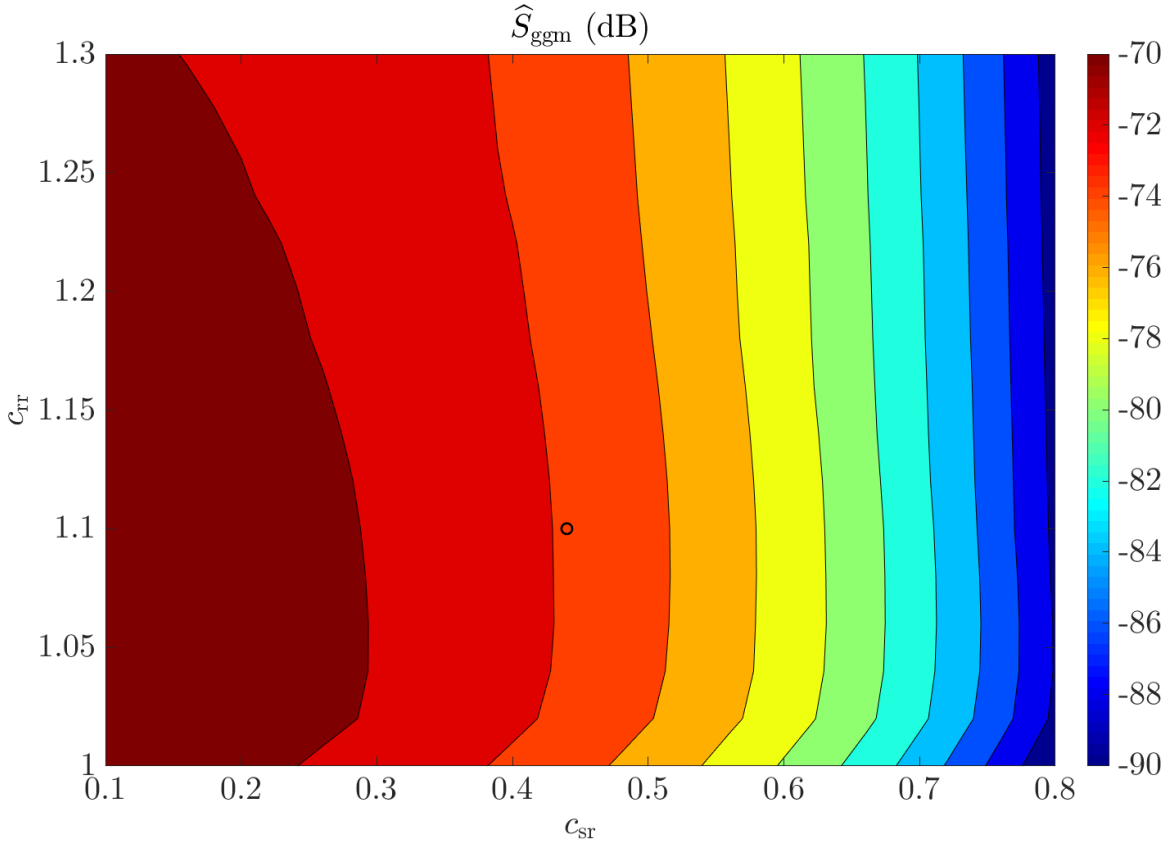

Figure 56: $\widehat{S}_{\mathrm{ggm}}$ in dB as a function of c_{rr} and c_{sr} for dipole/quadrupole coil heads.

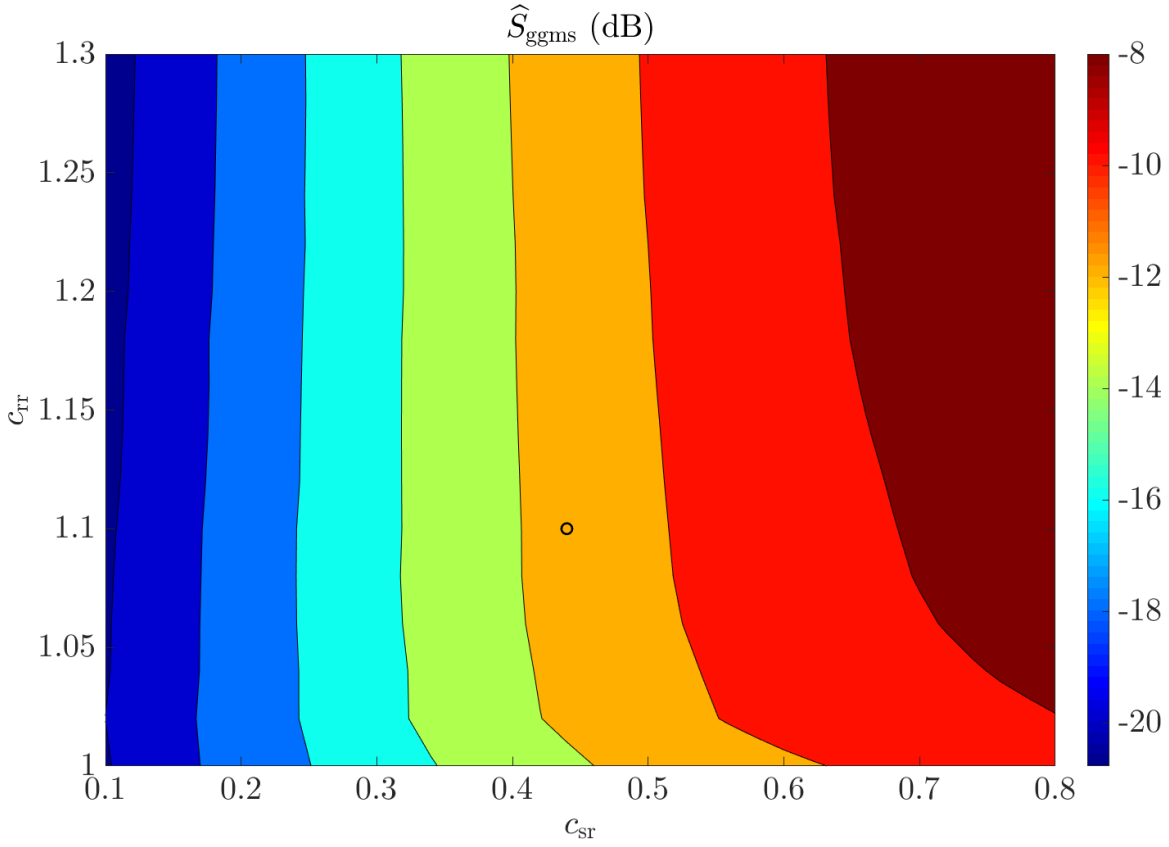

Figure 57: $\widehat{S}_{\mathrm{ggms}}$ as a function of c_{rr} and c_{sr} for all dipole/quadrupole coil heads.

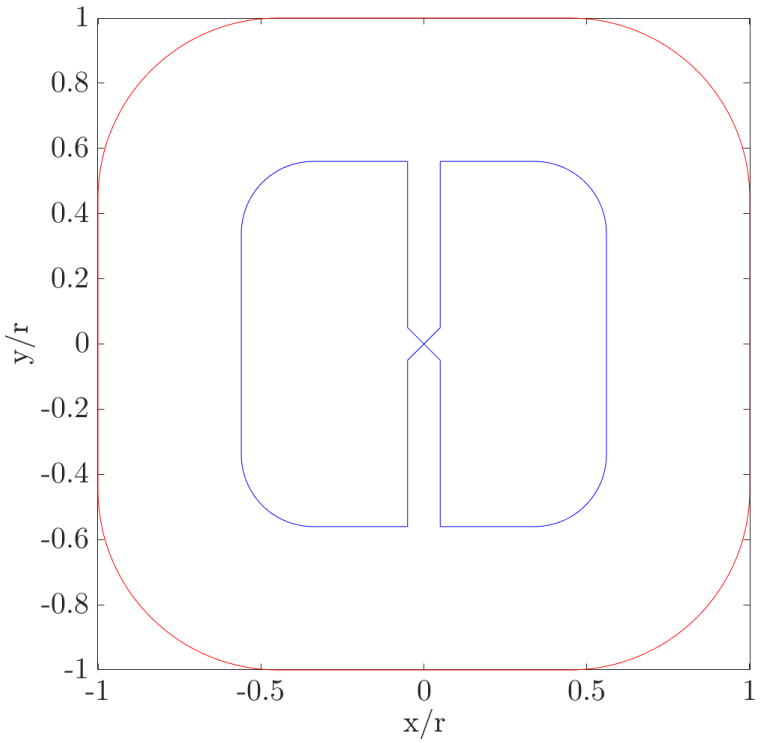

Figure 58: Optimal dipole/quadrupole coil.

This coil head has $\widehat{S}_{\text{ggm}} = -72.21$ dB and $\widehat{S}_{\text{ggms}} = -11.3$ dB and is denoted on Figure 62 by a black star. The sensitivity graphs in Figures 59 and 60 illustrate the off-center maximum sensitivity and nulled on-axis sensitivity of the dipole/quadrupole. Finally, Figure 61 is a graph of the soil sensitivity for various soil heights and tilts. The dipole/quadrupole soil sensitivity shows very little variation when tilted down-track, but it changes quite a bit when tilted cross-track. Of course, there is very little soil sensitivity at all (in the ideal case, it would be zero) when the coil head is level. It should be noted that, since the dipole/quadrupole soil sensitivity worsens instead of improves when it is tilted, the apparent target sensitivity performance of the dipole/quadrupole head relative to the soil sensitivity can be altered by adjusting the maximum tilt about the y-axis.

6.2 Conclusion

Now the optimized coil heads can be compared to one another and their traits summarized. Figure 62 is a plot of the $\widehat{S}_{\text{ggm}}$ against $\widehat{S}_{\text{ggms}}$ for all the coils considered in this paper. The red and blue regions span all the coil head configurations considered during optimization for the

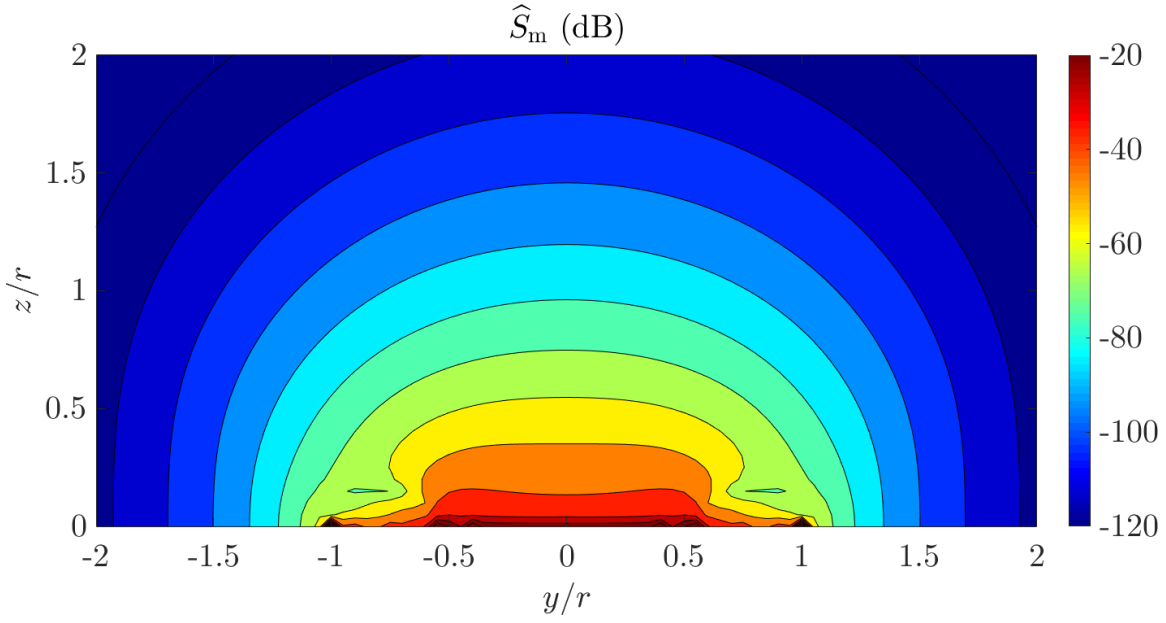

Figure 59: $\widehat{S}_{\mathrm{m}}$ of the optimal dipole/quadrupole coil head.

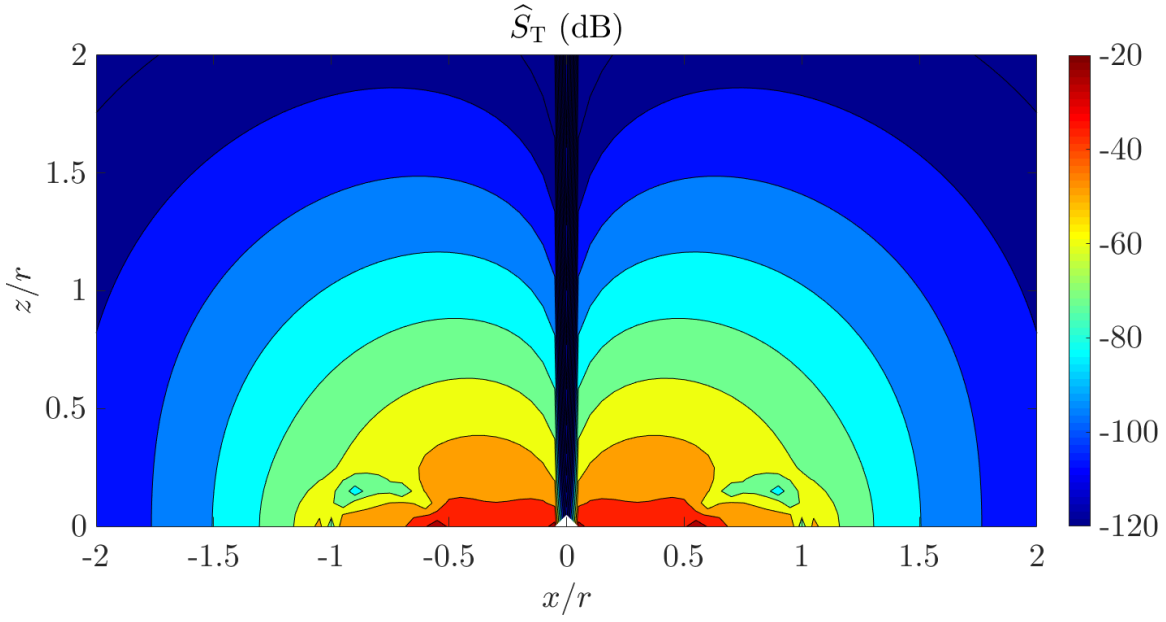

Figure 60: Target sensitivity in the x-z plane of the optimal dipole/quadrupole coil head.

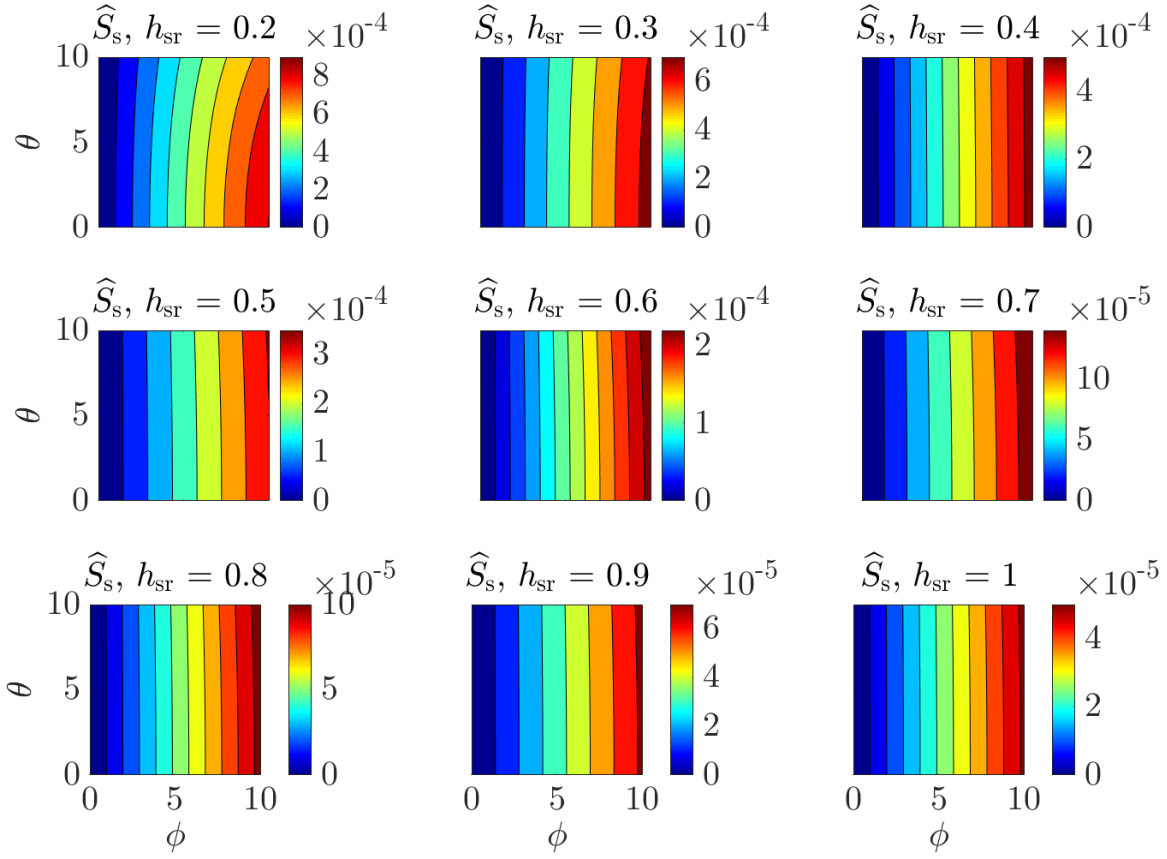

Figure 61: The soil sensitivity of the optimal dipole/quadrupole coil over a range of heights above the soil and tilts relative to the soil.

concentric and dipole/quadrupole coil heads, respectively, and the black line is the double-D coil heads. Within the geometries that are reasonable to produce, the concentric coil heads give the most opportunity for tweaking performance, while the double-D performance varies very little with shape. The region for the dipole/quadrupole is somewhat misleading because altering the amount of tilt changes the maximum soil response of the dipole/quadrupole. The dashed lines are lines of constant $^{\Delta\widehat{S}_{\mathrm{ggm}}}/_{\Delta\widehat{S}_{\mathrm{ggms}}}$, so moving along one of the dashed lines gives a constant tradeoff between target and soil sensitivity.

By this metric, the double-D coil head performs the best, the concentric is 1 dB down, and the dipole/quadrupole is 2 dB below the concentric. As can be seen in Figure 62 or read from Table 6, the order in terms of mean target sensitivity is different, with the concentric performing best, the double-D second, and the dipole/quadrupole last, and performance of the various coils is reversed when the soil is considered. Figure 63 is a plot of $\widehat{S}_{\mathrm{gm}}$, and Figure 64 shows the maximum soil sensitivity of the three coils versus soil height. By considering Figures 62, 63, and 64 together, a good picture of each coil head's performance can be formed.

The concentric coil head has very good target sensitivity at all depths but the worst soil rejection, so it would perform best in lightly mineralized soils. The double-D peforms less well than the concentric in terms of target sensitivity but much better when the soil is considered, hence its position as a good all-around coil that performs well in moderately mineralized soils. Finally, the dipole/quadrupole suffers with depth penetration as a result of the quadrupole receive coil, but its soil rejection is very good.

Common coil head types have been optimized and analyzed using metrics that remove various factors that influence coil head performance other than coil winding patterns. These results can be used for comparison to new coil head designs—such as those optimized using our partially convex algorithm—to determine their performance relative to existing coil heads [48].

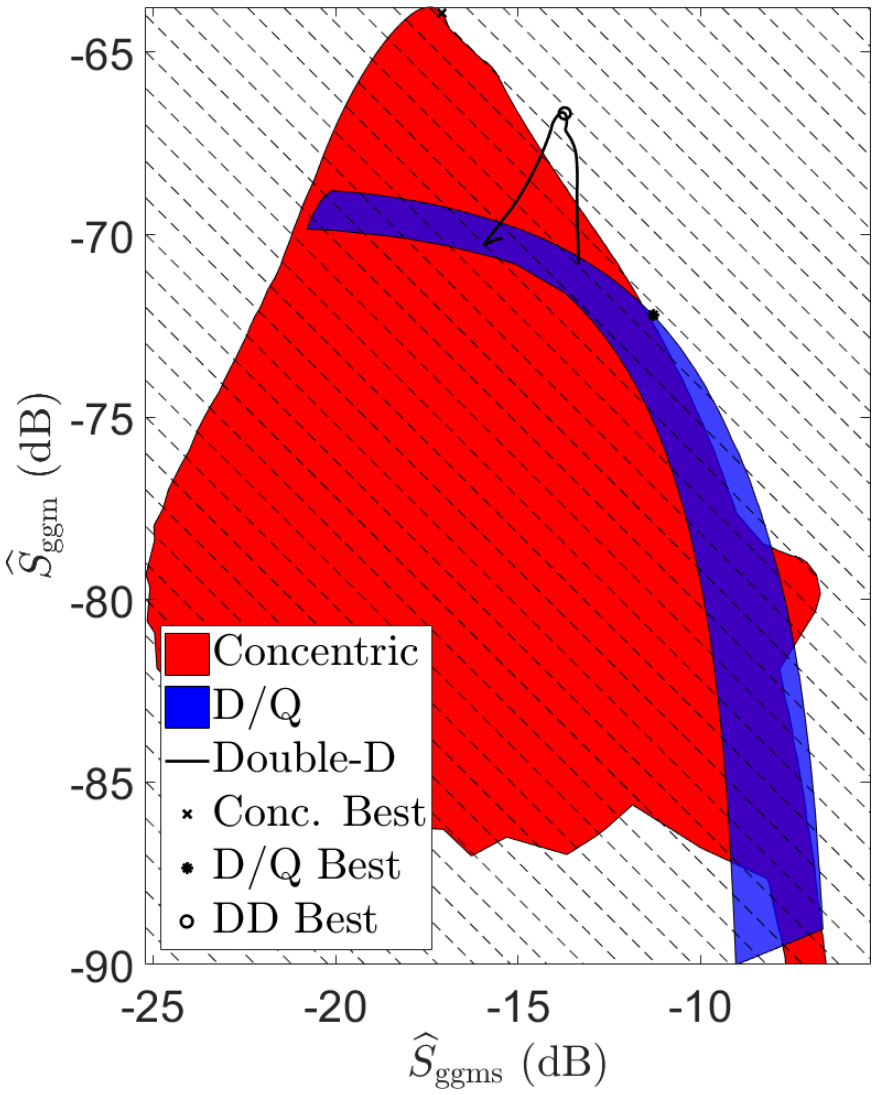

Figure 62: Plot of the volume sensitivity against the ratio of the volume sensitivity to soil sensitivity for all the coils considered in this paper. The red and blue regions span all the coils swept during optimization for the concentric and dipole/quadrupole coil heads, respectively. The black line denotes the double-D coil heads, and the markers are the optimal coils from each set.

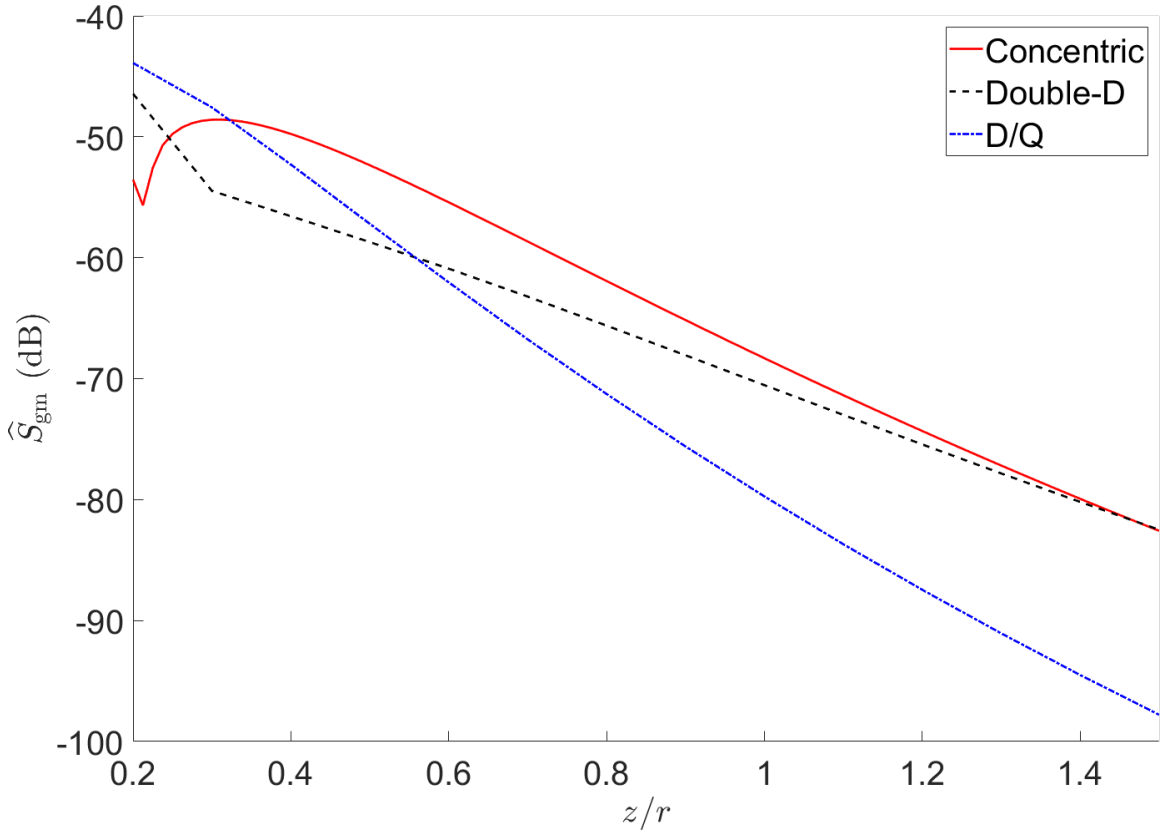

Figure 63: $\widehat{S}_{\mathrm{gm}}$ vs depth for each optimal coil.

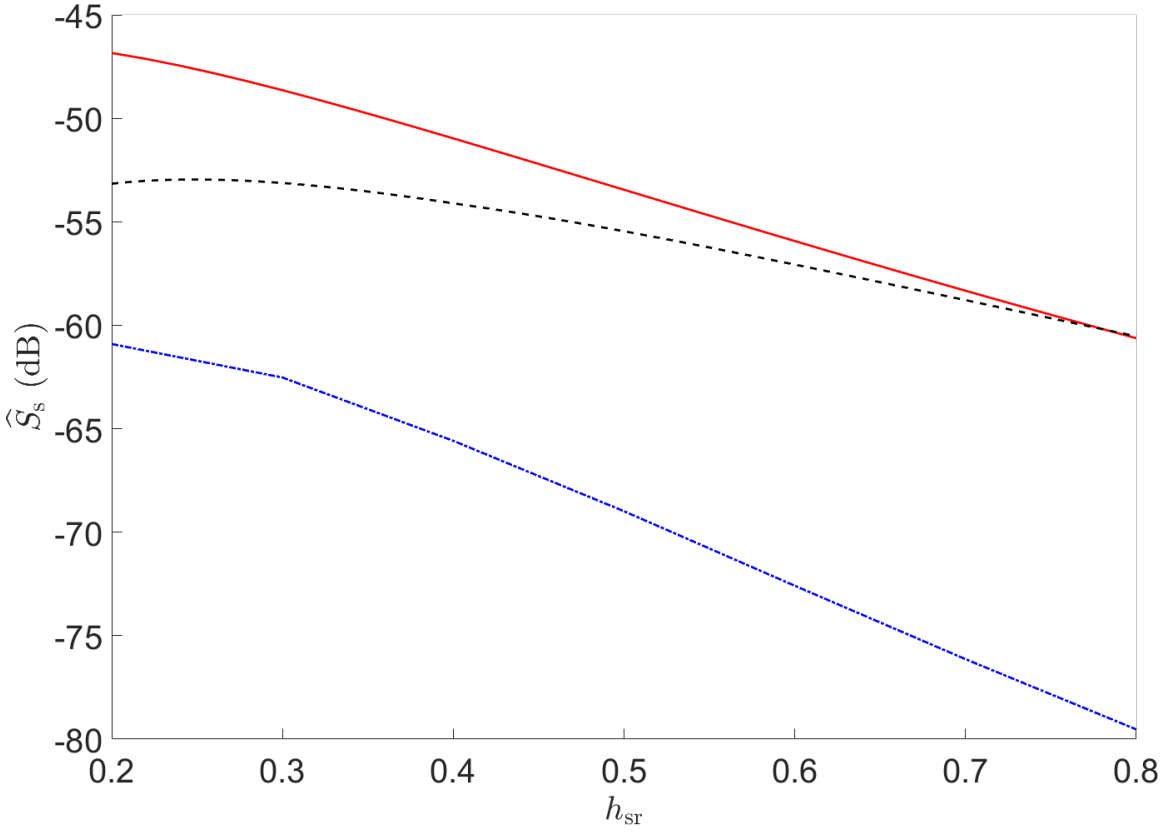

Figure 64: $\widehat{S}_s$ vs height for all three optimal coils.

Table 6: Optimal coil metrics

Coil Performance		
Coil head	$\widehat{S}_{\text{ggm}}$ (dB)	$\widehat{S}_{\text{ggms}}$ (dB)
Concentric	-63.93	-17.09
Double-D	-66.68	-13.72
Dipole/quadrupole	-72.21	-11.3

PART 3

Optimization and Comparison of Generalized Coil Geometries

CHAPTER VII

EVALUATION OF NORMALIZED METRICS FOR STREAM FUNCTIONS

In Chapter 2, wire-wound spiral coils were optimized using a simple basis function in polar coordinates, and in Chapter 6, wire-wound double-D, concentric, and dipole/quadrupole coils were optimized using simple parameterizations with few variables. These optimizations produced good results, but the parameterizations used needed to be very restrictive to make the problems tractable. For example, the basis function in Chapter 2 allows only concentrically-wound coils, so double-D and dipole/quadrapole-like coils are not possible. There are obviously more solutions than just these coils, such as those in Chapter 6, so a much more general parametrization is needed.

It is very difficult to generalize the optimization of wire-wound coils if the location of the wires is directly parameterized because the wires must be constrained not to cross for practical solutions. To overcome this difficulty, the current in a wire coil will be represented by a continuous surface current that can then later be approximated by a wire-wound coil. The surface current can then be represented by a stream-function on triangular mesh that is parameterized with linear pyramidal basis functions. The stream function inherently forces the current to be divergence free for any set of parameters for the mesh. To make a realizable coil, a normal component of the current cannot exist on the edge of the coil, which can be forced when the edge nodes are set to zero.

The stream function representation fulfills the need for more generalized coils while also being simple enough to optimize on a standard PC when the problem is formulated in a manner that can make use of a convex optimization algorithm, such as one used by CVX [18,19]. It does, however, introduce difficulties that did not exist with the wire-wound optimizations earlier in this work. In addition to maximizing the target sensitivity and minimizing the mutual coupling between the transmit and receive coils, a dissipated power

term must be introduced to restrict the optimization from simply adding infinite power to the coils.

In Chapters 5 and 6, the dissipated power was implicity constrained by the normalization in (30). In this chapter, the dissipated power must be explicitly constrained because of the representation needed for convex optimization. The power constraint is also more important here, because of the generality of the solution allowed by the stream function representation. Without the power constraint, the optimizer can null the mutual coupling between the coils by using large but tightly wound adjacent circulating currents on the transmit and receive coils. These large circulating currents are impractical both because they will cause a significant power loss in the coils and because they require an impractically large number of turns. The constraint on the power dissipation will penalize these large circulating currents and cause the the currents on the coils to vary more slowly. Two power constraints are considered: one that is suitable for a wire-wound coil, and one that is suitable for a coil that will be cut from a printed-circuit board (PCB).

As in Chapter 6, the soil sensitivity will also be included. It is a very important consideration as the soil becomes more magnetic or conductive and the targets become smaller or more weakly conductive because the signal created by the soil can begin to obscure targets.

Efficient methods for computing the target sensitivity, soil sensitivity, dissipated power, and mutual coupling metrics from the parameters for the stream function are developed in the following sections.

7.1 Formulation

Coils are typically wound using wires or traces on PCBs, but, given sufficient winding density, the wires can be approximated as surface currents, $\vec{K}$ [47]. The surface currents can then be represented by a stream function, ξ, as

$$\vec{K} = \hat{z} \times \nabla \xi \tag{52}$$

on a surface with the normal $\hat{z}$ [37]. Stream functions can be viewed as similar to potential functions, where the current density flows along equipotential curves, and the gradient of the stream function determines the magnitude and direction of the current density.

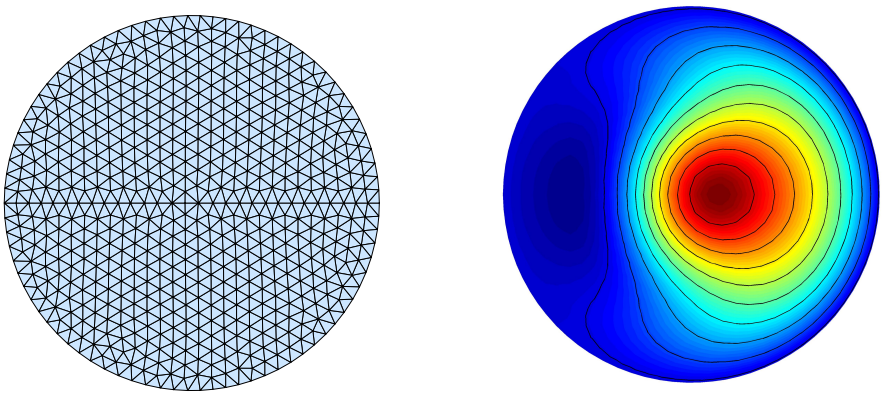

(a) Symmetric mesh. (b) Example stream function.

Figure 65: A symmetric mesh and example stream function.

The stream function, such as the one in Figure 65(b), is represented by the linear pyramidal basis functions that are commonly used in the finite-element method (FEM) on a triangular mesh, which was created here with DistMesh (Figure 65(a)). The mesh is symmetric about its y-axis, and the matching basis function coefficients are forced equal to one another. Forcing mesh symmetry is desirable as it creates a symmetrical sensitivity pattern that makes identifying target locations easier. Asymmetrical coils are undesirable as they create more complex sensitivity patterns, which makes the identification of target locations more difficult. Forcing symmetry has the additional desirable effect of halving the number of unknowns, removing solutions that are rotations of one another, decreasing the degrees of freedom, and improving optimization speed.

7.1.1 Basis Functions

Calculations on triangular patches are most easily done using local barycentric coordinates $\{L_1, L_2, L_3\}$, which are also used as the basis functions on each cell [42]. These coordinates can be expressed in terms of the x and y coordinates of the cell vertices by solving the following system of equations.

$$\begin{bmatrix} x \\ y \\ 1 \end{bmatrix} = \begin{bmatrix} x_1 & x_2 & x_3 \\ y_1 & y_2 & y_3 \\ 1 & 1 & 1 \end{bmatrix} \begin{bmatrix} L_1 \\ L_2 \\ L_3 \end{bmatrix} , \tag{53}$$

where (x_1, y_1), (x_2, y_2), and (x_3, y_3) are the coordinates of the triangular patch vertices and L_1, L_2, and L_3 are the barycentric coordinates and also the basis functions. Solving for the barycentric coordinates gives

$$L_i = \frac{1}{2A} \left(p_i + q_i x + r_i y \right) , \tag{54}$$

where p_i, q_i, and r_i are functions of the locations of the vertices:

$$p_i = x_{i+1} y_{i+2} - x_{i+2} y_{i+1} \tag{55}$$

$$q_i = y_{i+1} - y_{i-1} \tag{56}$$

$$r_i = x_{i-1} - x_{i+1} , \tag{57}$$

and the area of the triangular patch is

$$A = \left| \frac{1}{2} \left(q_{i+1} r_{i-1} - q_{i-1} r_{i+1} \right) \right| , \tag{58}$$

where (x_i, y_i) are the coordinates of the ith vertex of the triangle.

Within a cell, the basis functions are simply equal to the barycentric coordinates, L_1, L_2, and L_3. A pyramidal basis function (Figure 66), ξ_m, is centered on a mesh vertex and is created from the barycentric coordinates in the cells adjacent to each vertex.

Linear pyramidal basis functions in this coordinate system are simply equal to the barycentric coordinates L_1, L_2, and L_3. Because the basis functions are linear, their gradients are constants on each cell:

$$\nabla L_i = \frac{1}{2A} \left(\hat{x} q_i + \hat{y} r_i \right) , \tag{59}$$

which makes the current in each cell constant and easy to calculate.

The basis functions, ξ, as written have a maximum value of one and minimum of zero. They can then be scaled by coefficients $\mathbf{a} = \begin{bmatrix} a_0 & a_1 & \cdots & a_M \end{bmatrix}$ (transmit coil) and $\mathbf{b} =$

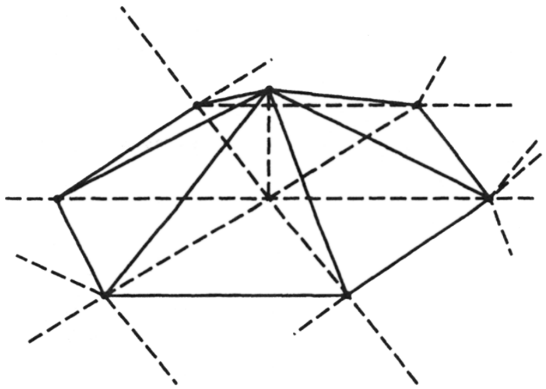

Figure 66: Linear pyramidal basis function centered on a mesh vertex [42].

$\begin{bmatrix} b_0 & b_1 & \cdots & b_N \end{bmatrix}$ (receive coil) to create a variable stream function based on the mesh. The stream functions representing the transmit and receive coils are now

$$\xi_{\mathrm{TX}} = \sum^{M} a_m \xi_m \,, \tag{60}$$

and

$$\xi_{\mathrm{RX}} = \sum^{N} b_n \xi_n \,. \tag{61}$$

7.1.2 Magnetic Field

The magnetic field created by current flowing on a closed path can be calculated from

$$\vec{H}\left(\vec{r}\right) = \frac{1}{4\pi} \oint_c \frac{I d\vec{L} \times \vec{r}}{|\vec{r}|^3} \,. \tag{62}$$

Using (60), the magnetic field, $\vec{H}_{\mathrm{TX}}$, of the coil at point $\vec{r}$ can be written as

$$\begin{aligned} \vec{H}_{\mathrm{TX}}\left(\vec{r}\right) &= \frac{1}{4\pi}\left(\int_{S'} \frac{\vec{K} \times \left(\vec{r} - \vec{r}'\right)}{|\vec{r} - \vec{r}'|^3} dS'\right) = \sum_n^N a_m \frac{1}{4\pi} \int_{S'} \frac{\left(\hat{z} \times \nabla \xi_m\right) \times \left(\vec{r} - \vec{r}'\right)}{|\vec{r} - \vec{r}'|^3} dS' \\ &= \begin{bmatrix} a_0 & a_1 & \cdots & a_M \end{bmatrix} \begin{bmatrix} h_0^x & h_0^y & h_0^z \\ h_1^x & h_1^y & h_1^z \\ \vdots & \vdots & \vdots \\ h_M^x & h_M^y & h_M^z \end{bmatrix} = \mathbf{a}^\top \mathbf{H}_{\mathrm{TX}} \,, \end{aligned} \tag{63}$$

where $\vec{r} - \vec{r}'$ is a vector from the source to the point of observation. Likewise, the receive field can be written as $\vec{H}_{\mathrm{RX}} = \mathbf{b}^\top \mathbf{H}_{\mathrm{RX}}$. The matrices $\mathbf{H}_{\mathrm{TX}}$ and $\mathbf{H}_{\mathrm{RX}}$ can be precomputed, so only

the coefficients must be adjusted during optimization, making it very efficient to compute $\vec{H}_{\mathrm{TX}}$ and $\vec{H}_{\mathrm{RX}}$. In the following sections, other parameters will be written in similar forms that allow basis function coefficients to be adjusted easily without heavy computation.

7.1.3 Dissipated Power

The dissipated power is used to constrain the coils to be smooth. Two power constraints were investigated. In both, the coils were modeled as conductive plates that support surface currents. Using the constant-resistance model, which has a plate of constant thickness, $R_{\mathrm{s}} = {}^{1}/_{\sigma t}$, the power dissipated can be written as

$$P_{\mathrm{d}} = \int_S R_{\mathrm{s}} \left|\vec{K}\right|^2 dS = \frac{1}{\sigma t} \int_S \left|\vec{K}\right|^2 dS\,, \tag{64}$$

where σ is the conductivity of the plate, and t is the thickness. Rewriting in terms of basis functions and their coefficients for the transmit coil gives

$$P_{\mathrm{d,con}} = \sum_{m=1}^{N}\sum_{n=1}^{N} a_m a_n \frac{1}{\sigma t}\int_S \nabla\xi_m \cdot \nabla\xi_n dS = \frac{1}{\sigma t}\mathbf{a}^\top \mathbf{P}_{\mathrm{TX}}\mathbf{a}\,, \tag{65}$$

where the integral results have been collected into the $\mathbf{P}_{\mathrm{TX}}$ matrix. This constant-resistance model is a good representation of a coil that will be cut from a PCB as it can have traces that vary in width with a small spacing between the traces.

The variable-resistance model is a good representation for a wire-wound coil. The varying resistance of the plate approximates the effects of the spacing for the constant diameter wire that is usually used to wind coils. The variable-resistance is made by adjusting the thickness of the copper plate based upon the closeness of the windings. A good approximation is to make the the thickness of the copper plate vary in proportion to the current density it supports, $t = c\left|\vec{K}\right|$, where c is simply a constant of proportionality with units ${}^{m^2}/_{\mathrm{A}}$. Substituting into P_{d},

$$P_{\mathrm{d}} = \int_S R_{\mathrm{s}} \left|\vec{K}\right|^2 dS = \int_S \frac{1}{\sigma c\left|\vec{K}\right|} \left|\vec{K}\right|^2 dS = \frac{1}{\sigma c}\int_S \left|\vec{K}\right| dS \tag{66}$$

Thus, the new power dissipation expression is

$$P_{\mathrm{d,prop}} = \frac{1}{\sigma c}\int_S \left|\vec{K}\right| dS\,. \tag{67}$$

The reformulation of (67) is troublesome because it cannot be written as in (65). For the optimization, $P_{\text{d,prop}}$ must be written in terms of a vector of basis function coefficients, so (67) is evaluated by summing the contributions of each triangular cell to the current. The current on the t-th cell is

$$\vec{K}_t = \sum_{i=1}^{3} \hat{z} \times \nabla a_i \xi_i \,, \tag{68}$$

where the indices, i, are local indices of basis functions at each corner of the cell. Since the basis functions are linear, the current is constant on a cell. The current on the t-th cell takes the form of $\vec{K}_t = K_{x,t}\hat{x} + K_{y,t}\hat{y}$, and so the magnitude of the current in the t-th cell is simply $K_t = \sqrt{K_{x,t}^2 + K_{y,t}^2}$. $P_{\text{d,prop}}$ is now

$$P_{\text{d,prop}} = \frac{1}{\sigma c} \sum_{t=1}^{T} K_t A_t \tag{69}$$

where T is the number of cells in the mesh and A_t is the area of the t-th cell.

Writing this expression in a form that can be recognized as convex by the program (CVX) used for optimization requires some minor re-writing. It must be written in terms of the coefficients, $\mathbf{a}$, and some form of the CVX function norms(). A $T \times M$ matrix, $\mathbf{C}_x$, that relates the basis function coefficients to the $\hat{x}$-directed current density on each cell, $\mathbf{k}_x$ - and therefore only has three non-zero entries per row - is created,

$$\mathbf{k}_x = \mathbf{C}_x \mathbf{a} \,, \tag{70}$$

where $\mathbf{k}_x$ is a vector with T entries. The $\mathbf{k}_y$ vector is similar,

$$\mathbf{k}_y = \mathbf{C}_y \mathbf{a} \,. \tag{71}$$

Each nonzero entry in $\mathbf{C}_x$ is the contribution of one basis function to the $\hat{x}$-directed current density on the corresponding cell. Combining (59) with (68) gives the current on a triangular cell as

$$\vec{K}_t = \frac{1}{2A_t} \sum_{i=1}^{3} -\hat{x} r_i + \hat{y} q_i \,. \tag{72}$$

A local basis function i maps to a global basis function m; therefore, a nonzero entry in $\mathbf{C}_x$ is $-\frac{1}{2A_t} r_i$, and one in $\mathbf{C}_y$ is $\frac{1}{2A_t} q_i$. $\mathbf{k}_x$ and $\mathbf{k}_y$ can be combined into a $T \times 2$ matrix, $\mathbf{K}$, as

$$\mathbf{K} = \begin{bmatrix} \mathbf{k}_x & \mathbf{k}_y \end{bmatrix} = \begin{bmatrix} \mathbf{C}_x \mathbf{a} & \mathbf{C}_y \mathbf{a} \end{bmatrix} \,. \tag{73}$$

$$\mathbf{K} = \begin{bmatrix} k_{x1} & k_{y1} \\ k_{x2} & k_{y2} \\ \vdots & \vdots \\ k_{xT} & k_{yT} \end{bmatrix} \tag{74}$$

The integral of the magnitude of the surface current density in (67) can be written in terms of the elements of $\mathbf{K}$ as

$$K_{\text{int}} = \sum_{t=1}^{T} \sqrt{|k_{xt}|^2 + |k_{yt}|^2}, \tag{75}$$

where the expression is recognized by CVX to be convex when written as sum(norms([Cx∗a, Cy∗a],2,2)), where norms() is special CVX function. The dissipated power is then

$$P_d = \frac{A}{\sigma c} K_{\text{int}}\,, \tag{76}$$

which is equivalent to the expression in (69).

Thus by way of (73), the expression for dissipated power in (76) is a function of the basis function coefficients, $\mathbf{a}$, and the surface current integral in (73) can be written as a sum of the l-2 norms of the rows of $\mathbf{K}$ using the norms() function, which is recognized as convex in CVX. This allows the use of the dissipated power within the coil optimization subroutine.

7.1.4 Mutual Energy

The mutual energy between the transmit and receive coils can be written in terms of their magnetic vector potential and the current density [56] as

$$W = \int_V \vec{K}_{\text{RX}} \cdot \vec{A}_{\text{TX}} dV\,. \tag{77}$$

Because the coils exist only on a surface, (77) can be written as

$$W = \int_S \vec{K}_{\text{RX}}(\vec{r}) \cdot \vec{A}_{\text{TX}}(\vec{r})\, dS\,, \tag{78}$$

where $\vec{K}$ is the current on the receive coil and $\vec{A}$ is the magnetic vector potential created by the transmit coil.

Substituting for $\vec{K}$ in the expression for the magnetic vector potential, $\vec{A}$, in all space resulting from $\vec{K}$ on S yields

$$\vec{A}_{\mathrm{TX}}(\vec{r}) = \frac{\mu_0}{4\pi}\int_{S'} \frac{\vec{K}(\vec{r}')}{|\vec{r}-\vec{r}'|}dS' = \sum_{m=0}^{M} a_m \underbrace{\frac{\mu_0}{4\pi}\int_{S'} \frac{\hat{z}\times\nabla\xi_m}{|\vec{r}-\vec{r}'|}dS'}_{M_m}, \tag{79}$$

where μ_0 is the magnetic permeability of free space. Then, substituting with the stream function basis gives

$$W = \int_S (\hat{z}\times\nabla\xi_{\mathrm{RX}})\cdot\vec{A}_{\mathrm{TX}}dS \tag{80}$$

$$= \int_S \left(\hat{z}\times\nabla\sum b_n\xi_n\right)\cdot\left(\sum a_m M_m\right)dS \tag{81}$$

$$= \sum_m\sum_n a_m b_n \underbrace{\int_{S'}(\hat{z}\times\nabla\xi_n)\cdot M_m dS}_{M'_{mn}} \tag{82}$$

where

$$M'_{mn} = \int_S (\hat{z}\times\nabla\xi_n)\cdot\left(\int_{S'}\frac{\mu_0}{4\pi}\frac{\hat{z}\times\nabla\xi_m}{|\vec{r}-\vec{r}'|}dS'\right)dS \tag{83}$$

$$M'_{mn} = \frac{\mu_0}{4\pi}\int_S\int_{S'}(\hat{z}\times\nabla\xi_n)\cdot\frac{(\hat{z}\times\nabla\xi_m)}{|\vec{r}-\vec{r}'|}dS'dS\,. \tag{84}$$

Using a vector identity,

$$(A\times B)\cdot(C\times D) = (A\cdot C)(B\cdot D) - (B\cdot C)(A\cdot D) \tag{85}$$

$$(A\times B)\cdot(A\times D) = (A\cdot A)(B\cdot D) - (B\cdot A)(A\cdot D) \tag{86}$$

$$= (B\cdot D) - (B\cdot A)(A\cdot D) \tag{87}$$

$$(\hat{z}\times\nabla\xi_m)\cdot(\hat{z}\times\nabla\xi_n) = (\nabla\xi_m\cdot\nabla\xi_n) - \underbrace{(\nabla\xi_m\cdot\hat{z})}_{0}\underbrace{(\hat{z}\cdot\nabla\xi_n)}_{0} \tag{88}$$

$$= \nabla\xi_m\cdot\nabla\xi_n \tag{89}$$

Then,

$$M'_{mn} = \frac{\mu_0}{4\pi}\int_S\int_S{}' \frac{\nabla\xi_m\cdot\nabla\xi_n}{|\vec{r}-\vec{r}'|}dS'dS\,, \tag{90}$$

and the mutual energy between the two coils can be written as

$$W_{\mathrm{M}} = \int_S \vec{K}_{\mathrm{RX}}(\vec{r})\cdot\vec{A}_{\mathrm{TX}}(\vec{r})\,dS = \sum_{m=0}^{M}\sum_{n=0}^{N} a_m b_n \frac{u_0}{4\pi}\int_S\int_{S'}\frac{\nabla\xi_m\cdot\nabla\xi_n}{|\vec{r}-\vec{r}'|}dS'dS = \mathbf{a}^\top\mathbf{M}\mathbf{b}\,, \tag{91}$$

which allows the coupling between the coils to be nulled during optimization. The coupling factor between the transmit and the receive coil is

$$c = \frac{W_{\mathrm{M}}}{\sqrt{2W_{\mathrm{T}}W_{\mathrm{R}}}}\,, \tag{92}$$

where W_{T} and W_{R} are the self energies of the transmit and receive coils. W_{T} and W_{R} can be calculated in a similar manner to W_{M}, but the singularity must be handled [33].

7.2 Sensitivity

The receive coil field is calculated in the same manner as the transmit coil field, and then the two are combined to calculate the sensitivity, S, at $\vec{r}$ as

$$S_{\mathrm{T}} = \vec{H}_{\mathrm{TX}}\left(\vec{r}\right) \cdot \hat{\bar{\bar{m}}} \cdot \vec{H}_{\mathrm{RX}}\left(\vec{r}\right) = \mathbf{a}^{\top}\mathbf{H}_{\mathrm{TX}}\mathbf{M}_{\mathrm{p}}\mathbf{H}_{\mathrm{RX}}^{\top}\mathbf{b}\,, \tag{93}$$

where $\bar{\bar{m}}$ is the magnetic polarizability of the target, and $\hat{\bar{\bar{m}}} = \bar{\bar{m}}/||\bar{\bar{m}}||$. As before, the polarizability dyad is chosen to be the identity matrix, which represents a sphere, and $\mathbf{M}_{\mathrm{p}} = \hat{\bar{\bar{m}}}$.

The normalized sensitivity of a wire coil was derived before as

$$\widehat{S}_{\mathrm{T}} = r^4 \frac{\vec{H}_{\mathrm{RX}} \cdot \hat{\bar{\bar{m}}} \cdot \vec{H}_{\mathrm{TX}}}{I_{\mathrm{RX}} l_{\mathrm{RX}} I_{\mathrm{TX}} l_{\mathrm{TX}}}\,, \tag{94}$$

and now an equivalent equation for the stream function coils is needed. The denominator $I_{\mathrm{RX}} l_{\mathrm{RX}} I_{\mathrm{TX}} l_{\mathrm{TX}}$ at first appears problematic because stream functions lack definable lengths of current paths, but this can be solved with a simple integration. The surface current density, $\vec{K}$, of the stream function is known. Because the current is confined to the surface, it flows in closed paths, which can be viewed as infinitesimally wide strips of current. The total current, ΔI flowing in a differential width Δw is $\Delta I = \left|\vec{K}\right| \Delta w$. Or,

$$I = \int \left|\vec{K}\right| dw\,, \tag{95}$$

which when integrated over differential area ($\Delta w \Delta l$) on the surface supporting the stream function gives $Il = \left|\vec{K}\right| \Delta w \Delta l$, or

$$Il = \int_S \left|\vec{K}\right| dS\,. \tag{96}$$

The normalized sensitivity of a stream function then becomes

$$\widehat{S}_{\mathrm{T}} = r^4 \frac{\vec{H}_{\mathrm{RX}} \cdot \hat{\bar{\bar{m}}} \cdot \vec{H}_{\mathrm{TX}}}{\int_S \left|\vec{K}_{\mathrm{RX}}\right| dS \int_S \left|\vec{K}_{\mathrm{TX}}\right| dS}\,, \tag{97}$$

or when written in matrix form using (75),

$$\widehat{S}_{\mathrm{T}} = r^4 \frac{\mathbf{a}^\top \mathbf{H}_{\mathrm{TX}} \mathbf{M}_{\mathrm{p}} \mathbf{H}_{\mathrm{RX}}^\top \mathbf{b}}{K_{\mathrm{int,TX}} K_{\mathrm{int,RX}}} \tag{98}$$

7.3 Soil Sensitivity

As before, the voltage induced in the receive coil by an isotropic magnetic soil can be written as

$$V_{\mathrm{s}} = j\omega \frac{\chi}{2+\chi} I_{\mathrm{TX}} \widehat{M}_{\widehat{\mathrm{TX}},\mathrm{RX}}\,, \tag{99}$$

where ω is the frequency of operation, χ is the magnetic susceptibility, I_{TX} is the current in the transmit coil, and $\widehat{M}$ is the mutual inductance between the receive coil and a transmit coil that has been mirrored across the air-soil interface, as in Figure 67 [13, 49]. V_{soil} can be normalized by the quantity $j\omega\frac{\chi}{2+\chi}$ and then multiplied by I_{RX} to yield the energy coupled through the soil between the transmit and receive coils that is independent of the magnetic susceptibility of the soil. $\widehat{M}$ can be written as matrix of mutual inductances between basis functions, making the soil energy

$$W_{\mathrm{soil}} = \mathbf{a}^\top \widehat{\mathbf{M}}_{\widehat{\mathrm{TX}},\mathrm{RX}} \mathbf{b}\,, \tag{100}$$

which has the same form as W_{m}. W_{soil} illustrates how the soil acts as a secondary coupling path for energy between the two coils. This, however, is not a particularly useful quantity because it is not normalized. V_{s} can be normalized in exactly the same fashion as in section 5.2 to obtain

$$\widehat{S}_{\mathrm{s}} = r \frac{\widehat{M}_{\widehat{\mathrm{TX}},\mathrm{RX}}}{2\mu_0 l_{\mathrm{TX}} l_{\mathrm{RX}}}\,. \tag{101}$$

This can the be modified to

$$\widehat{S}_{\mathrm{s}} = r \frac{I_{\mathrm{TX}} \widehat{M}_{\widehat{\mathrm{TX}},\mathrm{RX}} I_{\mathrm{RX}}}{2\mu_0 I_{\mathrm{TX}} l_{\mathrm{TX}} I_{\mathrm{RX}} l_{\mathrm{RX}}}\,, \tag{102}$$

which when written in matrix form for use with stream functions becomes

$$\widehat{S}_{\mathrm{s}} = \frac{r}{2\mu_0} \frac{\mathbf{a}^\top \widehat{\mathbf{M}}_{\widehat{\mathrm{TX}},\mathrm{RX}} \mathbf{b}}{K_{\mathrm{int,TX}} K_{\mathrm{int,RX}}}\,, \tag{103}$$

where K_{int} is defined in (75).

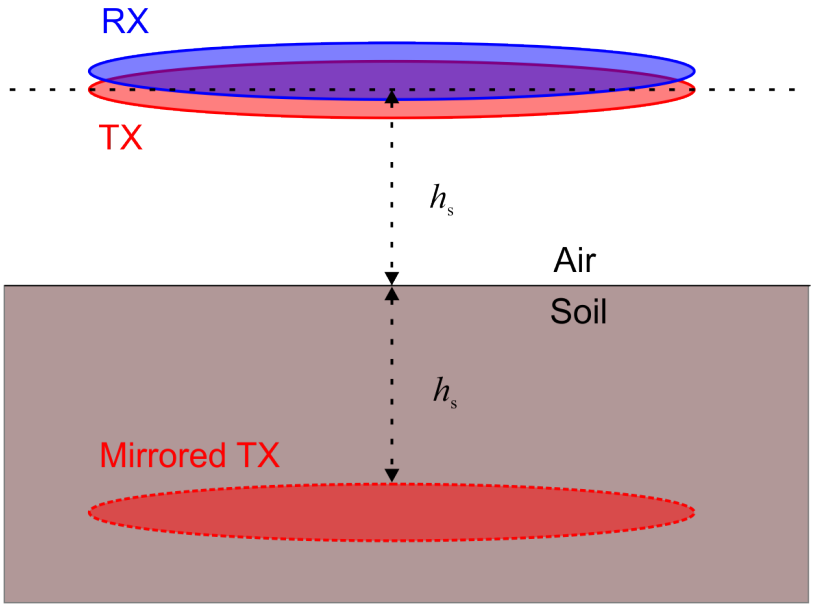

Figure 67: Receive coil and transmit coil that has been mirrored across the air/soil interface.

CHAPTER VIII

PROCEDURE FOR OPTIMIZING STREAM FUNCTIONS

In Chapter 7, a method of representing surface currents using a stream function defined on a triangular mesh was shown. Metrics for determining the goodness of coils that were first exhibited in Chapter 5 were then reformulated for stream functions in Chapter 7. These metrics can now be used to optimize coils represented by stream functions.

A brute force optimization method as was used in Chapter 6 is intractable for the purpose of optimizing stream functions with many degrees of freedom, so an ad hoc iterative convex optimization technique was developed to optimize sets of coils. Similar alternating convex searches exist in the literature, but this one was not designed following any particular method [16, 65].

The following sections detail the optimization procedure and the supporting mechanics that make it work. The sections have some overlap, but the aim is to provide the reader with an overview of the intricacies of the methods and algorithms developed for optimizing coils. Section 8.1 is a brief, high-level discussion of the two equations at the heart of the optimization, while Section 8.2 provides an overview of the processes surrounding these two equations. The remaining sections describe specific implementation issues relating to Section 8.2.

8.1 Basic Theory of Convex Optimization of EMI Coils Using Stream Functions

As an example of the difficulty of optimizing even simple coils, the wire coils from Chapter 6 with only two degrees of freedom took several days to optimize using a brute-force approach. The highly constrained nature of those coils allowed for the brute force optimization, which is simple to implement and guarantees an optimal solution if each parameter is sampled sufficiently. The stream function can represent a much greater range of coil geometries than the wire parameterizations of Chapter 6. As a result, the stream function has many more

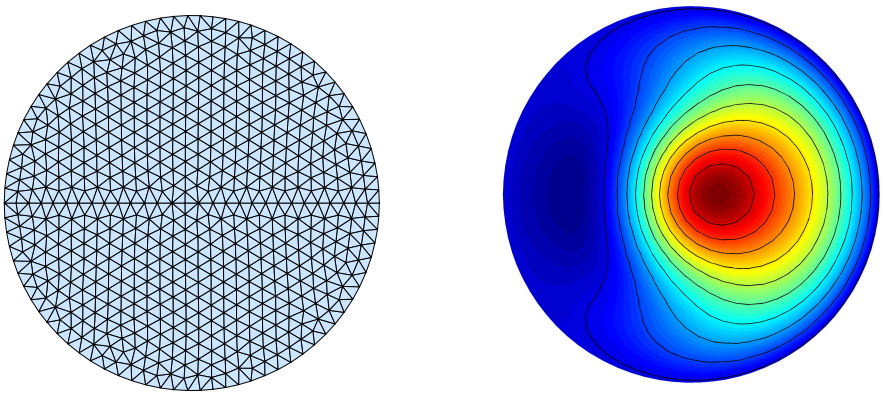

(a) Symmetric mesh. (b) Example stream function.

Figure 68: A mesh and an example associated stream function.

parameters, so a brute force optimization is not practical. For example, consider the stream functions defined on the triangular meshes that will be used in Chapter 9 (Figure 68). The stream functions have approximately 2,000 unknowns once symmetry and edge unknowns have been accounted for. If each coefficient were varied over 100 different levels, which is much less that would be required to get a good answer, and if the metrics could be evaluated in one second, which is shorter than the required time even using the pre-computed matrices of Chapter 7, then the calculation time would be approximately 10^{3992} years, which is clearly impractical.

Even other optimization methods such as gradient descent would have considerable difficulty as a result of the many local maxima and minima within the solution space. This can be seen in Figure 50 for a simple problem that is only a function of 2 parameters and has two local maxima. The ability to use a convex optimization is highly desirable for purposes of speed, but unfortunately, the expression for the target sensitivity is not convex. Fortunately, the problem can be broken into two halves, each of which is convex. These two halves are achieved by fixing the currents on one coil and solving for the currents on the other coil, as

shown in the following two equations.

$$\mathbf{a} = \underset{\mathbf{a}\in\mathbf{R}^N}{\arg\max}\{\underset{\vec{r}}{\text{GeoMean}}\left[S_{\text{T}}\left(\mathbf{a},\mathbf{b},\vec{r}\right)\right]\}, \tag{104}$$

subject to:

$$\underset{h,\theta,\phi}{\text{Max}}\left[\left|W_{\text{soil}}\left(\mathbf{a},\mathbf{b},h,\theta,\phi\right)\right|\right] < W_{0,\text{soil}},$$

$$W_m\left(\mathbf{a},\mathbf{b}\right) = 0,$$

$$P_{\text{d,TX}}\left(\mathbf{a}\right) < P_{0,\text{TX}}\,.$$

$$\mathbf{b} = \underset{\mathbf{b}\in\mathbf{R}^N}{\arg\max}\{\underset{\vec{r}}{\text{GeoMean}}\left[S_{\text{T}}\left(\mathbf{a},\mathbf{b},\vec{r}\right)\right]\}, \tag{105}$$

subject to:

$$\underset{h,\theta,\phi}{\text{Max}}\left[\left|W_{\text{soil}}\left(\mathbf{a},\mathbf{b},h,\theta,\phi\right)\right|\right] < W_{0,\text{soil}},$$

$$W_m\left(\mathbf{a},\mathbf{b}\right) = 0,$$

$$P_{\text{d,RX}}\left(\mathbf{b}\right) < P_{0,\text{RX}}\,.$$

The parameters in these equations are defined in (76), (91), (93), and (100). The objective function is a geometric mean over the target sensitivity at a number of points in space, which is a concave function that can be maximized. In addition to the concavity of the objective function, the constraints must also meet certain requirements within CVX [5, 17]. Both expressions for the dissipated power and the expression for the maximum of the magnitude of the soil sensitivity at any particular height or tilt are convex, and the mutual energy is affine. The optimization goes back and forth between solving these two equations until the solution converges. The techniques used to implement these equations in CVX are shown in Listing 8.1.

In equations (104) and (105), it might seem more natural to remove the power constraint and optimize the normalized sensitivity, $\widehat{S}_{\text{T}}$, instead of S_{T} as was done in Chapter 6. Unfortunately, the normalized quantities developed in Chapter 8 are not forms that will be recognized by CVX as valid expressions. However, optimizing S_{T} while constraining the power is equivalent, so the form in (104) and (105) is chosen since it fits into the CVX framework. Likewise, the soil energy (100) and mutual energy (91) between the coils are

used instead of the normalized soil sensitivity (103) and coil coupling factor (92). As a result, none of the expressions in Listing 8.1 are normalized, and the dissipated power must be included to both constrain the stored energy and enforce smoothness upon the stream function. It might at first appear that constraining the stored energy is also sensible, but this is not the case, as is seen in Appendix B.

Equations (104) and (105) make up the two gray boxes in the flow chart of Figure 70. All of the accompanying code and problem setup goes toward framing the problem parameters such that they can be input to these two equations, with their output being the basis function coefficients **a** and **b** that give coil analogues with maximum target sensitivity, $\widehat{S}_{\mathrm{T}}$, while constraining the soil sensitivity, W_{soil}, and the dissipated power, P_{d} and forcing the mutual energy between the coils, W_m, to zero.

8.2 Overview of a Practical Optimization Algorithm for Stream Functions

The algorithm for defining the system geometry, calculating important parameters, and solving for optimal coils is described in the flowcharts of Figures 69 and 70 and the code in Listing 8.1. Each flowchart is broken into two sections, the first being data setup for the second section, which is an optimization loop. The code listed in 8.1 nests within the two gray optimization boxes of Figure 70, and the entirety of Figure 70 nests within the gray optimization box of Figure 69.

Note that there are two nested optimization loops. The inner loop is the optimization described by (104) and (105). If this optimization could be performed perfectly, it would be the only optimization required, but this optimization is not perfect and can become trapped in any one of many local maxima. The outer optimization loop serves two purposes. First, it repeatedly calls the inner optimization loop with different initial guesses for **b**. By running the inner optimization multiple times it greatly increases the chance of finding the global maximum or at least a good local maximum. Second, the outer loop recomputes the metrics on a desired set of target positions. The best of these repeated runs on the complete set of metrics is chosen as the optimal solution.

In addition to issues with the optimization problem requiring multiple runs and iterations to find a good solution, the optimization would still be slow without taking more measures beyond formulating it as partially convex. The CVX code in Listing 8.1 is still very computationally intensive if it is performed on a full set of metrics, i.e. full grids of sensitivity points and of heights and tilts above the soil. The points at which the metrics are calculated are very sparse for the purposes of the optimization iterations, but after a run completes, the full grids can be calculated. Additionally, the full grids, such as those used to create Figures 109 to 111 for example, are still the results of very large matrices, which take very long to calculate. In Chapter 9, coils with multiple different soil constraints will be optimized, but they all use the same sets of precomputed matrices, greatly saving time.

8.3 Optimization Problem Setup

The optimization begins by defining the coil geometry, which includes the size and shape of the coils and their relation to one another (in this case, their separation). The examples in Chapter 9 solely consider coaxial circular planar coils that are separated by a set distance. However, the code can handle coils of any shape and orientation, provided that they can be defined as surfaces.

After defining the geometry of the surfaces, triangular meshes are created on those surfaces. In this instance, DistMesh, a function that uses a "Delaunay triangulation routine in MATLAB and tries to optimize the node locations by a force-based smoothing procedure," was used to create the mesh and the matrices containing node locations $\mathbf{p}$ and linkages $\mathbf{t}$ that define the mesh [40]. The initial edge length is set to determine the fineness of the resulting mesh. In this particular case, the mesh was mirrored because it was desired for the coils to be symmetrical about the $x-$axis, and the basis functions at the mirrored points were set equal to one another. The mirroring prevents identical solutions that are rotations of one another, which is believed to improve the convergence of the optimization in addition to reducing the number of unknowns. With the mirroring, the only identical rotational solutions that are allowed are those that are 180° from one another. As will be seen later, these rotated solutions are very apparent in the results. The mirrored meshes (such as Figure 68(a)) used

for the transmit and receive coils are identical for the example optimizations in the next chapter.

Other important system geometry parameters need to be defined as well. This includes h_{loc}, the discrete points in space at which the magnetic field of each coil will be calculated for purposes of optimizing the coil sensitivity. The soil response of the coils varies both with the height of the coils above the soil (h_{soil}) and with the tilt of the coils relative to the soil (θ,ϕ). Therefore, the soil response, which should be minimized, must be calculated over a range of heights and tilts during optimization. The number of sensitivity points and the number of heights and tilts all must be chosen wisely to keep calculation times to reasonable amounts. Even with the many tweaks made to improve speed, feeding too many variables to the optimization subroutine can drastically increase compute times to the point of intractibility.

Once the two meshes have been created, matrices needed for use within the optimization can be created. The matrices $\mathbf{S}_s$, $\mathbf{h}_{\text{TX}}$, and $\mathbf{h}_{\text{RX}}$ depend on both the meshes and on their relation to the soil or other points in space. The matrices $\mathbf{L}$, $\mathbf{P}$, $\mathbf{CC}_x$ and $\mathbf{CC}_y$ depend only upon the geometry of a single mesh, and the matrix $\mathbf{M}$ depends on the geometry of the meshes and their relation to one another. Once these matrices have been calculated, they must be compressed to remove any entries relating to vertices that lie on the edge of the meshes. This satisfies the condition that current cannot flow into or out of the surface that defines the coil and has the effect of reducing the number of unknowns.

The pre-calculation of these matrices is especially important to the speed of the actual optimization subroutine, as they allow only simple matrix multiplies to be needed. The soil response matrix is especially expensive to calculate (taking several hours, even with aggressive parallelization), as it contains the interactions between basis functions on two different meshes and spans several dimensions, including two different tilt variables and a height variable.

The flow chart in Figure 69 includes precomputation of important matrices to speed calculation during optimization and sets up the system geometry. The parameters are then passed to an optimization loop that performs multiple separate optimizations and then

calculates the metrics for each pair of coils. The optimization block from Figure 69 contains the flowchart of Figure 70, which contains the code to properly scale the inputs and then alternate between the two halves of the optimization until a solution is reached.

Finally, the optimization constraints must be defined. Within the optimization, the soil response can be constrained, and the dissipated power must be constrained to be less than a set value. The energy coupled directly between the coils must also be constrained to zero. As before, the dissipated power must be constrained to prevent the optimization attempting to add infinite power in an attempt to maximize the sensitivity. Since the dissipated power has been normalized, it can simply be set to one.

The soil sensitivity is more difficult because it does not vary with any set relation to the dissipated power. The soil sensitivity, does not, however, need to be constrained for the optimization to produce useful results, unlike the mutual coupling or the dissipated power. As a result, the optimization can be run without a soil constraint. In Chapter 9, examples with and without the soil contraint will be shown.

There also must be limits set for the maximum number of iterations and the maximum number of runs. These could be automated based upon several different metrics for convergence, but the author simply chose them empirically. They will be discussed more in later sections where they apply.

8.4 Outer Optimimization Loop

The meshes, matrices, and constraints from the previous section can now be fed to the outer optimization loop of Figure 69. The gray optimization box feeds these parameters to a subroutine that performs the optimization for a single set of coils, starting with a random guess for the basis function coefficients, and returns the best basis function coefficients, $\mathbf{a}$ and $\mathbf{b}$, and the associated *coarse* metrics ($\widehat{S}_{\mathrm{T}}$ and $\widehat{S}_{\mathrm{s}}$) mentioned in the prevous section.

These metrics were calculated either in space, in the case of target sensitivity, or heights above the soil and coil tilts, in the case of soil sensitivity. This was done to speed optimization, and is sufficient for this purpose. However, the true target and soil sensitivities of the optimized coils may not be exactly represented. Therefore, the metrics are recalculated over

a finer set of points ($\widehat{S}_{\mathrm{T,f}}$ and $\widehat{S}_{\mathrm{s,f}}$). From these, the aggregated metrics $\widehat{S}_{\mathrm{ggm}}$ and $\widehat{S}_{\mathrm{ggms}}$ are calculated. Run results are stored, and then the loop begins again with a different, random, initial guess. Once the specified number of runs is finished, $\widehat{S}_{\mathrm{ggm}}$ and $\widehat{S}_{\mathrm{ggms}}$ are used to choose the best coil pair from the set of runs.

Each run (outer optimization loop iteration) gives a single pair of optimized coils given a random initial guess.

8.5 Inner Optimization Input Initialization

Once the inputs from Figure 69 have been fed to the optimization function—which begins at the top of Figure 70—they must be scaled. The target sensitivity is being maximized subject to the energy coupled between the two coils being zero, the soil sensitivity being less than a chosen value, and the power being constrained. There must be scale factors for S_{T}, L, P, and S_{s} in order for the optimization to work properly. The solver within CVX will naturally struggle if these quantities vary over a large range, or for example, when attempting to make an already small value equal to zero, as in the case of the mutual energy.

It makes sense to scale the energy stored in each coil to approximately one. If this same scale factor is applied to the mutual energy calculation, the solver can produce meaningful results when forcing the mutual energy to zero during optimization. The scale factor used is the spectral norm of the self inductance matrix,

$$L_{\mathrm{scale}} = \sqrt{\max\left(\mathrm{eig}\left(\mathbf{L}^{\top}\mathbf{L}\right)\right)}\,. \tag{106}$$

Note that the soil sensitivity is represented in the optimization as the energy coupled through the soil between the two coils. Therefore, it makes sense to use the same scale factor for the soil as for the mutual energy, $S_{\mathrm{s,scale}} = L_{\mathrm{scale}}$. The target sensitivity must be also be scaled to bring its value into a reasonable range for CVX. Since its value is not necessarily in the same range as the energies, the target sensitivity is scaled separately as

$$S_{\mathrm{T,scale}} = \sqrt{\max\left(\mathrm{eig}\left(\mathbf{h}_{\mathrm{TX}}\mathbf{h}_{\mathrm{RX}}^{\top}\right)\right)}\,. \tag{107}$$

The dissipated power scaling is less straightforward as a result of the proportional equation.

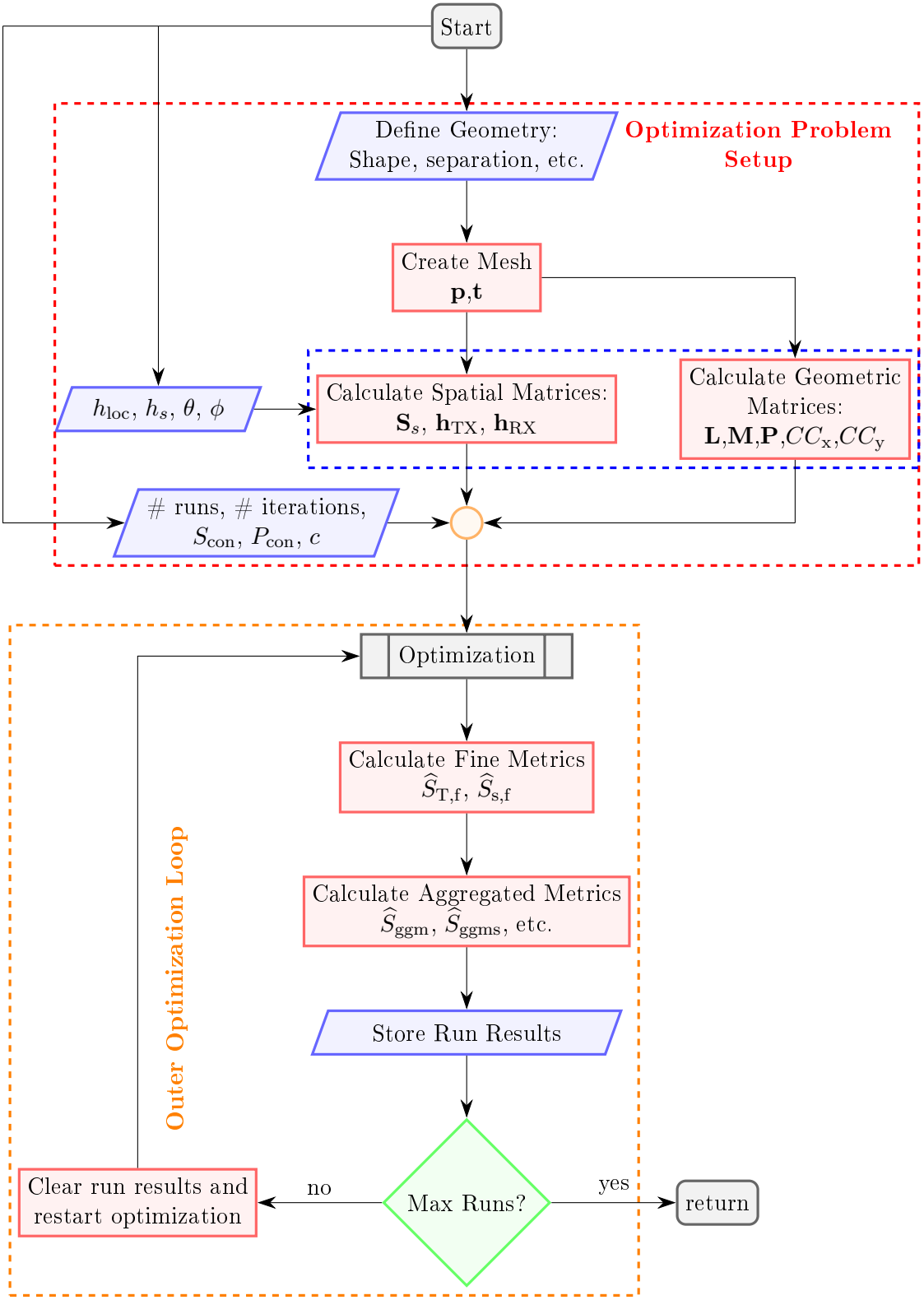

Figure 69: Optimization system setup and outer wrapper loop.

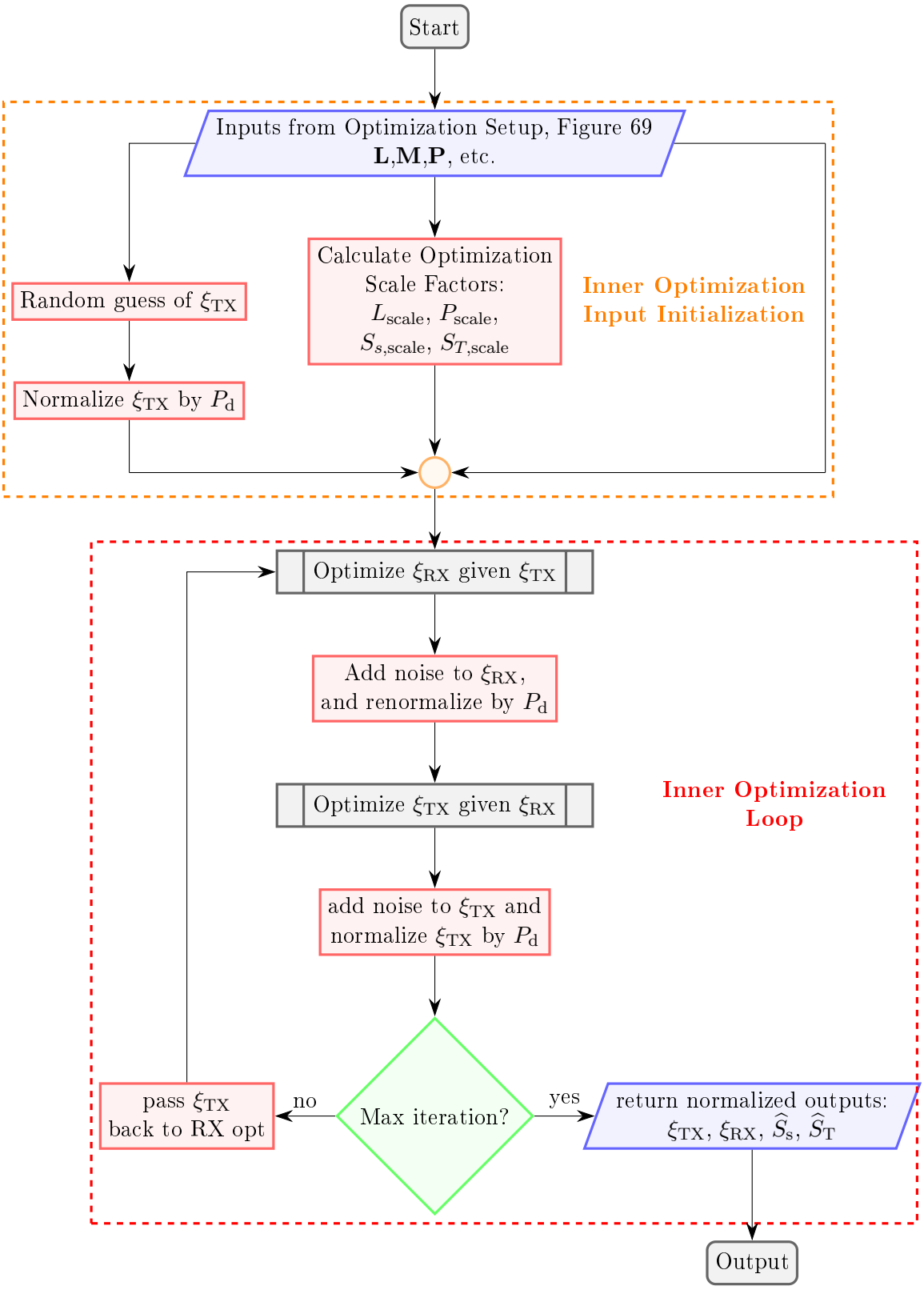

Figure 70: Scale factors and partially convex optimization.

Listing 8.1: Matlab optimization code

```
n = length(rxhVec(:,1,1));

cvx_begin quiet
        variable rx(n,1)
        expression St(size(yy))
        [ri,ci] = size(yy); %cols are y-axis, rows are z-axis
        count = 1;
    %calculate the sensitivity at each defined point in space
    for ic = 1:ci
        for ir = 1:ri
                St(ir,ic) = rx'*rxhVec(:,:,count)*(tx'*txhVec(:,:,count))'/
                    scale.St(count);
            count = count + 1;
        end
    end
    disp(['RX St size ' num2str(size(St))])
    maximize(geo_mean(geo_mean(St,1),2))
    subject to
            tx'*M*rx/scale.L == 0;
        cc*sum(norms([CCx*rx CCy*rx],2,2))/scale.P <= PCon;
        if ~isempty(SsCon)
                for ii = 1:length(Ss(1,1,:))
                        abs(tx'*Ss(:,:,ii)*rx*chi/scale.SsT(ii)) <= SsCon;
            end
        end
cvx_end


count = 1;
for ir = 1:ri
        for ic = 1:ci
        hRx(ri,ci,:) = rx'*rxhVec(:,:,count);
        count = count + 1;
    end
end
```

The power scaling

$$S_{\text{s,scale}} = T^{1/4}\sqrt{\max\left(\text{eigs}\left(\mathbf{C}_x^{\top}\mathbf{C}_x\right)\right) + \max\left(\text{eigs}\left(\mathbf{C}_y^{\top}\mathbf{C}_y\right)\right)} \tag{108}$$

was used to bring it into a reasonable range. Fortunately, the relative values of these quantities are not particularly important, and they will undergo a separate normalization for comparison purposes later.

Because the optimization works in two halves, where the stream function on one coil is optimized while the stream function on the other is held constant, an initial guess must be made to start the optimization loop. In this case, the receive coil is optimized first, so a random guess is made for ξ_{TX}, and then it is normalized by P_{d} and scaled by P_{scale} as in Listing 8.2.

Listing 8.2: Matlab optimization code

```
txxi = txxi/((cc*sum(norms([CCxT*txxi CCyT*txxi],2,2)))/scale.P)
```

8.6 Inner Optimization Loop

As has been stated, the overall problem cannot be solved all at once because the expressions for W_{soil}, W_{m}, and S_{T} are bilinear matrix inequalities, which are not convex. However, when split into two halves where the basis functions for one coil are fixed and those for the other coil are varied, these expressions become affine. Alternating back and forth between solving the two halves can produce a reasonable solution after a sufficient number of iterations, and since each half of the problem is convex, a solution to each half of the problem is guaranteed. This process is illustrated in the inner optimization loop box of Figure 70.

The normalized vector of random numbers, $\mathbf{b}_{\text{n}}$, from the previous section is passed to a subroutine that performs the procedure in (104), which finds the basis functions for a transmit coil that minimizes the coupling between the two coils, maximizes their target sensitivity, and constrains both their soil sensitivity and power dissipation. The code for this subroutine is given in Listing 8.1. Then the resulting transmit coil basis function coefficient vector, $\mathbf{a}$, is passed to (105), which performs the same convex optimization as (104) but for the receive coil. The optimization goes back and forth between (104) and

(105), adding a small, gradually decreasing amount of noise between each iteration, which speeds convergence

The power constraints $P_{0,\mathrm{TX}}$ and $P_{0,\mathrm{RX}}$ are typically set to the same value, which needs only to be chosen intelligently to allow the solver to work [46]. In this case, a value of one is appropriate for the solver. While this algorithm converges well, it does not always converge to the maximum possible value, so it must be run many times.

The value of $W_{0,\mathrm{soil}}$ is actually updated on each iteration because c_s is specified, and the energy stored in the coils changes with each iteration.

8.6.1 Noise

Noise, which decreases as the loop iterates, is added to the resulting stream function coefficients to lessen the chances of becoming caught in a local maxima.

$$\xi_{\mathrm{RX}} = \xi_{\mathrm{RX}} + \max\left(\mathrm{mean}\left(\left[\xi_{\mathrm{RX}}\,\xi_{\mathrm{TX}}\right]\right)\right)\left(-1 + 2 * \mathrm{rand}\left(N\right)0.9^{n_{\mathrm{opt}}}\right) \tag{109}$$

This is then normalized once again to force the power dissipated by the noisy coil to be equal to one. An identical process is performed to optimize the transmit coil given the receive from the previous step. Then noise is added to the resulting receive coil, the power is set back to one, and the process repeats until the maximum specified iterations are reached.

CHAPTER IX

STREAM FUNCTION EXAMPLE OPTIMIZATIONS

The optimization procedure described in Chapter 8 will now be used to optimize coil pairs. As before, these example coils are intended for use in a handheld system that can be swept side-to-side by an operator, and many of the design choices made are geared toward this goal. The coils are also desired to have good performance in magnetic and/or conductive soils and to be reasonable to construct.

9.1 System Geometry and Optimization Parameter Choices

The transmit and receive coils are represented by identical triangular meshes on discs (Figure 71). Other more complex meshes—or more than two meshes—could be used.

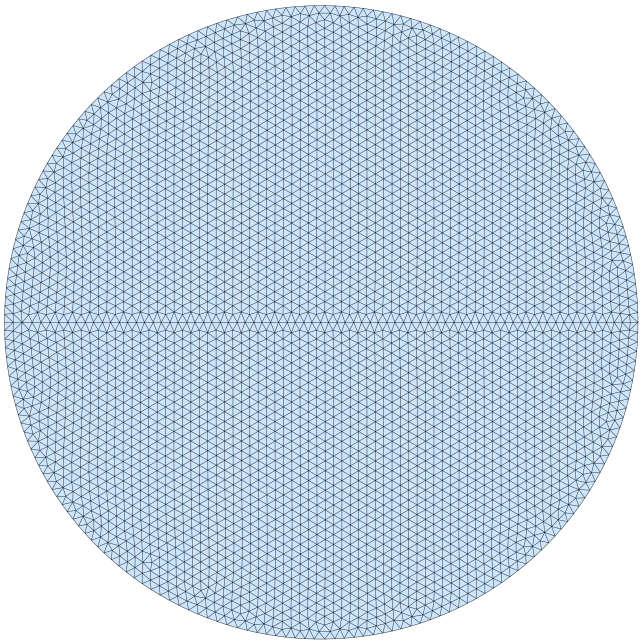

Figure 71: Coil mesh used for optimization.

The coils are arranged as in Figure 72. Both coils are centered on the z-axis, the transmit coil is at $z = 0$, and the receive coil is at $z = -\delta$. δ is the separation between the coils, with the intended search direction being $+z$, pointing into the ground.

Both meshes have radii, r, of 13.3 cm, and vertical, inter–mesh spacing, δ, of $r/25 = 5.3$ mm. DistMesh takes an initial edge length as an input, and this is chosen to be 0.004 mm, a condition that gives a mesh with 3,972 vertices. As before, the meshes are made symmetrical about the x-axis to force symmetry in the coil geometries. This has the added benefit of removing rotational solutions and reducing the number of unknowns that must be calculated.

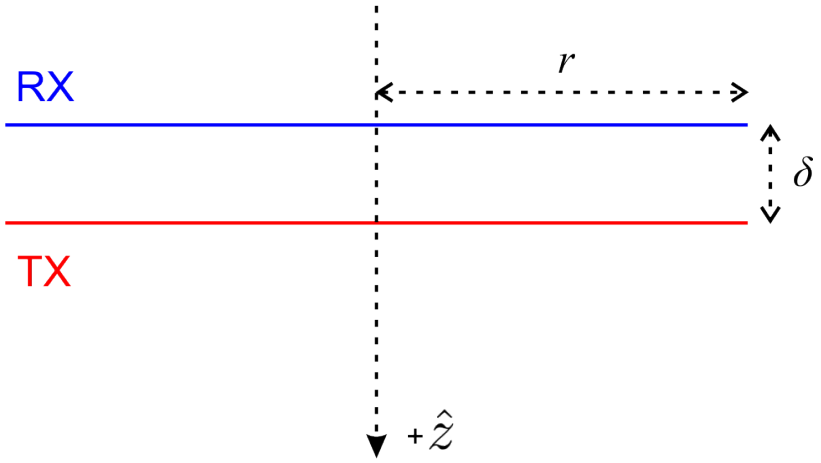

Figure 72: Coil geometry for optimization, where $+z$ points into the ground, and the transmit coil sits at z=0.

Two sets of spatial parameters must be defined for the basic optimization algorithm: target sensitivity and soil sensitivity. Once the points for these are defined, the matrices needed for target and soil sensitivity can be pre-calculated.

9.1.1 Target Sensitivity

The target sensitivity can be optimized over any set of points in space, but recall from Section 5.3.1 that both good depth performance and a broad pattern along the y-axis (down-track direction) are desirable, while the pattern in the x-direction (cross-track) is less important. The points need to be chosen appropriately to achieve the desired coil performance. Optimizing the target sensitivity at a single point in space does not give coils well-suited for good depth performance, nor does it create a pattern that is broad in the y-direction, as is desired. Optimizing the target sensitivity on a line of points on the $+z$ axis gives good depth performance, but it still does not give the broad pattern that is desired for target

Table 7: Regions over which the target sensitivity is calculated

	Inner Loop	Outer Loop
$x_{\min}$	—	$-0.2r$
Δx	—	$0.05r$
$x_{\max}$	—	$0.2r$
$y_{\min}$	0	0
Δy	$0.1r$	$0.05r$
$y_{\max}$	$0.8r$	$0.8r$
$z_{\min}$	$0.2r$	$0.2r$
Δz	$0.1r$	$0.05r$
$z_{\max}$	$1.5r$	$1.5r$

detection. It does however often result in concentric or near-concentric types of coils, which are interesting in the sense of a different coil configuration. Both of these deficiencies are as would be expected from the way the optimization is defined. Therefore, it was determined that optimizing the target sensitivity over a portion of the $y-z$ plane is the best method for creating coils that perform well given the definitions of $\widehat{S}_{\text{ggm}}$ and $\widehat{S}_{\text{ggms}}$. In addition, it is desirable to have coils that peak up near $x = 0$, so it is easier for an operator to locate a target. By choosing a plane of points instead of a volume of points, preference is given to coils with sensitivities that peak near $x = 0$ while also keeping the optimization problem tractable.

Recall from Section 8.4 that the optimization is set up to use a coarse set of points for the inner optimization and a fine set of points for the outer optimization because of computational issues. The coarse set of points was chosen to be on a plane for most of the optimization examples for the reasons mentioned above, but a few line optimizations will be presented to show how a different definition of the objective function affects the optimization results. The fine set of points are spaced over a volume in space and used to compute the aggregated metrics $\widehat{S}_{\text{ggm}}$ and $\widehat{S}_{\text{ggms}}$ that are described in Chapter 5. To further improve optimization times, the grid is calculated only over one half of the plane (as shown in Figure 73) because the other half can be inferred from symmetry, speeding calculations during optimization. The optimization points are shown in Table 7.

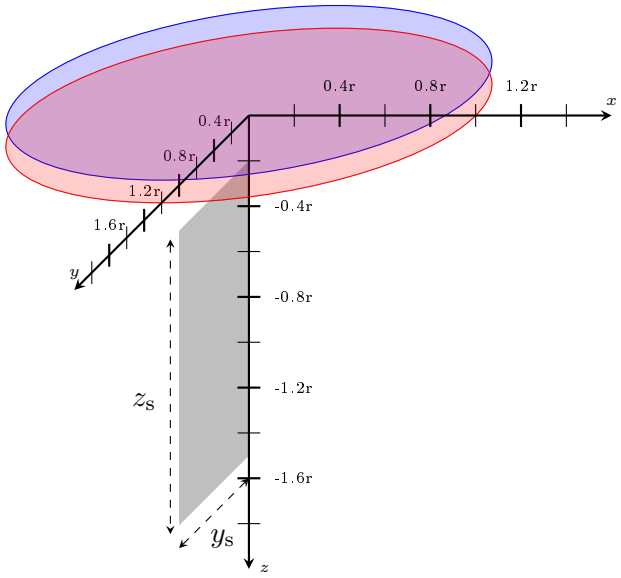

Figure 73: An illustration of the area over which the target sensitivity is calculated for optimization.

9.1.2 Soil Sensitivity

As explained in Chapter 5, the soil sensitivity is crucial for coil performance in magnetic or conductive soils. It can be calculated over a range of heights and tilts, as illustrated in Figure 74. The soil sensitivity is generally worse the closer a coil is to the soil; only a few heights close to the soil are necessary to capture the worst-case soil sensitivity. The sensitivity changes—and is typically worse—when the coil is tilted relative to the ground. There is no guarantee the coil will be held completely parallel to the soil, nor is the ground guaranteed to be flat; it may be bumpy. Calculating the soil response when the coil is tilted relative to a flat plane should roughly account for both of these situations.

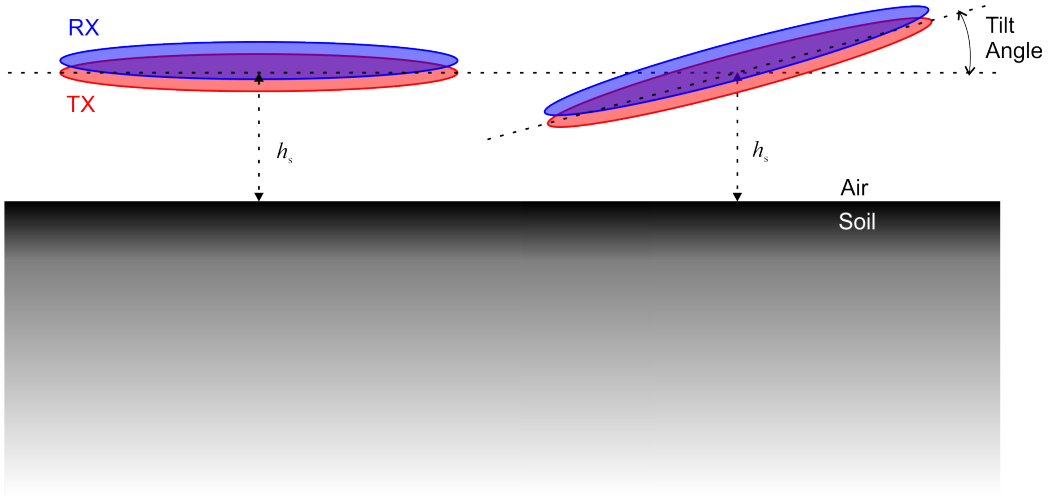

Figure 74: Illustration of the geometry used for the soil sensitivity calculations, showing the height (h_s) and tilt (angles δ and/or ϕ) relative to the soil. Note that h_s is measured to the center of the transmit coil.

Unfortunately, the calculations for soil sensitivity are very expensive, both to create the soil response matrix and to use within the optimization, so a very sparse set of points must be used (Table 8). Ideally, a much finer set of points would be used because these are not guaranteed to be the worst soil response within the range of -10 to +10 degrees.

The full soil response matrix (steps of one degree) can take over a day to calculate on an eight core AMD Ryzen 7 2700 clocked at 3.8 GHz, and a set of tilts for one soil height can create a matrix of approximately 25 GB. For example, the four graphs of Figure 101 are the result of 100 GB of data, which does not fit into the memory of most desktop computers.

Table 8: Range of parameters over which the soil sensitivity is calculated

	Inner Loop	Outer Loop
θ_{min} (deg)	-10	-10
$\Delta\theta$ (deg)	10	10
θ_{max} (deg)	10	10
ϕ_{min}	-10	-10
$\Delta\phi$	10	10
ϕ_{max}	10	10
$h_{\text{s,min}}$	$0.2r$	$0.2r$
Δh_{s}	$0.1r$	$0.1r$
$h_{\text{s,max}}$	$0.4r$	$0.5r$

9.2 Optimizing Example Coils

There are several layers to the idea of optimizing coils using the partially convex procedure of Chapter 8. That optimization is not guaranteed to find a global maximum because it is only partially convex. Therefore, the optimization must be run multiple times to have a better chance of finding a good answer. This will be called an optimization set, where each set is composed of multiple runs of the outer optimization in Figure 69 with identical inputs save for the random initial guess. Each run has multiple iterations of the inner optimization of Figure 70, where the optimzation bounces between equations 104 and 105, which are solved using SeDuMi within CVX [57]. CVX can translate convex optimization problems to give to several solvers, the default being SDPT3, but due to problems with SDPT3, SeDuMi was used.

For the purpose of these examples, identically defined coil pairs were optimized for two different target sensitivity calculations and also for several different soil constraints. The two different target sensitivity calculations are for points on both a grid on the $y-z$ plane and on a line on the z-axis. For each different combination of soil constraint and target sensitivity parameters, a different optimization set of 100 runs was executed, where each set was composed of 100 back-and-forth iterations. Rather than a set number of iterations, it would probably be more efficient to use an adaptive convergence metric, but for this work 100 iterations should be more than sufficient to achieve convergence. For simplicity, each set is identified by an alphanumeric code as shown in the first column of Table 9.

Prior to optimization, practical values for the constraint $W_{0,\text{soil}}$ used in equations 104 and 105 are not known. The maximum value of aggregate normalized target sensitivity, $\widehat{S}_{\text{ggm}}$, is partially dependent upon the maximum soil sensitivity that is allowed. That is, the constraint on the soil sensitivity, and therefore the soil energy, W_{soil}, also indirectly constrains the energy stored in each coil. Reducing the stored energy also reduces the target sensitivity. However, the exact relationship between the target and soil sensitivity is not known a priori. Additionally, as a result of the manner in which the optimization works, the maximum possible value of the soil sensitivity is not known either.

In order to choose a practical range for this constraint, an optimization set was run

without a soil constraint. The average of the soil sensitivity resulting from these runs was then calculated, and this averaged value, $W_{0,\text{soil}} = 0.1504$, is shown in Table 9 for the optimization set G100[1]. Percentages of the averaged soil sensitivity, e.g. 75%, 50%, 25%, etc., can be used as soil constraints in later optimizations, as shown in Table 9.

Table 9: Target Sensitivity Variables

Opt Set	Target Points	Soil Constraint (%)	$W_{0,\text{soil}}$	$P_{0,\text{TX}}$	$P_{0,\text{RX}}$
G100	Grid	none	0.1504	1	1
G50	Grid	50	0.0752	1	1
G25	Grid	25	0.0376	1	1
G15	Grid	15	0.0226	1	1
G10	Grid	10	0.0150	1	1
L100	Line	none	0.1432	1	1
L50	Line	50	0.0716	1	1
L25	Line	25	0.0358	1	1

The optimization sets were run for the percentages of the average soil response that are shown in Table 9 and for the two different target senstivity calculation types of Table 7. The values of $\widehat{S}_{\text{ggm}}$ and $\widehat{S}_{\text{ggms}}$ are tabulated for the best coil from each optimization in Table 10.

With major matrices (primarily the soil sensitivity matrix) precalculated, a grid sensitivity set of 100 runs takes approximately 1.5 days to complete using a Ryzen 7 2700 processor clocked at 3.8 GHz, while a line target sensitivity set of 100 runs completes in around one day. These calculations times can vary greatly depending on the number of nodes in the mesh and the number of target and soil sensitivity points and height/tilts.

[1]Note that this average response will vary as a function of optimization setup.

Table 10: $\widehat{S}_{\text{ggm}}$ and $\widehat{S}_{\text{ggms}}$ for the best coil from every optimization set

Target Points	Soil Constraint (%)	$\widehat{S}_{\text{ggm}}$ (dB)	$\widehat{S}_{\text{ggms}}$ (dB)	Run Number
Grid	none	-63.8	-16.9	27
Grid	50	-65.4	-12.3	36
Grid	25	-67.3	-8.2	30
Grid	15	-69	-5.4	11
Grid	10	-70.4	-3.3	25
Line	none	-67.1	-15.3	43
Line	50	-67.9	-14.3	72
Line	25	-69.8	-10.3	63

As before, plotting $\widehat{S}_{\text{ggm}}$ against $\widehat{S}_{\text{ggms}}$ is convenient for helping choose the "best" coils, by providing an easy visual comparison between target and soil sensitivity. There is a tradeoff between the two, where typically increased target sensitivity (desirable) brings increased soil sensitivity (undesireable). The relationship between the two, however, is not one-to-one, and different applications may have different requirements for soil rejection.

Figure 75 shows a comparison plot of $\widehat{S}_{\text{ggm}}$ against $\widehat{S}_{\text{ggms}}$ for the wire coils of Chapter 6 and the various stream function optimization sets. For every set, the best coil is marked with a larger corresponding symbol. The sets optimized with the target sensitivity on a line are worse than those optimized on a grid, as is to be expected. The manner in which $\widehat{S}_{\text{ggm}}$ and $\widehat{S}_{\text{ggms}}$ are calculated inherently favors a broader pattern than will be created by optimizing on a line on the z-axis. The grid sensitivity optimized without a soil constraint matches the aggregate target sensitivity of the best of the wire-wound coils, and it is also the best target sensitivity of all of the stream function coils. This too is as should be expected, since all of the other sets were optimized with a constrained soil sensitivity that reduces the maximum possible target sensitivity. Note how the coil sets that have a constrained maximum soil sensitivity all lie on lines (with the exception of some failed optimization runs). This is simply a function of the soil constraint since $\widehat{S}_{\text{ggms}}$ is the sum of $\widehat{S}_{\text{ggm}}$ and the

maximum value of the soil response. The optimization naturally forces the soil response to its maximum, making the relationship between the two values constant for all answers.

The G50 and G25 set answers will be used for detail analysis later in the chapter, both due to their varied families of coils and their improvements over existing coils. Note how the 50% soil constraint case shows a loss of 2.4 dB in target sensitivity while gaining 4.6 dB of soil rejection. Clearly there are gains to be had with respect to the soil with intelligent winding of coils.

Figures 76 and 77 show $\widehat{S}_{\mathrm{gm}}$ versus height and $\widehat{S}_{\mathrm{T}}$ on boresight for the best coils from each optimization set. These are largely as would be expected. Coils created with the same target sensitivity calculation but with less constrained soil sensitivity perform best, and the line sensitivity coils' target sensitivity performs better on boreight close to the coil than it does in $\widehat{S}_{\mathrm{gm}}$ relative to the grid target sensitivity coils.

Figure 78 shows the maximum of the soil sensitivity for the best coil of every set as a function of height above the soil. The coils optimized on a line for target sensitivity actually perform favorably in comparison to the grid sensitivity calculations. An analysis with more tilts and heights than shown here and in Table 8 would be preferable for increased accuracy, but for purposes of example, these are deemed sufficient.

The differences in the coil "winding" configurations created by the optimization are of interest. Different constraints (e.g. soil sensitivity, target sensitivity, etc.) create different coil current paths, which are equivalent to windings in a wire coil. The coil "winding" configurations are related to the shape of the stream function, so the shape of the stream function can be used as a proxy for comparing coils. To this end, a metric of the difference of the shapes between every coil pair of every set was calculated, accounting for the 180° rotational possibility and the fact that either coil in a pair could be used as the transmit coil. This difference is shown graphically in the dendrogram of Figure 79, where each leaf is a different coil pair. A cutoff of 3.8 was used to color sets of similar coils, and their values of $\widehat{S}_{\mathrm{ggm}}$ and $\widehat{S}_{\mathrm{ggms}}$ are plotted in matching colors on Figure 80, which matches the sets of Figure 75. There are various outliers from the sets, but in large part each optimization set contains one or two coil families that are distinct from every other set. That is, each

optimization set creates a different coil shape by way of the different constraints used for each set. Note the best performing coil of the G15 set is an outlier, which demonstrates that the optimization routine is imperfect as a result of its biconvex property.

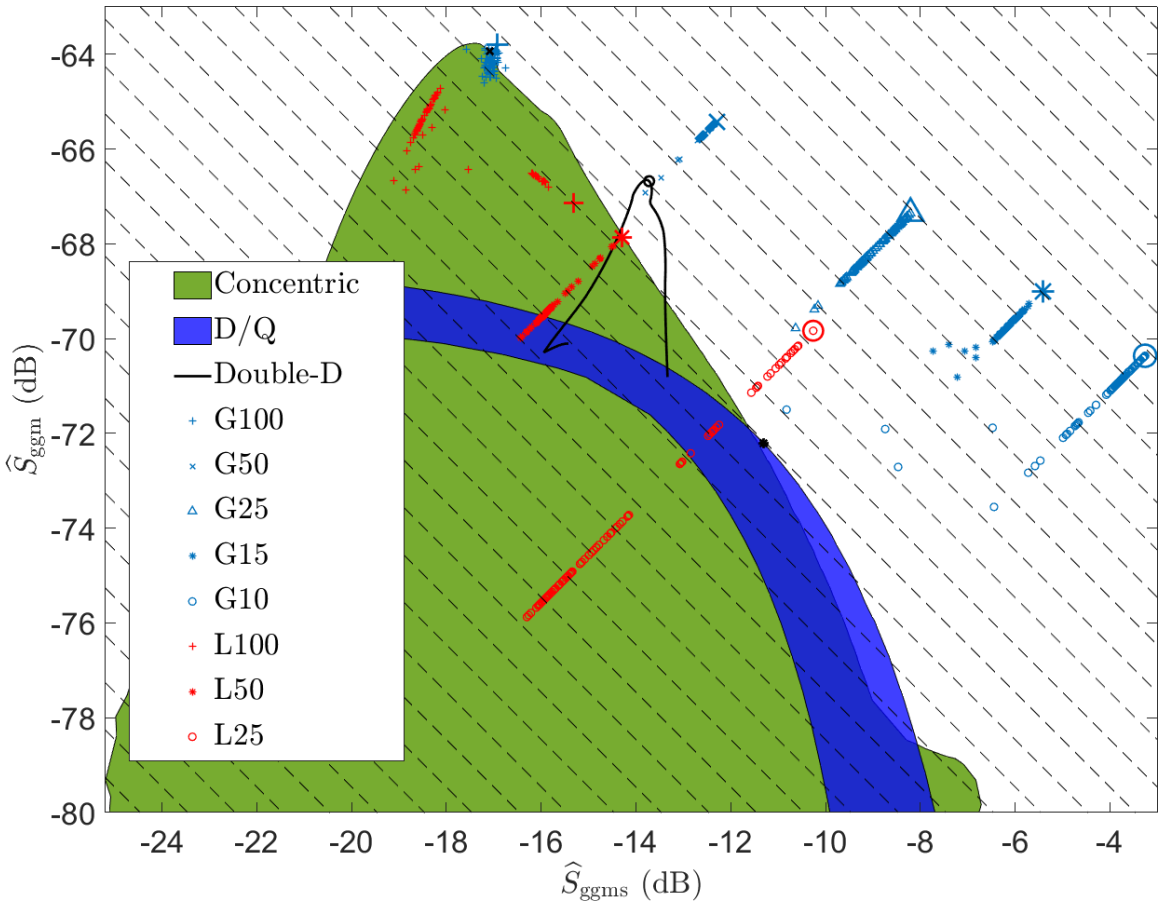

Figure 75: $\widehat{S}_{\mathrm{ggm}}$ plotted against $\widehat{S}_{\mathrm{ggms}}$ for the wire comparison coils of Chapter 6 and for stream function coils optimized over different soil constraints and target sensitivity points.

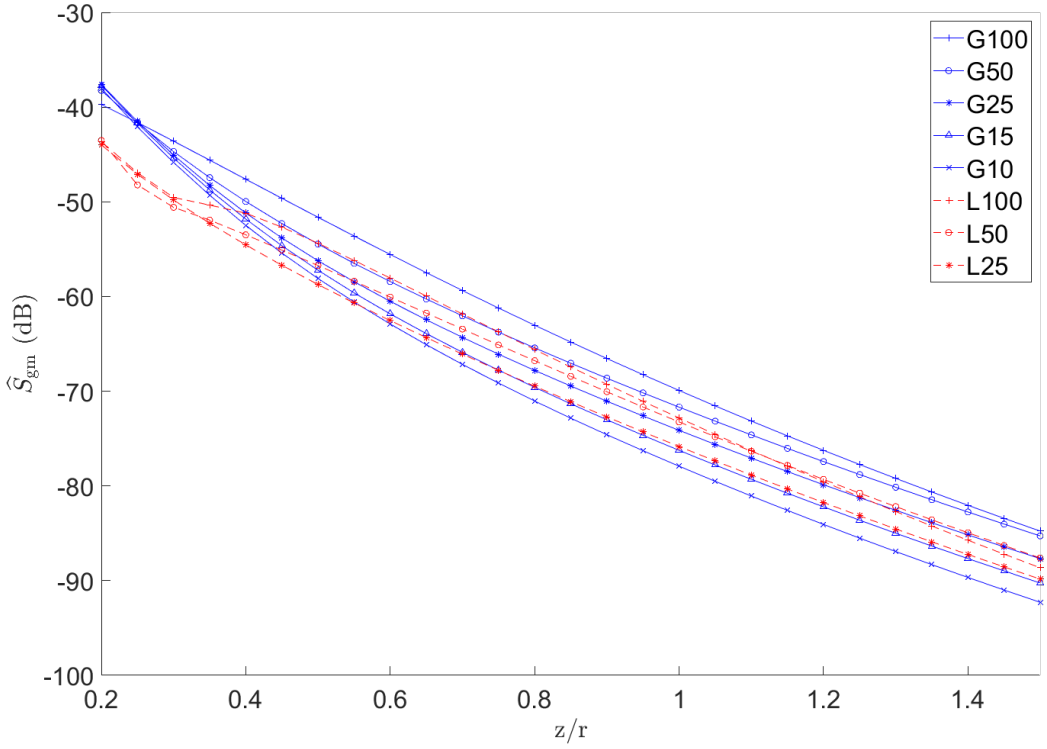

Figure 76: $\widehat{S}_{\mathrm{gm}}$ versus distance from the coil for the best coil from every optimization set.

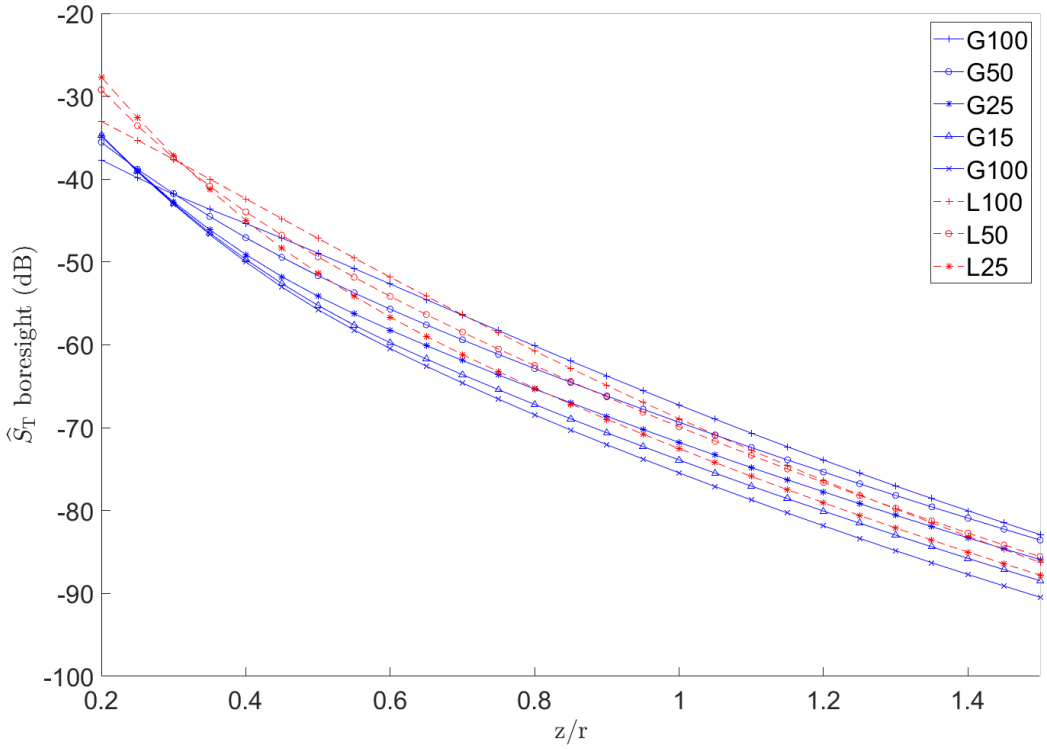

Figure 77: Target sensitivity on coil boresight for the best coil from every optimization set.

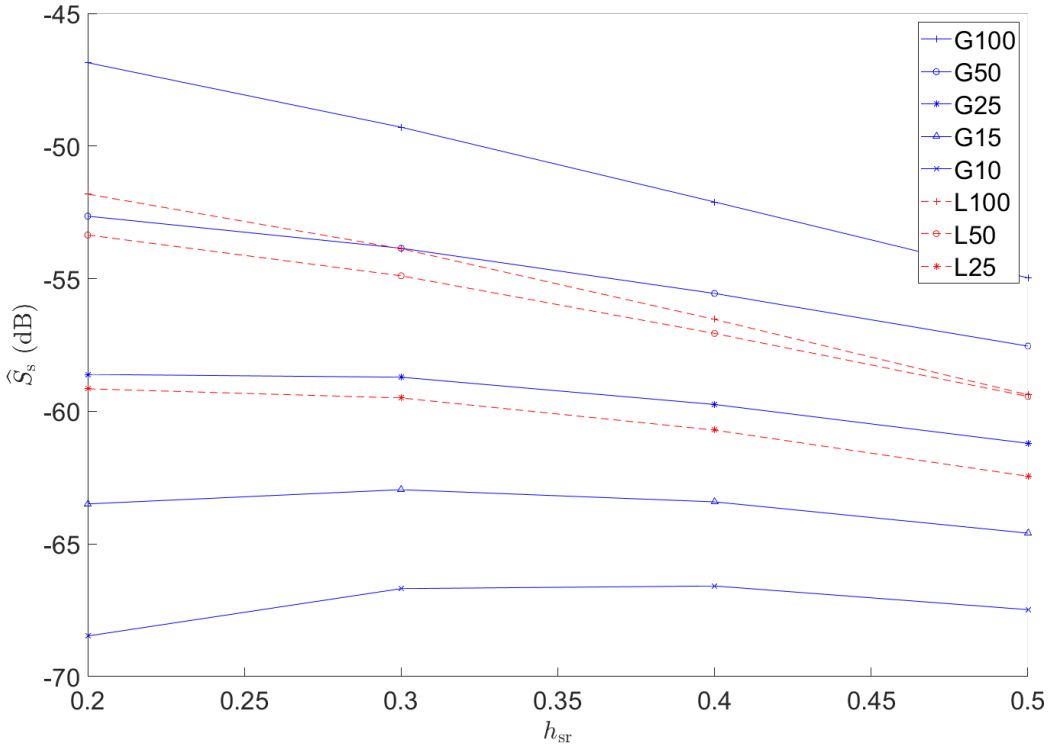

Figure 78: Maximum of the soil sensitivity over all tilts plotted against the height above the soil for the best coil from every optimization set.

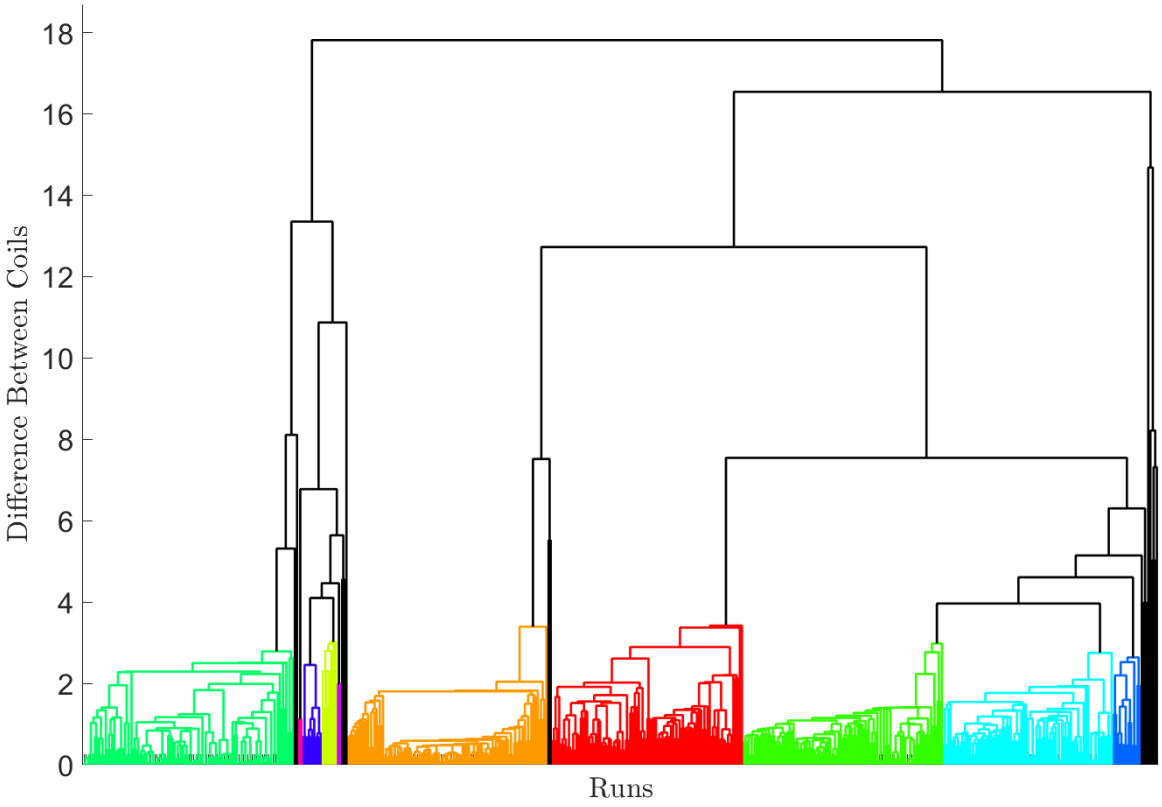

Figure 79: A dendrogram created with a cutoff of 3.8 for all the stream function coils of all the grid optimization sets.

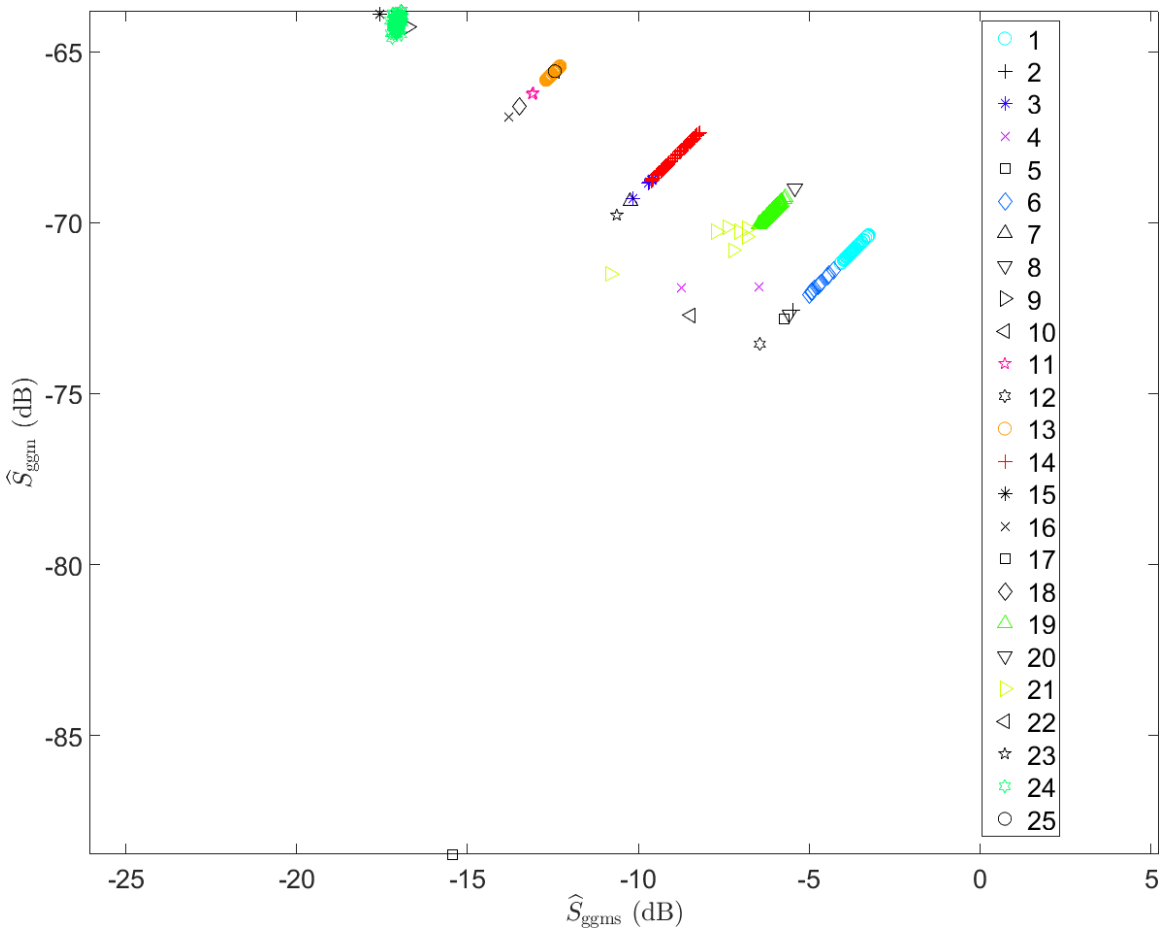

Figure 80: $\widehat{S}_{\text{ggm}}$ plotted against $\widehat{S}_{\text{ggms}}$ for every grid stream function coil. The colors and legend are matched to the dendrogram of Figure 79.

9.3 Optimization Convergence

The coils resulting from the 50% and 25% soil constraints within the grid target sensitivity optimization sets demonstrate desirable improvements over the common wire coils of Chapter 6. The following analysis shows the convergence within runs of the 50% soil constraint and also the convergence of the optimization set of the 25% case. Additionally, examination of the 25% case demonstrates how the stream functions, and therefore the coils, can vary within a single set with the same constraints.

9.3.1 Example of Run Convergence Within G50 Optimization Set

To illustrate convergence and the differences possible between stream functions within a set of runs over one soil constraint, the G50 set will now be examined. First, consider the best answer from this set. Figures 81 to 84 illustrate the changes in the stored and mutual energies, dissipated power, soil response, and target sensitivity as the optimization iterates within a single inner optimization run (in this case, the best answer from the set). Note how the optimization immediately forces the dissipated power to its maximum value as it places as much energy into the coil as possible while still constraining the mutual energy to zero. The oscillations visible at the beginning of all four graphs are a result of the noise added between each iteration. The soil sensitivity is also gradually pushed to its maximum constraint—as would be expected—to add more energy and consequently more target sensitivity. Finally, the objective function usually converges within approximately 70 iterations.

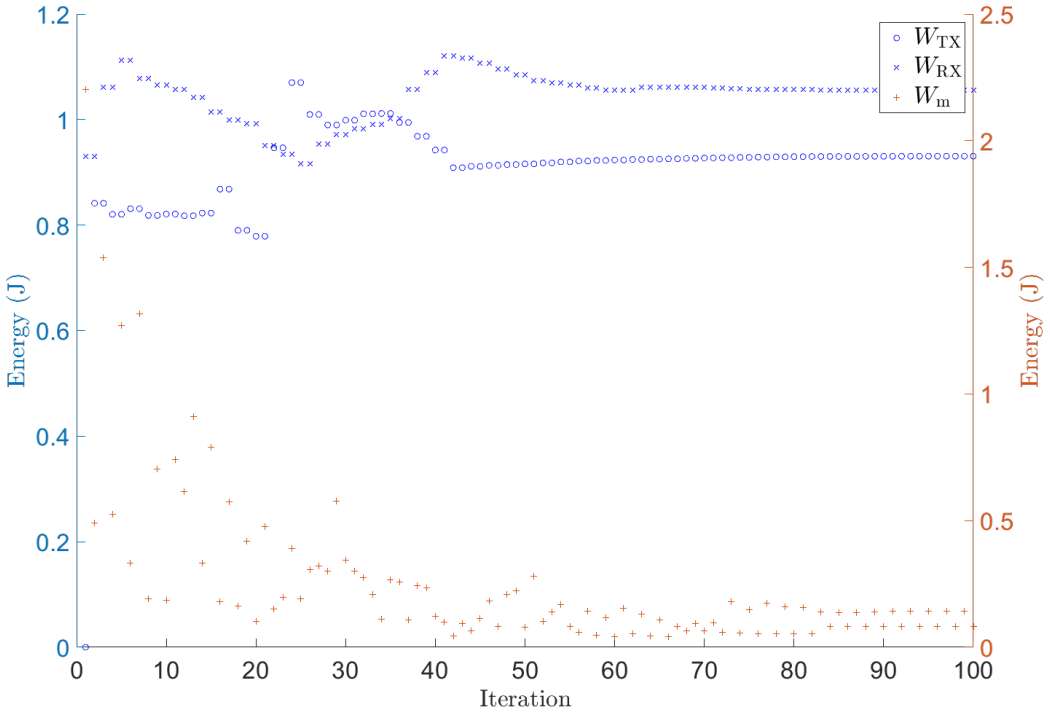

Figure 81: The self and mutual energies over the course of the inner optimization loop from the best coil of the 50% soil grid set.

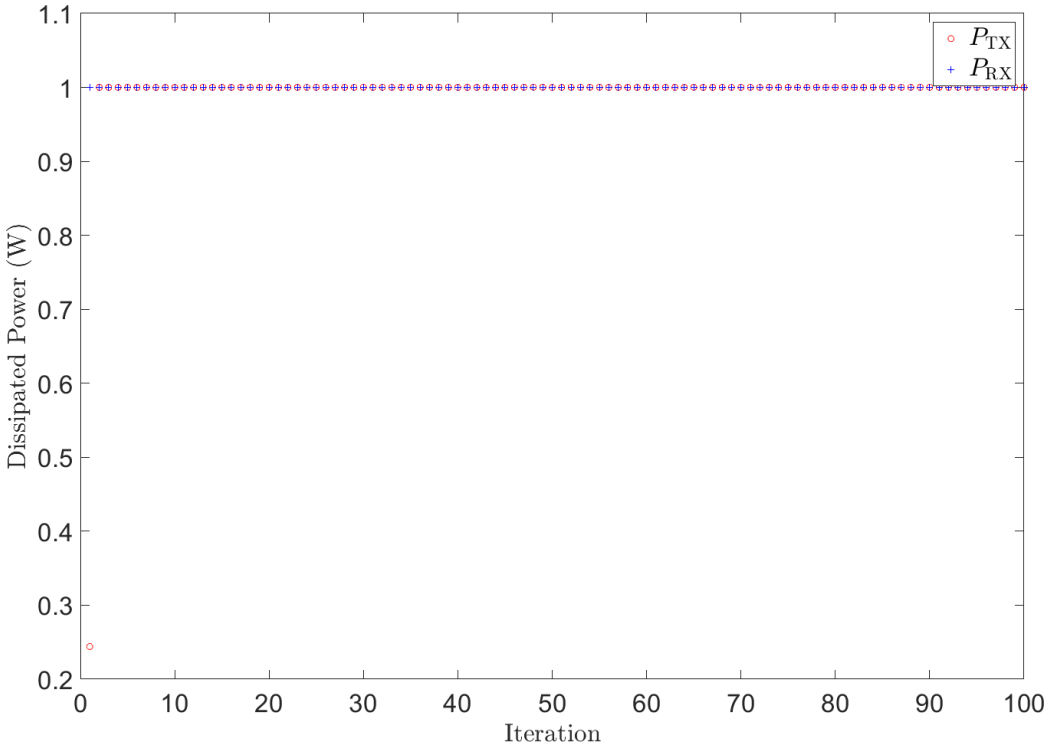

Figure 82: The dissipated power over the course of the inner optimization loop for the G50 case.

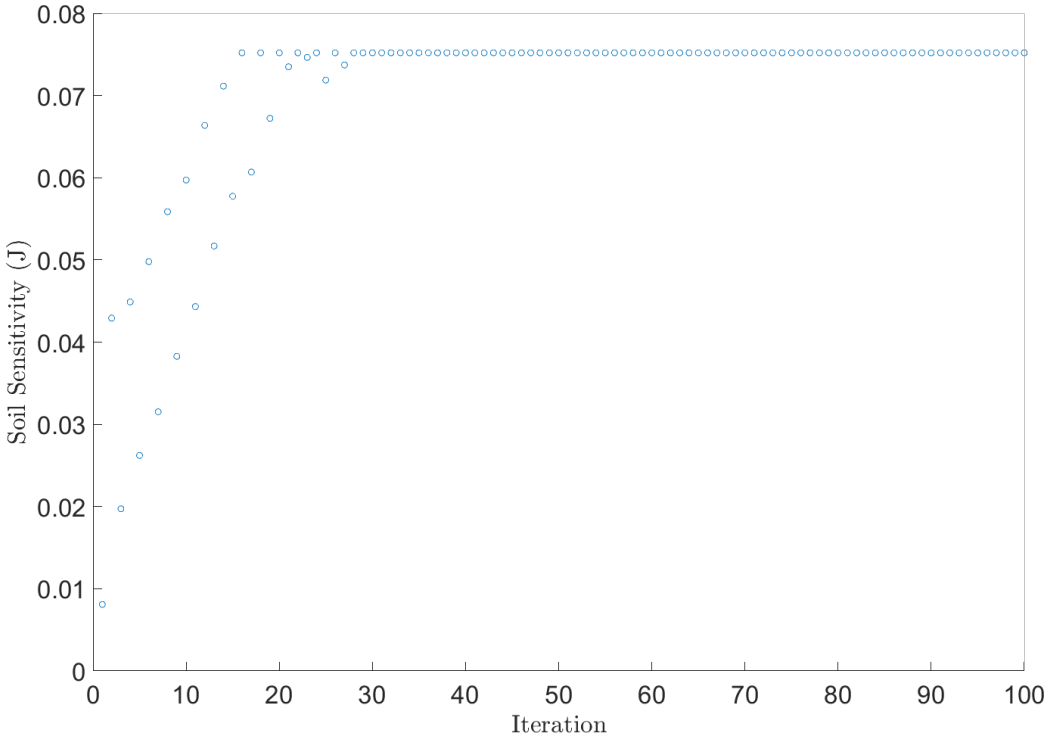

Figure 83: Soil sensitivity convergence over the course of the inner optimization loop for the G50 case.

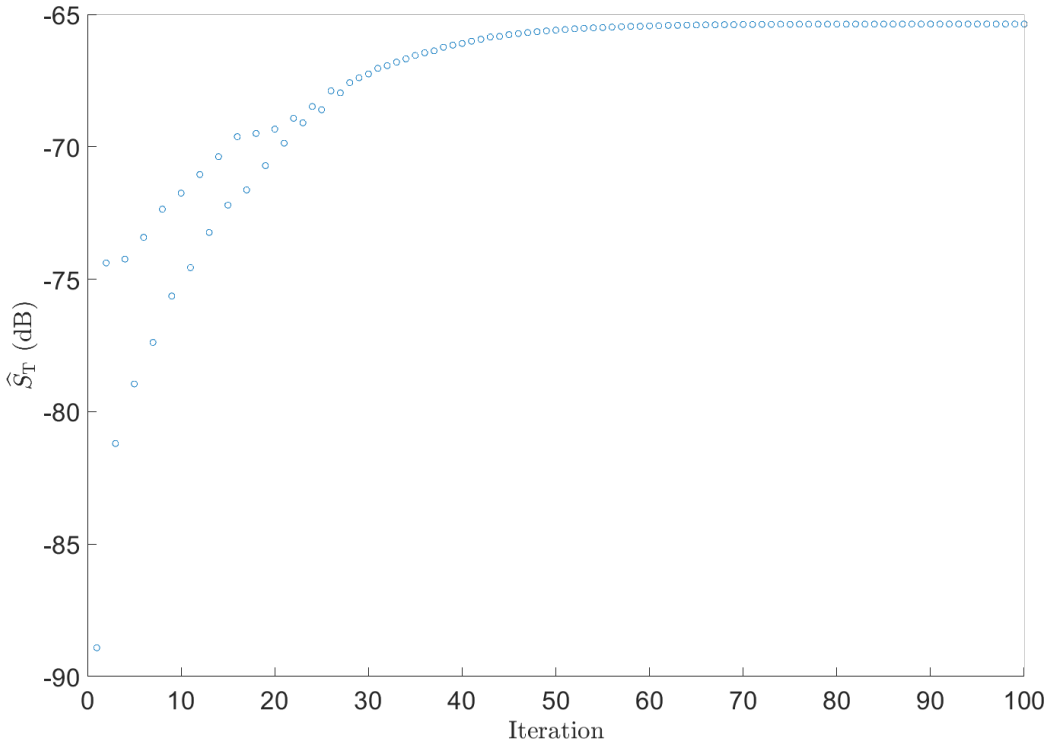

Figure 84: Target sensitivity convergence over the course of the inner optimization loop for the G50 case.

Figures 85 and 86 show the normalized target sensitivity and the soil energy, W_{soil}, for each of the 100 runs for the G50 case plotted as the optimization algorithm iterates back and forth. As can be seen, the target sensitivity generally converges within 70 iterations. The few points which appear to have not converged early are a result of a failed convex optimization that has been restarted with a new random guess.

The soil sensitivity reaches its constraint early on, and demonstrates the same split that results from the two separate optimizations with added noise. As expected, the solver places the soil sensitivity at its maximum constraint in an attempt to add as much energy as possible to the coils. However, it is interesting that SeDuMi is unable to push the soil to its maximum immediately (Figures 83 and 86), unlike the dissipated power of Figure 82.

Figures 85 and 86 demonstrate again that the algorithm converges well for all but a few cases where SeDuMi has failed.

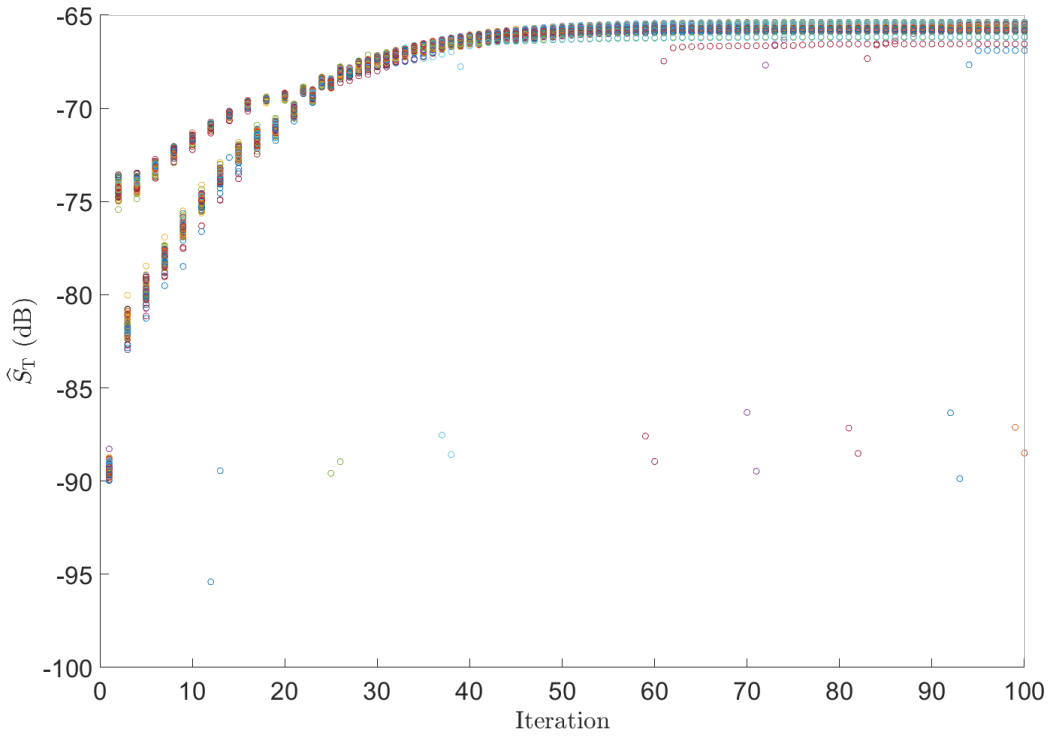

Figure 85: Target sensitivity convergence over the course of the inner optimization loop for every run within the G50 set. Outliers in the 85 to 95 dB range are a result of failed convex solver restarts.

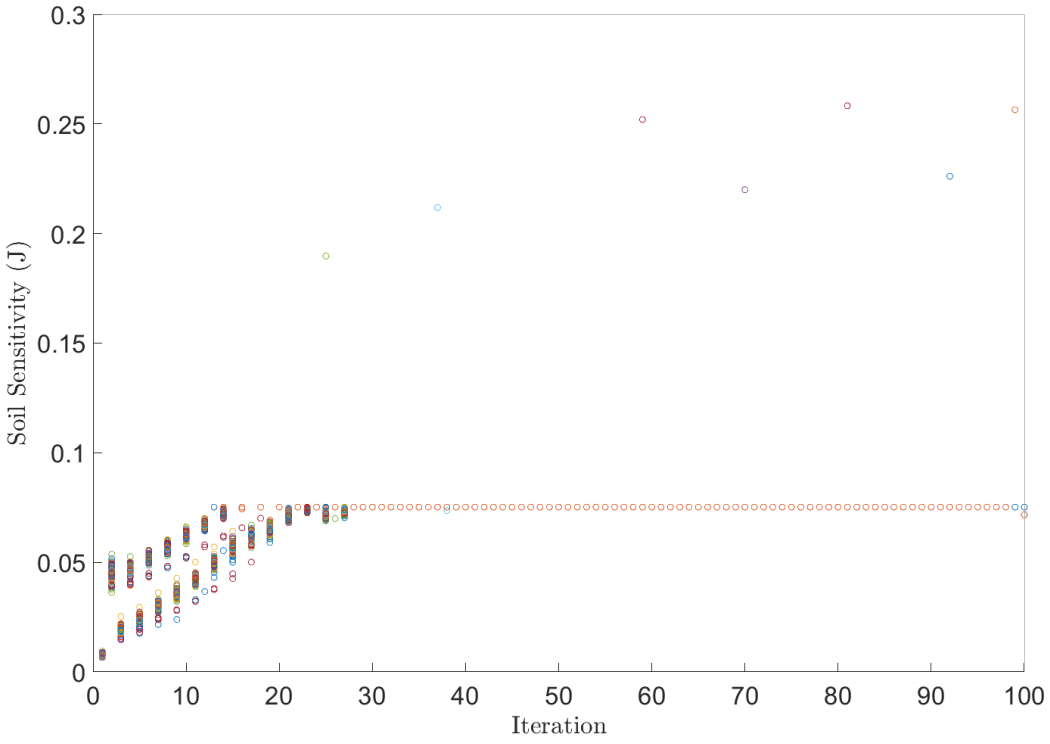

Figure 86: Soil energy, W_{soil}, convergence over the course of the inner optimization loop for every run within the G50 set.

9.3.2 Example of Optimization Set Convergence within the G25 Optimization Set

Now consider, for example, the stream functions from the G25 optimization set. As in Figure 79, by taking the average of the norm of the difference between stream functions from different runs, the coils can be grouped by physical similarity. This is illustrated in Figure 87, which is a dendrogram of the differences between stream functions, where each leaf is a different coil pair, and a threshold of four has been set to color the different clusters of coils. Six clusters result, though three are single coils, with the sole coil of cluster two being very similar to clusters one and five.

The colors from the multi-coil clusters are carried over to the plot of $\widehat{S}_{\text{ggm}}$ versus $\widehat{S}_{\text{ggms}}$ in Figure 88. Clusters one and five make up the majority of the solutions, with the coils from cluster one being generally better than those of cluster five, though they do make up two distinct sets. These sets are evident in the histograms of Figures 89, 90 and 92, where there are two distinct peaks corresponding to clusters one and five. The histograms demonstrate that the optimization has converged to two primary types of solutions with the two peaks. Because many solutions are in the best group (group 1), it is reasonable to assume that the best solution is somewhat optimal. It is certain that they are better than the answers reached with simple wire coils. However, because of the bi-convex nature of the optimization, these are not guaranteed to be the absolute best possible answers.

The best coils within each cluster are plotted in Figures 93 to 98. The similarity of the best coils within each cluster indicate that the solutions are somewhat optimal. The physical similarity between the stream functions of clusters one, two, and five is evident in Figures 93, 94 and 97. These stream functions all resemble double-D coils with a few extra balancing turns. The better coils of cluster one show larger loops that run closer to the edge of the disc however, which give them their superior depth performance. The coils of clusters three, four, and six do not perform as well by the metrics set in previous chapters, but they do have an interesting shape (Figures 95, 96 and 98). They are non-circular concentric coils with smaller balancing turns off to the sides.

Note that Figure 89 is a histogram of the final $\widehat{S}_{\text{ggm}}$ calculation, and Figure 90 is a

histogram of the value of $\widehat{S}_{gg}$ as it is output from the optimization with reduced points. The two values are plotted against each other in Figure 91. The roughly diagonal line of Figure 91 shows that optimizing on the plane is a good surrogate for optimizing over a much larger cube of points, which would be much more computationally expensive.

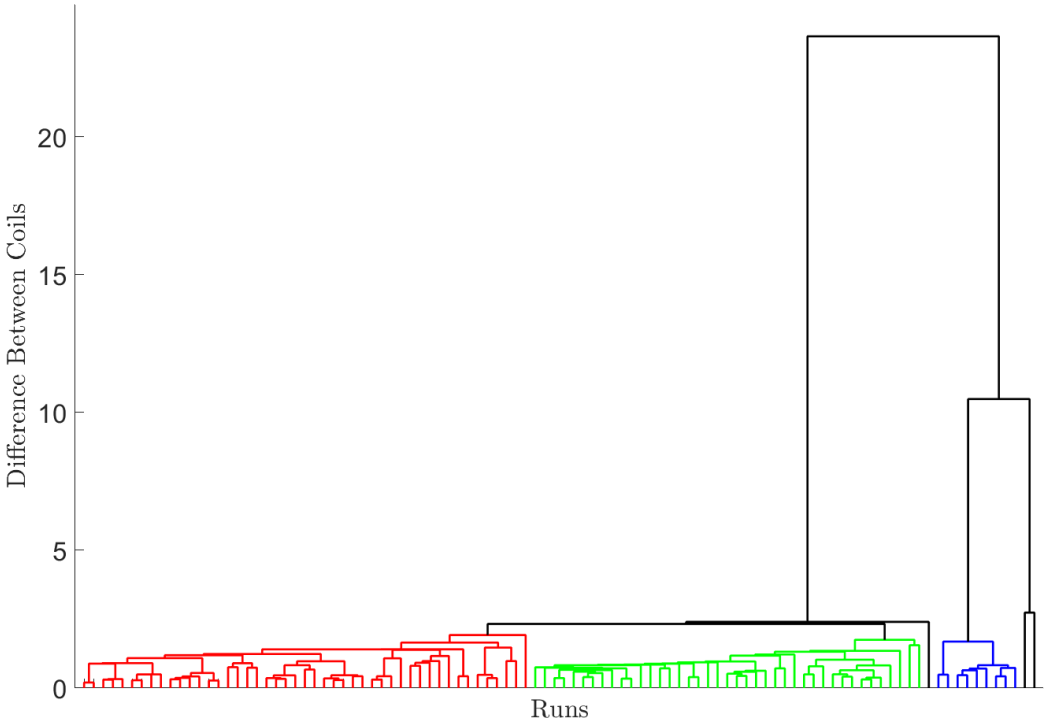

Figure 87: Dendrogram illustrating the difference between stream functions from the G25 set.

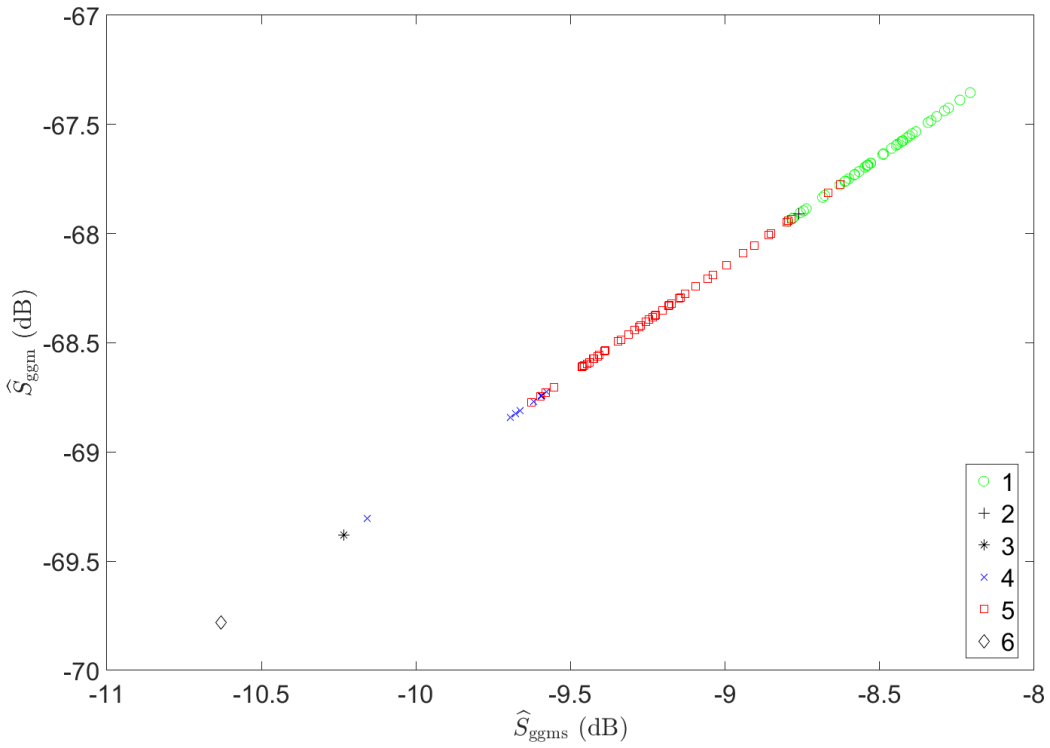

Figure 88: $\widehat{S}_{\text{ggm}}$ plotted against $\widehat{S}_{\text{ggms}}$ for the G25 set, with colors matched to the dendrogram in Figure 87.

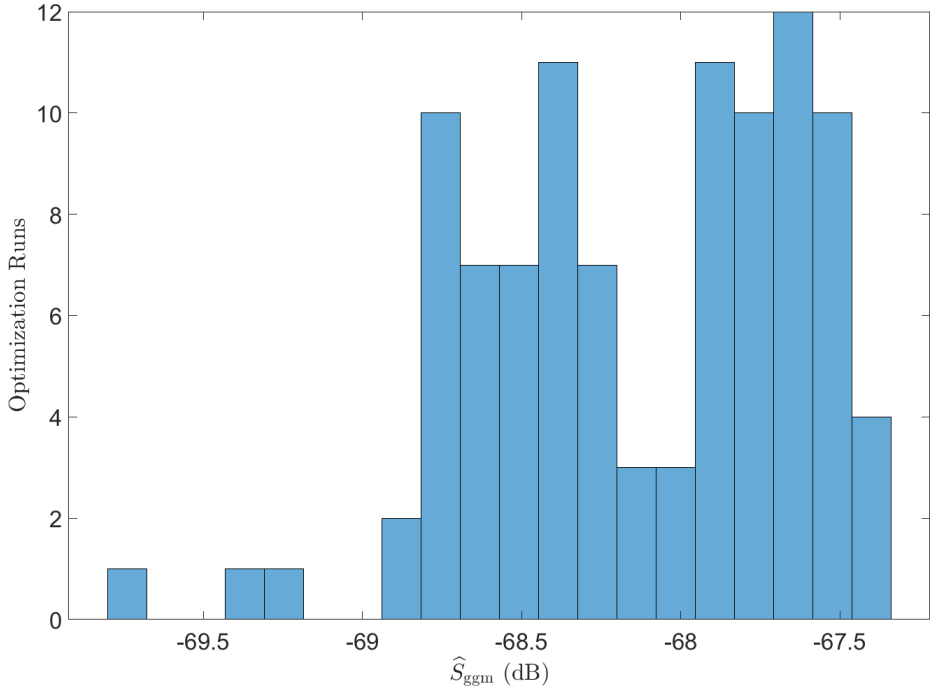

Figure 89: A histogram of $\widehat{S}_{\text{ggm}}$ for the G25 set.

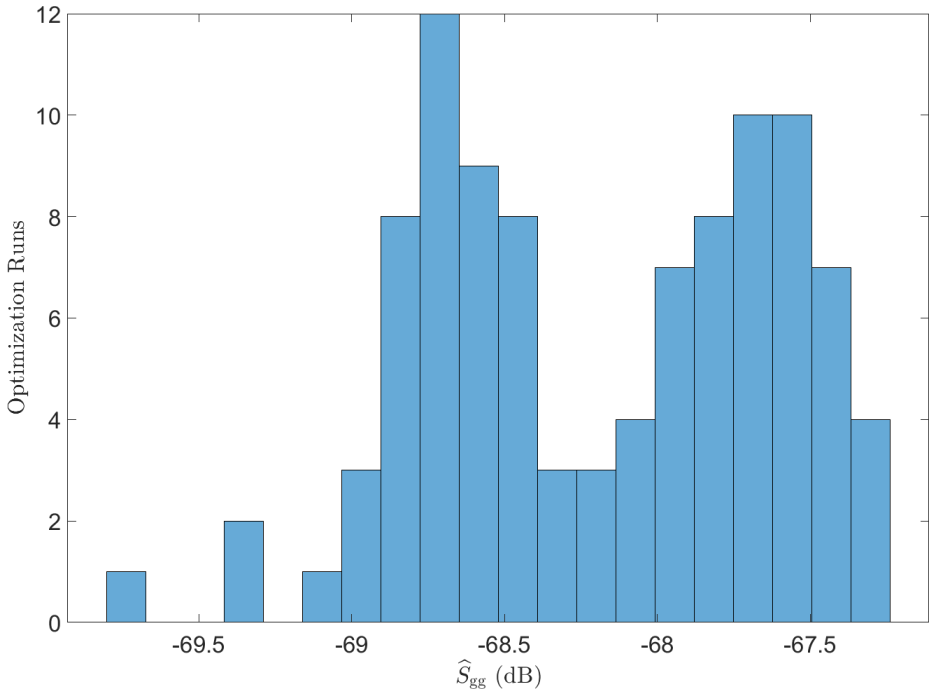

Figure 90: A histogram of the normalized objective function of the G25 set. In this case, it is the geometric mean of the target sensitivity at the optimization points on the target grid.

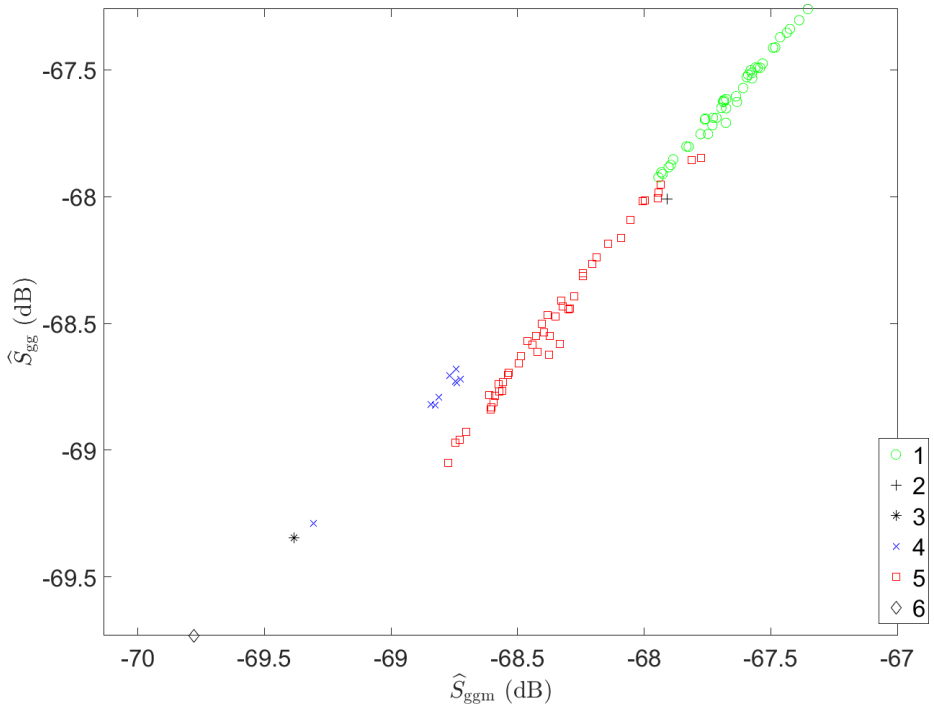

Figure 91: $\widehat{S}_{gg}$ (the normalized objective function from optimization) plotted against $\widehat{S}_{ggm}$.

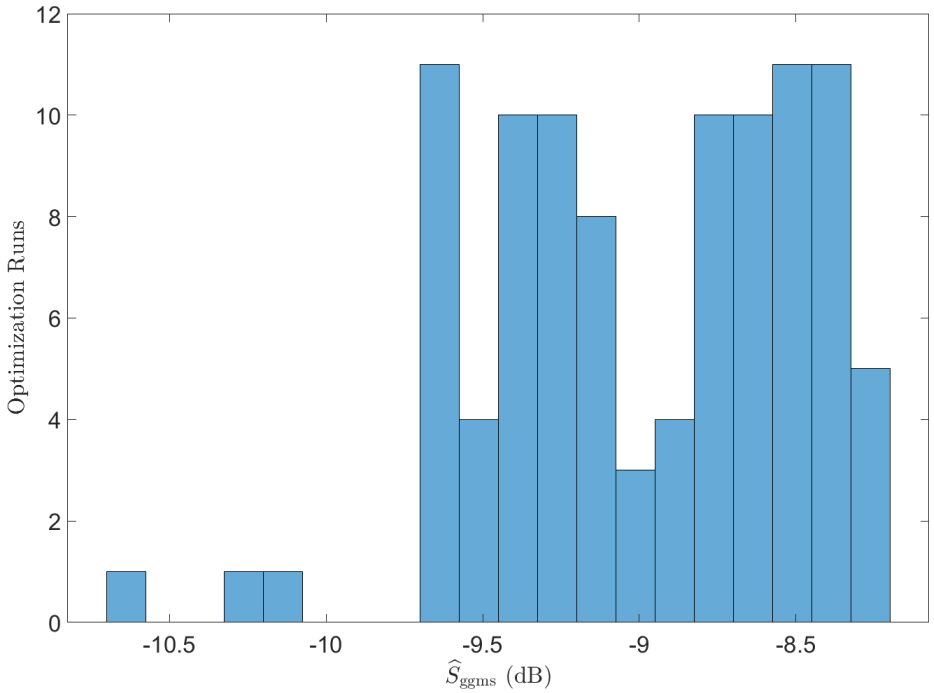

Figure 92: A histogram of $\widehat{S}_{\text{ggms}}$ for the G25 set.

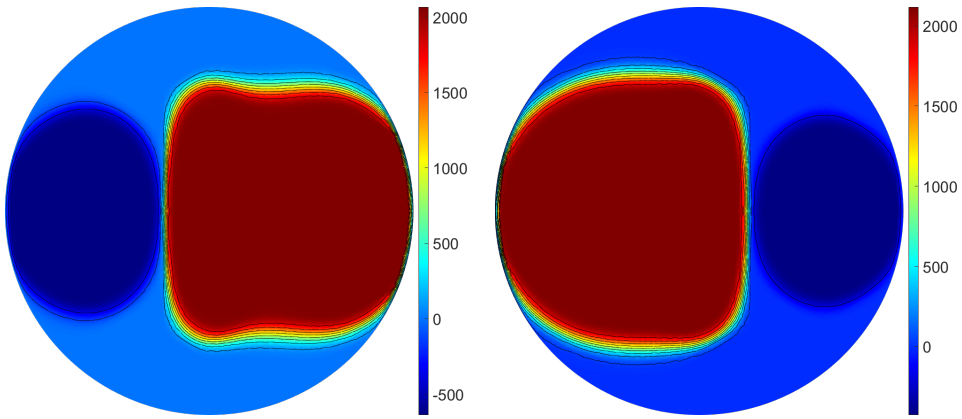

(a) TX. (b) RX.

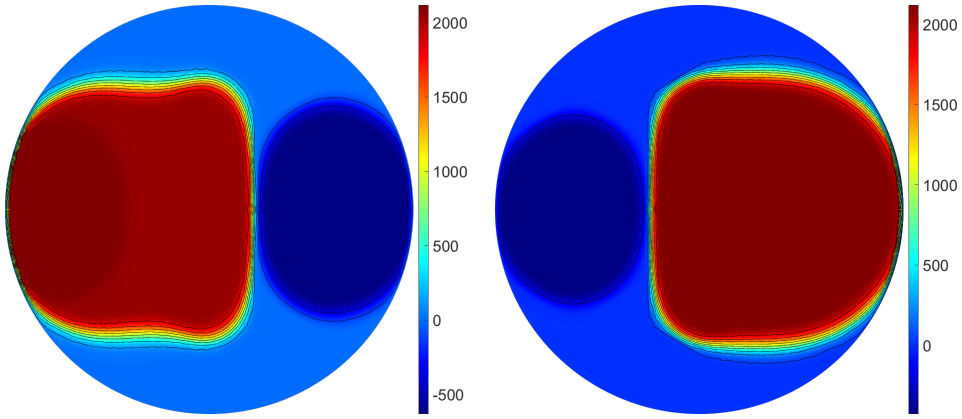

(c) TX. (d) RX.

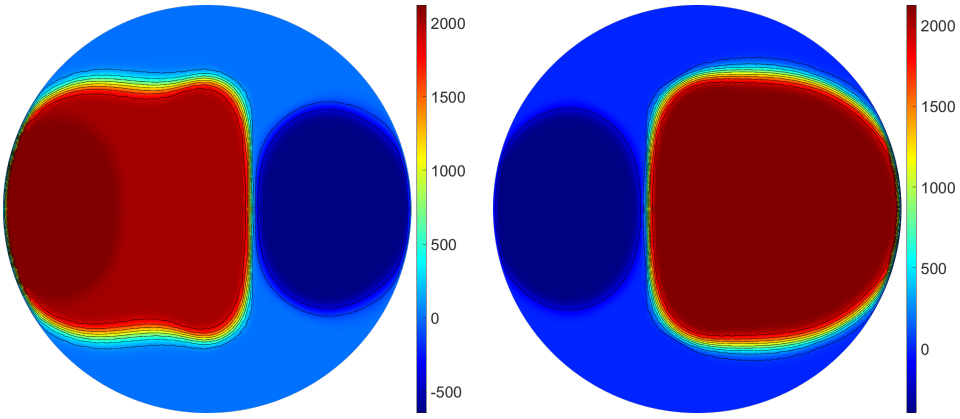

(e) TX. (f) RX.

Figure 93: The three best coils from cluster 1 of the G25 set.

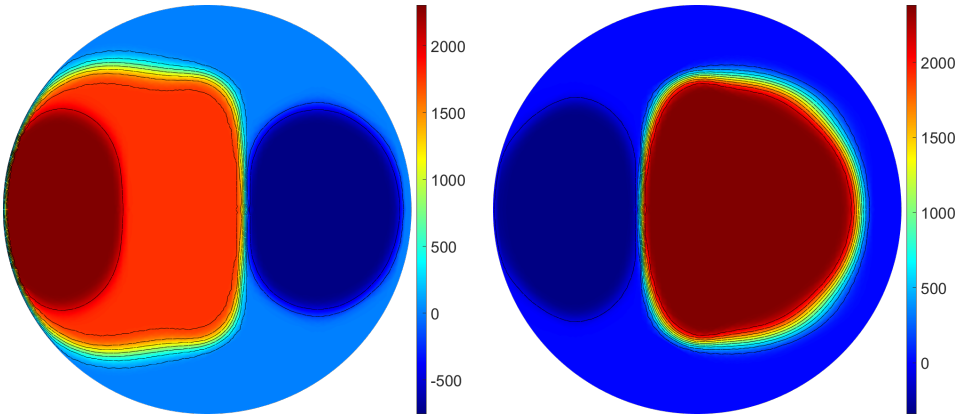

(a) TX. (b) RX.

Figure 94: The only coil solution from cluster 2 of the G25 set.

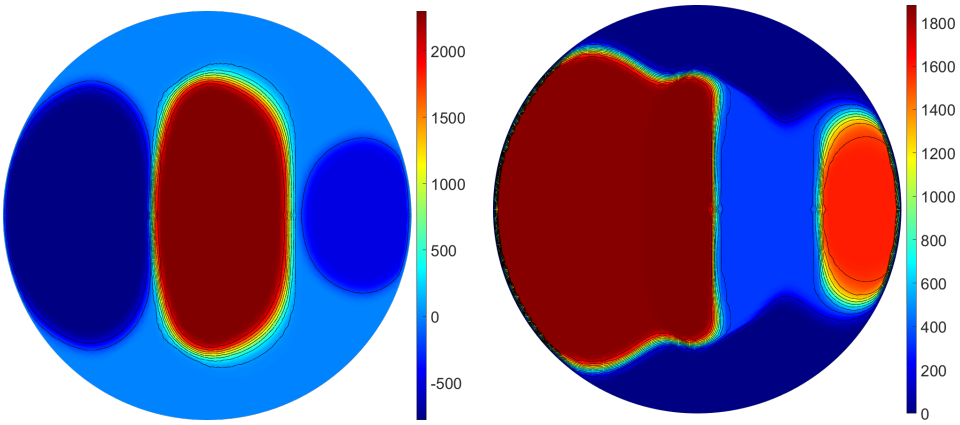

(a) TX. (b) RX.

Figure 95: The only coil solution from cluster 3 of the G25 set.

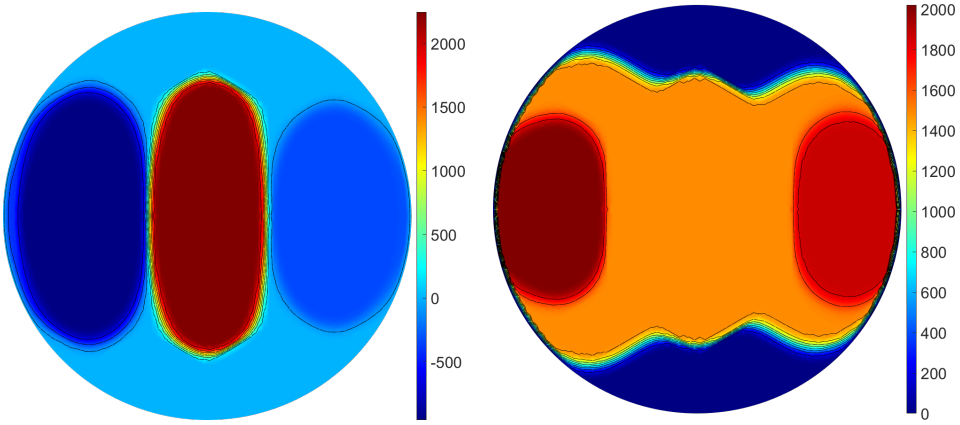

(a) TX. (b) RX.

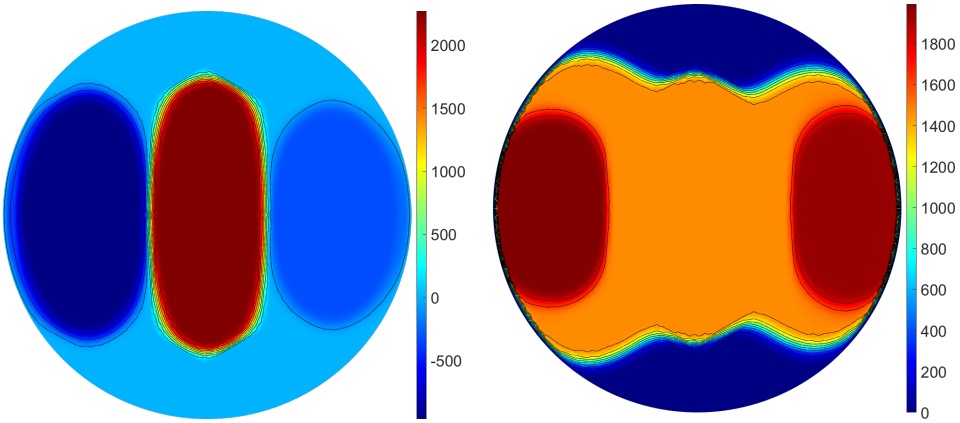

(c) TX. (d) RX.

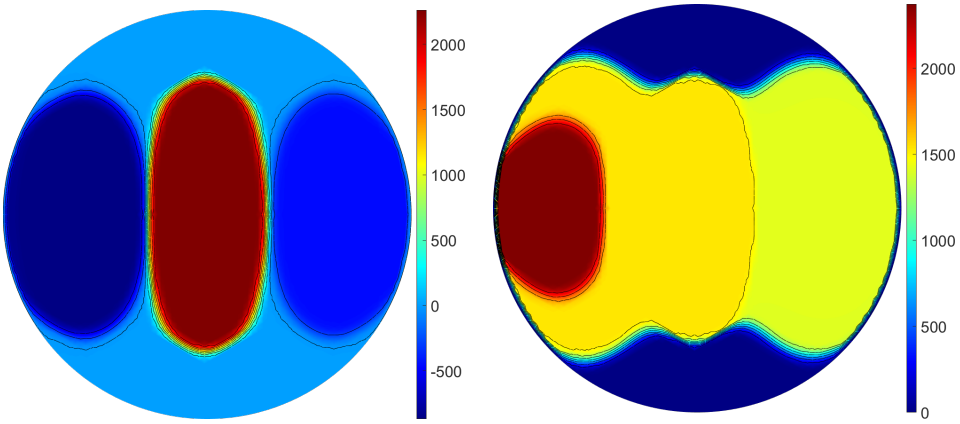

(e) TX. (f) RX.

Figure 96: The three best coils from cluster 4 of the G25 set.

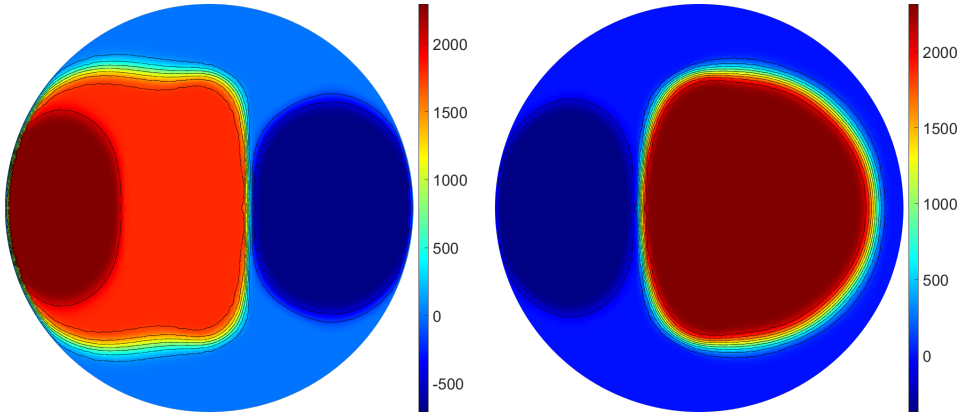

(a) TX. (b) RX.

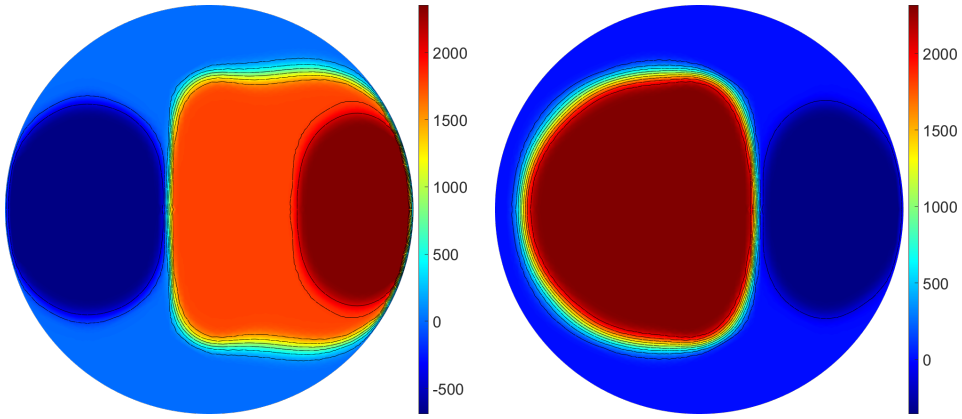

(c) TX. (d) RX.

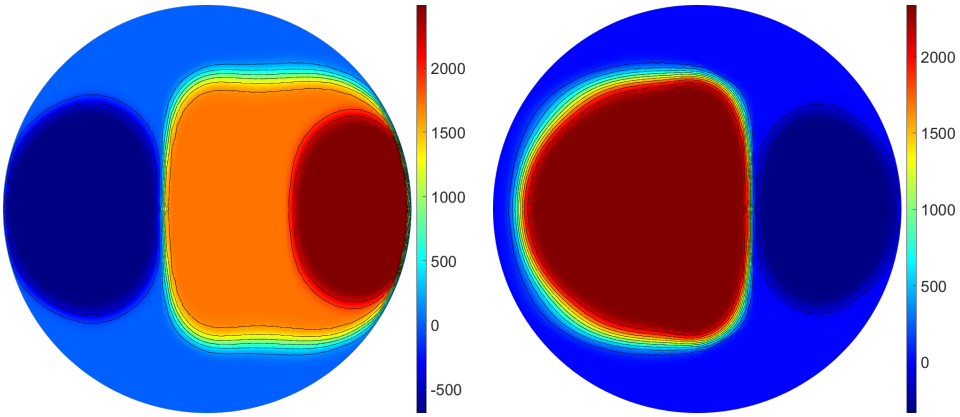

(e) TX. (f) RX.

Figure 97: The three best coils from cluster 5 of the G25 set.

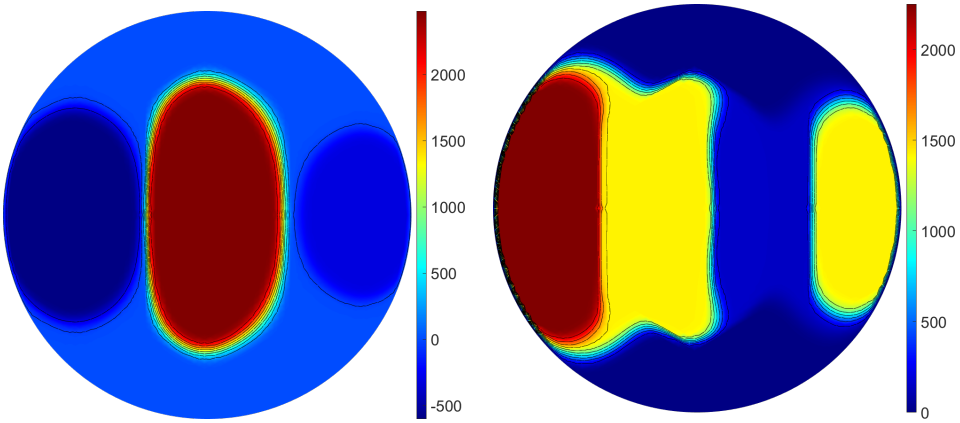

(a) TX. (b) RX.

Figure 98: The only coil solution from cluster 6 of the G25 set.

9.4 Best Results from Each Optimization Set

The following three sections are analyses of some of the characteristics of the best coils resulting from each of the eight different optimization sets.

9.4.1 Best Stream Functions from Each Set

The stream functions of the best answers from the grid and line target sensitivity optimization sets are shown in Figures 99 and 100, respectively.

Within the grid target sensitivity analysis, the solutions are all broadly similar except for the set with unconstrained soil response. The G100 set without a soil constraint is a concentric coil pair with a small balancing loop off to the side to minimize the coupling between the transmit and receive coils. It is interesting that the receive coil from this set has not had its turns pushed to the edge where they would provide maximum depth performance. Rather, the turns do not take up the entire diameter of the coil, similar to the concentric answers of Chapter 6. The other four coil pairs are broadly similar to double-D coils, with a small balancing winding opposite the larger primary winding. The area contained within the primary windings of these coils gradually decreases as the soil response constraint tightens, and eventually the primary windings begin to separate from the edges of the full coil surface, reducing the target sensitivity.

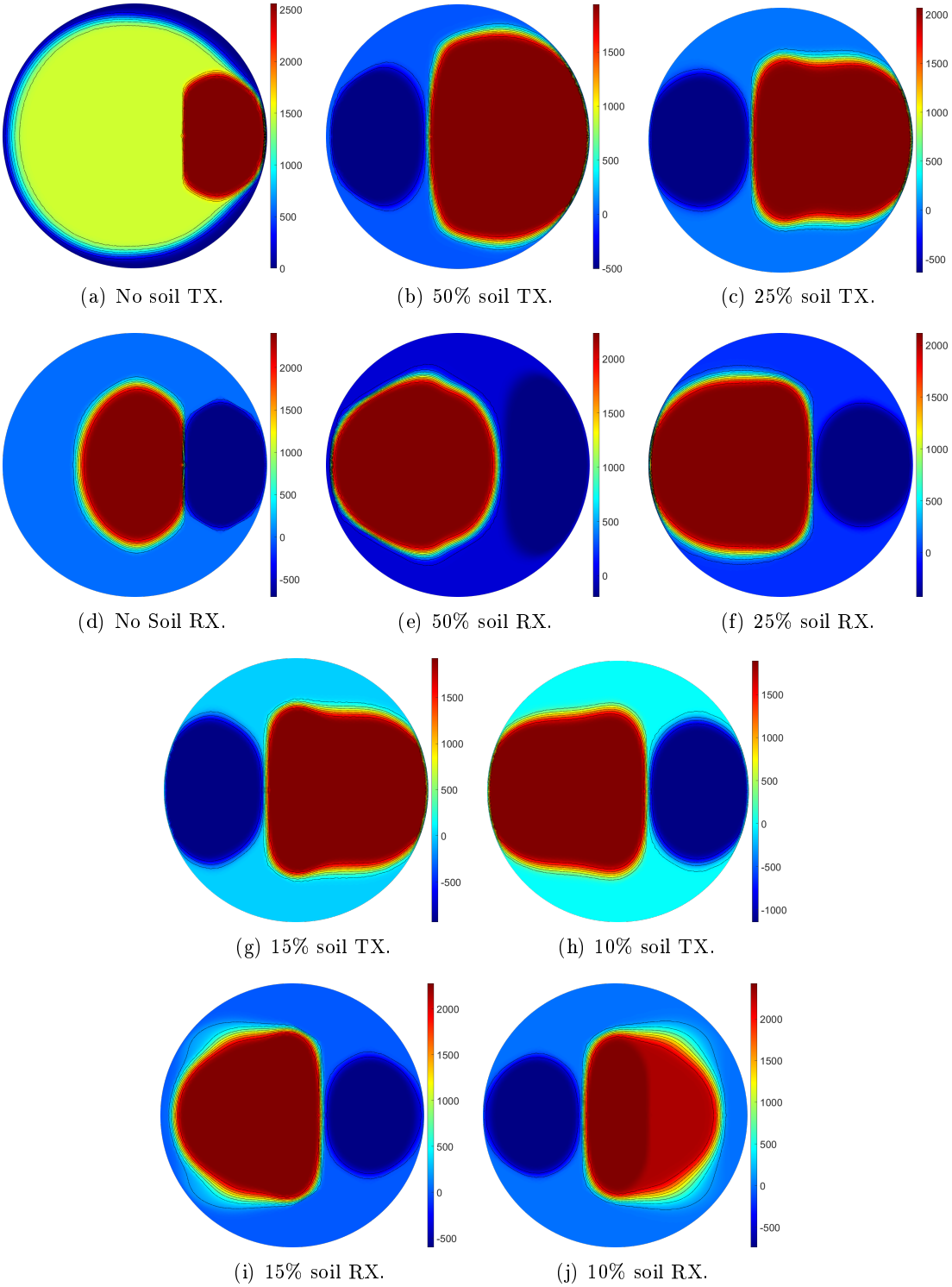

(a) No soil TX. (b) 50% soil TX. (c) 25% soil TX.

(d) No Soil RX. (e) 50% soil RX. (f) 25% soil RX.

(g) 15% soil TX. (h) 10% soil TX.

(i) 15% soil RX. (j) 10% soil RX.

Figure 99: The best coils from each grid target sensitivity optimization set.

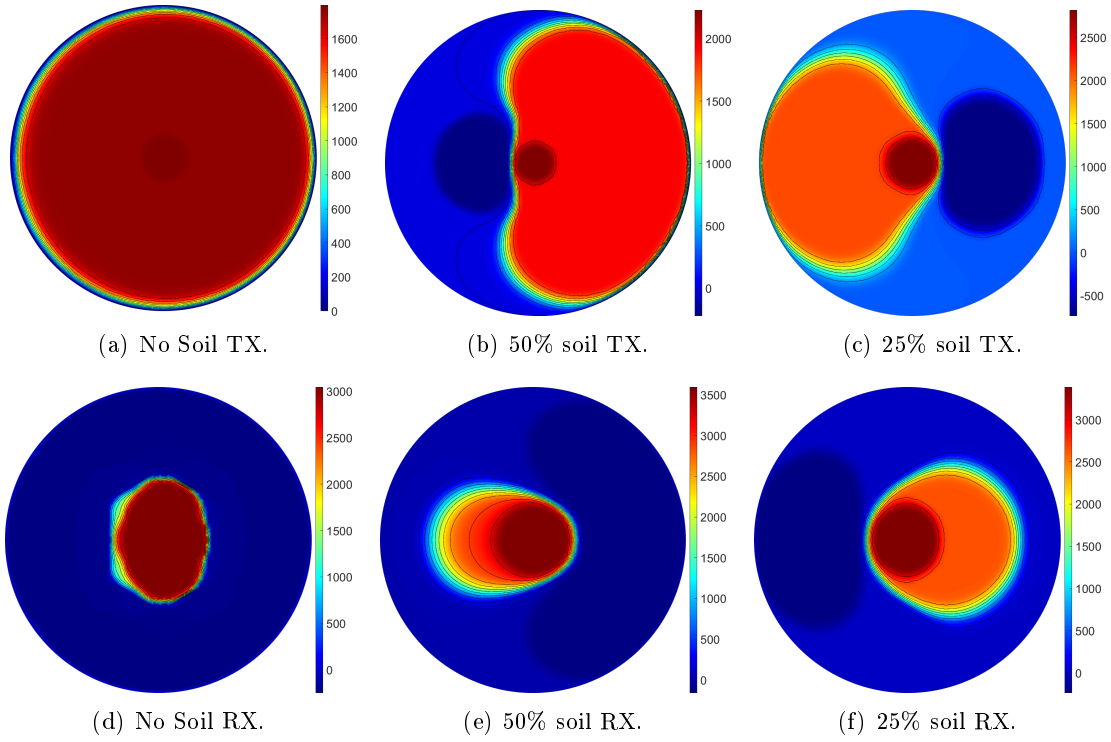

(a) No Soil TX. (b) 50% soil TX. (c) 25% soil TX.

(d) No Soil RX. (e) 50% soil RX. (f) 25% soil RX.

Figure 100: The best coils from each line target sensitivity optimization set.

9.4.2 Soil Sensitivity of the Best Coils from each Set

The soil sensitivity over a range of heights, h_{sr}, and tilts, θ and ϕ, is shown in Figures 101 to 108 for the best coil from every optimization set.

Unlike the tilt calculations from the optimization, these plots were made with tilts in steps of one degree. With a few exceptions, the maximum soil response does not necessarily occur at the maximum tilt as it did with earlier wire coils. The ten degree steps used during optimization still provide a reasonably accurate soil sensitivity calculation, but given enough time and computer memory, more granularity may be desirable for a more thorough optimization.

The marked asymmetry of the coils from the grid sensitivity optimization is noticeable in the soil sensitivity with respect to tilt in Figures 101 to 105. For these coils, the soil sensitivity shows a much greater change with respect to tilt in ϕ than it does to tilt in θ, as would be expected from a coil that approximates a double-D.

The soil sensitivity of the coils from the line sensitivity optimization demonstrates a much more balanced change with respect to ϕ and θ in Figures 106 to 108, as would be expected from coils that are much more rotationally symmetric than those from the grid optimizations.

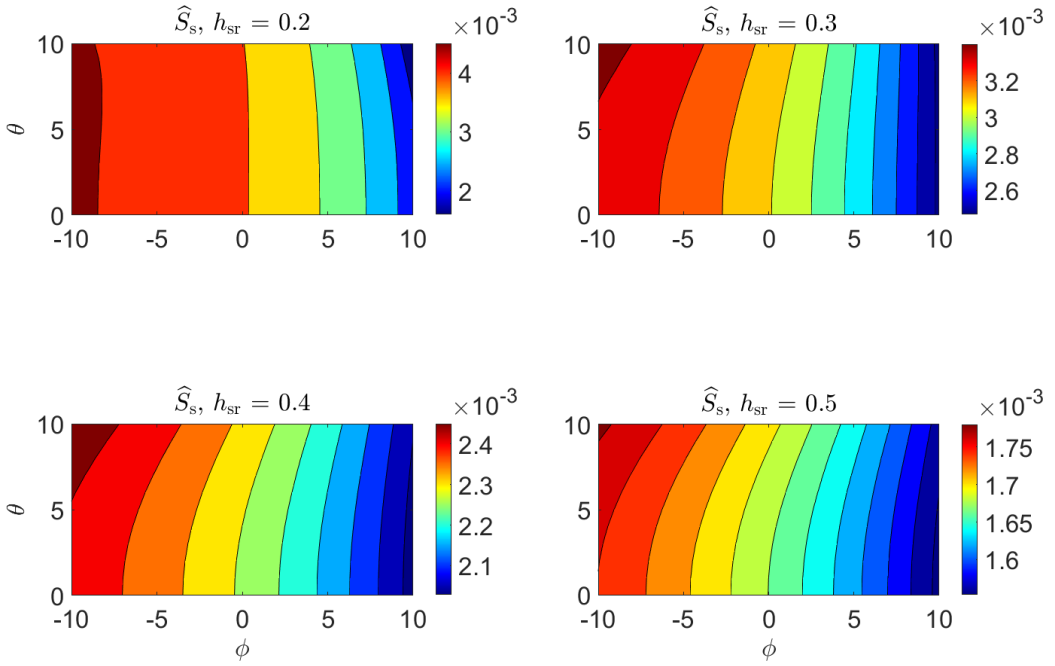

Figure 101: The normalized soil sensitivity for the best coil from the G100 set plotted over a range of heights above and tilts reltaive to the soil.

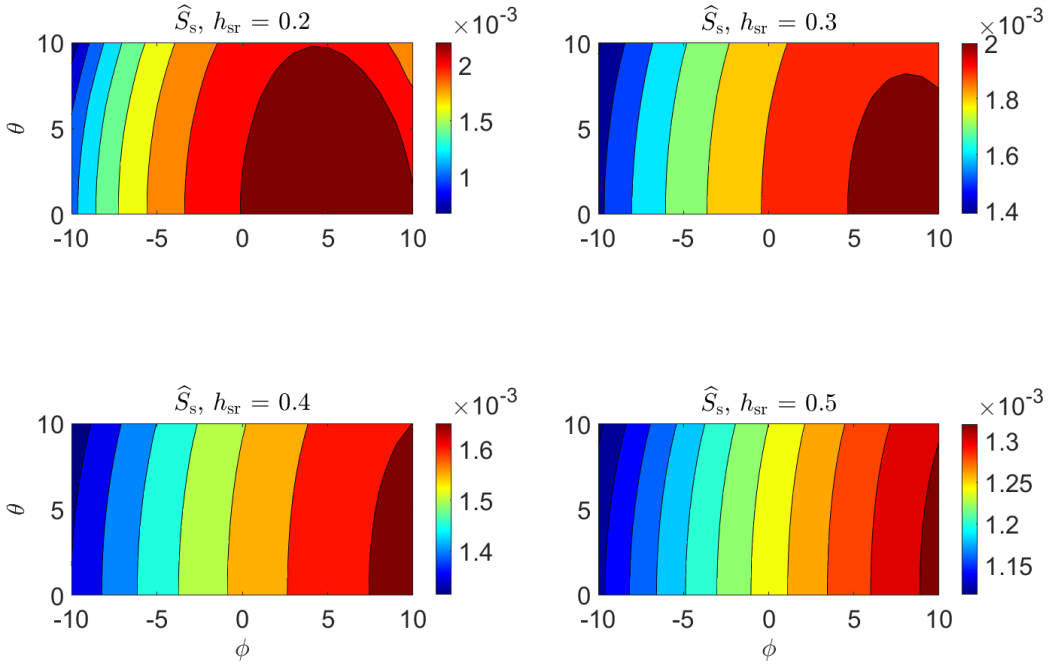

Figure 102: The normalized soil sensitivity for the best coil from the G50 set plotted over a range of heights above and tilts relative to the soil.

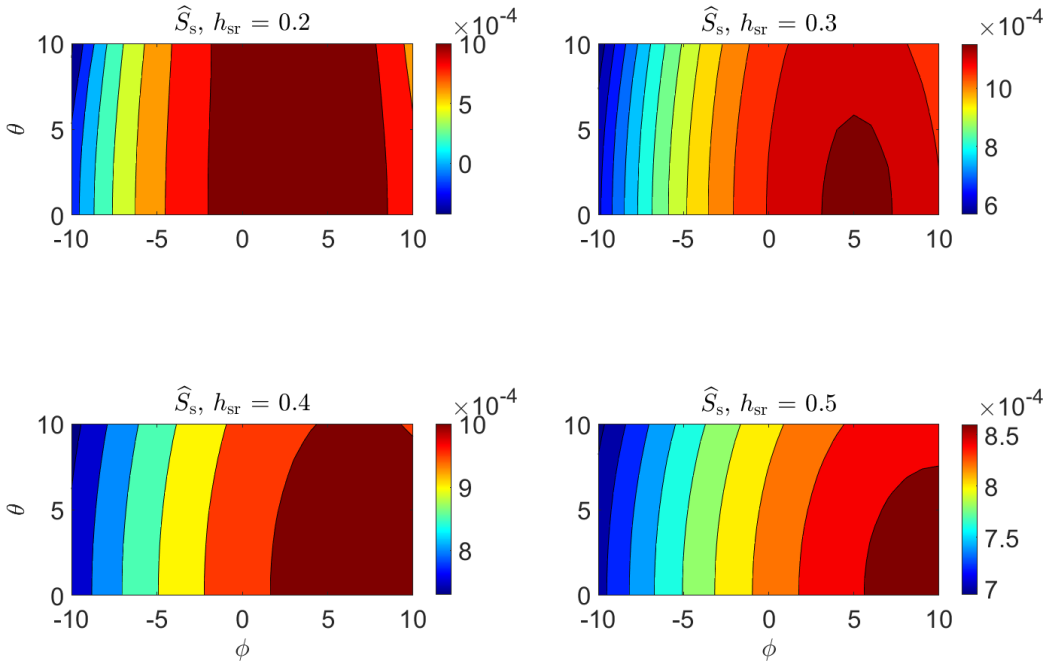

Figure 103: The normalized soil sensitivity for the best coil from the G25 set plotted over a range of heights above and tilts relative to the soil.

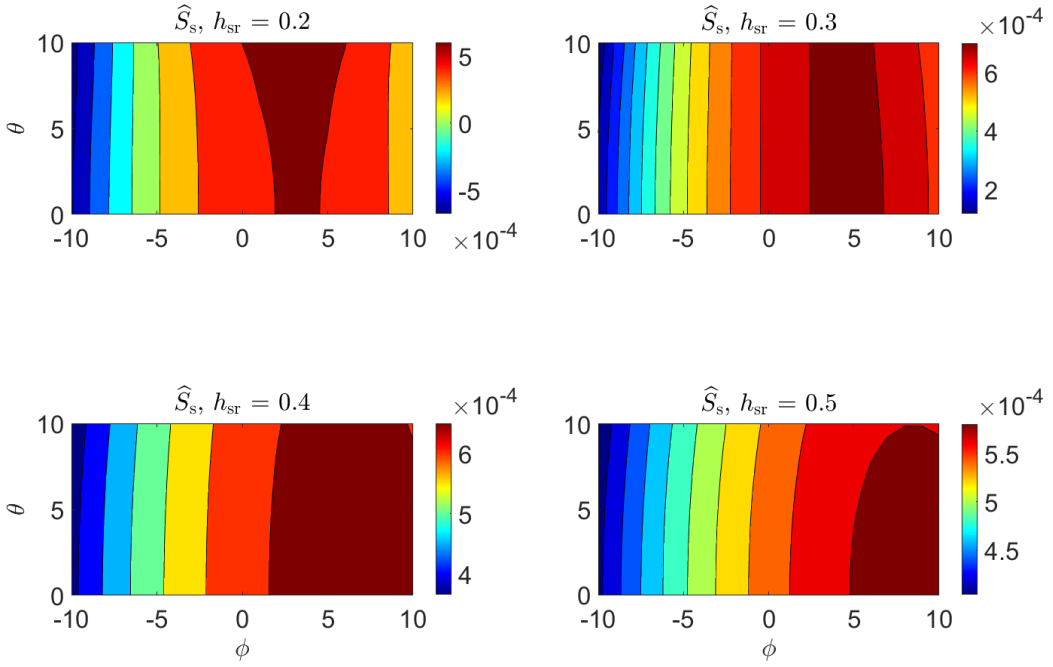

Figure 104: The normalized soil sensitivity for the best coil from the G15 set plotted over a range of heights above and tilts relative to the soil.

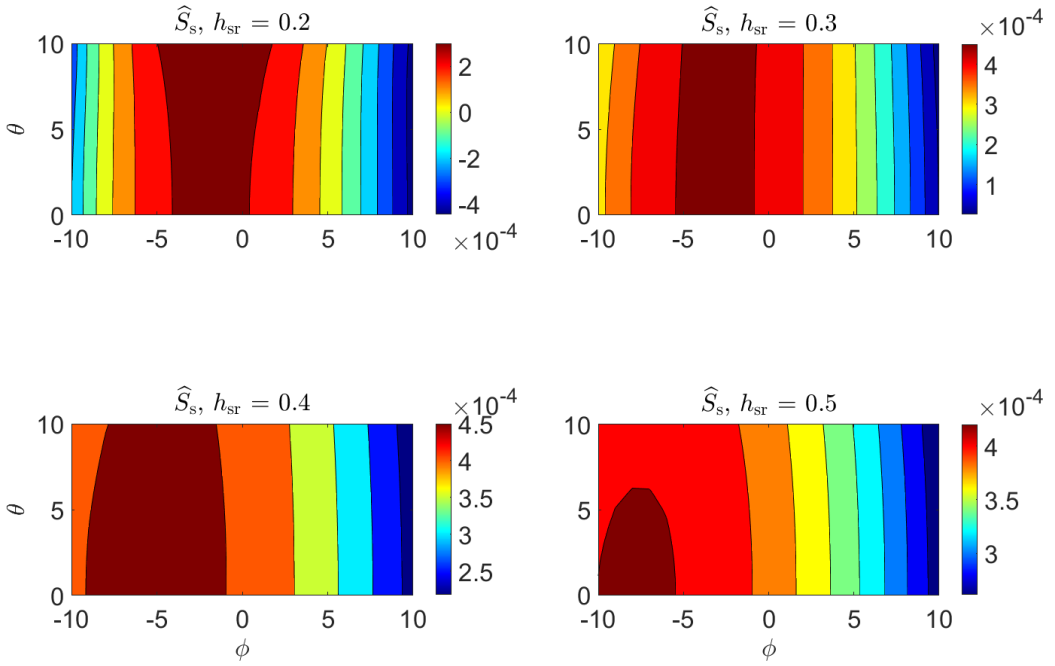

Figure 105: The normalized soil sensitivity for the best coil from the G10 set plotted over a range of heights above and tilts relative to the soil.

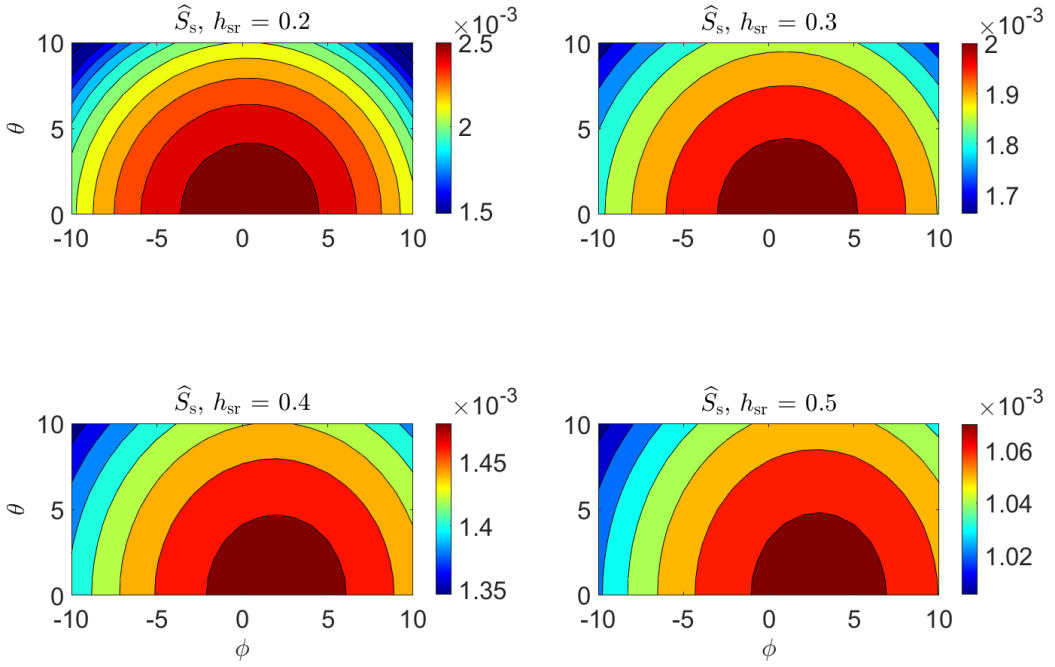

Figure 106: The normalized soil sensitivity for the best coil from the L100 set plotted over a range of heights above and tilts relative to the soil.

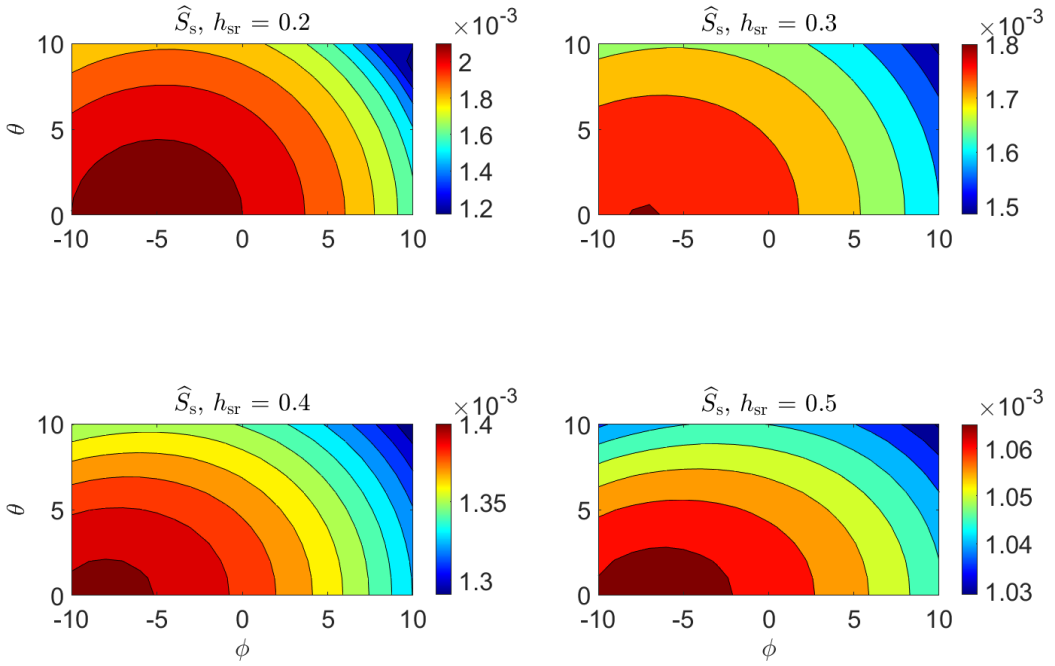

Figure 107: The normalized soil sensitivity for the best coil from the L50 set plotted over a range of heights above and tilts relative to the soil.

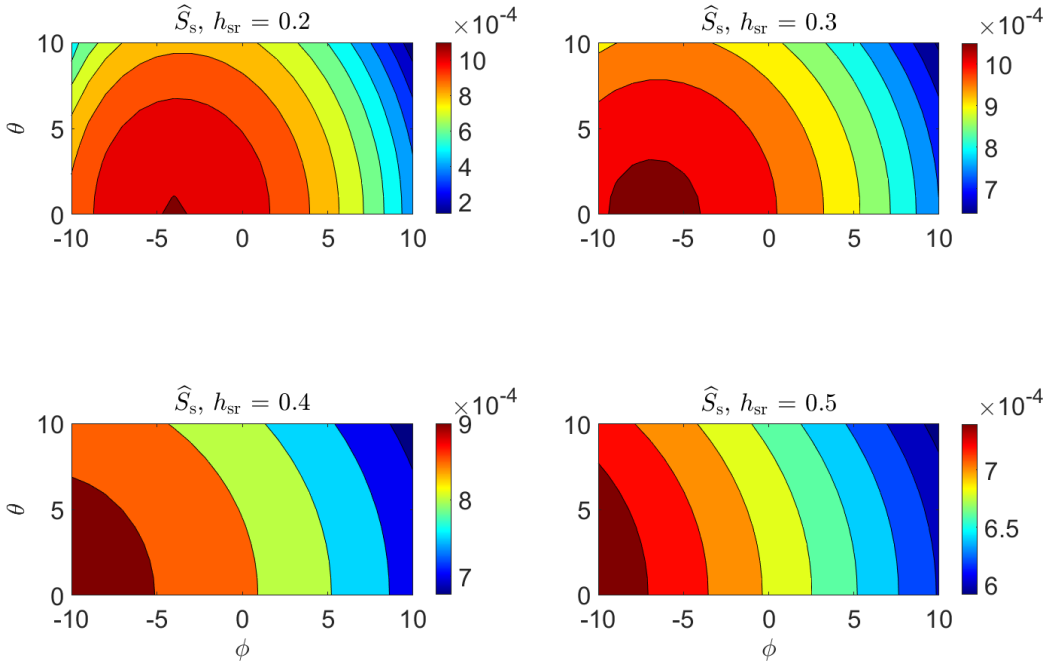

Figure 108: The normalized soil sensitivity for the best coil from the L25 set plotted over a range of heights above and tilts relative to the soil.

9.4.3 Target Sensitivity of the Best Coils from each Set

Plots of various cuts of the target sensitivity for the best coil from each optimization set are shown in Figures 109 to 123 for the grid target sensitivity calculations and in Figures 124 to 132 for the line target sensitivity calculations. While at points close to the coils' surfaces, the field can be quite variable, as distance from the coil face increases, all the coils begin to look like dipoles, as would be expected.

The patterns are, of course, consistent with the coil windings, but it is interesting to note the sensitivity pattern characteristics of the various coils. In Figures 109 to 111, the G100 case demonstrates notable asymmetry on the right half of the coil where the optimization placed the balancing turns. While its overall target sensitivity is quite good, the asymmetry in the sensitivity could cause minor target localization problems at shallow depths.

In contrast to the G100 case, the sensitivity patterns of the other four grid target sensitivity optimization sets are much more similar to one another. These patterns, shown in Figures 112 to 123, are also similar to the double-D coil patterns of Chapter 6. Symmetry in the $x-$ and $y-$ axes is good, with a nice peak in the center that is elongated along the $y-$axis, as was intended to happen as a result of the grid used for target sensitivity optimization. Of these four, the G25 coil has the most symmetrical stream functions, and as a result it also has the most symmetrical target sensitivity pattern. These attributes are desirable both from a manufacturing standpoint and from a useability perspective.

The L100 case of Figures 124 to 126 shows good rotational symmetry, as would be expected of a coil that approximates a concentric coil. The L50 and L25 cases of Figures 127 to 129 and 130 to 132 begin to exhibit more lopsided-ness, both in their winding and subsequenty in their senstivity patterns, as the soil sensitivity is constrained and the optimization attempts to meet that constraint.

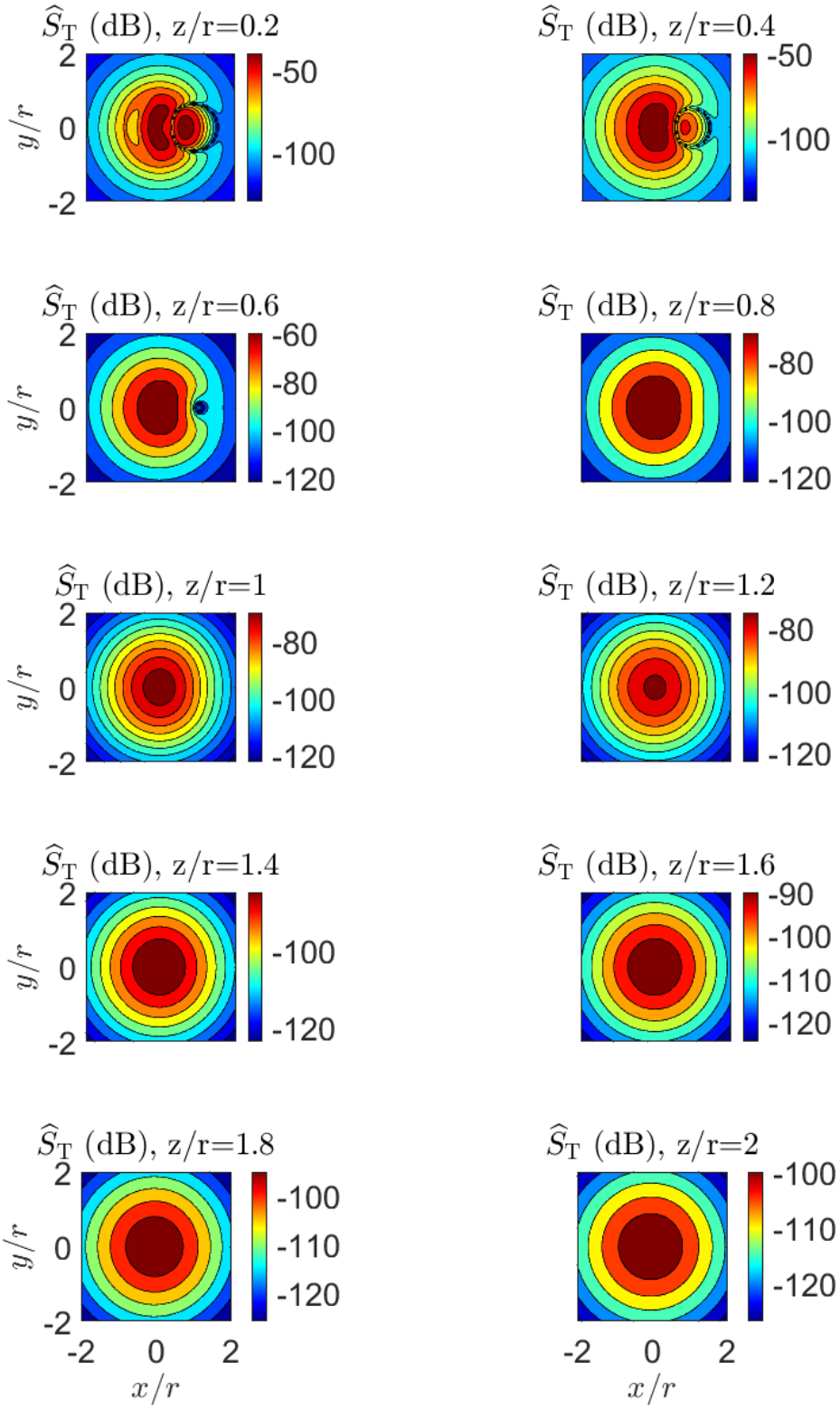

Figure 109: The normalized target sensitivity, $\widehat{S}_{\mathrm{T}}$, of the best answer for the G100 case on $x-y$ cuts at various distances from the coil pair.

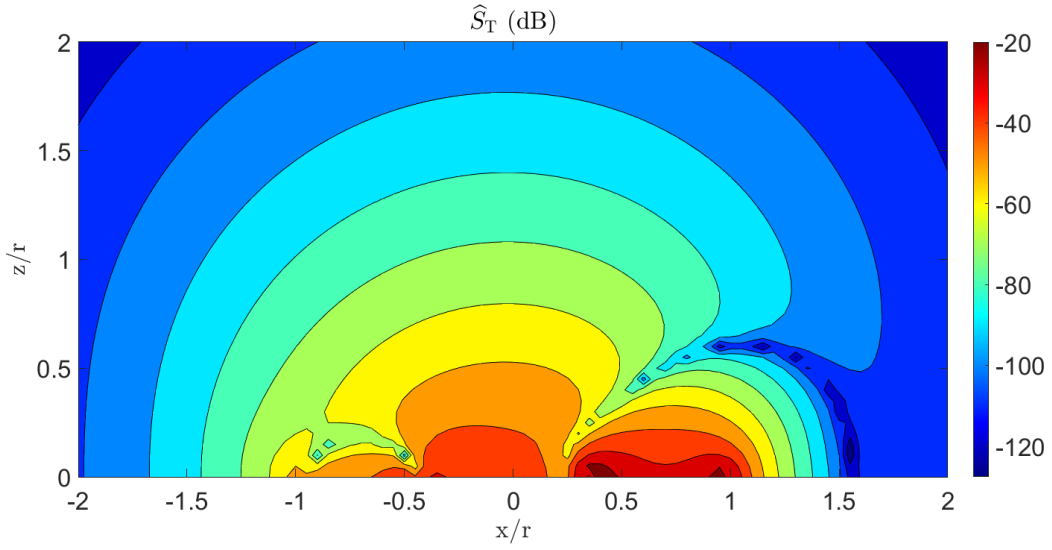

Figure 110: The normalized target sensitivity, $\widehat{S}_{\mathrm{T}}$, of the best answer for the G100 case on the $x-z$ plane.

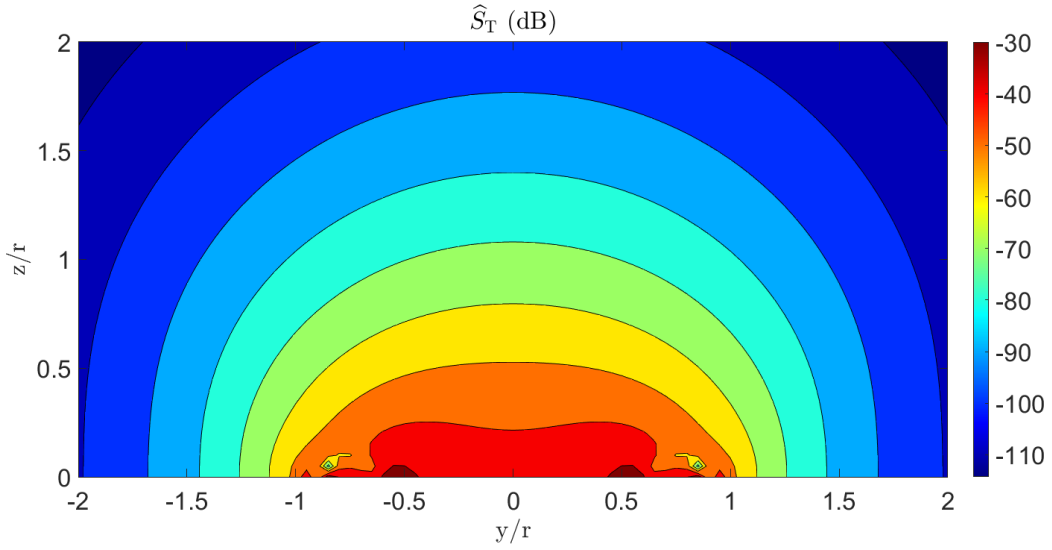

Figure 111: The normalized target sensitivity, $\widehat{S}_{\mathrm{T}}$, of the best answer for the G100 case on the $y-z$ plane.

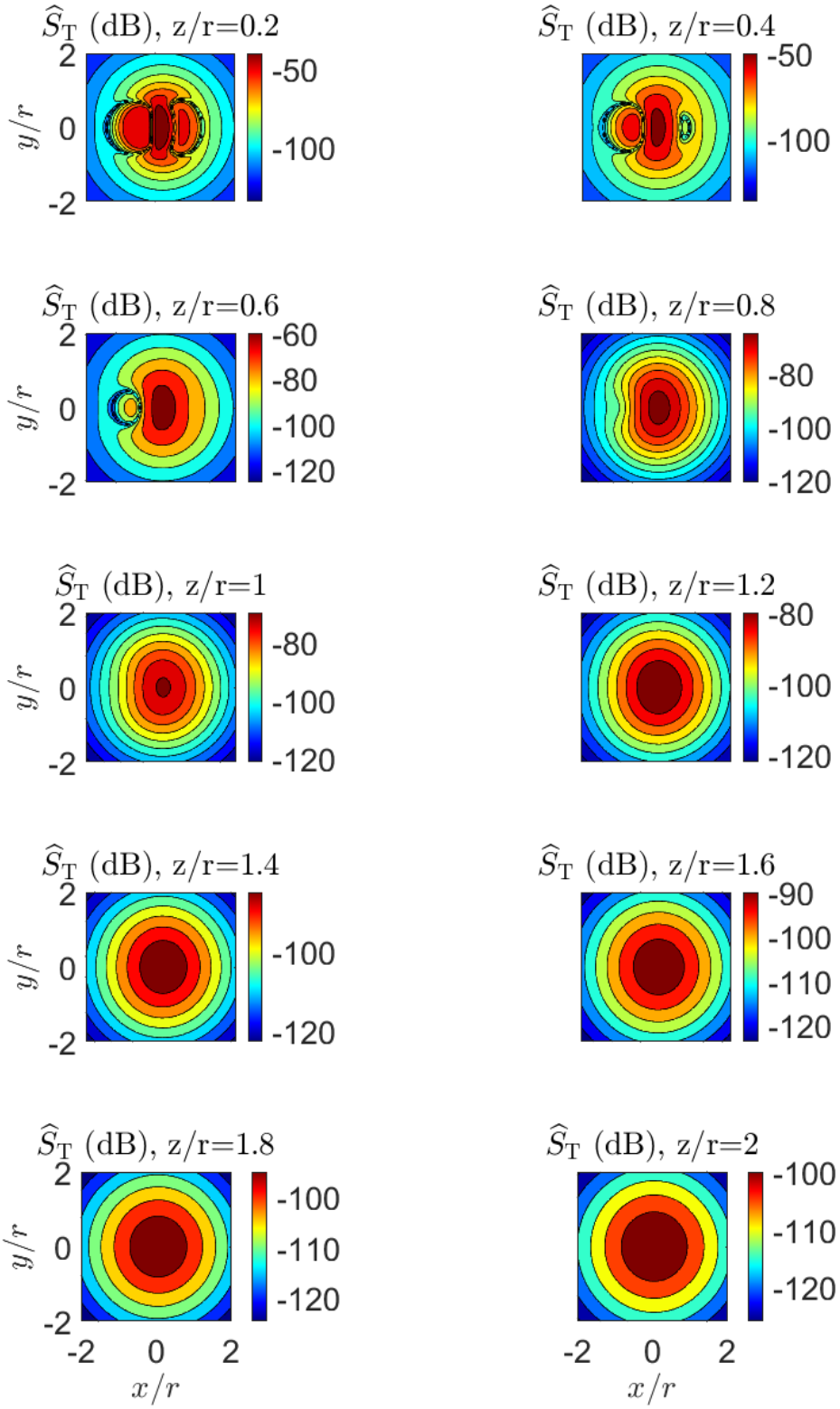

Figure 112: The normalized target sensitivity, $\widehat{S}_{\mathrm{T}}$, of the best answer for the G50 case on $x-y$ cuts at various distances from the coil pair.

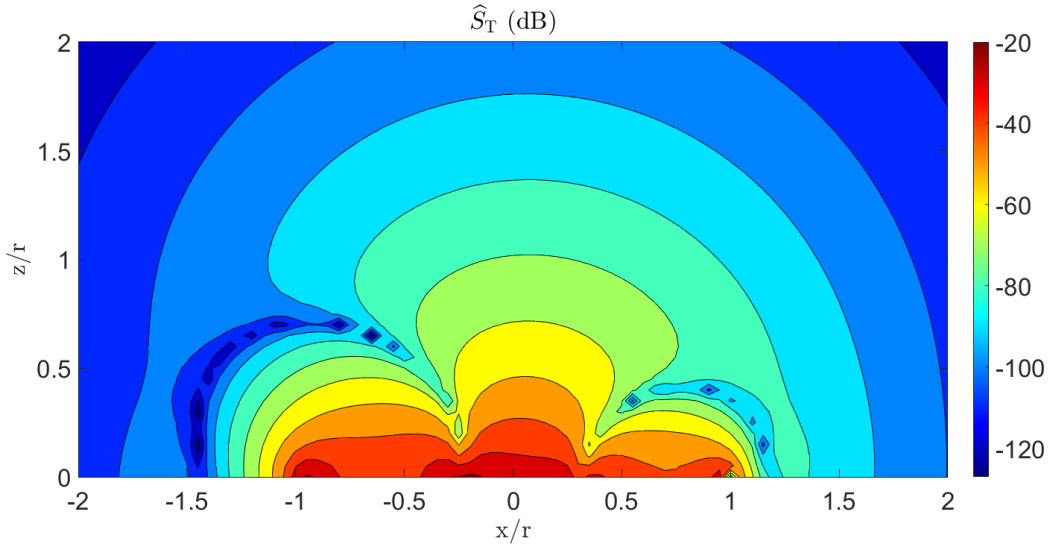

Figure 113: The normalized target sensitivity, $\widehat{S}_{\mathrm{T}}$, of the best answer for the G50 case on the $x-z$ plane.

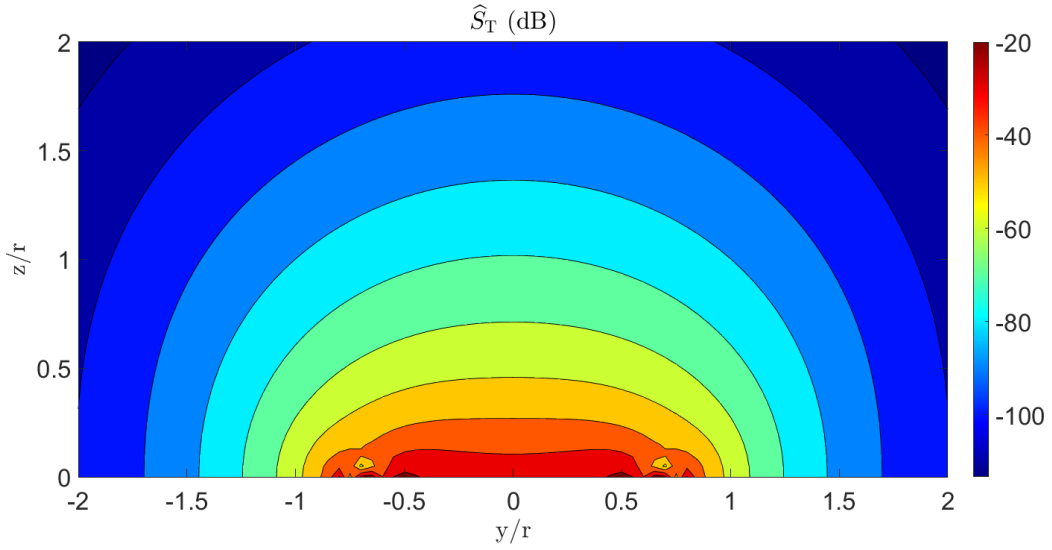

Figure 114: The normalized target sensitivity, $\widehat{S}_{\mathrm{T}}$, of the best answer for the G50 case on the $y-z$ plane.

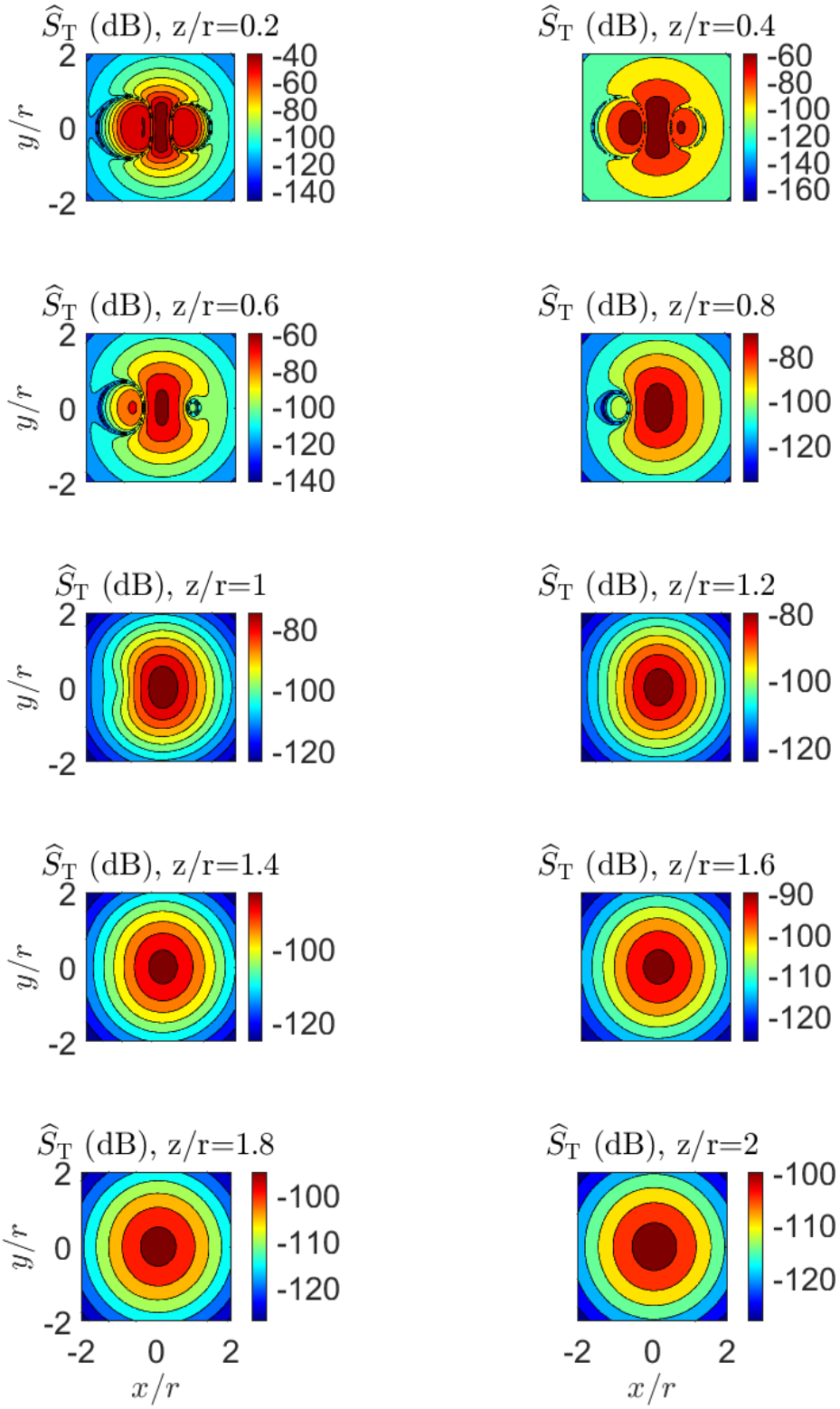

Figure 115: The normalized target sensitivity, $\widehat{S}_{\mathrm{T}}$, of the best answer for the G25 case on $x-y$ cuts at various distances from the coil pair.

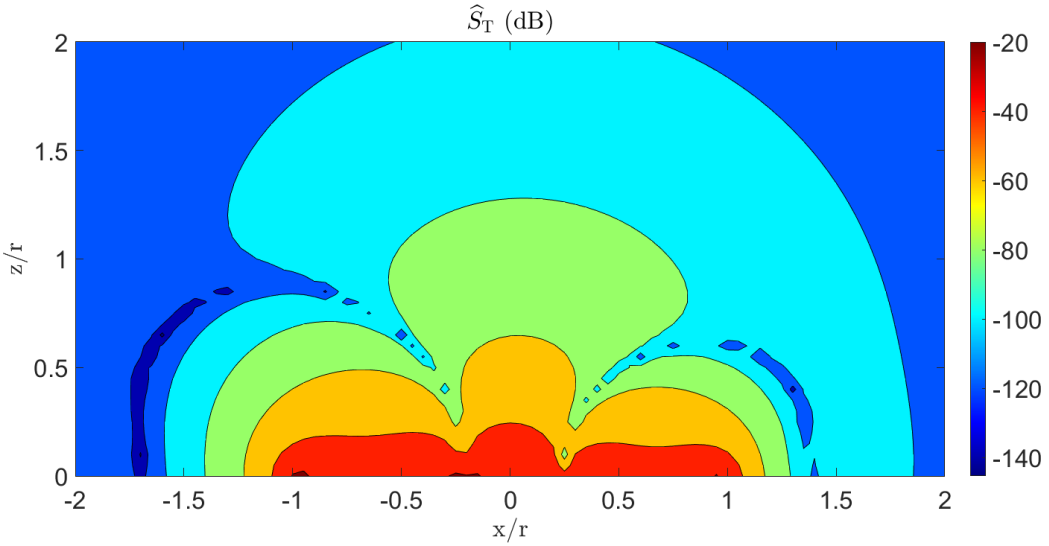

Figure 116: The normalized target sensitivity, $\widehat{S}_{\mathrm{T}}$, of the best answer for the G25 case on the $x-z$ plane.

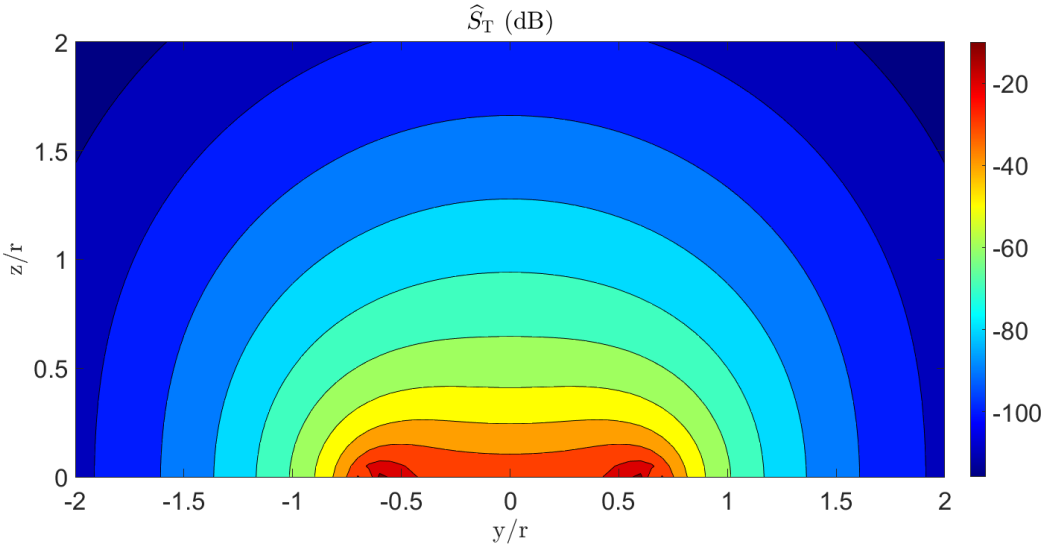

Figure 117: The normalized target sensitivity, $\widehat{S}_{\mathrm{T}}$, of the best answer for the G25 case on the $y-z$ plane.

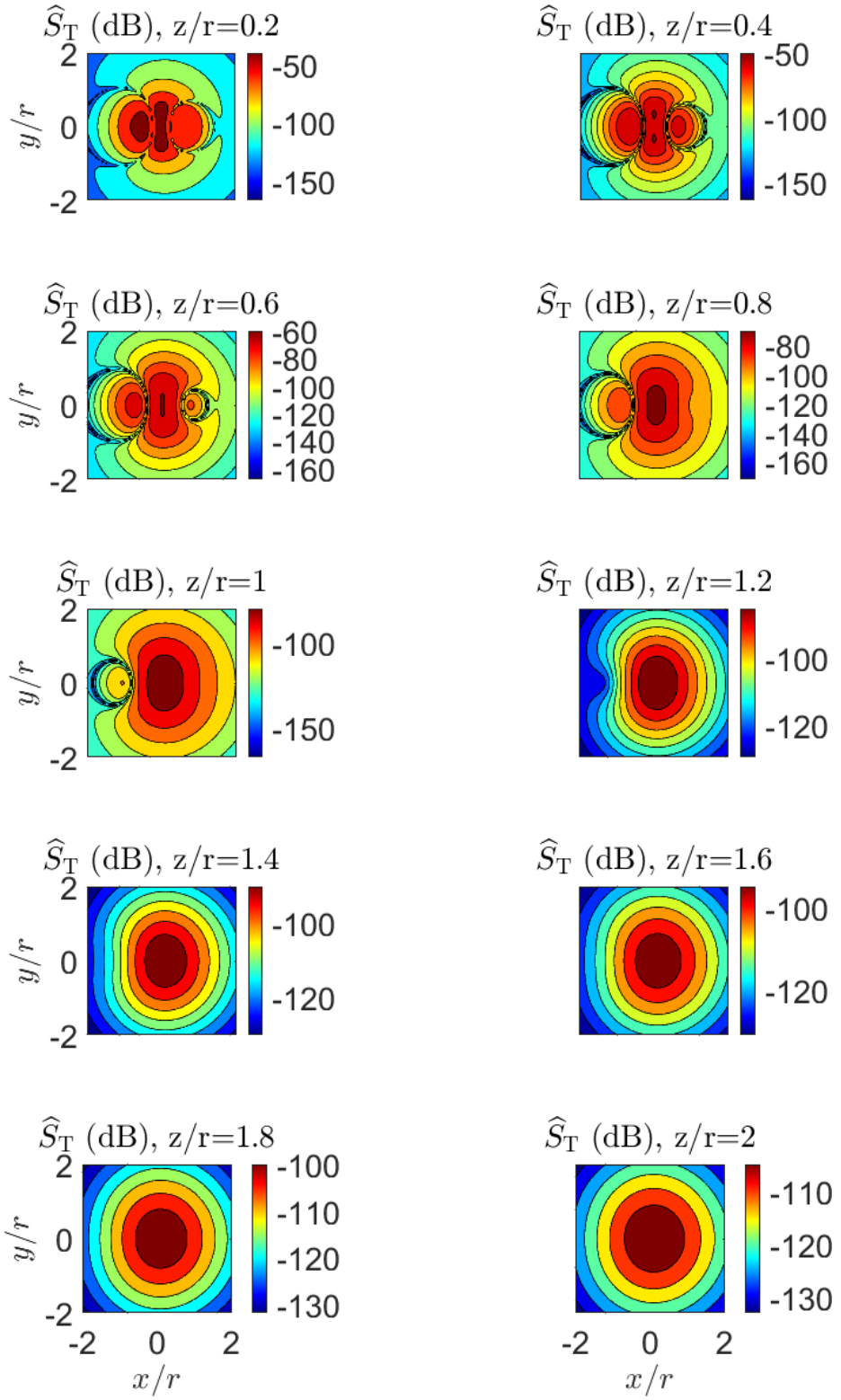

Figure 118: The normalized target sensitivity, $\widehat{S}_{\mathrm{T}}$, of the best answer for the G15 case on $x-y$ cuts at various distances from the coil pair.

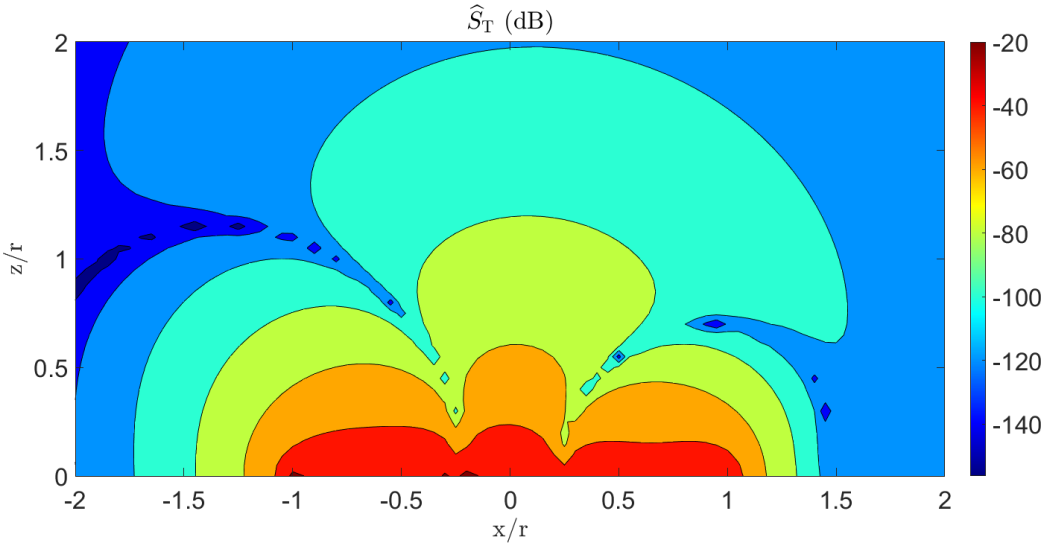

Figure 119: The normalized target sensitivity, $\widehat{S}_{\mathrm{T}}$, of the best answer for the G15 case on the $x-z$ plane.

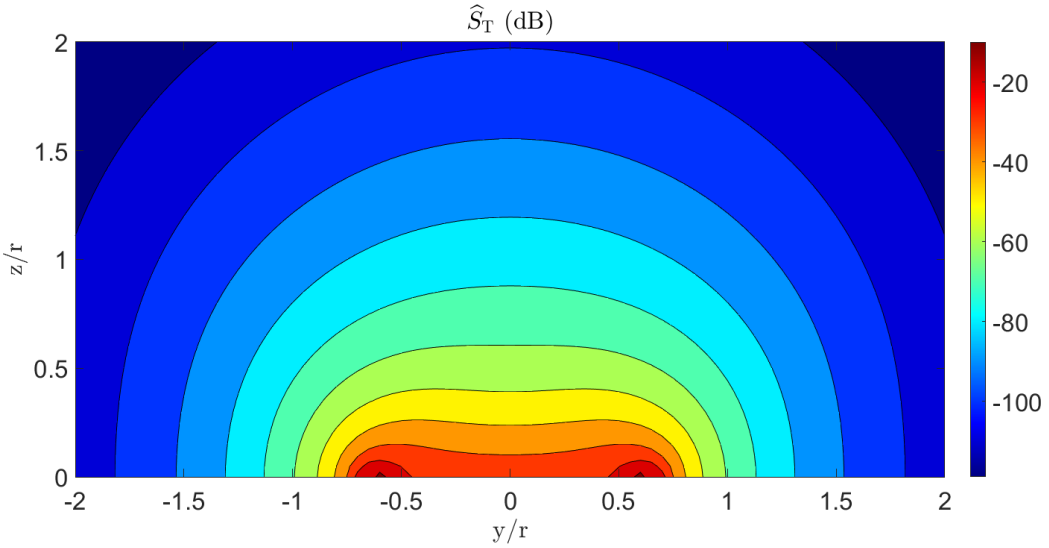

Figure 120: The normalized target sensitivity, $\widehat{S}_{\mathrm{T}}$, of the best answer for the G15 case on the $y-z$ plane.

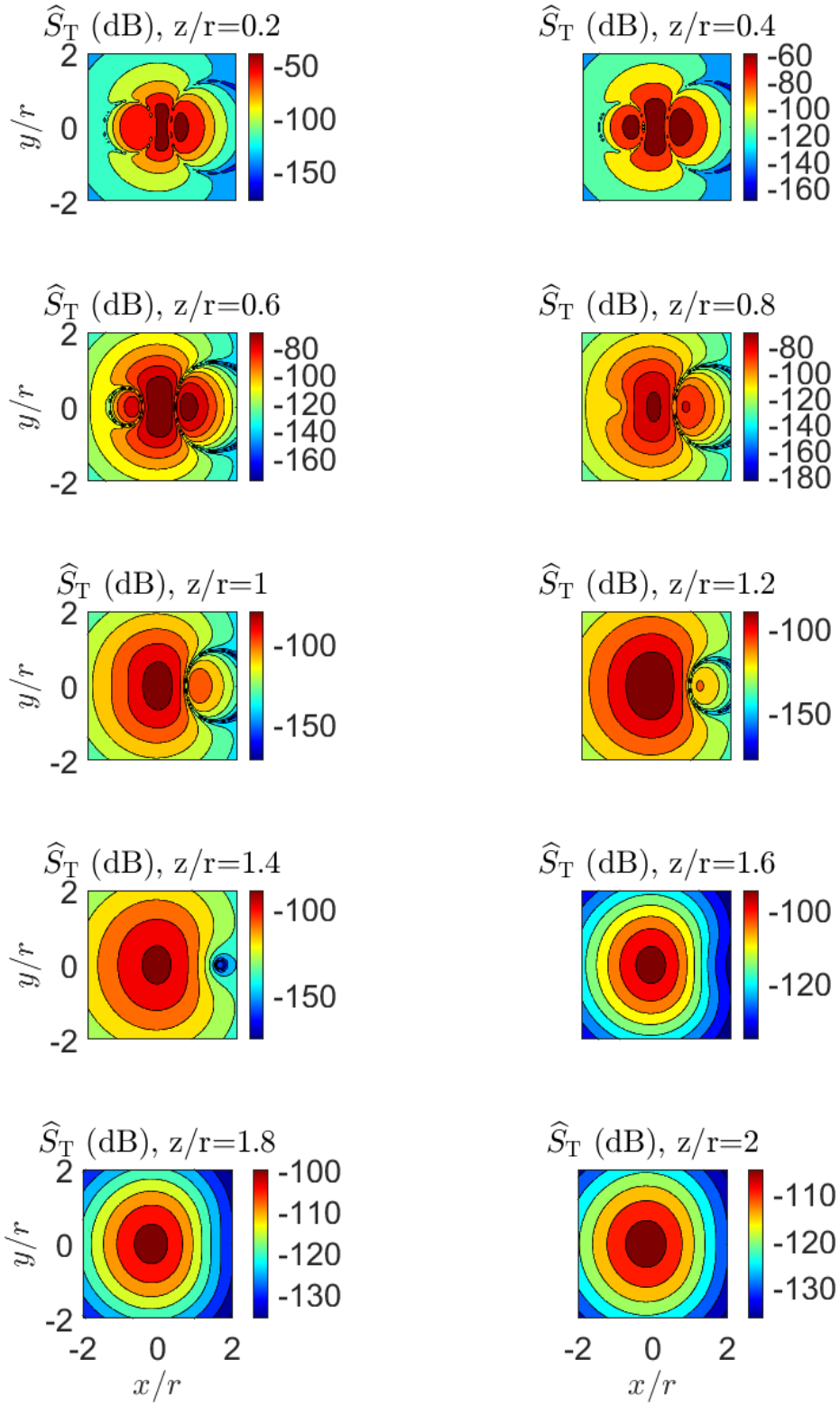

Figure 121: The normalized target sensitivity, $\widehat{S}_{\mathrm{T}}$, of the best answer for the G10 case on $x-y$ cuts at various distances from the coil pair.

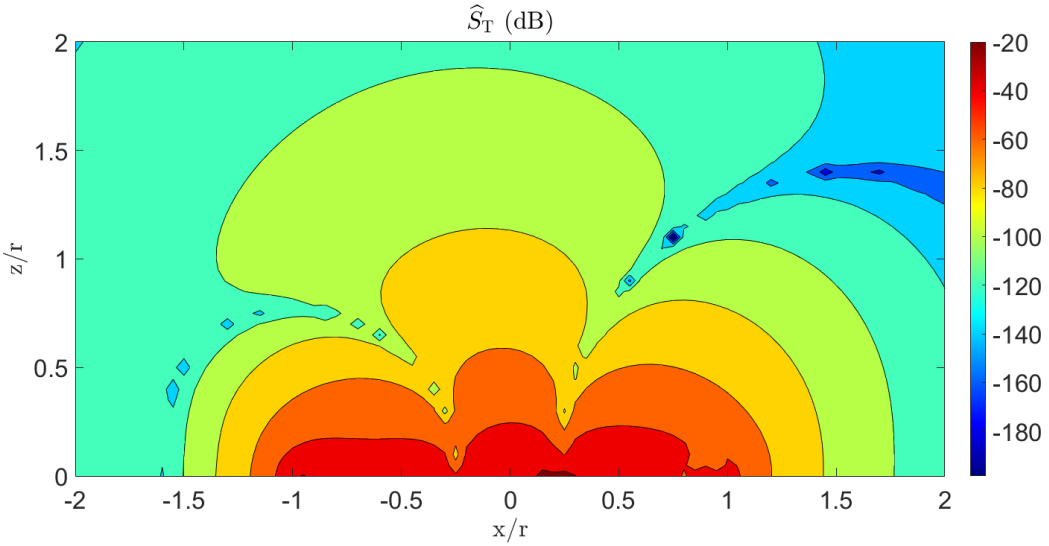

Figure 122: The normalized target sensitivity, $\widehat{S}_{\mathrm{T}}$, of the best answer for the G10 case on the $x-z$ plane.

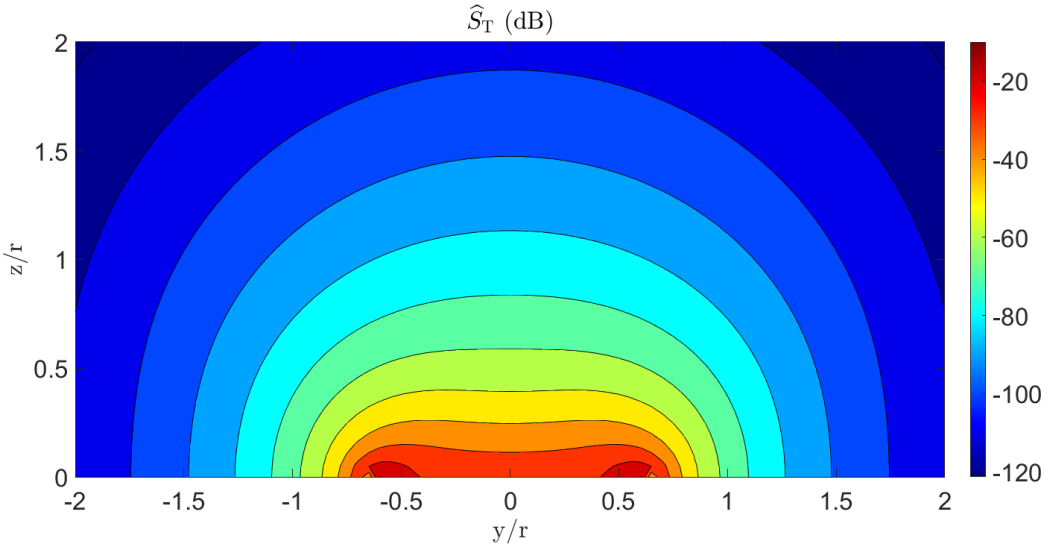

Figure 123: The normalized target sensitivity, $\widehat{S}_{\mathrm{T}}$, of the best answer for the G10 case on the $y-z$ plane.

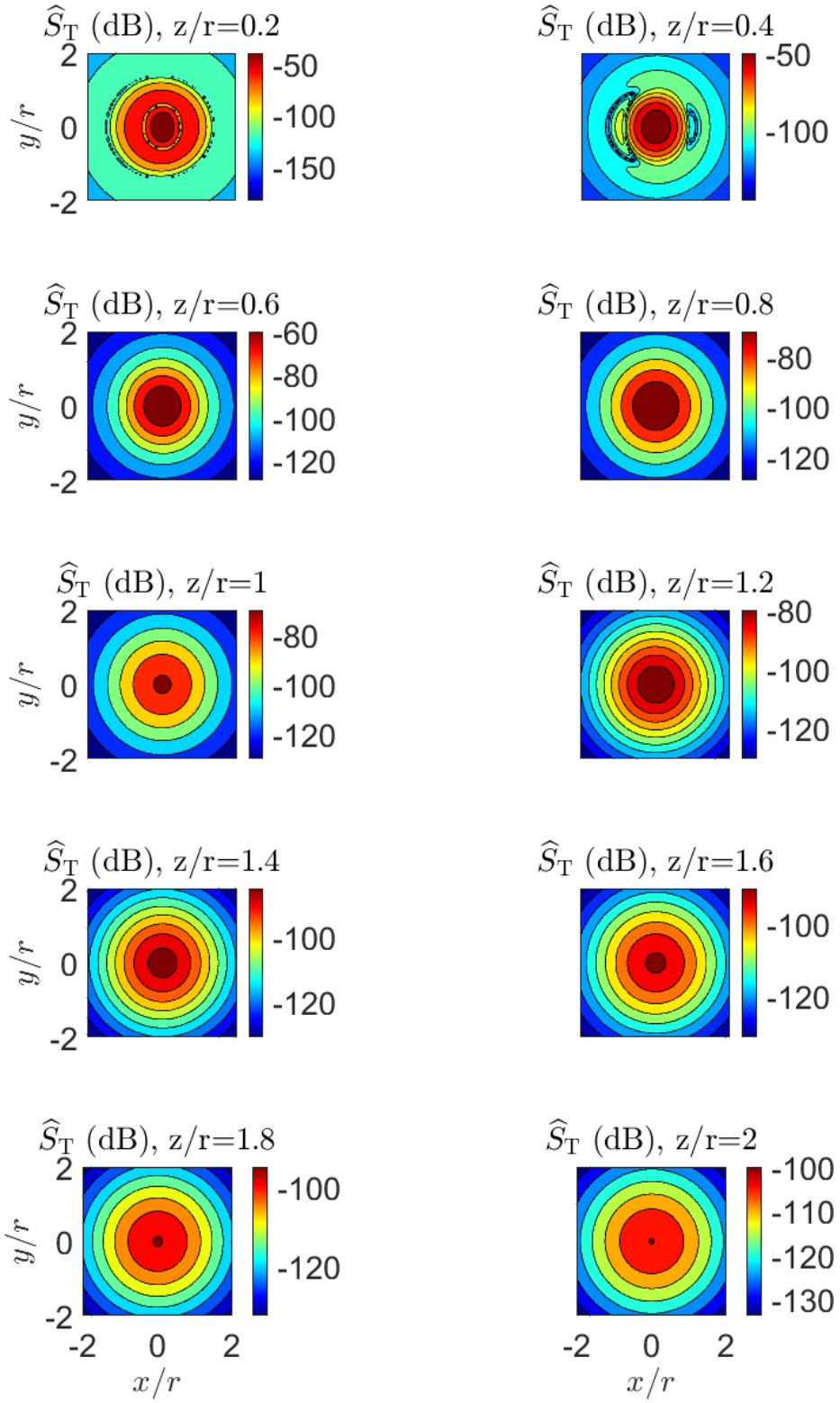

Figure 124: The normalized target sensitivity, $\widehat{S}_{\mathrm{T}}$, of the best answer for the L100 case on $x-y$ cuts at various distances from the coil pair.

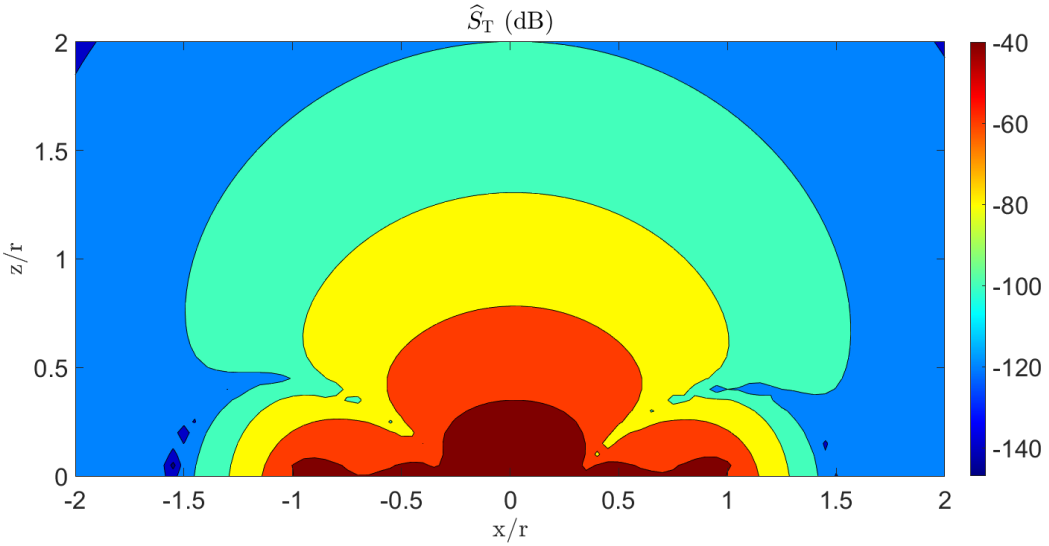

Figure 125: The normalized target sensitivity, $\widehat{S}_{\mathrm{T}}$, of the best answer for the L100 case on the $x-z$ plane.

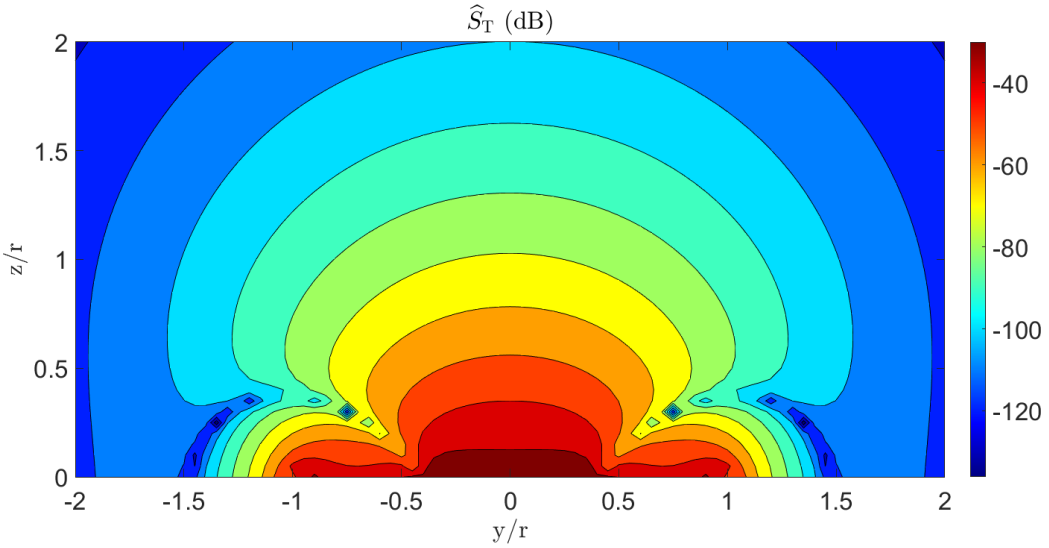

Figure 126: The normalized target sensitivity, $\widehat{S}_{\mathrm{T}}$, of the best answer for the L100 case on the $y-z$ plane.

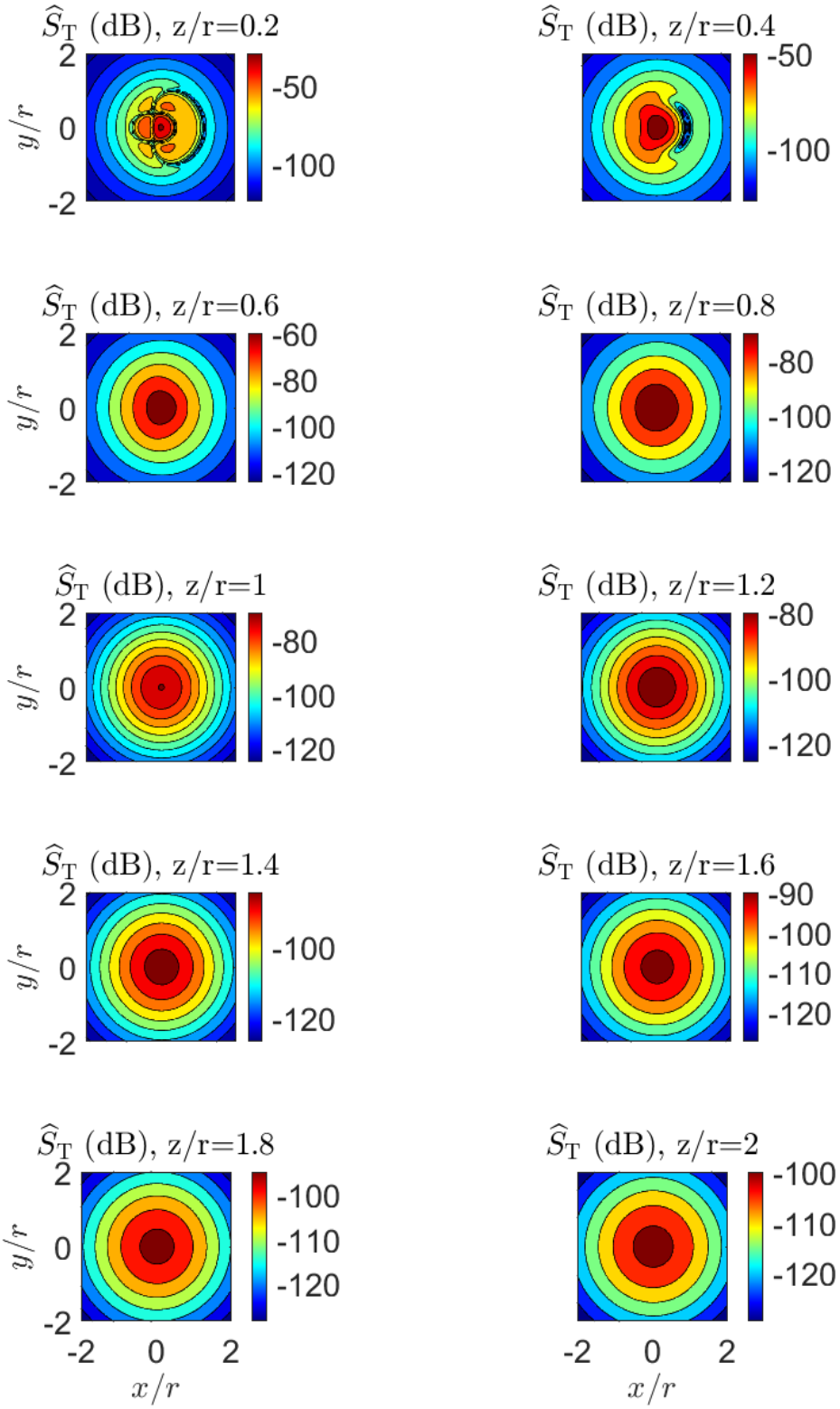

Figure 127: The normalized target sensitivity, $\widehat{S}_{\mathrm{T}}$, of the best answer for the L50 case on $x-y$ cuts at various distances from the coil pair.

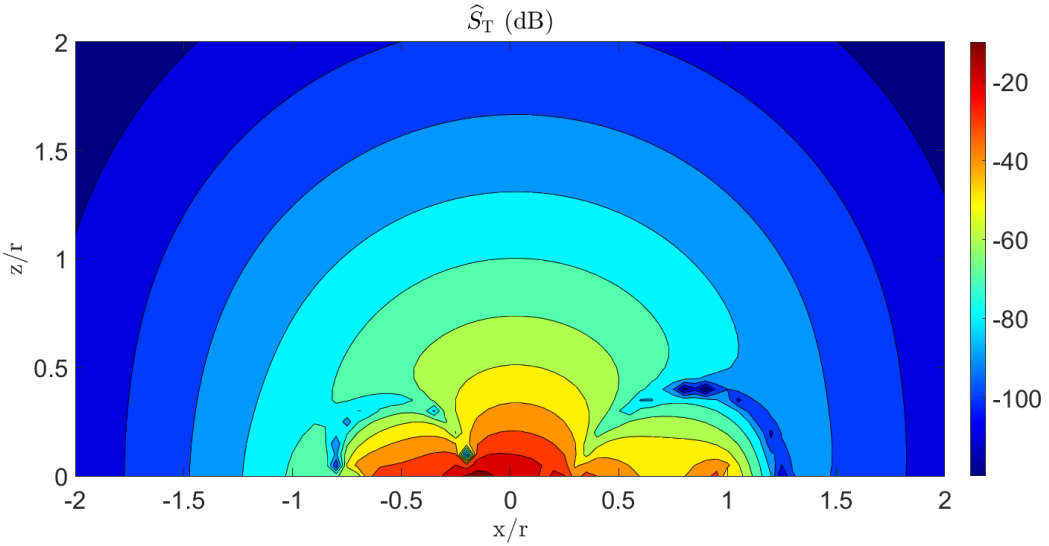

Figure 128: The normalized target sensitivity, $\widehat{S}_{\mathrm{T}}$, of the best answer for the L50 case on the $x-z$ plane.

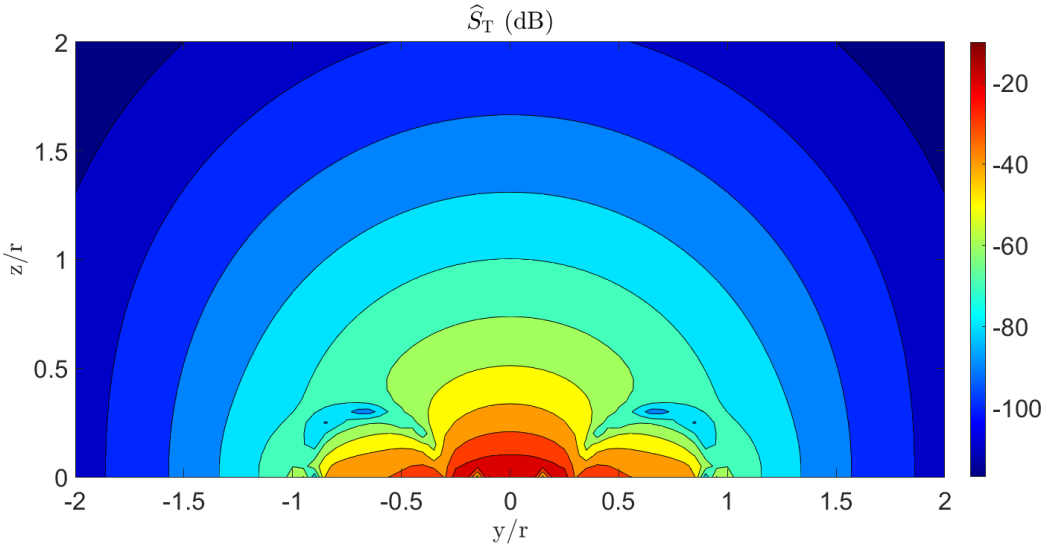

Figure 129: The normalized target sensitivity, $\widehat{S}_{\mathrm{T}}$, of the best answer for the L50 case on the $y-z$ plane.

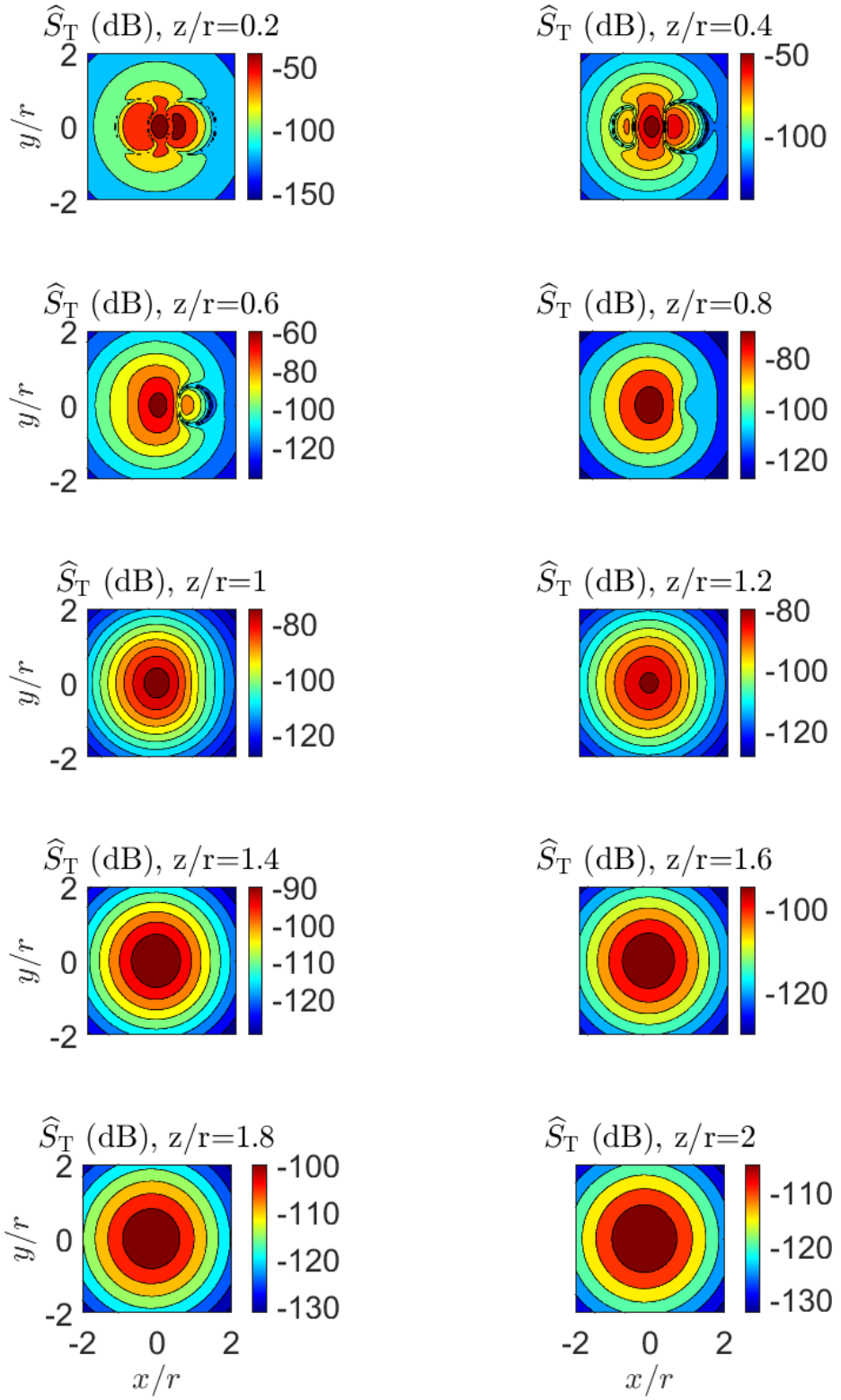

Figure 130: The normalized target sensitivity, $\widehat{S}_{\mathrm{T}}$, of the best answer for the L25 case on $x-y$ cuts at various distances from the coil pair.

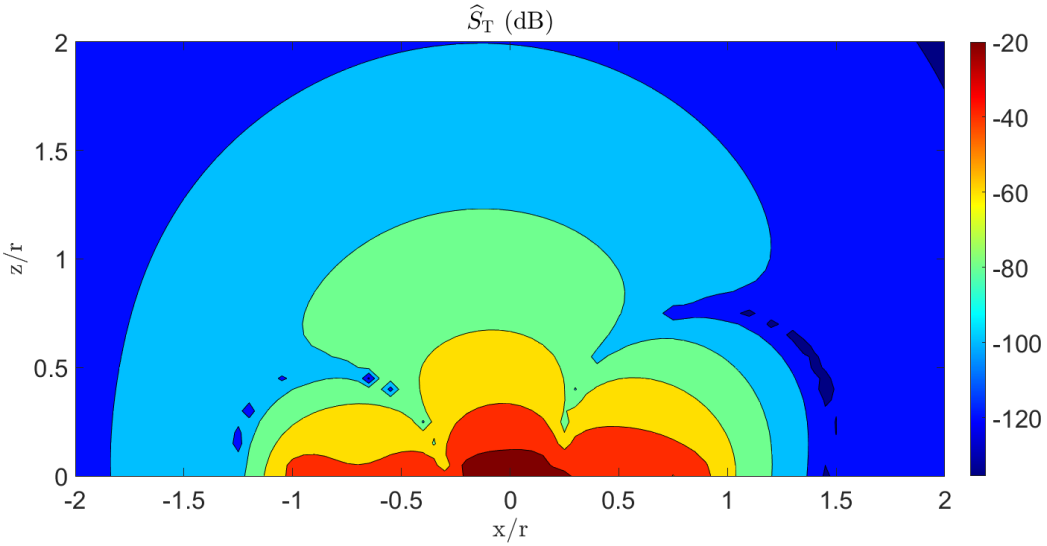

Figure 131: The normalized target sensitivity, $\widehat{S}_{\mathrm{T}}$, of the best answer for the L25 case on the $x-z$ plane.

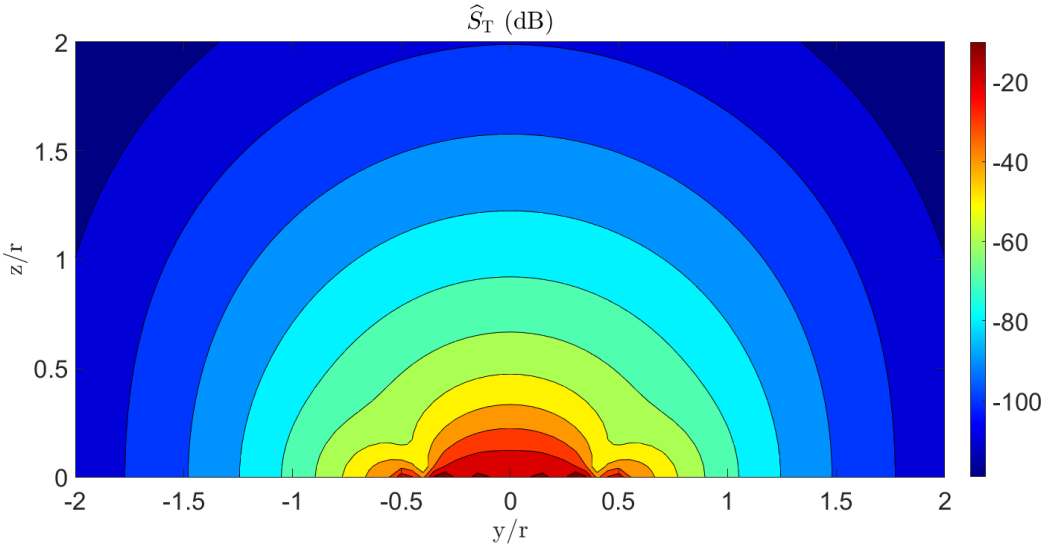

Figure 132: The normalized target sensitivity, $\widehat{S}_{\mathrm{T}}$, of the best answer for the L25 case on the $y-z$ plane.

9.5 Conversion of Stream Functions to Wire Coils

It is not possible to build a coil that exactly replicates a stream function, but the stream functions can be approximated by wire coils. The wires used to form each coil should be a single, continuous current path that closely approximates the currents in the stream function. Ideally, the path will be a smooth spiral path; however, it is nontrivial to compute such a path. A simpler but less elegant way to form the path is to use equal level contours for the path. This technique uses the the well-known feature of stream functions that the current flows parallel to the contours, and equal current flows between equally spaced level contours. The contours can then be connected in series to from a single coil.[2]

In a practical coil, it is necessary to put the coils in series, but in the computer model, it is only necessary to put the same current on each of the contours. For example, the level curves of the stream function in Figure 133(c) can be converted to wires like those in Figure 133(b).

The best coils from the G50 and G25 sets were converted to concentric wire coils as a proof of concept. They can be analyzed using the same codes that were used for the wire coils of Chapters 5 and 6. These codes are based on simple, well-known procedures, such as Biot-Savart and Neumann's formula. As these codes are formulated in a completely different and well-tested manner than the stream function codes, there is reasonable confidence that the stream function optimization is working as intended because the two separate solutions (wire coil and stream functions) match with acceptable accuracy.

The G25 coil is a particularly nice candidate for a wire conversion in that its transmit and receive coils are very symmetric, and it has both good target sensitivity and soil rejection. The G50 coil is not quite as symmetric as the G25 case, but it is also a reasonable solution that could be simply constructed.

[2]The countours can be simply connected in series using the method used for the concentric coil in Figure 44(a). The unconnected turns can also be reformed to create a spiral as was done in Chapter 4, though a spiral conversion from a stream function is non-trivial.

9.5.1 Wire Conversion Process

A modified version of the Matlab function `tricontour()` was used to determine the level curves of the stream function [21]. It was modified to place a contour in the center of a strip of current, such as in Appendix A, where each level curve is equally spaced in the value of the stream function. The stream functions and the resulting contours are shown in Figures 133(a) to 133(f) and Figures 134(a) to 134(d).

9.5.2 Wire Coil Smoothing

Unfortunately, these contours are not particularly smooth as a result of the discretization of the stream function across the triangular mesh of the discs, as can be seen in Figures 133(a) and 133(e), which are the raw output of `tricontour()`. More triangles could be added to the mesh used for the stream function to smooth the level curves, but this becomes computationally expensive very quickly. Instead, the contours can first be re-sampled to more evenly space the points on the curves; if this is not done, the inductance and magnetic field calculations can be problematic. In this case, the points are spaced so that they are approximately dl apart, where

$$dl = \frac{r_{\max}}{100}\,, \tag{110}$$

and $r_{\max}$ is the maximum coil radius. Then the contours can be smoothed using `sgolayfilt()` with a second order polynomial. The coils were smoothed with a window length of 25, and the transmit and receive coils for the G25 case are shown in Figures 133(b) and 133(f). Larger smoothing windows were considered, but a window of 25 points was deemed to be sufficient. In both raw and smoothed wire coil representations, red turns are clockwise and blue turns are counterclockwise.

Important metrics were calculated for the coils when the number of level contours varies from 10 to 45. Results are shown for the no smoothing case, G25-N, and the smoothing case, G25-S and shown in Tables 11 and 12. The metrics do not change appreciably between the stream function case and the raw and smoothed cases, so the smoothed coils are reasonable for use in this analysis.

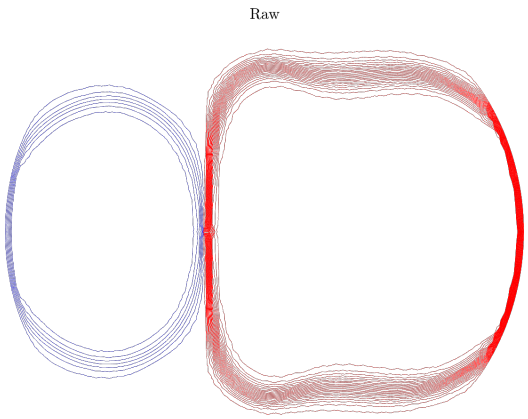

(a) Transmit coil for G25-N30 case.

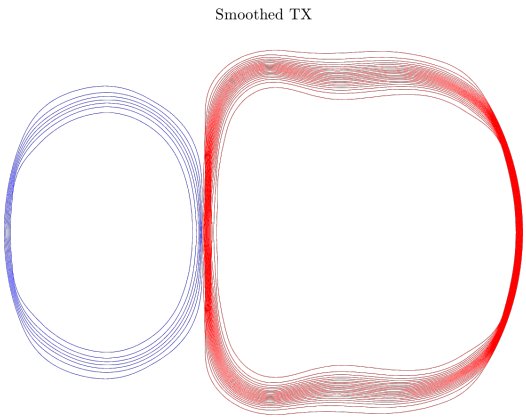

(b) Smoothed transmit coil for the G25-S30 case.

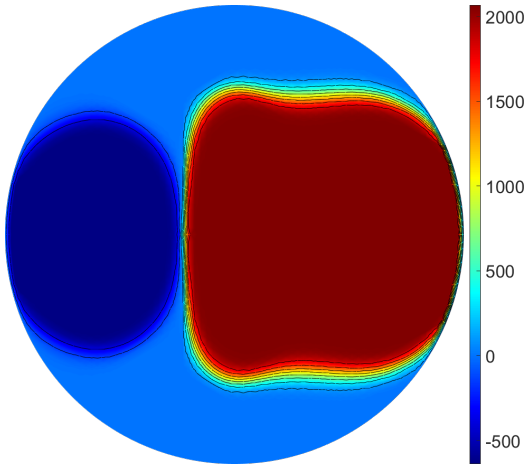

(c) Transmit coil stream function for the G25 case.

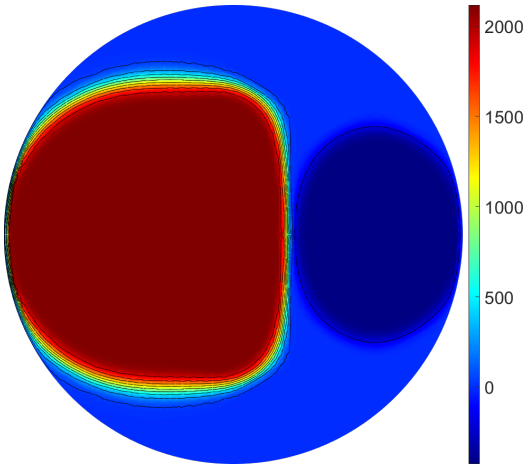

(d) Receive coil stream function for the G25 case.

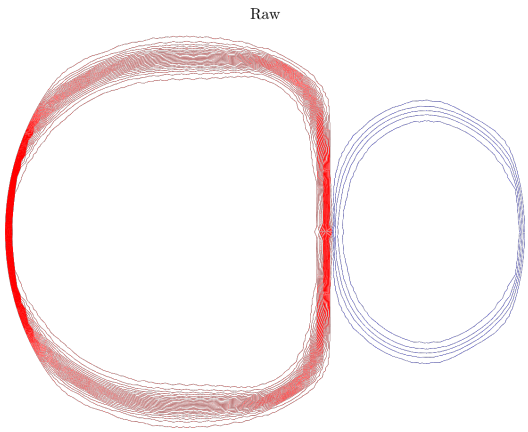

(e) Receive coil for G25-N30 case.

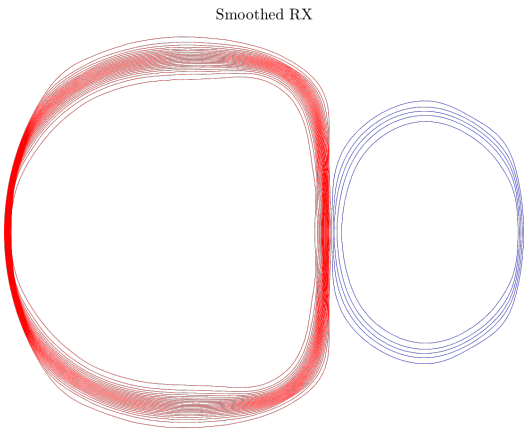

(f) Smoothed receive coil for the G25-S30 case.

Figure 133: Illustrations of the conversion of coils from stream functions to raw wire coils and then to smoothed wire coils for the G25 case.

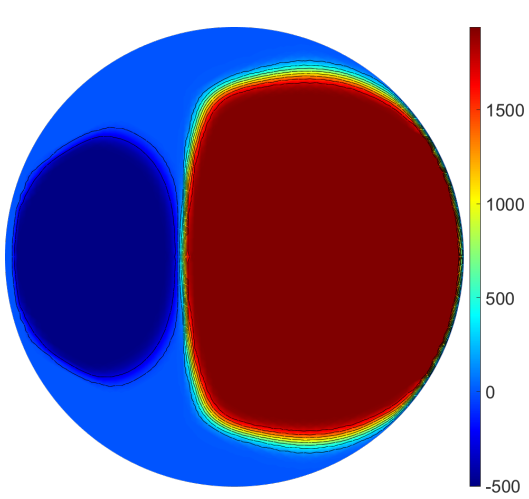

(a) Receive coil stream function for the G50 case.

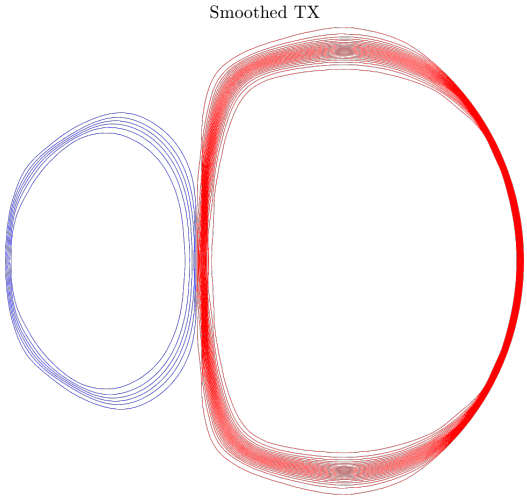

(b) Transmit coil for the G50-S30 case.

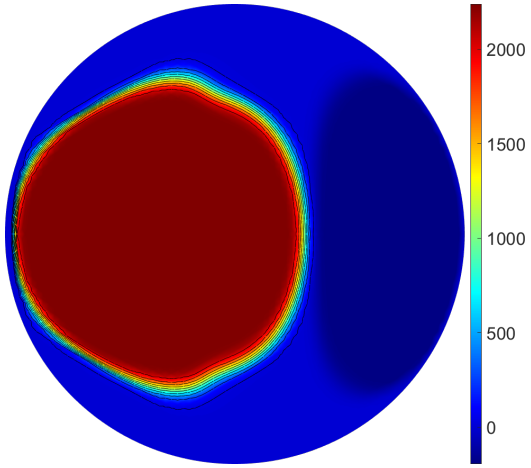

(c) Receive coil stream function for the G50 case.

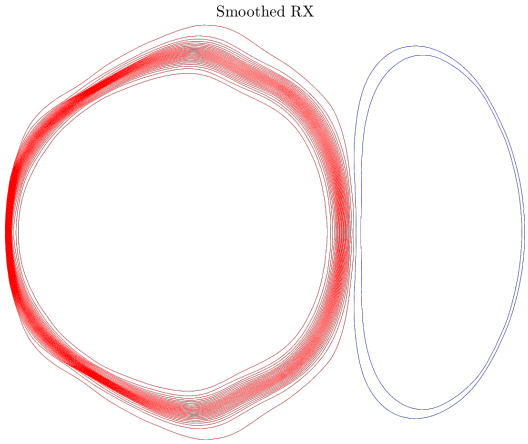

(d) Receive coil for the G50-S30 case.

Figure 134: Illustrations of the conversion of coils from stream functions to smoothed wire coils for the G50 case.

9.5.3 Wire Coil Coupling Correction

The coupling between the transmit and receive coils for varying numbers of contours is listed in Tables 11, 12 and 14 and plotted in Figure 135, and the coupling is not sufficiently nulled for any of the cases. This is not unexpected, since the coupling is very sensitive to small geometric changes in the current paths[3]. As was done in Chapter 3 with the double-sided spirals, the coupling can be "re-nulled" by altering the spacing between the transmit and receive coils or by shifting one of the coils in the x-y plane. The coupling was calculated for the G50-S30 and G25-S30 cases (the 30 turn cases) for sweeps of the separation (z) and for translations in the x-y plane. The results are plotted in Figure 136. While the coupling can theoretically be nulled by shifting the coils relative to one another in any of the three axes, a shift in the x-direction is the most sensitive, so that is the approach that will be used here to re-null the coil coupling before examining the effectiveness of the simple conversion to wire coils.

The coils were "re-nulled" by shifting them relative to each other in the x-direction, and the amount of shift is presented in Table 13. The amount of shift varied from -5.7 to 1.1 mm depending on the number of contours. The shift significantly reduces the coupling but has an insignificant impact on the other metrics.

[3]The coupling of the optimized stream-function answers is mostly numerical noise, and is listed as approximately zero in the tables

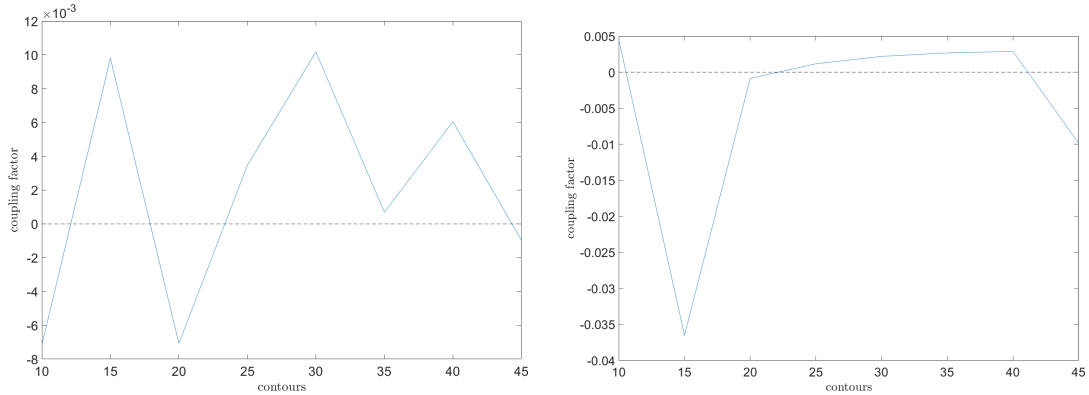

(a) G50-S case. (b) G25-S case.

Figure 135: Coupling versus contours.

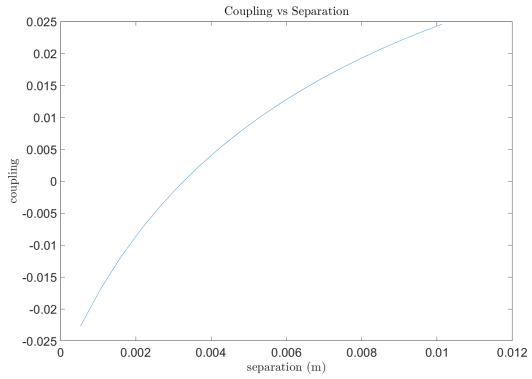

(a) Coupling versus separation for the G50-S30 case.

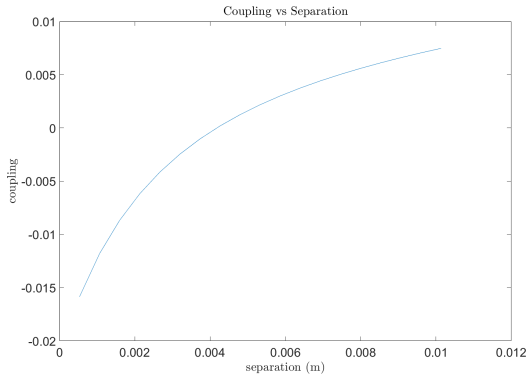

(b) Coupling versus separation for the G25-S30 case.

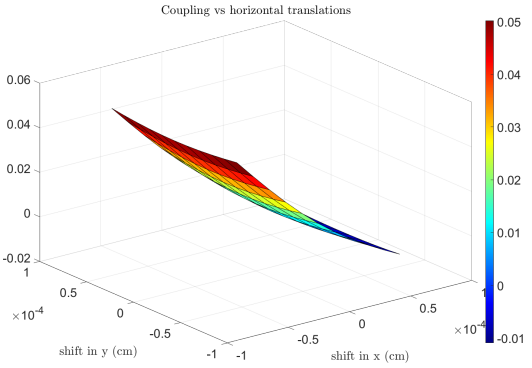

(c) Coupling versus translation for the G50-S30 case.

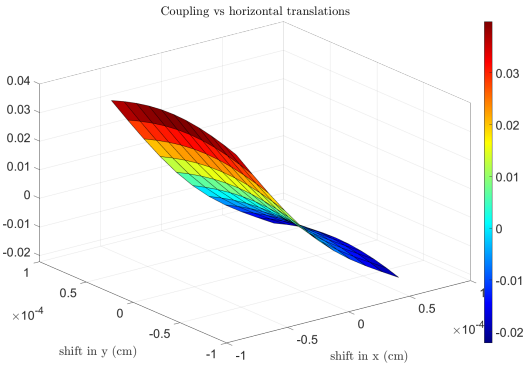

(d) Coupling versus translation for the G25-S30 case.

Figure 136: Coupling versus separation and translation for the G25 and G50 cases.

9.5.4 Number of Turns

$\widehat{S}_{\text{ggm}}$, $\max\left(\widehat{S}_{\text{s}}\right)$, and $\widehat{S}_{\text{ggms}}$ were calculated for a range of contours for the G25 and G50 cases and are shown in Tables 11 to 14 and plotted in Figures 137, 138, 141 and 142. As should be expected, $\widehat{S}_{\text{ggm}}$ and $\widehat{S}_{\text{s}}$ are not perfectly consistent as the number of contours changes. The soil sensitivity was also plotted against height above the soil for different numbers of contours in Figures 140 and 144 and against the number of contours for several different heights above the soil in Figures 139 and 143. These figures show that the metrics are a surprisingly good match to the stream function as the number of contours varies. Even with only ten contours, the metrics are in reasonable agreement with the stream function. Therefore, these wire coils will perform almost as well as the stream function coils.

Table 11: G25-N Results

# contours	$\widehat{S}_{\text{ggm}}$ (dB)	$\max\left(\widehat{S}_{\text{s}}\right)$ (dB)	$\widehat{S}_{\text{ggms}}$ (dB)	L_{TX} (H)	L_{RX} (H)	coupling
stream	-67.3	-59.1	-8.2	N/A	N/A	≈ 0
10	-67.1	-57.4	-9.68	2.70e-5	2.78e-5	4.8e-3
15	-68.5	-57.4	-11.0	5.59e-5	6.32e-5	3.6e-2
20	-67.2	-57.4	-9.84	1.03e-4	1.22e-4	5.7e-4
25	-67.2	-57.4	-9.82	1.64e-4	1.89e-4	1.5e-3
30	-67.2	-57.4	-9.80	2.39e-4	2.71e-4	2.5e-3
35	-67.2	-57.4	-9.77	3.29e-4	3.67e-4	3.0e-3
40	-67.2	-57.4	-9.76	4.32e-4	4.78e-4	3.2e-3
45	-67.6	-58.9	-8.65	5.34e-4	6.03e-4	9.7e-3

Table 12: G25-S Results

# contours	$\widehat{S}_{\text{ggm}}$ (dB)	$\max\left(\widehat{S}_{\text{s}}\right)$ (dB)	$\widehat{S}_{\text{ggms}}$ (dB)	L_{TX} (H)	L_{RX} (H)	coupling
stream	-67.3	-59.1	-8.2	N/A	N/A	≈ 0
10	-67.1	-57.4	-9.67	2.70e-5	2.78e-5	4.5e-3
15	-68.4	-57.4	-11.0	5.59e-5	6.32e-5	3.7e-2
20	-67.2	-57.4	-9.83	1.03e-4	1.22e-4	8.7e-4
25	-67.2	-57.4	-9.80	1.64e-4	1.89e-4	1.2e-3
30	-67.1	-57.4	-9.78	2.39e-4	2.71e-4	2.2e-3
35	-67.1	-57.4	-9.76	3.29e-4	3.67e-4	2.7e-3
40	-67.1	-57.4	-9.74	4.32e-4	4.78e-4	2.9e-3
45	-67.6	-58.9	-8.63	5.35e-4	6.04e-4	9.9e-3

Table 13: G25-S Results with Adjusted Translation

# contours	$\widehat{S}_{\text{ggm}}$ (dB)	$\max\left(\widehat{S}_{\text{s}}\right)$ (dB)	$\widehat{S}_{\text{ggms}}$ (dB)	coupling	translation in x (mm)
10	-67.3	-58.2	-9.11	2.15e-5	1.1
15	-67.4	-58.1	-9.33	9.69e-5	-5.7
20	-67.2	-57.3	-9.92	3.15e-6	-0.20
25	-67.2	-57.5	-9.68	1.35e-6	0.28
30	-67.2	-57.7	-9.54	1.73e-6	0.54
35	-67.2	-57.8	-9.45	3.12e-5	0.65
40	-67.2	-57.8	-9.41	5.90e-5	0.70
45	-67.2	-57.6	-9.66	2.59e-5	-2.0

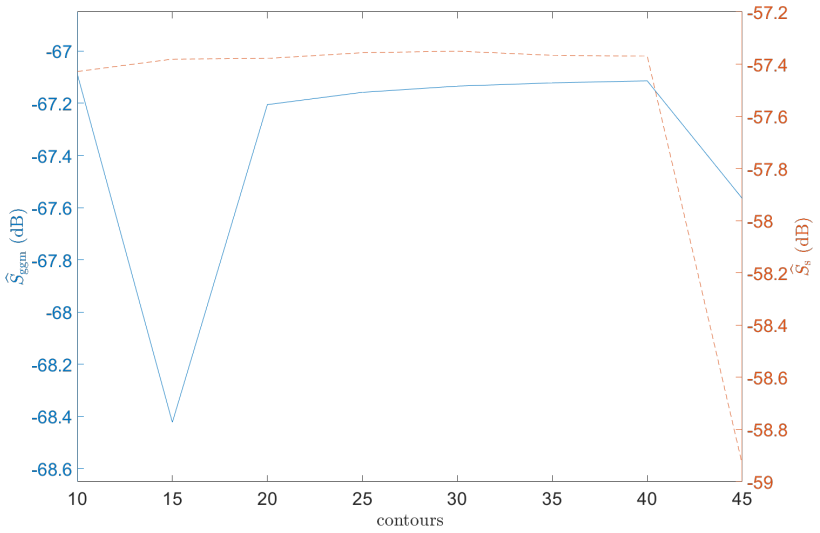

Figure 137: $\widehat{S}_{\mathrm{ggm}}$ and $\widehat{S}_{\mathrm{s}}$ versus contours for the G25-L case.

Table 14: G50-S Results

# contours	$\widehat{S}_{\mathrm{ggm}}$ (dB)	max $\left(\widehat{S}_{\mathrm{s}}\right)$ (dB)	$\widehat{S}_{\mathrm{ggms}}$ (dB)	L_{TX} (H)	L_{RX} (H)	coupling
stream	-65.4	-53.1	-12.3	N/A	N/A	≈ 0
10	-65.5	-53.3	-12.2	3.18e-5	3.12e-5	7.2e-3
15	-65.0	-51.9	-13.1	7.23e-5	7.41e-5	9.8e-3
20	-65.5	-53.4	-12.1	1.30e-4	1.27e-4	7.1e-3
25	-65.2	-52.5	-12.7	2.04e-4	2.04e-4	3.5e-3
30	-65.0	-51.9	-13.1	2.94e-4	3.00e-4	10.2e-3
35	-65.3	-52.7	-12.6	4.02e-4	4.00e-4	6.92e-4
40	-65.1	-52.2	-12.8	5.27e-4	5.32e-4	6.1e-3
45	-65.3	-52.8	-12.5	6.68e-4	6.62e-4	0.97e-3

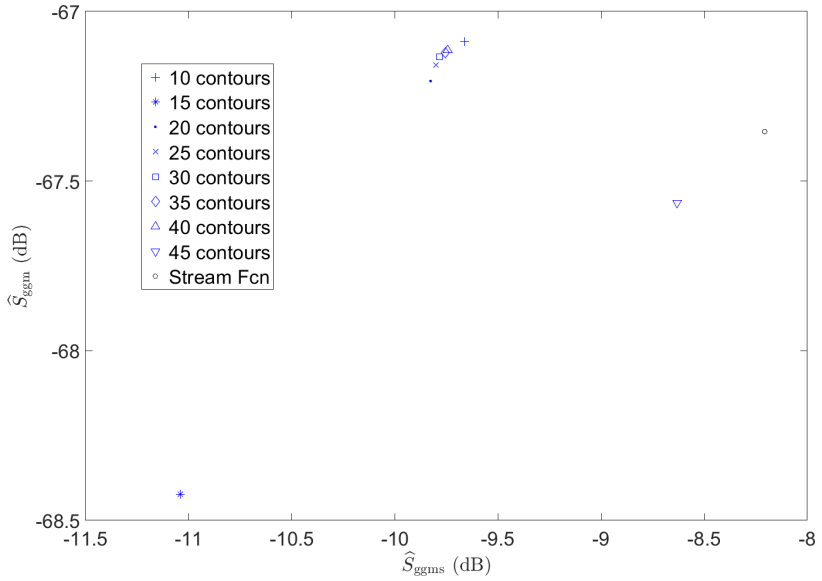

Figure 138: $\widehat{S}_{\mathrm{ggm}}$ and $\widehat{S}_{\mathrm{ggms}}$ versus contours for the G25-L case.

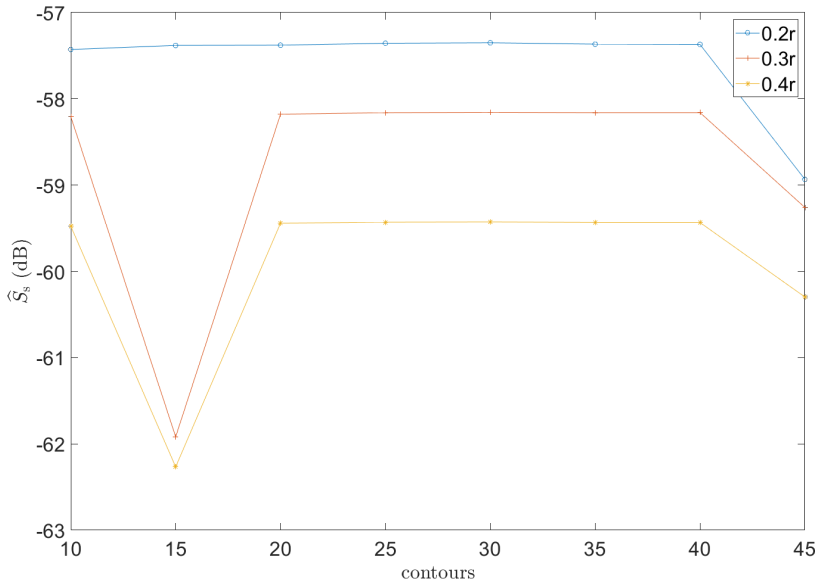

Figure 139: $\widehat{S}_{\mathrm{s}}$ versus contours for the G25-S case.

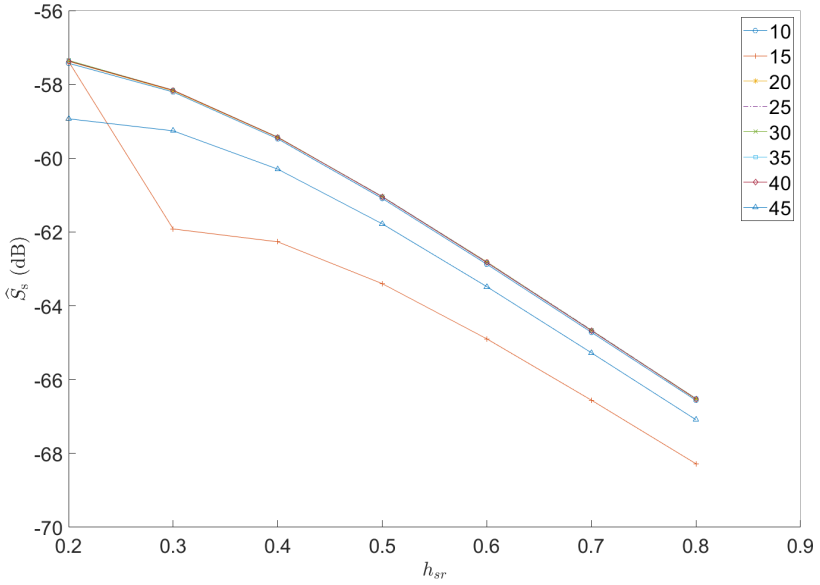

Figure 140: $\widehat{S}_{\mathrm{s}}$ versus h_{sr} for different numbers of contours for the G25-S case.

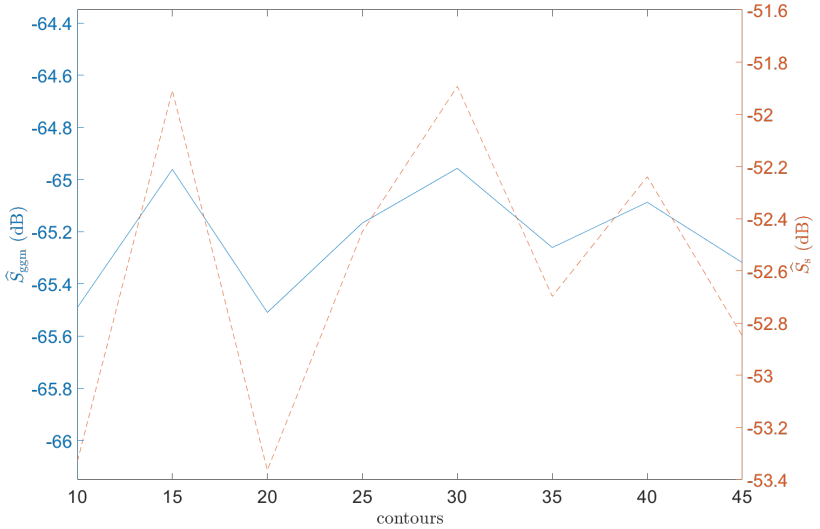

Figure 141: $\widehat{S}_{\mathrm{ggm}}$ and $\widehat{S}_{\mathrm{s}}$ versus contours for the G50-S case.

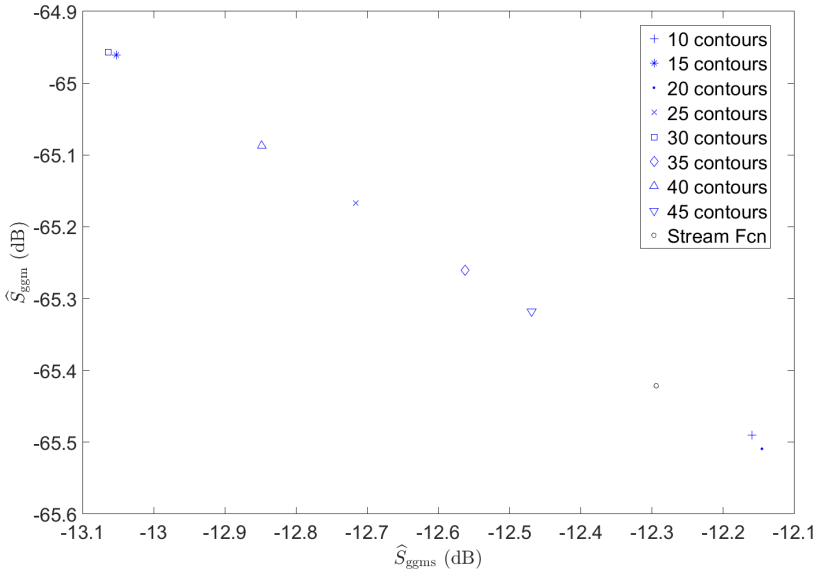

Figure 142: $\widehat{S}_{\text{ggm}}$ and $\widehat{S}_{\text{ggms}}$ versus contours for the G50-S case.

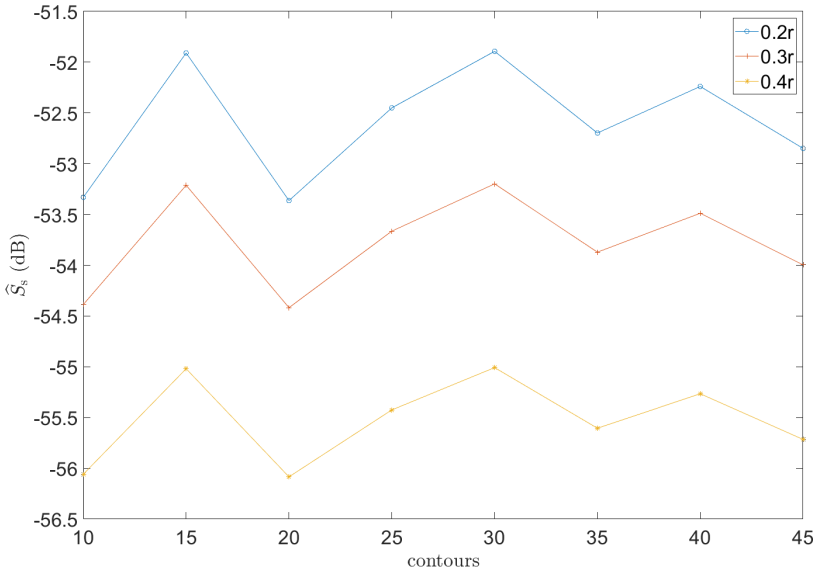

Figure 143: $\widehat{S}_{\text{s}}$ versus contours for the G50-S case.

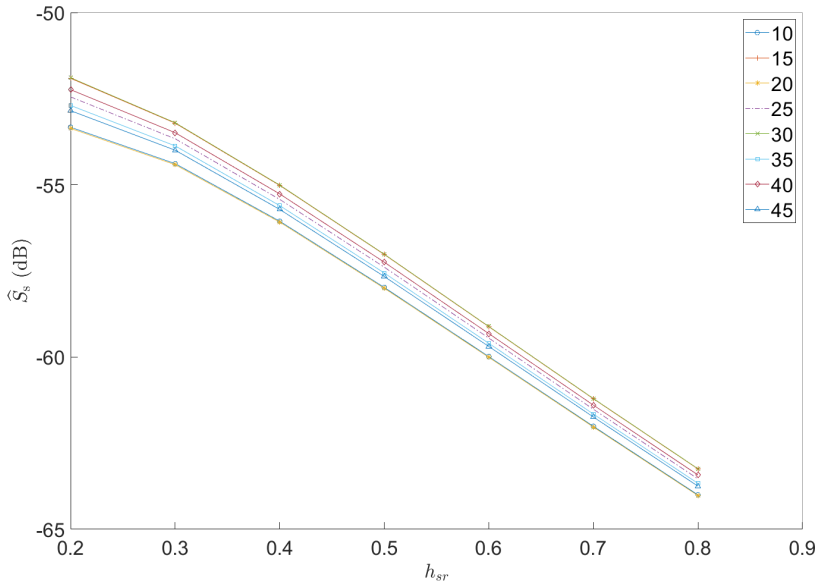

Figure 144: $\widehat{S}_{\mathrm{s}}$ versus h_{sr} contours for the G50-S case.

9.5.5 Self Inductance

The self inductance is dependent upon the number of contours chosen, which is set by the number of turns chosen for the coils. In a practical implementation, the allowable inductance for the coil will be tied to the peformance of the other electronics in the EMI systems, such as the transmit and receive amplifiers. There is also an upper limit to the number of turns based on how tightly the turns can be wound together. The Georgia Tech EMI system desires coils with a self inductance on the order of 300 μH, which is approximately 30 turns for these coils. Coils with 30 turns will therefore be used as examples to show how wire coils compare to the stream functions from which they were derived. The raw inductances versus contours of Figures 145(b) and 145(d) were divided by the number of turns and plotted in Figures 145(a) and 145(c). Note how the inductance goes as roughly the square of the number of turns, as should be expected.

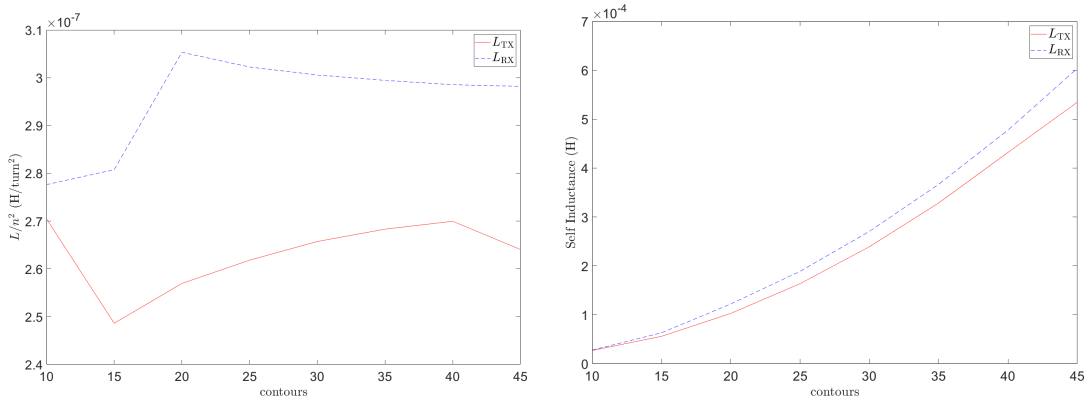

(a) L/n^2 for the G25-S case.

(b) L for the G25-S case.

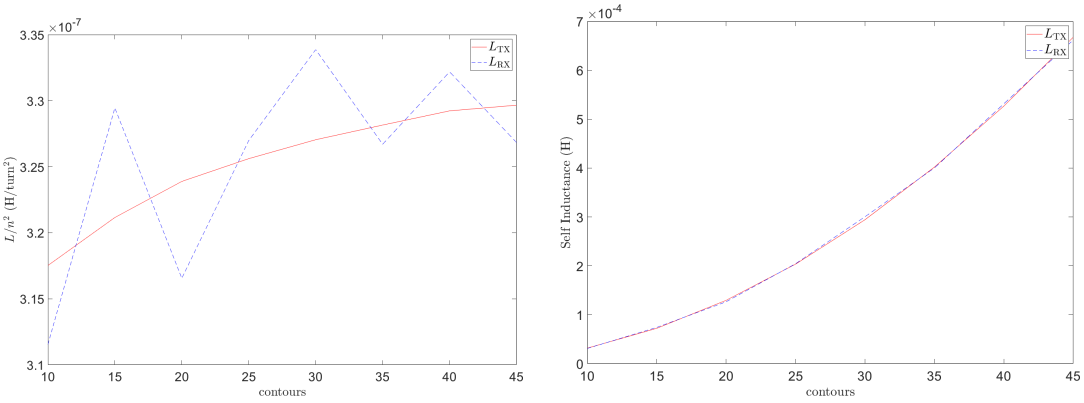

(c) L/n^2 for the G50-S case.

(d) L for the G50-S case.

Figure 145: Self inductances of coils plotted against contours.

9.6 Target and Soil performance

Once the coils have been converted to wires and smoothed, and their coupling fixed by shifting the coils relative to one another in the x-direction, their target sensitivity and soil sensitivity performance can be analyzed and compared to the stream functions from which they are derived.

Cuts in $x-y$, $x-z$, and $y-z$ of the target sensitivity for the G25-S30 and G50-S30 wire coils are shown in Figures 146 to 148 and Figures 149 to 151. Overall, the sensitivity patterns compare very well with the patterns from their corresponding stream functions (Figures 112 to 114 and 115 to 117).

The soil sensitivity for different heights and tilts is shown for the wire coils and stream functions in Figures 152(a), 152(b), 153(a) and 153(b). At first glance, the soil response does not appear to be overly similar, particularly for the G25 case. This is not surprising because the soil sensitivity is sensitive to small changes in the coil geometry, as is covered in more detail in Appendix C. However, the maximum values of these graphs—which is the soil sensitivity, $\widehat{S}_{\mathrm{s}}$, that is used in the metrics—and these maximum values of the same soil sensitivity for the stream-function coils do not vary much between the stream function and wire coil cases.

9.7 Conclusions

Example coils using the new optimization method based on stream functions have been demonstrated for several cases. The resulting coils have new, interesting wire paths. The coils are superior to the canonical wire coils from Chapter 6, and their combined metric, $\widehat{S}_{\mathrm{ggm}} + \widehat{S}_{\mathrm{ggms}}$, is from 2.3 to 10.2 dB better depending on which groups of coils (excluding the G100 set) are being compared. If one cares most about target sensitivity, the G100 and concentric coils are the best.

However, if one cares most about $\widehat{S}_{\mathrm{ggms}}$, the stream-function coils are very interesting. The G10 stream-function coils perform the best of all the coils with regards to the soil, but the tradeoff in target sensitivity is significant. The significant tradeoff with target sensitivity is the reason for focusing on analysis and wire conversion of the G50 and G25 coils in the

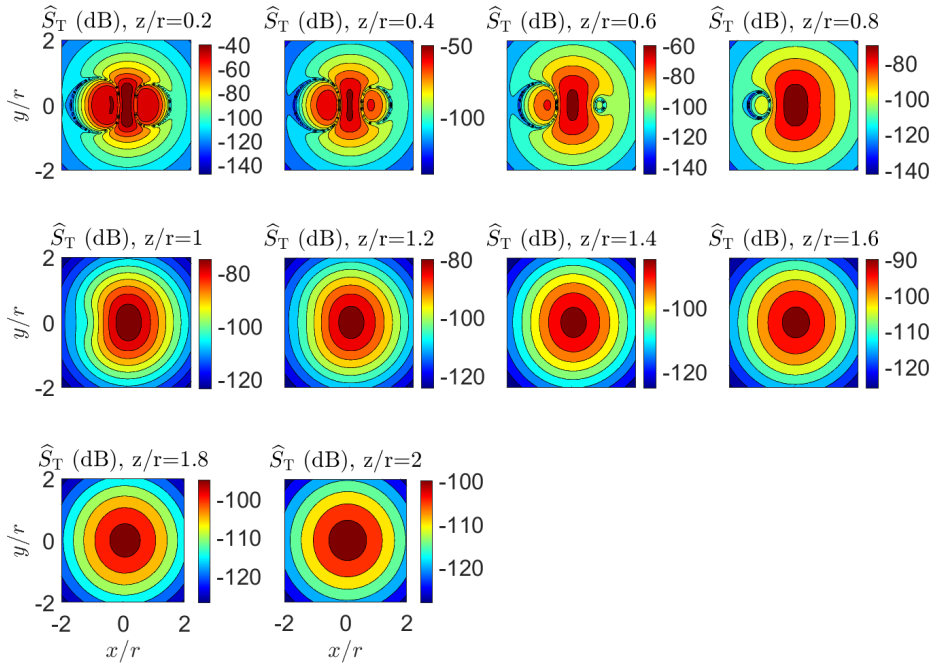

Figure 146: $x-y$ cuts of $\widehat{S}_{\mathrm{T}}$ for the G25-S30 case.

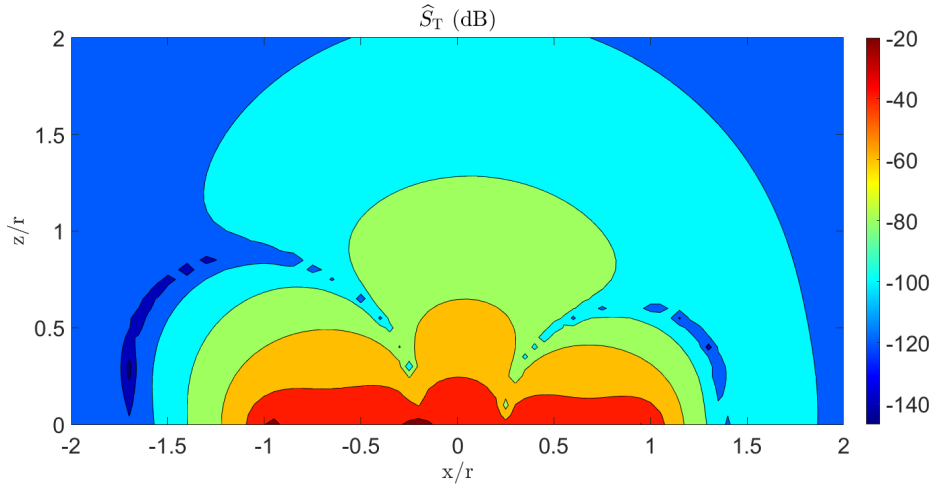

Figure 147: $x-z$ cut of $\widehat{S}_{\mathrm{T}}$ for the G25-S30 case.

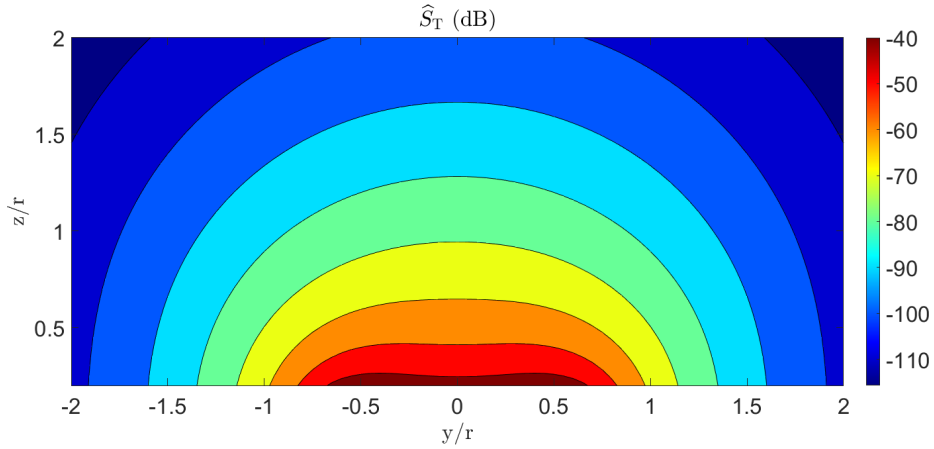

Figure 148: $y-z$ cut of $\widehat{S}_{\mathrm{T}}$ for the G25-S30 case.

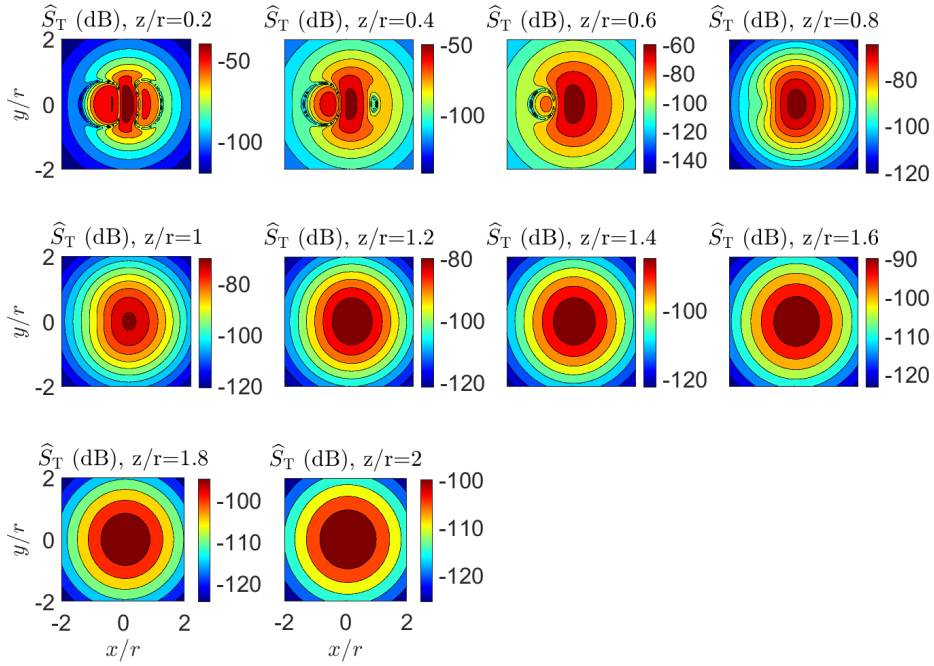

Figure 149: $x-y$ cuts of $\widehat{S}_{\mathrm{T}}$ for the G50-S30 case.

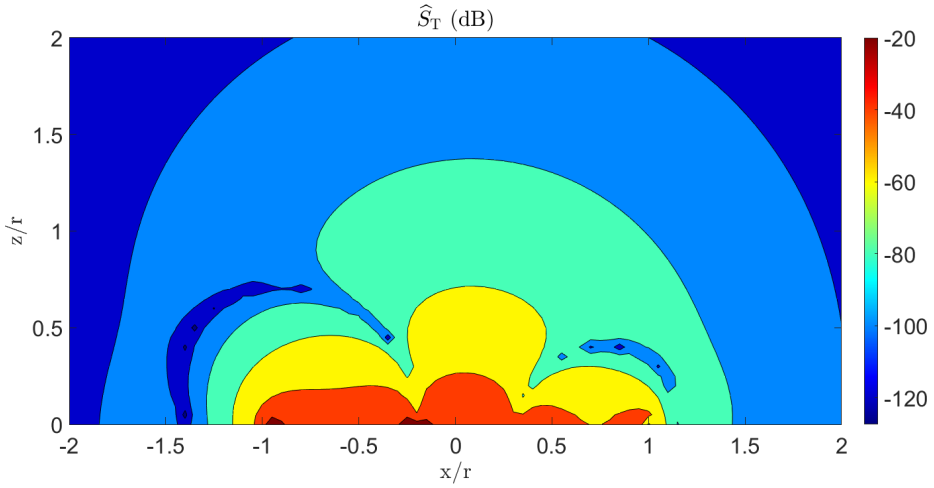

Figure 150: $x-z$ cut of $\widehat{S}_{\mathrm{T}}$ for the G50-S30 case.

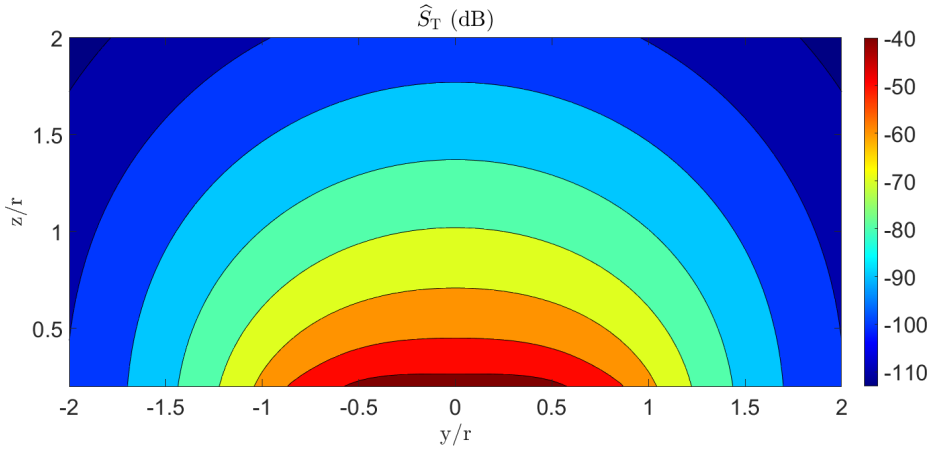

Figure 151: $y-z$ cut of $\widehat{S}_{\mathrm{T}}$ for the G50-S30 case.

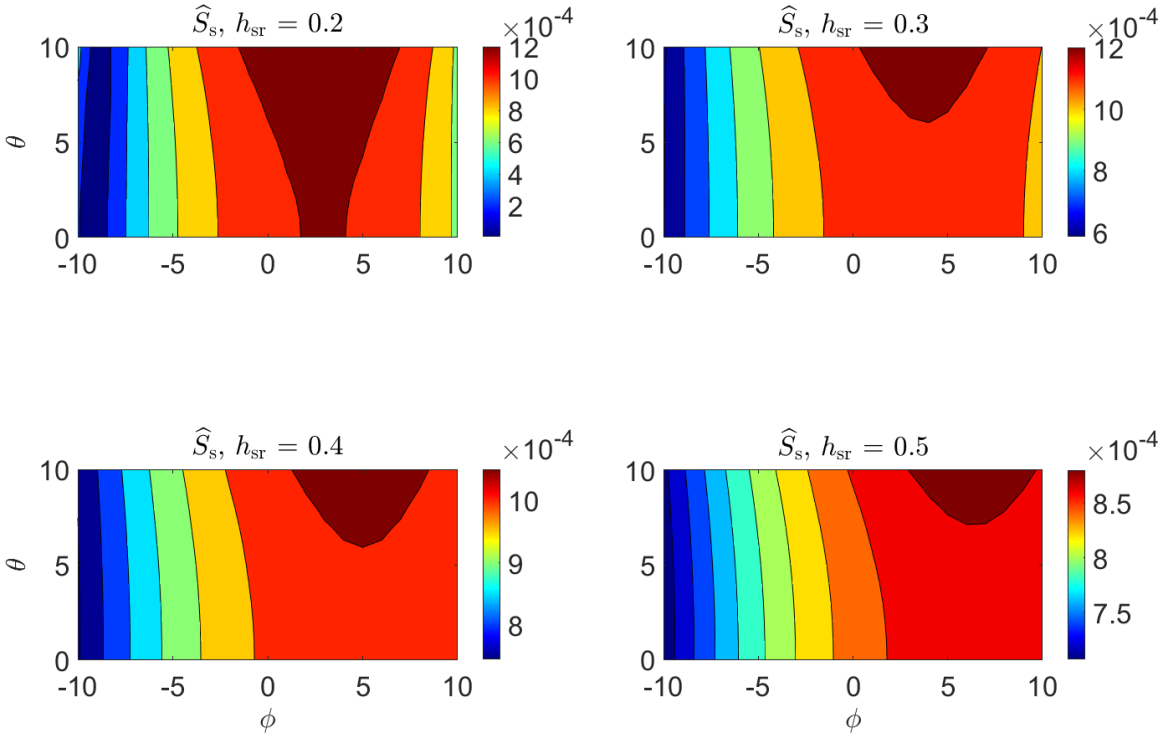

(a) G25-S30 case (wires).

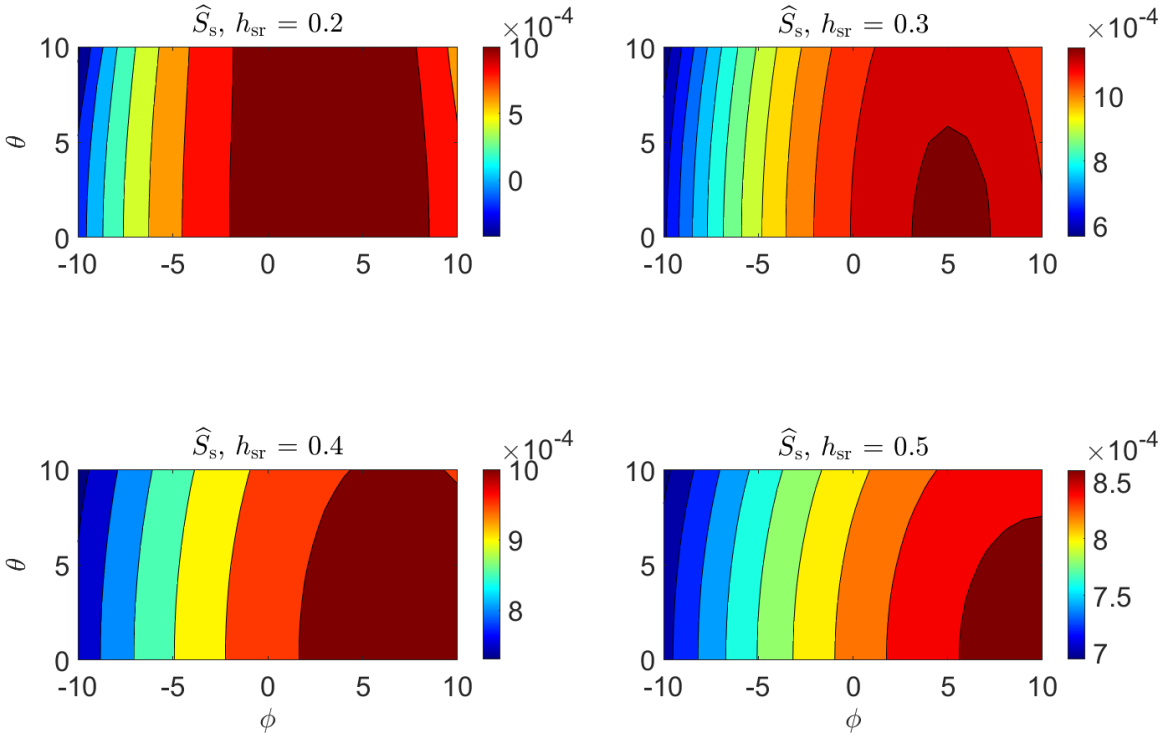

(b) G25 stream function case.

Figure 152: Soil sensitivities versus height and tilt for the G25 case with both wires and stream functions.

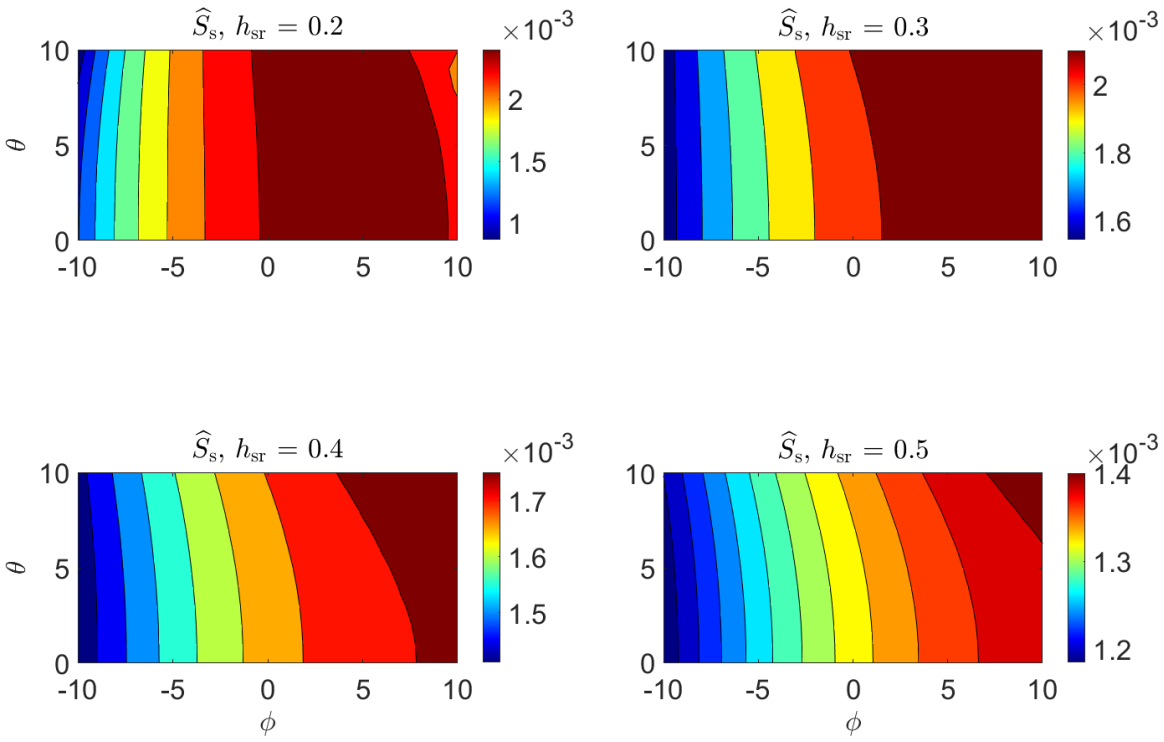

(a) G50-S30 case (wires).

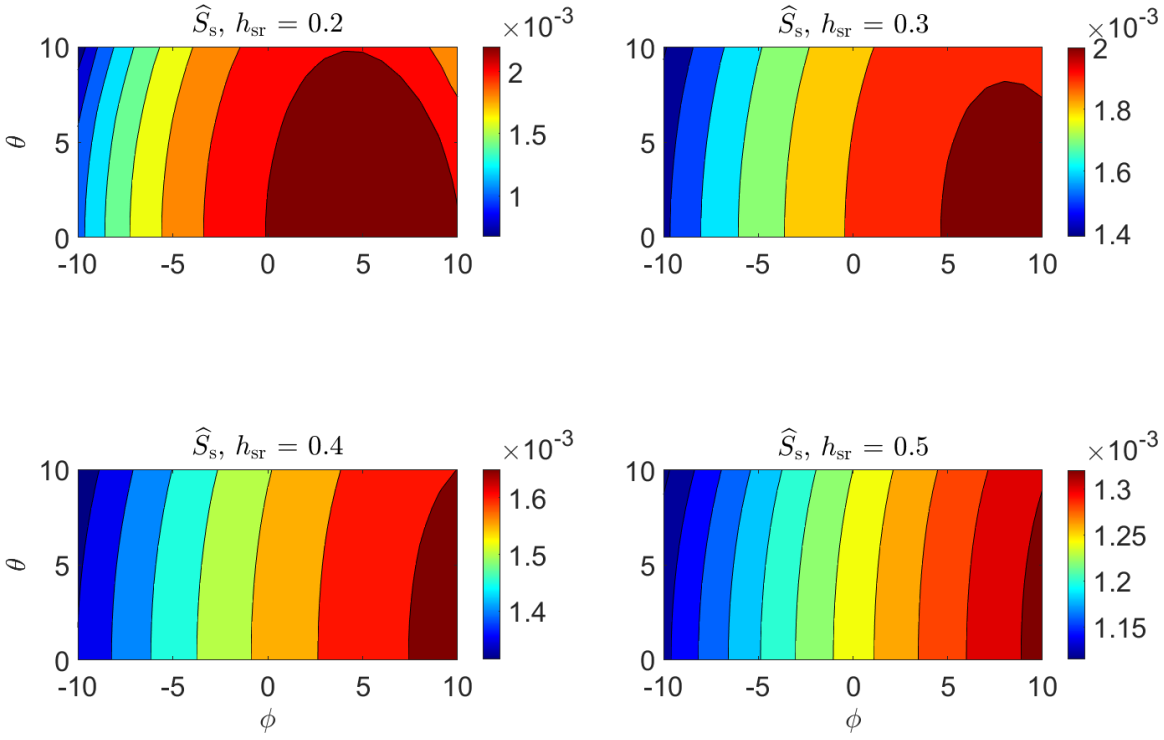

(b) G50 stream function case.

Figure 153: Soil sensitivities versus height and tilt for the G50 case with both wires and stream functions.

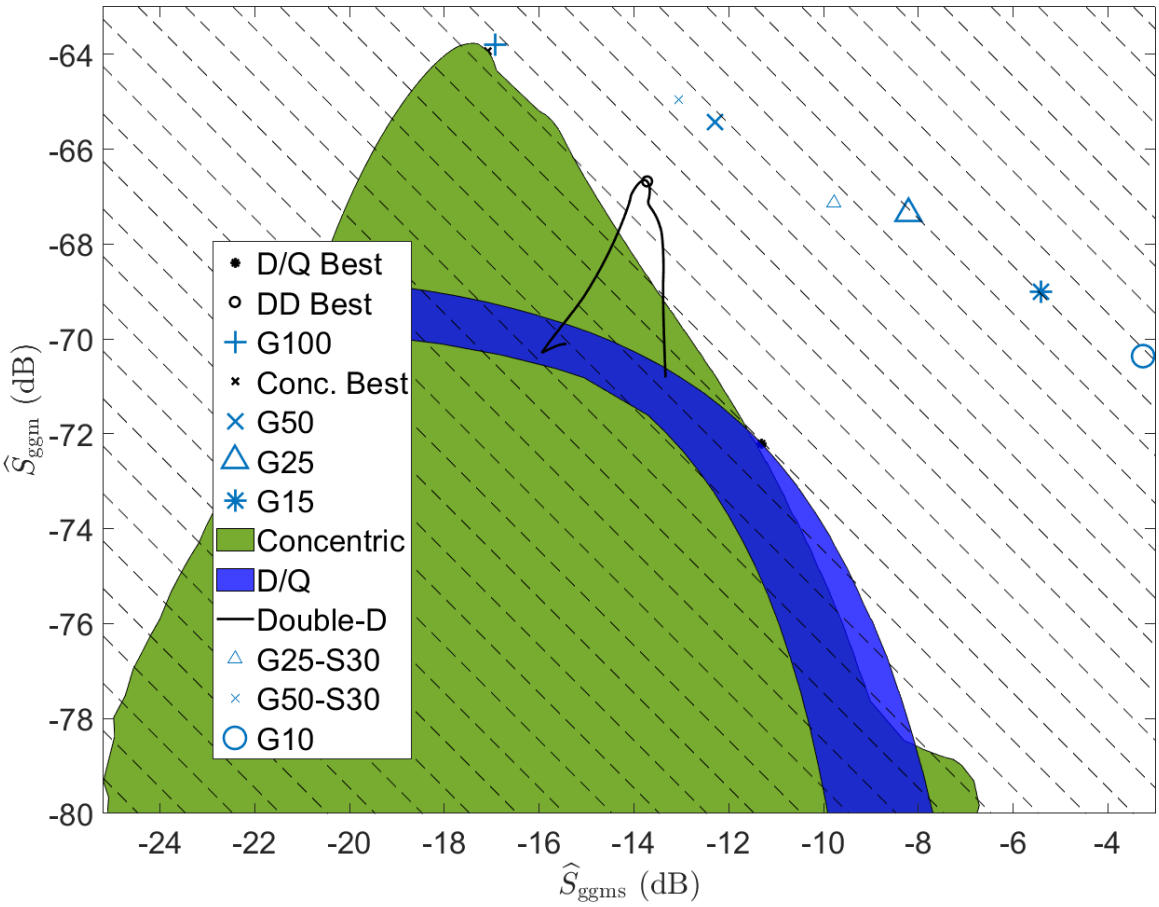

Figure 154: Summary of $\widehat{S}_{\mathrm{ggm}}$ versus $\widehat{S}_{\mathrm{ggms}}$ for the canonical wire coils, the best stream functions, and the wire conversions of the G25-S30 and G50-S30 cases.

preceding sections. For the G50 coil, trading 1.6 dB of $\widehat{S}_{\mathrm{ggm}}$ gives a gain of 3.7 db of $\widehat{S}_{\mathrm{ggms}}$, and for the G25 coil trading off 3.6 dB of $\widehat{S}_{\mathrm{ggm}}$ gives a gain of 8.7 db in $\widehat{S}_{\mathrm{ggms}}$. Once converted to wire coils, the G25 and G50 coils do not perform quite as well as their corresponding stream functions, as can be seen in Figure 154, but they are still within 1.3 dB of the stream functions in the $\widehat{S}_{\mathrm{ggm}} + \widehat{S}_{\mathrm{ggms}}$ metric.

CHAPTER X

CONCLUSIONS AND FUTURE WORK

10.1 Conclusions

An initial investigation of the feasibility of optimizing spiral coils using a simple polynomial basis function was made. These coils proved promising, but they demonstrated the need for a fair means of comparing coils and also demonstrated the need for canonical coils to which new coils can be compared. The polynomial basis that was used restricted the coils to concentric, non-uniformly wound spirals, which showed a need for a more general representation. The general representation was later created by representing coils as stream functions.

To quantify the goodness of coils, new metrics were introduced that can be used to fairly compare coils. These metrics take into account important coil parameters such as target sensitivity, soil sensitivity, power dissipation, thermal noise, etc. The metrics are normalized to allow fair comparison between all types of wire- and stream-function-based coils. The target and soil sensitivity metrics in particular are normalized so that they are independent of such parameters as wire diameter, coil size, transmit and receive electronics, etc. In other words, it is desirable to remove these system-dependent parameters to allow easy and fair comparison of the performance of different current paths.

Simple, brute-force optimization methods could be used to null the coupling of double-D, dipole/quadrupole, and concentric coils, all of which are common coil types in use today. The new normalized metrics were then used to analyze and compare these conventional wire coil designs for two-coil EMI system heads. The optimized wire coils could then be used as a baseline to which the target and soil sensitivity of new coils could be compared.

A more general coil representation was then created by using stream functions instead of discrete current paths. The stream functions allow optimization of coils without first

specifying a geometry. Discretizing and optimizing wire-wound coils is generally very restrictive in the sense that the optimization of wire-wound coils using conventional methods is restricted to a chosen configuration. Starting with a concentric coil as a base will not produce a more optimal double-D coil as a result. Problems with wires crossing and the choice of initial coil representation forcing a particular final coil configuration are obviated.

While the stream function is a very general manner to represent a coil by converting divergence-free surface currents to a simple surface, the discretization of the stream function leads to a very large number of unknowns. The large number of unknowns would make a brute-force optimization method unfeasible. For example, the stream functions on the triangular meshes used in this dissertation would be impossible to optimize with current computing capabilities using brute-force methods. The optimization problem that creates a pair of coils with minimum mutual coupling and maximum target sensitivity for a given soil sensitivity could fortunately be formulated as a bi-convex problem, and some of the geometrical symmetry could also be exploited to reduce optimization times to be on the order of a day.

Examples using the new optimization method based on stream functions were demonstrated for several soil sensitivity cases in Chapter 9. In the same chapter, the new stream-function coils were converted to wire coils and were shown to have essentially the same performance. The resulting coils are superior to the canonical wire coils from Chapter 6, and their combined metric, $\widehat{S}_{\text{ggm}} + \widehat{S}_{\text{ggms}}$, is from 2.3 to 10.2 dB better depending on which groups of coils (excluding the G100 set) are being compared.

If only target sensitivity and not soil sensitivity is a concern, the concentric coils and the stream-function coils with no soil sensitivity constraint (G100 case) are almost equal in performance. However, if the soil sensitivity is important, the new stream-function coils with a soil constraint can perform significantly better. For the G50 coil, trading off 1.6 dB of $\widehat{S}_{\text{ggm}}$ gives a gain of 3.7 db of $\widehat{S}_{\text{ggms}}$, and for the G25 coil trading off 3.6 dB of $\widehat{S}_{\text{ggm}}$ gives a gain of 8.7 db in $\widehat{S}_{\text{ggms}}$. Once converted to wire coils, the G25 and G50 coils do not perform quite as well as their corresponding stream functions, as can be seen in Figure 154, but they are still within 1.3 dB of the stream functions in the $\widehat{S}_{\text{ggm}} + \widehat{S}_{\text{ggms}}$ metric.

10.2 Future Work

Many small improvements could be made to the system representation and optimization. For example, improved granularity of the soil sensitivity calculations (more heights and tilts) can be considered to improve the accuracy of the soil metrics at the possible expense of computer time. There are certainly more speed and efficiency improvements that could be made.

It could also be desirable to force the transmit and receive coils to be mirror images of one another, such as in the double-D coils of Chapter 6; however, it is not immediately clear how this may be achieved while still retaining the partial convexity exploited during optimization.

External correlated interference signals, such as the noise from power lines or switching power supplies could be included in the optimization. Canceling these noise sources can be desirable because they can be large enough to cause problems detecting weak targets. Dipole/quadrupole coils do cancel these correlated noise sources, but they do so with a considerable reduction in target sensitivity over a coil like a double-D.

It is relatively straightforward to implement the stream-function coils for a low-bandwidth and low-frequency system; however, there are a bevy of challenges to physically implementing the wire coils created in Chapter 9 for a wideband system. There almost certainly will be resonance issues like those encountered in Chapter 4 that impact coil performance and will have to be overcome. Ideally, the capacitive effects that cause these problems would be modeled, but they are beyond the scope of this work. It is likely that when physically built, the coil coupling will not null properly because of the sensitivity to the relative positioning of the two coils. This can be manually tweaked after the two coils have been produced as is shown in 11(a) in Chapter 3 and also in Chapter 9 in Figures 136(a) to 136(d).

The metrics and bi-convex optimization method have been developed in a general manner so that they are valid in far more situations than could be considered in this dissertation. The optimization can be extended to much more complex coil arrangements, such as coils of varying shapes, coils with surfaces that are non-planar, systems with more than two coils, or arrays of coils. For example, coils that wrap elegantly around a GPR could be optimized.

This would require a complex surface to wrap around the GPR and would be relatively straightforward using the metrics and bi-convex optimization that has been developed. This is useful because GPRs and EMI sensors are often used together, and co-locating the two sensors is often problematic.

The metrics and methods developed here for EMI coils for subsurface sensing could also be extended for applications to geophysical sensing, medical imaging, nondestructive testing, wireless, short-range power transfer, and other inductive systems that use coils.

All of the coils—with the exception of the dipole/quadrupole—in this work were optimized while assuming an isotropic target. It would be interesting to see what kind of coils the stream function optimization would make for other target symmetries. For example, would optimization produce a dipole/quadrupole coil if an x-directed target symmetry were chosen? Or would a new type of coil be produced? Using these ideas it would be possible to make coils that exploit the symmetry of a specific target.

The coils developed from the stream functions in Chapter 9 are fairly complex, but they have a somewhat simple underlying pattern. Many of the coils in Chapter 9 look very similar, and their pattern may be a useful new coil type. This pattern is a cross between the double-D and dipole/quadrupole coils of Chapter 6. It would be interesting to make a parametric path that describes these patterns and to use the optimization procedure of Part 2 to optimize coils based on this path. These coils could possibly outperform the coils of Part 2 and almost match the performance of the new coils in Part 3.

In this work, the raw target response of the sensor was optimized with the idea of it being scanned side-to-side by hand to locate targets like a conventional metal detector. If the sensor is scanned by a robot or other machine, and the position of the sensor is known at all times, it is possible to invert the data to acquire more target information [23, 27, 30]. For this application, it would be best to optimize the inverted data instead of the raw target response. By combining the work in this dissertation with the work in [27] on computing bounds of the inverse, it should be possible to optimize a sensor to improve the quality of the inverted data.

APPENDIX A

NUMERICAL CALCULATION OF COIL ENERGY

To easily calculate the mutual energy of two annuli of current, each annulus is divided into a series of smaller concentric annuli of equal width, $\Delta\rho$, as in Figure 155. The total magnetic field from the transmit coil, $\vec{H}_{\mathrm{TX}}$, divided into K annuli, will be the sum of the fields from each individual annulus, $\vec{H}_k$,

$$\vec{H}_{\mathrm{TX}} = \sum_{k=1}^{K} \vec{H}_k \,, \tag{111}$$

where the k-th annulus is located at position ρ_k. $\vec{H}_{\mathrm{RX}}$ is computed similarly,

$$\vec{H}_{\mathrm{RX}} = \sum_{l=1}^{L} \vec{H}_l \,. \tag{112}$$

Substituting these two expressions into (8) gives the mutual energy of the transmit and receive coils,

$$W_m = \sum_{k=1}^{K} \sum_{l=1}^{L} \mu \int_{\mathrm{V}} \vec{H}_k \cdot \vec{H}_l dv \,. \tag{113}$$

The integral in (113) is the mutual energy between the k-th annulus of current on the transmit coil and the l-th annulus of current on the receive coil. This mutual energy can also be expressed in terms of the mutual inductance between annuli k and l and the total

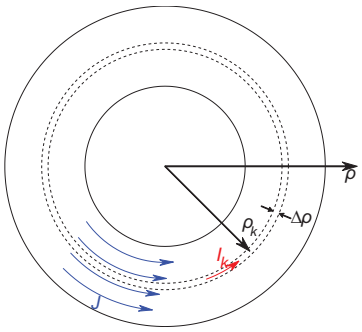

Figure 155: Illustration of the method used to divide an annulus first into K annuli of width $\Delta\rho$ and then into loops of current. Here, the k-th loop of current, I_k, is found from the current density, J, on the annulus of current.

current carried by each [56],

$$W_{kl} = \mathrm{M}_{kl}\mathrm{I}_k\mathrm{I}_l = \mu \int_{\mathrm{V}} \vec{H}_k \cdot \vec{H}_l dv \,. \tag{114}$$

Substituting this equation into (113) yields

$$W_m = \sum_{k=1}^{K}\sum_{l=1}^{L} \mathrm{M}_{kl}\mathrm{I}_k\mathrm{I}_l \,, \tag{115}$$

which, when written in matrix form becomes

$$W_m = \mathbf{I}_{\mathrm{RX}}^{\top}\mathbf{M}\mathbf{I}_{\mathrm{TX}} \,. \tag{116}$$

For purposes of calculation, each annulus of width $\Delta\rho$ can be approximated as a current carrying filament, which henceforth will be referred to as a "loop," with a radius equal to the average radius of the corresponding annulus.

$\mathbf{I}_{\mathrm{TX}}$ is a vector of length K where each entry is the current on one of the loops in our multiple-loop approximation to an annulus. The vector $\mathbf{I}_{\mathrm{RX}}$ of length L for the receive coil is defined analogously to $\mathbf{I}_{\mathrm{TX}}$. Entries of the matrix $\mathbf{M}$ are the mutual inductances between the loops in the two structures (but not between loops in the same structure). As a result, they can be quickly calculated as follows [56],

$$M_{kl} = \frac{2\mu_0}{\sqrt{m}}\sqrt{r_k r_l}[(1-\frac{1}{2}m)K(m) - E(m)] \,, \tag{117}$$

$$m = \frac{4r_k r_l}{(r_k + r_l)^2 + \delta^2} \,, \tag{118}$$

where r_k and r_l are the radii of loops in the transmit and receive coils and K and E are the complete elliptic integrals of the first and second kinds. The mutual inductance matrix, $\mathbf{M}$, describes the mutual inductance between the two annuli.

The mutual energy between the transmit and receive coils has been written in terms of currents, $\mathbf{I}_{\mathrm{TX}}$ and $\mathbf{I}_{\mathrm{RX}}$, on the coils. Now (116) can be written in terms of $\mathbf{M}$ and the basis function coefficients $\mathbf{a}$ and $\mathbf{b}$. The surface current density on the transmit coil has been represented with basis functions,

$$J_{\mathrm{TX}} = \sum_{n=0}^{N} a_n F_n(\rho) \,. \tag{119}$$

Now current flowing on the loops must be calculated. If the loops are spaced $\Delta\rho$ apart, then loop $k = 1$ is located at $\rho_1 = \rho_{min} + \frac{\Delta\rho}{2}$ and loop $k = K$ is located at $\rho_K = \rho_{max} - \frac{\Delta\rho}{2}$. The current flowing in the k-th loop, as illustrated in Figure 155, is

$$I_{\mathrm{TX},k} = \int_{\rho_k - \frac{\Delta\rho}{2}}^{\rho_k + \frac{\Delta\rho}{2}} J_{\mathrm{TX}} d\rho\,,\ k = 1, \ldots, K\,. \tag{120}$$

Combining (119) and (120) gives the current of a single loop at position ρ_k,

$$I_{\mathrm{TX},k} = \sum_{n=0}^{N} a_n \mathrm{Y}_{nk}\,, \tag{121}$$

$$\mathrm{Y}_{nk} = \int_{\rho_k - \frac{\Delta\rho}{2}}^{\rho_k + \frac{\Delta\rho}{2}} F_n(\rho) d\rho\,. \tag{122}$$

Making the substitution of (122) and converting to matrix notation gives

$$\mathbf{I}_{\mathrm{TX}} = \mathbf{Ya}\,. \tag{123}$$

$\mathbf{I}_{\mathrm{RX}}$ can be defined analogously as

$$\mathbf{I}_{\mathrm{RX}} = \mathbf{Zb}\,. \tag{124}$$

Substituting (123) and (124) into (116) yields,

$$W_m = (\mathbf{Zb})^\top \mathbf{M}(\mathbf{Ya}) = \mathbf{b}^\top \underbrace{\mathbf{Z}^\top \mathbf{MY}}_{\mathbf{S}} \mathbf{a}\,. \tag{125}$$

After some simple algebra in (125), a form for the calculation of the mutual energy of the transmit and receive coils in terms of the basis function coefficients is derived,

$$W_m = \mathbf{b}^\top \mathbf{Sa}\,. \tag{126}$$

Equations (10) and (11) can be derived in a manner similar to that used to find (9). Because $\mathbf{S}$ is part of an optimization constraint and is also computed prior to optimization, this method is very fast.

APPENDIX B

OPTIMIZATION CONSTRAINTS AND COIL Q FACTOR

The concept of a coil quality factor was developed in the author's early investigations on optimizing coils using stream functions, which were before the introduction of normalized metrics. The following discussion deals with optimizing stream function coils using a convex optimization much like the one introduced in Chapter 8, where the two equations are

$$\mathbf{a} = \underset{\mathbf{a}\in\mathbf{R}^Q}{\arg\max}\{H_{\mathrm{TX}}(\mathbf{a})\hat{z}\cdot H_{\mathrm{RX}}(\mathbf{b})\hat{z}\},$$

$$\text{subject to: } W_{\mathrm{TX}} < W_{max}, W_m = 0, P_{d,TX} < P_{d,max}\,, \quad (127)$$

and

$$\mathbf{b} = \underset{\mathbf{b}\in\mathbf{R}^Q}{\arg\max}\{H_{\mathrm{TX}}(\mathbf{a})\hat{z}\cdot H_{\mathrm{RX}}(\mathbf{b})\hat{z}\},$$

$$\text{subject to: } W_{\mathrm{RX}} < W_{max}, W_m = 0, P_{d,RX} < P_{d,max}\,. \quad (128)$$

The goal of this discussion is to understand the interplay between coil sensitivity, dissipated power, and stored energy when using an optimization that exploits the partial convexity of Equations 127 and 128. This knowledge is used to explain the reasoning for the choices of optimization constraints. For simplicity, only coils with equal power dissipations were considered, and both transmit and receive coils used the same mesh.

B.1 Coil Parameters and Optimization

A pair of example coils was optimized and then used to explain some of the characteristics of the solution space. The example coils are represented by a pair of discs arranged as in Figure 4, each with a radius of 13.33 cm, spaced apart by 9.0 mm, and optimized for maximum field product at 0.5334 m away from the transmit coil along the z-axis. Each disc is represented with a triangular mesh, and the stream function on each disc is represented

with linear pyramidal basis functions. Finally, the discs are arbitrarily chosen to consist of 0.5 mm thick copper sheets, giving a surface resistance of $8.4 \times 10^{-6}\Omega/sq$.

To illustrate the relationship between the stored energy and power dissipation, the optimization procedure presented in [46] was run on the example coils with the stored energy unconstrained and the dissipated power constrained. When this optimization is done for different maximum dissipated powers and the resulting stored energy from each optimization is plotted against the dissipated power constraint, the line labeled Q'_{max} in Figure 156 results. Therefore, coils with values of dissipated power and stored energy that lie in the shaded area in Figure 156 labeled "exclusion zone" cannot exist.

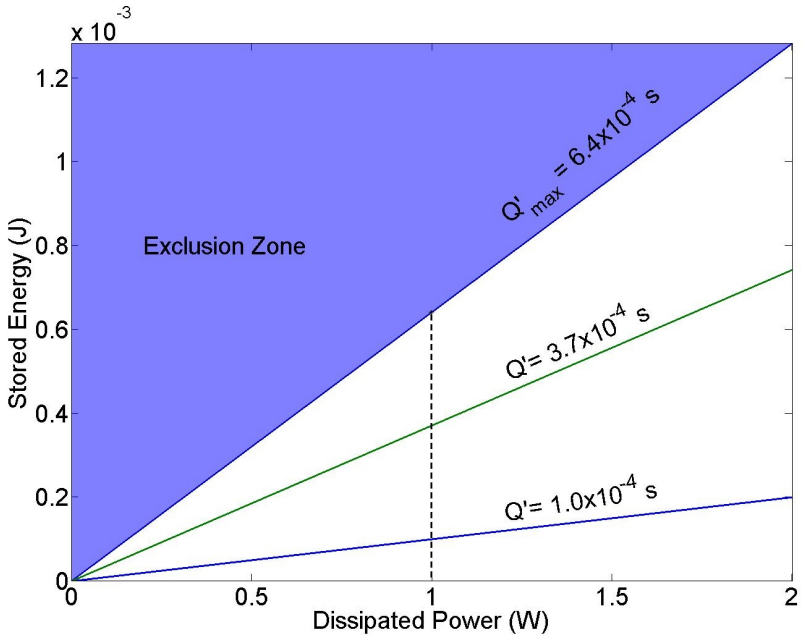

Figure 156: Achievable values of Q'.

B.2 Quality Factor

The quality factor of a component can be defined by $Q = {}^{\omega W}/_{P_d}$, where ω is the angular frequency at which the system operates, W is the energy stored in the coil, and P_d is the average dissipated power. This definition makes it convenient to define a second quantity, Q', such that $Q' = {}^{Q}/_{\omega}$. Now, the edge of the exclusion zone is defined by coils with a Q' of 6.4×10^{-4} sec. The stream functions of these coils of the same Q' are all simply scaled (and possibly rotated) versions of each other. For example, if the surface currents corresponding

to the solutions with $Q' = Q'_{max}$ were doubled, then the dissipated power, stored energy, and sensitivity would increase by factors of four, but the stream functions would have the same profiles. Examples of optimized transmit and receive coil stream functions with a Q' of 6.4×10^{-4} sec are shown in Figure 157. These solutions have been normalized to have a dissipated power of 1 W.

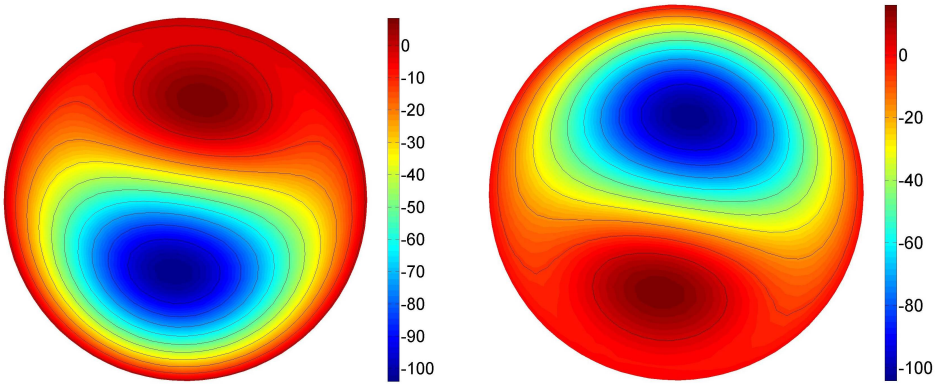

(a) Transmit coil. (b) Receive coil.

Figure 157: Stream functions (units of amps) with a Q' of 6.4×10^{-4} sec.

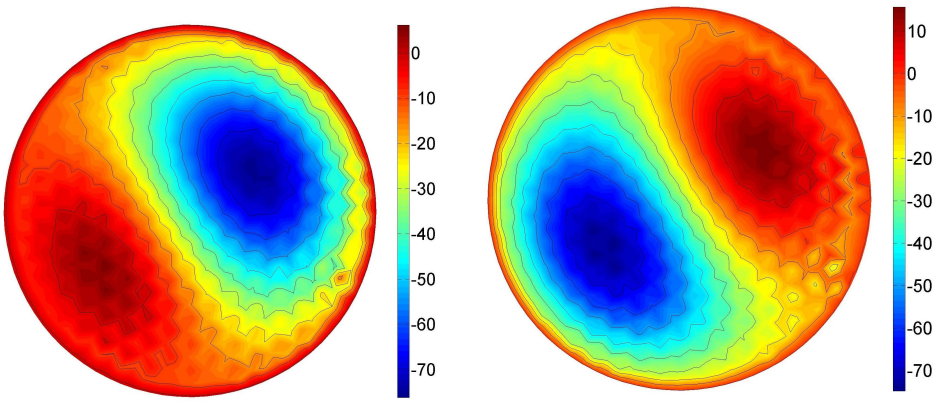

(a) Transmit coil. (b) Receive coil.

Figure 158: Stream functions (units of amps) with a Q' of 3.7×10^{-4} sec.

Since all solutions with the same Q' are scaled versions of each other, the possible stored energy and power dissipation combinations that can be solutions to this optimization problem can be reduced to a single line. For example, the dotted line in Figure 156 at 1

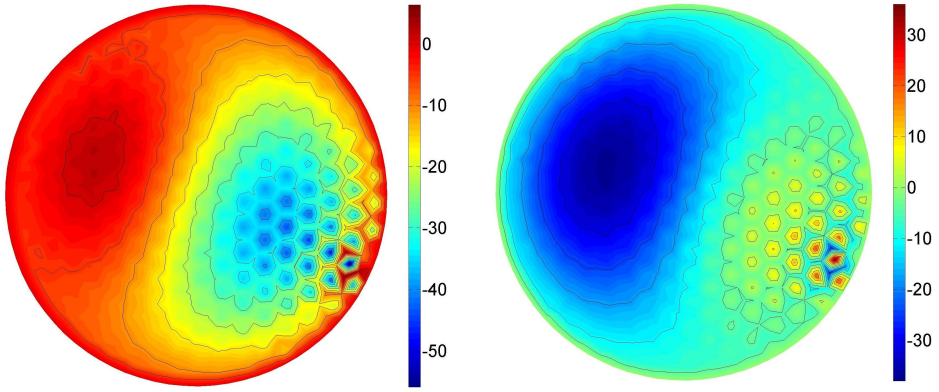

(a) Transmit coil. (b) Receive coil.

Figure 159: Stream functions (units of amps) with a Q' of 1.0×10^{-4} sec.

W spans all possible values of Q' and therefore all the possible stream functions (to within some multiplicative scale factor).

To illustrate how the stream function solution changes when Q' is varied, two more optimizations were performed, one with a Q' of 3.7×10^{-4} (Figure 158), and the second with a Q' of 1.0×10^{-4} (Figure 159), as illustrated by the two other lines of constant Q' in Figure 156. The solutions have both been normalized to have a dissipated power of 1 W as before, so they are represented by the intersections of the lines of constant Q' with the dashed line of constant power in Figure 156. The sensitivities of the three sets of coils that have been optimized at different values of Q' and equal power dissipated power are shown in Figure 160. The sensitivity is highest for the biggest Q' when the dissipated power is held constant. Also, the stream functions of higher Q' solutions are much smoother than low Q' solutions, as illustrated by the change in smoothness over Figures 157, 158, and 159. Therefore, the "best" solution is the one with the highest Q', not only because a higher sensitivity is desirable, but because a smoother solution is much easier to convert to a wire-wound coil.

B.3 Optimization Constraint Implications

What does this mean for optimization constraints? For a given dissipated power, there is a maximum stored energy that cannot be exceeded. Changing the dissipated power constraint

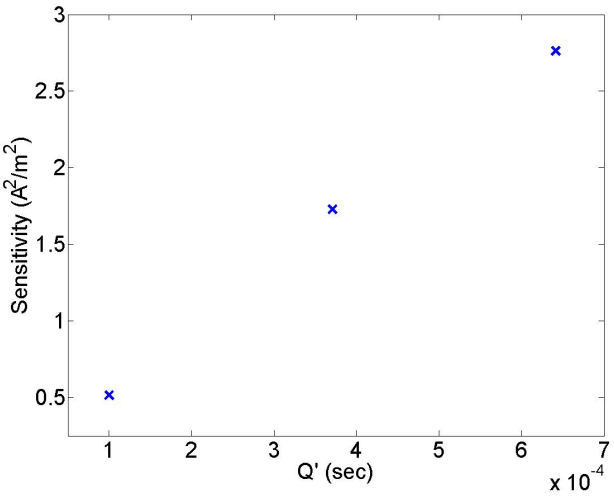

Figure 160: Comparison of the on-axis sensitivity for various values of Q' at a constant dissipated power of 1 W.

without constraining the stored energy will simply give a scaled and possibly rotated pair of equivalent stream functions, all with the same Q'. Constraining the stored energy below its maximum is possible, but it has no useful purpose because it lowers the sensitivity for a given dissipated power.

The stored energy is implicitly constrained by constraining the dissipated power, and therefore a stored energy expression is not needed in the final optimization. The exact value of the dissipated power constraint is unimportant because an optimization with an unconstrained stored energy will give solutions of constant Q'.

APPENDIX C

STREAM FUNCTION AND WIRE COIL SOIL EQUIVALENCY

Most of the important parameters related to coil performance do not change greatly when a stream function coil is converted to a wire coil. However, the changes in the magnetic fields produced by the coils do cause a noticeable change in the coil coupling and the coil soil response. As treated in Chapter 3, the coil coupling can be re-nulled by shifting the coils relative to one another.

The soil response is more difficult. It might be possible to improve the soil response through a secondary optimization procedure on the newly created wire coils, but that is beyond the scope of this work. It is however possible to briefly analyze the effects of the stream to wire conversion on the soil response.

The coil coupling is the most sensitive parameter to the conversion because the distances between segments on the two coils are very small. The soil response is calculated by first mirroring the transmit coil across the air-soil interface, so the distance between the two coils is greater for this calculation, making coils that couple strongly to the soil insensitive to the conversion process.

C.1 Dipole/Dipole Test

This can be illustrated by examining two simple, identical dipoles like the one in Figure 161(b) that is built on the mesh of Figure 161(a). When converted to wires, the coils look like Figure 161(c). The soil response can be calculated for both the stream function and the wires, and it is plotted in Figure 162.

These coils couple strongly both when level and when tilted. The absolute difference between the two is shown in Figure 163(a) and is much smaller than response. As a result, the error between the wire and stream function representations, shown in Figure 163(b), is acceptably low.

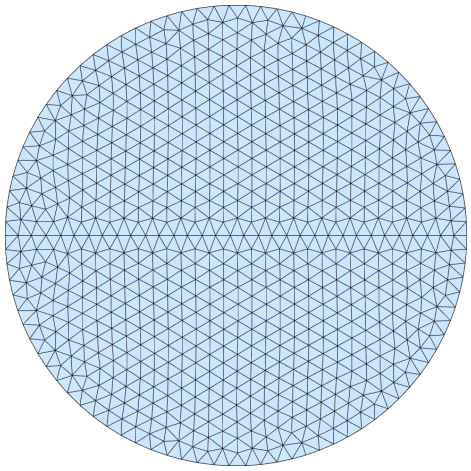

(a) Mesh basis.

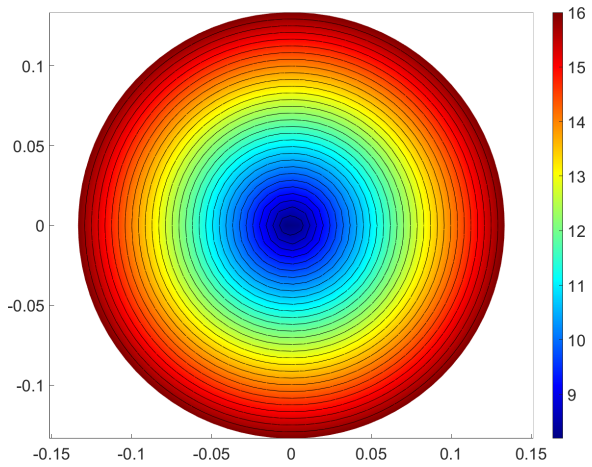

(b) A simple stream-function dipole test coil.

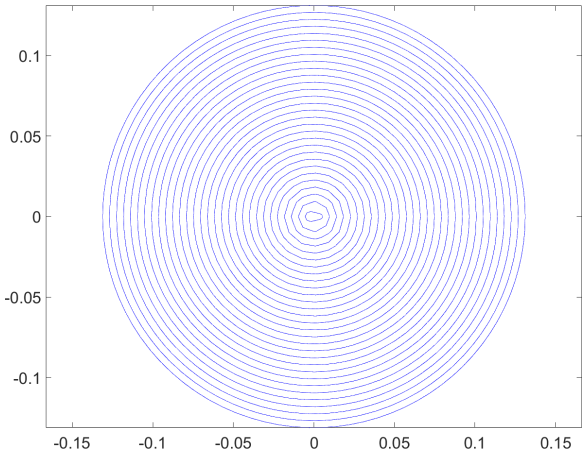

(c) A simple wire dipole test coil.

Figure 161: Test coils.

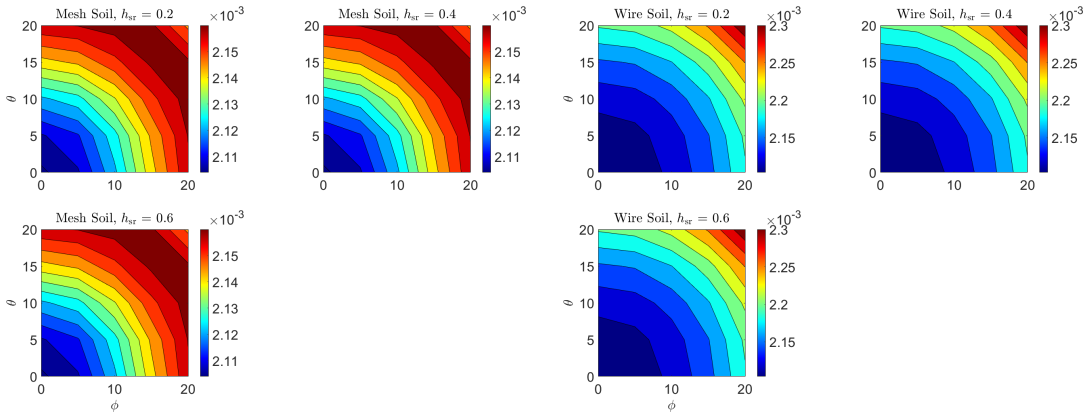

(a) Stream function.

(b) Wire coils.

Figure 162: Soil response over various heights and tilts for the dipole/dipole test coils.

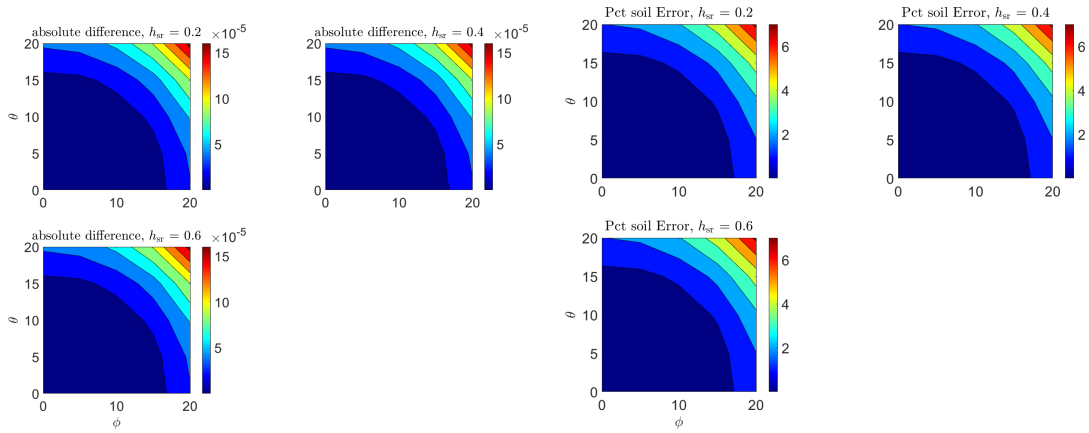

(a) Absolute difference between the soil response of the stream function and wire coils.

(b) Percent error between the soil response of the stream function and wire coils.

Figure 163: Errors between the soil response of the stream function and the wire coil conversion for the dipole/dipole coils.

C.2 Dipole/Quadrupole Test

Testing the same scenario using a dipole/quadrupole representation, as shown in Figures 164(a) and 164(b) as stream functions and in Figures 164(c) and 164(d) as wires, yields a somewhat different result to the dipole/dipole coils. When level, the dipole/quadrupole coils do not couple well to the soil, and as a result of the quadrupole symmetry, when tilted in Θ, the soil response does not change much, while there is considerable change when tilted in ϕ, as can be seen in Figure 165. While the soil responses actually match well, there is a large percent error when the coils are level as a result of the deep null in the soil response in this orientation (Figure 166).

C.3 Soil Response and Wire Conversions

The conversion to wires from stream functions does cause small errors in the soil response. These differences are only noticeable when the soil response is nulled. Also, somewhat surprisingly, the number of turns used for the wire conversion does not appear to greatly impact the accuracy.

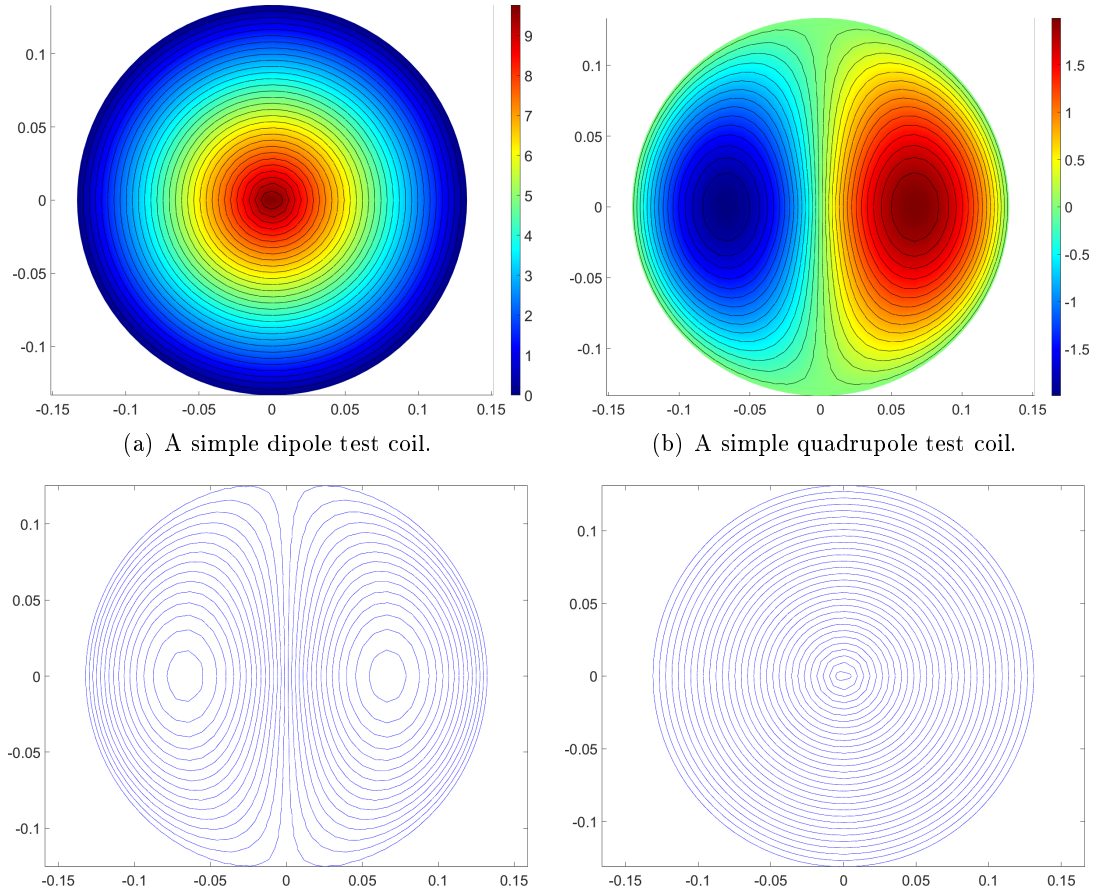

(a) A simple dipole test coil.

(b) A simple quadrupole test coil.

(c) Wire conversion of the dipole coil.

(d) Wire conversion of the quadrupole coil.

Figure 164: Illustration of the conversion of a dipole and quadrupole stream function test coils to the associated wire coils.

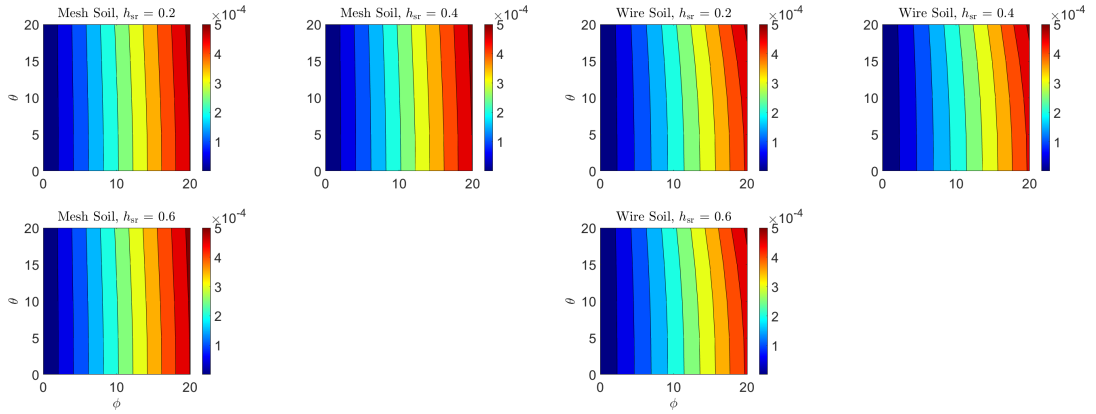

(a) Stream function.

(b) Wire coils.

Figure 165: Soil response over various heights and tilts for the dipole/quadrupole test coils

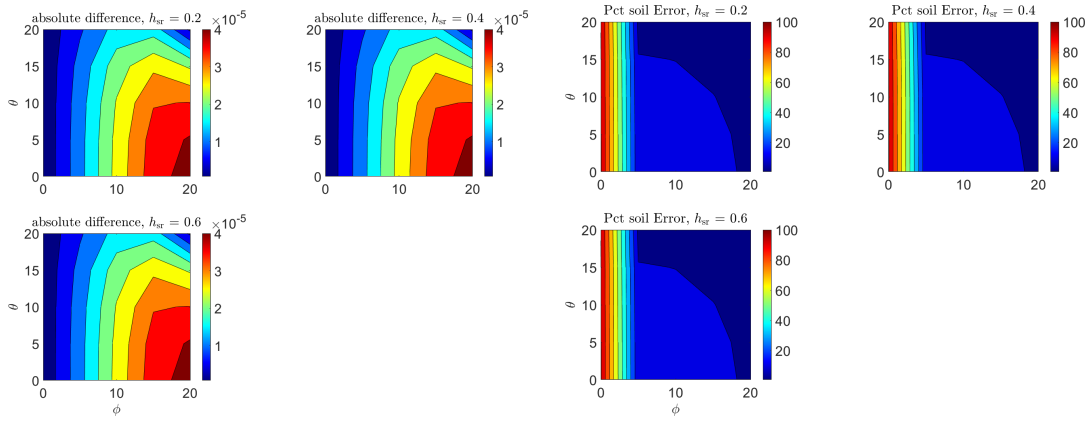

(a) Absolute difference between the soil response of the stream function and wire coils.

(b) Percent error between the soil response of the stream function and wire coils.

Figure 166: Errors between the soil response of the stream function and the wire coil conversion for the dipole/quadrupole coils.

APPENDIX D

VARIABLE RESISTANCE

D.1 Conversion to Spiral

The coils are first viewed as rotationally symmetric, such that they consist of discs or annuli that support a surface current density, $\vec{K}$, with zero divergence. Therefore, the surface current density is only directed in the $\hat{\phi}$ direction and has a profile such as that in Figure 167. The total current, I, flowing on a surface perpendicular to a line segment, Δr, can be written as $I = \vec{K}\Delta r$. It is desirable to approximate this surface current with a spiral. Obviously, this would be simple to do with loops of current, but unconnected loops of current require multiple driving sources. A spiral seems to be the obvious choice. Of course, the spiral will introduce a small amount of error because the current will now be partially $\hat{\rho}$-directed instead of completely $\hat{\phi}$-directed.

In transforming to a spiral, I must be constant because only one wire will be used. For a given Δr, there must also be some movement, $\Delta\phi$, in the $\hat{\phi}$ direction for a given current density, $\vec{K}$. If there is movement in Δr along a current distribution such as that in Figure 168, then there must also be movement in $\Delta\phi$ around the disc in order to place enough current into the space $\Delta\phi\Delta r$. Therefore,

$$\vec{K} = \frac{I}{\Delta r}\frac{\Delta\phi}{2\pi}\,. \tag{129}$$

$$K = \frac{I}{\Delta r}\frac{\Delta\phi}{2\pi} = \frac{I}{2\pi}\frac{d\phi}{d\rho} = \sum_{n=0}^{N} a_n F_n(\rho)\,. \tag{130}$$

This smears I over an area of $\Delta r\Delta\phi$. Expand ϕ as

$$\phi = \sum_{m=0}^{M} g_m(\rho)\,. \tag{131}$$

$$\frac{d\phi}{d\rho} = \frac{2\pi}{I}\sum_{n=0}^{N} F_n(\rho)\,. \tag{132}$$

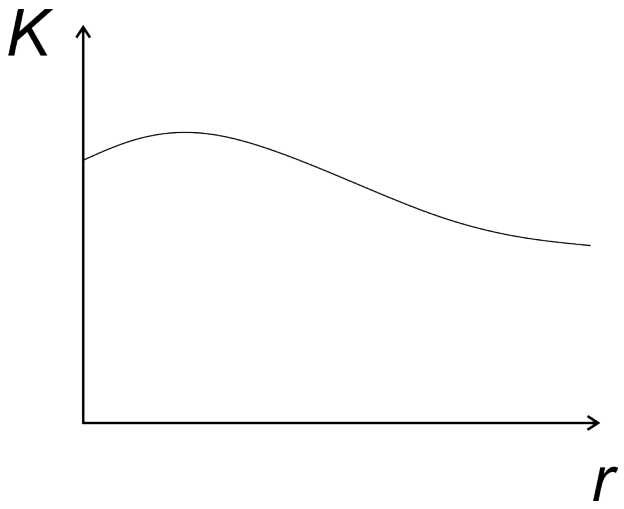

Figure 167: K vs r for a given value of ϕ.

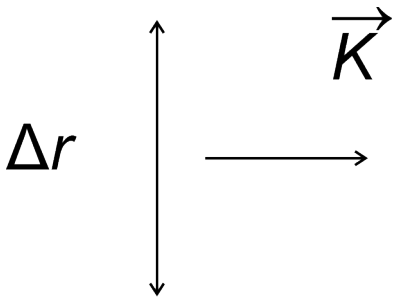

Figure 168: Surface Current.

Then, rearranging terms,

$$d\phi = \frac{2\pi}{I}\sum_{n=0}^{N} F_n(\rho)d\rho\,. \tag{133}$$

$$\phi = \frac{2\pi}{I}\sum_{n=0}^{N}\int F_n(\rho)d\rho = \sum_{m=0}^{M} g_m\,. \tag{134}$$

$$\phi = \frac{2\pi}{I}\underbrace{\int F_n(\rho)d\rho}_{Q(\rho)}\,. \tag{135}$$

$$\phi(\rho) = \frac{2\pi}{I}[Q(\rho)+c]\,. \tag{136}$$

Simultaneous equations can now be written to solve for the current and constant c given a chosen number of turns and starting point of $\phi = 0$. Choose $2\pi z$ for an even number of spiral turns.

$$0 = \frac{2\pi}{I}Q(\rho_{min}) + c\,. \tag{137}$$

$$2\pi z = \frac{2\pi}{I}Q(\rho_{max}) + c\,. \tag{138}$$

$$\begin{bmatrix} 2\pi Q(\rho_{min}) & 1 \\ 2\pi Q(\rho_{max}) & 1 \end{bmatrix}\begin{bmatrix} \frac{1}{I} \\ c \end{bmatrix} = \begin{bmatrix} 0 \\ 2\pi z \end{bmatrix}\,. \tag{139}$$

where $B_{min} = \frac{2\pi Q_{min}}{I}$ and $B_{max} = \frac{2\pi Q_{max}}{I}$.

Take a given surface current density distribution, J. Then the total current flowing in the $\hat{\phi}$ direction is $I_{tot} = \int_{\rho_{min}}^{\rho_{max}} Jd\rho$, and the value for I is determined by $I = \frac{I_{tot}}{Numturns}$. If a specific number of turns is chosen and there are still an even number of turns, then the following can be done (note, "turns" denotes the total amount of ϕ traversed by the spiral, thus a reversal can cause a non-integer number of turns)

$$\begin{bmatrix} 0 & -1 \\ 2\pi & -1 \end{bmatrix}\begin{bmatrix} z \\ c \end{bmatrix} = \begin{bmatrix} B_{min} \\ B_{max} \end{bmatrix}\,. \tag{140}$$

Now the polynomial representing the current density returned by the optimization algorithm will not pass through zero ϕ at either edge of the coil unless the coil has no hole in the center.

REFERENCES

[1] Baum, C. E., Detection and Identification of Visually Obscured Targets, ch. 6. Taylor and Francis, 1999.

[2] Baum, C. E., "Two-dimensional coils for low-frequency magnetic illumination and detection," Sensor and Simulation Notes, vol. 406, pp. 1–49, Nov. 1996.

[3] Baum, C. E., "Three-dimensional coils for low-frequency magnetic illumination and detection," Sensor and Simulation Notes, vol. 411, pp. 1–64, May 1997.

[4] Bell, A. G., Upon the Electrical Experiments to Determine the Location of the Bullet in the Body of the Late President Garfield: and upon a Successful Form of Induction Balance for the Painless Detection of Metallic Masses in the Human Body. Washington, D.C.: Gibson Brothers Printers, 1882.

[5] Boyd, S., Boyd, S. P., and Vandenberghe, L., Convex optimization. Cambridge university press, 2004.

[6] Candy, B. H., "A method and apparatus of discrimination detection using multiple frequencies to determine a recognizable profile of an undesirable substance," July 1990. US Patent 4,942,360.

[7] Candy, B. H., "Pulse induction time domain metal detector," Nov. 1996. US Patent 5,576,624.

[8] Chew, W. C., Waves and Fields in Inhomogeneous Media, pp. 485–487. Piscataway, NJ: IEEE Press, 1995.

[9] Collins, L. M. and others, "Sensor fusion of EMI and GPR data for improved land mine detection," in Proc. SPIE, vol. 4742, pp. 872–879, Aug. 2002.

[10] Druyts, P., Analysis of Environmental Effects on Electromagnetic Induction Sensors. PhD thesis, ENSTA Bretagne, France, 2011.

[11] Druyts, P. and others, "Modeling the response of electromagnetic induction sensors to inhomogeneous magnetic soils with arbitrary relief," IEEE Trans. Geosci. Remote Sens., vol. 47, pp. 2627–2638, Aug. 2009.

[12] Druyts, P., Analysis of Environmental Effects on Electromagnetic Induction Sensors. PhD thesis, Institute of Information and Communication Technologies, Electronics and Applied Mathematics, Université Catholique de Louvain, Louvain-la-Neuve, Belgium, Oct. 2011.

[13] Druyts, P., Das, Y., Craeye, C., and Acheroy, M., "Modeling the response of electromagnetic induction sensors to inhomogeneous magnetic soils with arbitrary relief," IEEE Trans. Geosci. Remote Sens., vol. 47, pp. 2627–2638, Aug. 2009.

[14] Fisher, G. R., "Metalloscope," Jan. 1937. US Patent 2,066,561.

[15] Geophex, "Sensor configurations [online]." Available: http://www.geophex.com/Pubs/SensorConfigurations.htm, April 2016. Directional GEM-5 and GEM-5 Array.

[16] Gorski, J., Pfeuffer, F., and Klamroth, K., "Biconvex sets and optimization with biconvex functions: a survey and extensions," Mathematical methods of operations research, vol. 66, no. 3, pp. 373–407, 2007.

[17] Grant, M. and Boyd, S., "The cvx user's guide, release 2.0. user manual (2013)," URL: http://web. cvxr. com/cvx/doc/CVX. pdf, 2018.

[18] Grant, M. and Boyd, S., "Graph implementations for nonsmooth convex programs," in Recent Advances in Learning and Control (Blondel, V., Boyd, S., and Kimura, H., eds.), Lecture Notes in Control and Information Sciences, pp. 95–110, Springer-Verlag Limited, 2008. `http://stanford.edu/~boyd/graph_dcp.html`.

[19] Grant, M. and Boyd, S., "CVX: Matlab software for disciplined convex programming, version 2.1." `http://cvxr.com/cvx`, Mar. 2014.

[20] Gurbuz, A. C., Scott Jr., W. R., and McClellan, J. H., "Location estimation using a broadband electromagnetic induction array," in Proc. SPIE, vol. 7303, pp. 73030U–1–73030U–9, May 2009.

[21] Hanselman, D., Contour PLot for Scattered Data, 2021. [Online].

[22] Haus, H. A. and Melcher, J. R., Electromagnetic Fields and Energy, ch. 3, pp. 71–76. Prentice Hall, 1989.

[23] Hayes, C. E., Low-rank model exploitation of electromagnetic induction sensors. PhD thesis, Georgia Institute of Technology, 2020.

[24] Hedden, C. A., "Transformer for a metal locator," Sept. 1938. US Patent 2,129,058.

[25] Hirschi, R. E., "Induction balance metal detector with inverse discrimination," May 1977. US Patent 4,024,468.

[26] Johnson, D. L., "Balanced search loop for metal detector," Oct. 1981. US Patent 4,293,816.

[27] Kerr, A. J., Theoretical performance bounds for the estimation of target parameters from electromagnetic induction data. PhD thesis, Georgia Institute of Technology, 2020.

[28] Kim, S. and Yoo, S., "Comparison of planar type coils for efficient power supply to implantable devices," Biomedical Engineering Letters, vol. 2, pp. 179–185, Sept. 2012.

[29] Kohler, H. W., "Sensing coil arrangement for a metal detector," June 1971. US Patent 3,588,687.

[30] Kreuger, K. R., Model design for algorithmic efficiency in electromagnetic sensing. PhD thesis, Georgia Institute of Technology, 2013.

[31] Kumar, A. and Bottomley, P. A., "Optimized quadrature surface coil designs," Magnetic Resonance Materials in Physics, Biology and Medicine, vol. 21, no. 1, pp. 41–52, 2008.

[32] Lemdiasov, R. A. and Ludwig, R., "Design and implementation of uniplanar gradient field coil for magnetic resonance imaging," IEEE Trans. Magn., vol. 40, no. 4, pp. 17–29, 2004.

[33] Lopez-Pena, S., Polimeridis, A. G., and Mosig, J. R., "On the analytic-numeric treatment of weakly singular integrals on arbitrary polygonal domains," Progress In Electromagnetics Research, vol. 117, no. ARTICLE, pp. 339–355, 2011.

[34] MacDonald, J. and Lockwood, J. R., Alternatives for landmine detection. Santa Monica, CA, USA: RAND, 2003.

[35] Minelab, "Coil selection guide [online]." Available: http://www.minelab.com, May 2017. KBA 02-5.

[36] Neumann, F. E., "Allgemeine gesetze der inducirten elektrischen ströme," Annalen der Physik, vol. 146, no. 1, pp. 31–44, 1846.

[37] Peeren, G. N., "Stream function approach for determining optimal surface currents," J. Computational Phys., vol. 191, pp. 305–321, Oct. 2003.

[38] Pellicer-Guridi, R., Vogel, M. W., Reutens, D. C., and Vegh, V., "Towards ultimate low frequency air-core magnetometer sensitivity," Scientific reports, vol. 7, no. 1, p. 2269, 2017.

[39] Penland, R. S., "Metal detecting device with inductively coupled coaxial transmitter and receiver coils," Oct. 1969. US Patent 3,471,773.

[40] Persson, P.-O. and Strang, G., "A simple mesh generator in matlab," SIAM review, vol. 46, no. 2, pp. 329–345, 2004.

[41] Peters, A. M. and Bowtell, R. W., "Biplanar gradient coil design by simulated annealing," Magnetic Resonance Materials in Physics, Biology and Medicine, vol. 2, no. 3, pp. 387–389, 1994.

[42] Peterson, A. F., Ray, S. L., and Mittra, R., Computational Methods for Electromagnetics, pp. 112–115. IEEE Press, 1998.

[43] Pissanetzky, S., "Minimum energy MRI gradient coils of general geometry," Measurement Science and Technology, vol. 3, no. 7, pp. 667–673, 1992.

[44] Podhrasky, R. J., "Compact metal detector of the balanced induction type," Dec. 1983. US Patent 4,423,377.

[45] Poole, M. and others, "Minimax current density coil design," J. Phys. D: Appl. Phys., vol. 43, no. 9, pp. 1–13, 2010.

[46] Reed, M. A. and Scott, Jr., W. R., "Optimization of planar coils for electromagnetic induction systems," in Geoscience and Remote Sensing Symposium (IGARSS), pp. 2613–2616, July 2014.

[47] Reed, M. A. and Scott Jr., W. R., "Formulation of a method for the optimization of coils for electromagnetic induction systems in the presence of magnetic soil," in Geoscience and Remote Sensing Symposium (IGARSS), pp. 4304–4307, IEEE, 2015.

[48] Reed, M. A. and Scott Jr., W. R., "Formulation for a practical implementation of electromagnetic induction coils optimized using stream functions," in SPIE Defense+Security, pp. 982304–982304, International Society for Optics and Photonics, 2016.

[49] Reed, M. A. and Scott Jr., W. R., "Improved method for the optimization of coils in the presence of magnetic soil," in Geoscience and Remote Sensing Symposium (IGARSS), 2016 IEEE International, pp. 7489–7492, IEEE, 2016.

[50] Scott, Jr., W. R., "Broadband electromagnetic induction sensor for detecting buried landmines," in IEEE Geosci. Remote Sens. Symp., pp. 22–25, July 2007.

[51] Scott, Jr., W. R., "Broadband array of electromagnetic induction sensors for detecting buried landmines," in IEEE Geosci. Remote Sens. Symp., vol. 2, pp. II–375–II–378, July 2008.

[52] Scott, Jr., W. R. and others, "Experimental detection and discrimination of buried targets using an improved broadband CW electromagnetic induction sensor," in Proc. SPIE, vol. 9072, pp. 90720C–1–90720C–15, May 2014.

[53] Scott, Jr., W. R. and Larson, G. D., "Measured dipole expansion of discrete relaxations to represent the electromagnetic induction response of buried metal targets," in Proc. SPIE, vol. 7664, pp. 76640E–1–76640E–11, Apr. 2010.

[54] Shoemaker, D. K., "Metal detector with circuits for automatically screening out the effects of offset and mineralized ground," Nov. 1988. US Patent 4,783,630.

[55] Silvester, P. P. and Omeragic, D., "Sensitivity maps for metal detector design," IEEE Trans. Geosci. Remote Sens., vol. 34, pp. 788–792, May 1996.

[56] Smythe, W. R., Static and Dynamic Electricity, ch. 8, pp. 310–318. McGraw-Hill Book Company, Inc., second ed., 1950.

[57] Sturm, J. F., "Using sedumi 1.02, a matlab toolbox for optimization over symmetric cones," Optimization methods and software, vol. 11, no. 1-4, pp. 625–653, 1999.

[58] Thompson, F. H., "Coil arrangement for search head of a metal detector," Mar. 1981. US Patent 4,255,711.

[59] Tomasi, D. and others, "Fast optimization of a biplanar gradient coil set," Journal of Magnetic Resonance, vol. 140, no. 2, pp. 325–339, 1999.

[60] Turner, R., "A target field approach to optimal coil design," J. Phy. D: Appl. Phy., vol. 19, no. 8, p. L147, 1986.

[61] Turner, R., "Minimum inductance coils," J. Phys. E: Sci. Instrum., vol. 21, pp. 948–952, May 1988.

[62] Vesselle, H. and Collin, R. E., "The signal-to-noise ratio of nuclear magnetic resonance surface coils and application to a lossy dielectric cylinder model - part I: Theory," IEEE Trans. Biomed. Eng., vol. 42, pp. 497–506, Aug. 1995.

[63] Weaver, B. C., "Dual field metal detector," Oct. 1999. US Patent 5,969,528.

[64] Wei, M., Scott, Jr., W. R., and McClellan, J. H., "Robust estimation of the discrete spectrum of relaxations for electromagnetic induction responses," IEEE Trans. Geosci. Remote Sens., vol. 48, pp. 1169–1179, Mar. 2010.

[65] Wendell, R. E. and Hurter Jr, A. P., "Minimization of a non-separable objective function subject to disjoint constraints," Operations Research, vol. 24, no. 4, pp. 643–657, 1976.

[66] Westersten, A., "Metal detector with improved receiver coil," Feb. 2010. US Patent 7,656,153.

[67] Wheeler, H. A., "Electrical apparatus for locating bodies having anomalous electrical admittances," Dec. 1936. US Patent 2,066,135.

[68] Wilson, P. S., "Anti-falsing and zero nulling search head for a metal detector," Aug. 1982. US Patent 4,345,208.

[69] Windsor, H. H., "Buried shells found by induction balance," Popular Mechanics, p. 205, February 1916.

[70] Won, I. J., "Apparatus and method for detecting a weak induced magnetic field by means of two concentric transmitter loops," Sept. 1996. US Patent 5,557,206.

[71] Wu, X., Tian, J., and others, "Comparison of radiofrequency body coils for mri at 3 tesla: a simulation study using parallel transmission on various anatomical targets," NMR in biomedicine, pp. 1332–1344, Oct. 2015.

VITA

Mark Reed is a Georgia native. He graduated from Glynn Academy in Brunswick, GA in 2005 and received the BSEE and MSECE degrees from the Georgia Institute of Technology in 2009 and 2011, respectively. His research interests span areas within low frequency electromagnetics, including design and optimization of electromagnetic induction coils for subsurface sensing, and also other areas such as ground penetrating radar, antenna design, and RF engineering.